

NASA Contractor Report 195283

Development of Sensors for Ceramic Components in Advanced Propulsion Systems

Phase II – Temperature Sensor Systems Evaluation

W. H. Atkinson, M. A. Cyr and R. R. Strange
United Technologies Corporation
Pratt & Whitney
East Hartford, Connecticut

October 1994

Prepared for
Lewis Research Center
Under Contract NAS3-25141

Page intentionally left blank

TABLE OF CONTENTS

<i>Section</i>		<i>Page</i>
1. SUMMARY		1
2. INTRODUCTION		2
3. PYROMETRY		5
3.1 Emittance Measurements		5
3.2 Pyrometry Uncertainty Analysis – Emittance Effects		14
3.3 Translucency Testing		25
3.4 Results		29
3.5 Conclusions		30
3.6 Recommendations		30
4. THIN-FILM SENSORS		31
4.1 Sample Preparation		31
4.2 Application Methods		31
4.2.1 Ion Beam Etch Deposition		31
4.2.2 Evaporation Plus Ion Implantation		36
4.2.3 Radio Frequency Sputtering		37
4.3 Testing Procedure		38
4.4 Results		69
4.5 Conclusions		69
4.6 Recommendations		69
5. THERMOGRAPHIC PHOSPHORS		70
5.1 Introduction		70
5.2 Sample Preparation		70
5.3 Test Procedure		82
5.4 Results		83
5.5 Data Analysis		90
5.6 Sample Analyses		92
5.6.1 YAG:Tb Electron Beam Deposited on Si ₃ N ₄ Substrate – Analysis Results ..		99
5.6.2 YAG:Tb Electron Beam Deposited on a ZrO ₂ Substrate – Analysis Results ..		99
5.7 Conclusions		112
5.8 Recommendations		112
APPENDIX A Tabular Data from the Thin-Film Thermocouple Testing		113
APPENDIX B Summary of Samples and Testing Times		137
APPENDIX C Sample Raw Data of the Phosphor Systems		141
REFERENCES		144

Trade names or manufacturers' names are used in this report for identification only. This usage does not constitute an official endorsement, either expressed or implied, by the National Aeronautics and Space Administration.

LIST OF ILLUSTRATIONS

<i>Figure</i>		<i>Page</i>
1	Sample Materials As Received	4
2	Schematic Diagram of Thermogage Emissometer	6
3	Photograph of Thermogage Emissometer	6
4	Emissometer Oscilloscope Trace	7
5	Measured Normal Spectral Emittance of Silicon Nitride	7
6	Measured Normal Spectral Emittance of Silicon Carbide	8
7	Measured Normal Spectral Emittance of Compglas®	8
8	Measured Normal Spectral Emittance of 7% Yttria Stabilized Zirconia	9
9	Measured Normal Spectral Emittance of Mullite	9
10	Compiled Normal Spectral Emittance of Silicon Nitride	11
11	Compiled Normal Spectral Emittance of Silicon Carbide	11
12	Compiled Normal Spectral Emittance of Compglas®	12
13	Compiled Normal Spectral Emittance of 7% Yttria Stabilized Zirconia	12
14	Compiled Normal Spectral Emittance of Mullite	13
15	Results of Tests to Investigate the Variation of the Spectral Emittance of 7% Yttria Stabilized Zirconia	13
16	Error in Indicated Temperature as a Function of Emittance Error	16
17	Summary of Pratt & Whitney Emittance Data on Silicon Nitride	17
18	Nominal Pyrometer Corrections for Silicon Nitride at 1925K	18
19	Indicated Temperature Uncertainty for Silicon Nitride at 1925K	18
20	Summary of Pratt & Whitney Emittance Data on Silicon Carbide	19
21	Nominal Pyrometer Corrections for Silicon Carbide at 1925K	19
22	Indicated Temperature Uncertainty for Silicon Carbide at 1925K	20

LIST OF ILLUSTRATIONS (continued)

<i>Figure</i>		<i>Page</i>
23	Summary of Pratt & Whitney Emittance Data on Compglas®	20
24	Nominal Pyrometer Corrections for Compglas® at 1925K	21
25	Indicated Temperature Uncertainty for Compglas® at 1925K	21
26	Summary of Pratt & Whitney Emittance Data on 7% Yttria Stabilized Zirconia	22
27	Nominal Pyrometer Corrections for 7% Yttria Stabilized Zirconia at 1925K ..	22
28	Indicated Temperature Uncertainty for 7% Yttria Stabilized Zirconia at 1925K	23
29	Summary of Pratt & Whitney Emittance Data on Mullite	23
30	Nominal Pyrometer Corrections for Mullite at 1925K	24
31	Indicated Temperature Uncertainty for Mullite at 1925K	24
32	Normal Spectral Transmittance of McDaniel Mullite from Reference 3	26
33	Schematic Diagram of Transmission Test	26
34	Measured Transmission Data for Sapphire and Zirconia at 0.9 Microns	28
35	Perfect Lambertian Scatterer	28
36	Typical Loss Curves for Fiber Optic Materials	29
37	Ion Beam Etch Deposition Sensors Applied to Silicon Nitride	33
38	Ion Beam Etch Deposition Sensor Applied to Compglas®	33
39	Ion Beam Etch Deposition Sensor Applied to Mullite	34
40	Ion Beam Etch Deposition Sensor Applied to 7% Yttria Stabilized Zirconia ..	34
41	Ion Beam Etch Deposition Sensor Applied to Silicon Carbide	35
42	Ion Beam Etch Deposition Sensors Applied to Silicon Nitride After the Substrate Was Heat Treated	35
43	Ion Beam Etch Deposition Sensor Applied to Silicon Nitride After Post Application Heat Treat	36

LIST OF ILLUSTRATIONS (continued)

<i>Figure</i>		<i>Page</i>
44	Tube Furnace with Top Half Removed Showing Sample in Position for Thermal Testing	39
45	EMF Data from Sensor SCC-S5	39
46	Photograph of Junction Area of Sample SCC-S5 After Two Cycles to 800K. Black regions are areas where the films have lifted from the silicon nitride.	40
47	EMF Data from Sensor SCC-S3	42
48	Photograph of Sensor SCC-S3 After One Cycle to 915K	42
49	Photograph of the Junction Area of Sensor SCC-S3 After One Cycle to 915K	43
50	Photograph of Platinum Leg of Sensor SCC-S3 After One Cycle to 915K	43
51	Photograph of Rhodium Leg of Sensor SCC-S3 After One Cycle to 915K	44
52	EMF Data for Sensor SCC-S4	44
53	EMF Data for Sensor SCC-S1	45
54	EMF Data for Sensor SCC-S1 with 30-Minute Holds at Each Temperature Level	45
55	Experimental Platinum Rhodium Wire Thermocouple Data Versus Book Values	46
56	EMF Data for Sensor SCC-C1	46
57	Cameca – Microbeam Spectrum of Platinum Leg on Sensor SCC-C2	48
58	Cameca – Microbeam Spectrum of Rhodium Leg on Sensor SCC-C2	49
59	EMF Data on Sensor IIE-S1 – First Four Cycles	50
60	EMF Data on Sensor IIE-S1 – Last Seven Cycles	50
61	Photograph of Junction Area of Sensor IIE-S1 After One Cycle to 1144K	51
62	Photograph of Platinum Leg of Sensor IIE-S1 After One Cycle to 1144K Showing the Platinum Bubbled at the Edge	52
63	Photograph of Entire Sample of Sensor IIE-S1 After Seven Cycles to 1144K ..	53

LIST OF ILLUSTRATIONS (continued)

<i>Figure</i>		<i>Page</i>
64	Photograph of Sensor IIE-S1 After Seven Cycles to 1144K	53
65	Photograph of Rhodium Leg of Sensor IIE-S1 After Seven Cycles to 1144K ..	54
66	Photograph of Junction Area of Sensor IIE-S1 After Seven Cycles to 1144K ..	54
67	EMF Data of Sensor IIE-S2	55
68	Photograph of Junction Area of Sensor IIE-S2 As Fabricated	55
69	Photograph of Sensor IIE-S2 As Fabricated Showing Cracks in the Overlap Area	56
70	Photograph of Platinum Leg of Sensor IIE-S2 As Fabricated	56
71	Photograph of Rhodium Leg of Sensor IIE-S2 As Fabricated	57
72	Photograph of Entire Sample of Sensor IIE-S2 After One Cycle to 1144K	57
73	Photograph of Sensor IIE-S2 After One Cycle to 1144K	58
74	Photograph of Junction Area of Sensor IIE-S2 After One Cycle to 1144K	58
75	Photograph of Junction Area of Sensor IIE-S2 After One Cycle to 1144K	59
76	EMF Data for Sensor IIE-C1	59
77	Photograph of Junction Area of Sensor IIE-C1 After One Cycle to 1144K	60
78	EMF Data for Sensor IIE-C2	60
79	Photograph of Sensor IIE-C2 After Four Cycles to 1144K	61
80	Photograph of Junction Area of Sensor IIE-C2 After Four Cycles to 1144K ...	61
81	Photograph of Junction Area of Sensor IIE-C2 After Four Cycles to 1144K ...	62
82	Photograph of Platinum Leg of Sensor IIE-C2 After Four Cycles to 1144K ...	62
83	EMF Data for Sensor RFS-S1	63
84	Photograph of Sensor RFS-S1 After Two Cycles to 1144K	63
85	Photograph of Junction Area of Sensor RFS-S1 After Two Cycles to 1144K ...	64
86	Photograph of Platinum Leg of Sensor RFS-S1 After Two Cycles to 1144K ...	64

LIST OF ILLUSTRATIONS (continued)

<i>Figure</i>		<i>Page</i>
87	EMF Data for Sensor RFS-S2	65
88	Photograph of Junction Area of Sensor RFS-S2 As Fabricated	66
89	Photograph of Rhodium Leg of Sensor RFS-S2 As Fabricated	66
90	Photograph of Sensor RFS-S2 After One Cycle to 1144K	67
91	Photograph of Junction Area of Sensor RFS-S2 After One Cycle to 1144K	67
92	Photograph of Rhodium Leg of Sensor RFS-S2 After One Cycle to 1144K	68
93	EMF Data for Sensor IIE-S3	68
94	Plot of Film Versus Junction and Film Versus Clamp Temperatures for Sensor IIE-C1	71
95	Plot of Film Versus Junction and Film Versus Clamp Temperatures for Sensor IIE-C2	71
96	DoE Calibration for $\text{Y}_2\text{O}_3:\text{Eu}$ Phosphor	77
97	DoE Calibration for YAG:Tb Phosphor	77
98	Emission Spectra for $\text{Y}_2\text{O}_3:\text{Eu}$ Pressed Pellet Standard	78
99	Emission Spectra for $\text{Y}_2\text{O}_3:\text{Eu}$ As Deposited and After Heat Treat	79
100	Emission Spectra for YAG:Tb Pressed Pellet Standard	80
101	Emission Spectra for YAG:Tb As Deposited and After Heat Treat	81
102	Schematic Diagram of UTRC Fluorescence Testing Setup	82
103	UTRC Calibration Data for $\text{Y}_2\text{O}_3:\text{Eu}$ Phosphor	84
104	UTRC Calibration Data for YAG:Tb Phosphor	84
105	Durability Test of $\text{Y}_2\text{O}_3:\text{Eu}$ Electron Beam Deposited on 7% Yttria Stabilized Zirconia	86
106	Thermal Cycling Test of $\text{Y}_2\text{O}_3:\text{Eu}$ Electron Beam Deposited on 7% Yttria Stabilized Zirconia	86
107	Durability Test of $\text{Y}_2\text{O}_3:\text{Eu}$ Electron Beam Deposited on Silicon Nitride	87

LIST OF ILLUSTRATIONS (continued)

<i>Figure</i>		<i>Page</i>
108	Durability Test of Y ₂ O ₃ :Eu RF Sputtered on 7% Yttria Stabilized Zirconia	87
109	Durability Test of Y ₂ O ₃ :Eu RF Sputtered on Silicon Nitride	88
110	Durability Test of YAG:Tb Electron Beam Deposited on 7% Yttria Stabilized Zirconia	89
111	Thermal Cycling Test of YAG:Tb Electron Beam Deposited on 7% Yttria Stabilized Zirconia	89
112	Comparison Between DoE and UTRC Calibrations for Y ₂ O ₃ :Eu	90
113	Comparison Between DoE and UTRC Calibrations for YAG:Tb	91
114	UTRC Data Reduction Method	91
115	Simulation of UTRC Data System 100 Nanosecond Decay Time	93
116	Simulation of UTRC Data System 250 Nanosecond Decay Time	94
117	Simulation of UTRC Data System 500 Nanosecond Decay Time	95
118	Simulation of UTRC Data System 1 Microsecond Decay Time	96
119	Simulation of UTRC Data System 1.5 Microsecond Decay Time	97
120	Simulation of UTRC Data System 2 Microsecond Decay Time	98
121	YAG:Tb Electron Beam Deposited on Silicon Nitride After Heat Treating and After Thermal Testing	100
122	SEM Analysis of YAG:Tb Electron Beam Deposited on Silicon Nitride	101
123	EDS Analysis of YAG:Tb Electron Beam Deposited on Silicon Nitride	102
124	Electron Microprobe Scanning Image of Coating of YAG:Tb Electron Beam Deposited on Silicon Nitride After Thermal Cycling to 1773K	103
125	Electron Microprobe Scanning Image of Coating/Substrate Interface of YAG:Tb Electron Beam Deposited on Silicon Nitride After Thermal Cycling to 1773K	104
126	YAG:Tb Electron Beam Deposited on Zirconia After Heat Treating and After Thermal Testing	105
127	SEM Analysis of YAG:Tb Electron Beam Deposited on 7% Yttria Stabilized Zirconia	106

LIST OF ILLUSTRATIONS (continued)

<i>Figure</i>		<i>Page</i>
128	EDS Analysis of YAG:Tb Electron Beam Deposited on 7% Yttria Stabilized Zirconia	107
129	XPS Surface Analysis of YAG:Tb Electron Beam Deposited on 7% Yttria Stabilized Zirconia	108
130	XPS Surface Analysis of YAG:Tb Electron Beam Deposited on 7% Yttria Stabilized Zirconia After Thermal Testing	109
131	Electron Microprobe Scanning Image of YAG:Tb/Zirconia Interface of YAG:Tb Deposited on 7% Yttria Stabilized Zirconia After Heat Treat	110
132	Electron Microprobe Scanning Image of YAG:Tb/Zirconia Interface of YAG:Tb Deposited on 7% Yttria Stabilized Zirconia After Thermal Testing .	111

LIST OF TABLES

<i>Table</i>		<i>Page</i>
1	Chemical Analysis of Tested Mullite and Si ₃ N ₄	10
2	Emittance Uncertainties	16
3	Thin-Film Sensors Test Result Summary	70
4	Sample Intensities	74
5	Summary of Fluorescence Modeling Results	92

1. SUMMARY

The objectives of the "Development of Sensors for Ceramic Components in Advanced Propulsion Systems" program are to analyze, evaluate and recommend sensor concepts for the measurement of surface temperature, strain and heat flux on ceramic components for advanced propulsion systems and to conduct laboratory development of sensor systems for the measurement of surface temperatures. Such sensor systems require unique properties and exceptional durability due to both the need for compatibility with the nonmetallic materials expected to be used in advanced propulsion systems and the need to operate in an extremely hostile environment with regard to temperature, pressure and cycling.

The "Development of Sensors for Ceramic Components in Advanced Propulsion Systems" program is separated into two phases. The objective of Phase I was to provide a survey and analysis of sensor system concepts for measuring surface temperature, strain and heat flux on ceramic components in advanced propulsion systems. Possible designs, components, and promising concepts for development were identified. An analysis was performed to determine which of the promising concepts are the most appropriate for ceramic components in advanced propulsion systems. Three most promising approaches in each category were recommended for further development. Pyrometry, thin-film sensors, and thermographic phosphors were selected for temperature measurement.

The objectives of Phase II are to fabricate and conduct laboratory demonstration tests of these three systems. This report provides a detailed description of the Phase II effort, including conclusions and recommendations for each of the systems evaluated.

2. INTRODUCTION

In Phase I of this program, a survey of measurement techniques for temperature, strain and heat flux applicable for use on ceramic materials at very high temperatures was conducted. An evaluation of the identified techniques was then performed to select the three most promising approaches in each category. The evaluation considered a number of factors, but the useable temperature range and compatibility with the ceramic or composite materials were the major constraints. The desire to go to 2260K makes noncontact optical techniques very appealing. On this basis, pyrometry and thermographic phosphors were selected. A surface mounted contact sensor would be required if optical access was not feasible. Thin-film thermocouples are amenable to the ceramic and composite materials. Even though the thin-film thermocouples are temperature limited, they were selected as a sensor concept feasible for moderate temperature applications. A discussion of the survey results and evaluation procedure is given in Reference 1 and the results are summarized below.

Pyrometry is a noncontact technique and, hence, is not temperature limited. In fact, the higher the temperature, the more energy the pyrometer has to work with. There are drawbacks that complicate the implementation of pyrometry. Accurate measurement of temperatures by pyrometry requires a knowledge of the emittance of the surface. For ceramic materials the emittances vary widely, and in some instances are a strong function of both wavelength and temperature. The transparency or translucency of the materials give rise to problems in interpreting the results. Pyrometry is also sensitive to the presence of reflected radiation which can produce a significant bias in the results.

The emittance of the materials is being measured both at Pratt & Whitney and United Technologies Research Center (UTRC). A commercial emissometer is currently being used at Pratt & Whitney to measure the emittance of ceramic materials at different wavelengths and temperatures. The results obtained with this device indicate that most of the ceramic materials of interest have emittances that are high and independent of temperature at the long wavelengths (from 8 to 14 microns). This has prompted the consideration of long wavelength pyrometry in this program as appropriate for the ceramic and composite materials.

Thermographic phosphors offer a novel approach to the temperature measurement problem. The technique is noncontact and the phosphor materials are high-temperature ceramics. Hence, the technique does not appear to be temperature limited. The technique has been shown to work well in the presence of both reflected radiation and flame. There have been very significant advances in this technique during the past year. A concern for this technique is the durability of the phosphors at temperatures above 1475K. Various bonding techniques are being investigated by the Department of Energy (DoE) under an Air Force contract. In order to use the same materials as in the Air Force work and to make use of the existing coating technology, the two phosphors applied by DoE personnel to our samples were yttrium oxide doped with europium ($Y_2O_3:Eu$) and YAG doped with terbium (YAG:Tb).

Thin-film sensors were being considered for use on the ceramic materials as a method not requiring optical access. Conventional wire thermocouple installation methods, such as tack welding and embedding wires into trenches, are not applicable for the ceramic materials for reasons of both mechanical disturbance, point defects due to machining, cracks due to mismatch in thermal expansion and thermal disturbances (mismatch in thermal conductivity and specific heat). The thin-film sensors fabricated with metallic elements are limited in their maximum temperature capabilities, but will be very useful for a significant portion of the laboratory test requirements.

Thin-film sensors offer other advantages in their size, installation and performance. The sensors are very thin and introduce a negligible amount of mechanical, thermal, or aerodynamic

and, therefore, provide a true measure of the surface temperature. They add a relatively small mass to the test piece and do not change the physical or mechanical properties. This becomes more significant when thin structures or small test pieces are involved. Thin-film sensors are installed with no structural modification to the test piece and can be located anywhere on the test piece. These factors make the thin-film sensors very attractive despite their temperature limitations.

The materials being considered under this program vary widely in physical and mechanical properties. A thin-film thermocouple program to develop application techniques for each of these materials has not been defined. Therefore, the scope was limited to two electrically nonconducting ceramic materials, and to evaluate three different application techniques: R.F. sputtering, ion beam etch deposition, and ion implantation and evaporation. The intent was to evaluate the current technology in each of these techniques in applying films to silicon nitride and Compglas® substrates rather than develop application techniques. The thin-film work was performed both at Pratt & Whitney Florida and United Technologies Research Center.

One of the major concerns with thin-film sensors is the ability to provide electrical insulation from substrates which are electrical conductors at high temperatures. The oxide insulators used tend to become semiconductors at the elevated temperatures. For this reason, a two-part approach to the thin-film sensors was used. For low to moderate temperatures, noble metal temperature sensors were applied to the ceramic materials.

The materials considered under this program were selected by mutual agreement with NASA and Pratt & Whitney. Six materials were investigated during this program. These were considered as engineering materials, and were intended to be commercial samples rather than very high purity laboratory samples. Silicon nitride (Si_3N_4) was purchased from Kyocera. Silicon carbide was obtained from Carborundum. Mullite was obtained from Coors. General Plasma supplied zirconia. Pratt & Whitney supplied Compglas® and a silicon nitride/silicon carbide composite material. Figure 1 shows the first five materials as received from the vendors. These materials were then cut to different sample sizes for the different measurement techniques.

Sample sizes were chosen based on the facilities involved in testing each of these three methods. The pyrometry samples were cut to 1.27 x 1.27 cm squares in order to fit in the Thermogage emissometer. This apparatus was used to make some of the emittance measurements. The thermographic phosphor samples were 2.54 x 2.54 cm square to fit in the oven in the laser diagnostic facility at United Technologies Research Center (UTRC). The thin-film thermocouple samples were made into 1.27 x 8.13 cm bars to fit into the thin-film testing facility at UTRC.

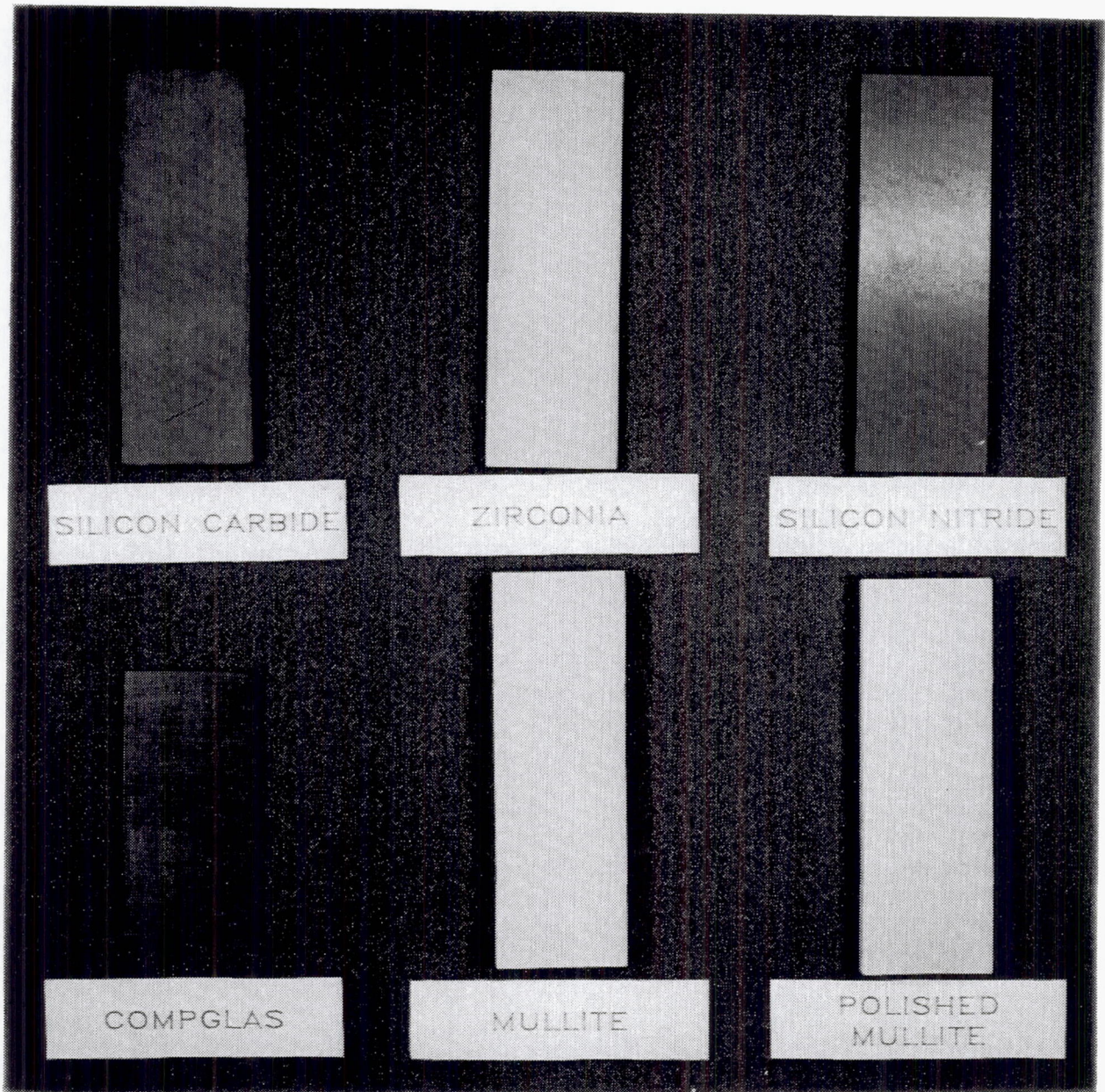


Figure 1 *Sample Materials As Received*

3. PYROMETRY

3.1 Emittance Measurements

At Pratt & Whitney, emittance measurements of various surfaces at high temperature have been made using a Thermogage emissometer. Figure 2 shows a schematic of that device, while the device itself is shown in Figure 3. For emittance measurements, the test specimen is mounted on a graphite rod connected to a hydraulic actuator. This allows the specimen to be translated rapidly from the center of the black body furnace where it is surrounded by hot walls, to the end of the furnace where the sample surroundings are cool. A radiometer is positioned so that it can view the test specimen at both locations. Depending on the purpose of the test, a broad spectrum radiometer may be used to obtain "total normal" emittance, or a narrow spectral band radiometer may be used to obtain data in a particular spectral band. The output from the radiometer is connected to a digital oscilloscope to record the data taken during emittance testing.

At the start of the emittance testing, the sample is brought up to the test temperature of interest, and allowed to reach equilibrium within the black body. The radiometer is positioned to obtain data from the specimen. A trace on the oscilloscope is triggered. The radiometer is then shuttered for a short time (to obtain a zero energy baseline). The radiometer is unshuttered and the black body energy is measured; then the specimen is propelled out to the end of the black body tube and the energy from the specimen is measured. The movement is fast enough that the change in specimen temperature is negligible. This produces a trace similar to Figure 4. The emissivity of the specimen is calculated from the ratio of the energy emitted by the specimen at the end of the tube to the energy emitted by the specimen inside the black body. During the test series, data are acquired in all spectral ranges at the lowest test temperature of interest. Testing then proceeds to successively higher temperatures.

Emittance tests were performed on five ceramics. Figures 5 through 9 show emittance data obtained for Si_3N_4 , SiC, Compglas®, 7% yttria stabilized zirconia, and mullite, respectively. For most materials, data were obtained over the range of approximately 0.9 to 14 microns and over a temperature range of about 1255K to 1925K. The Compglas® data were limited to 1475K due to material failure at high temperatures.

During the emittance testing, two materials seemed to have chemical reactions take place inside the black body furnace at high temperatures. The silicon nitride samples started as a black material, but after exposure to 1925K a white material was seen on the surface. The white mullite sample was taken to 1925K and turned gray. Both samples were taken to the Pratt & Whitney Materials Engineering and Research Labs (MERL) for chemical analysis. Table 1 shows the results of the analysis. A resident chemist has explained the results as indicating that a chemical reduction process is occurring within the carbon furnace with a nitrogen purge. Under company funding, the test facility is being modified to allow an argon purge to be used for high temperature testing.

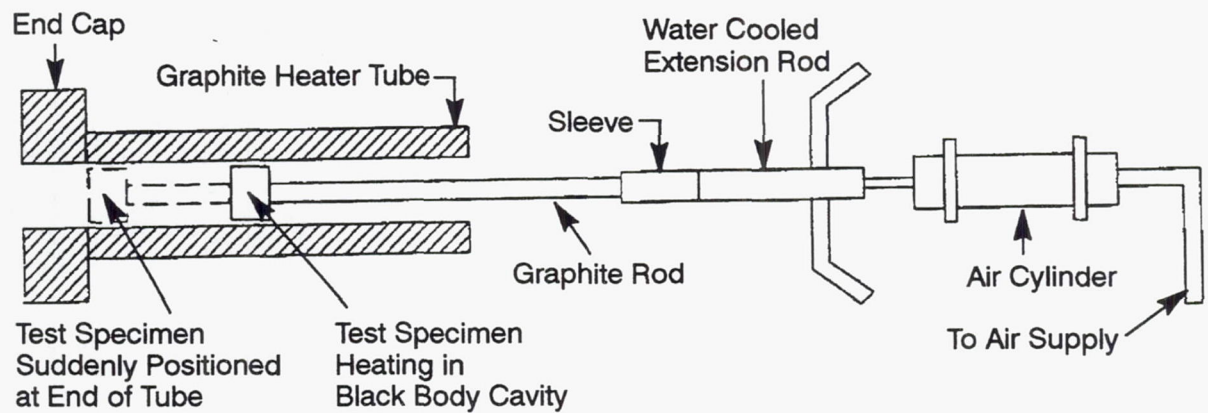


Figure 2 Schematic Diagram of Thermogage Emissometer

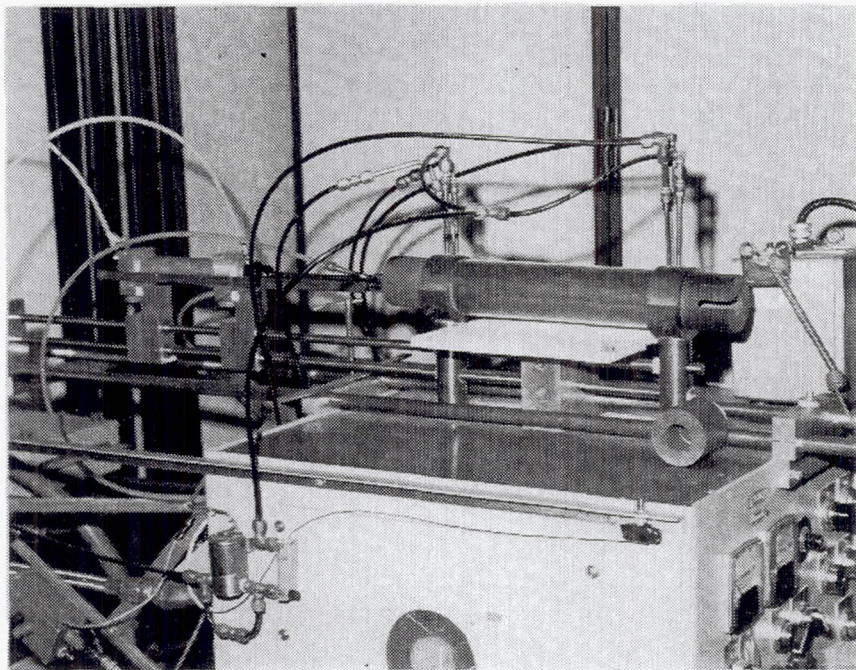


Figure 3 Photograph of Thermogage Emissometer

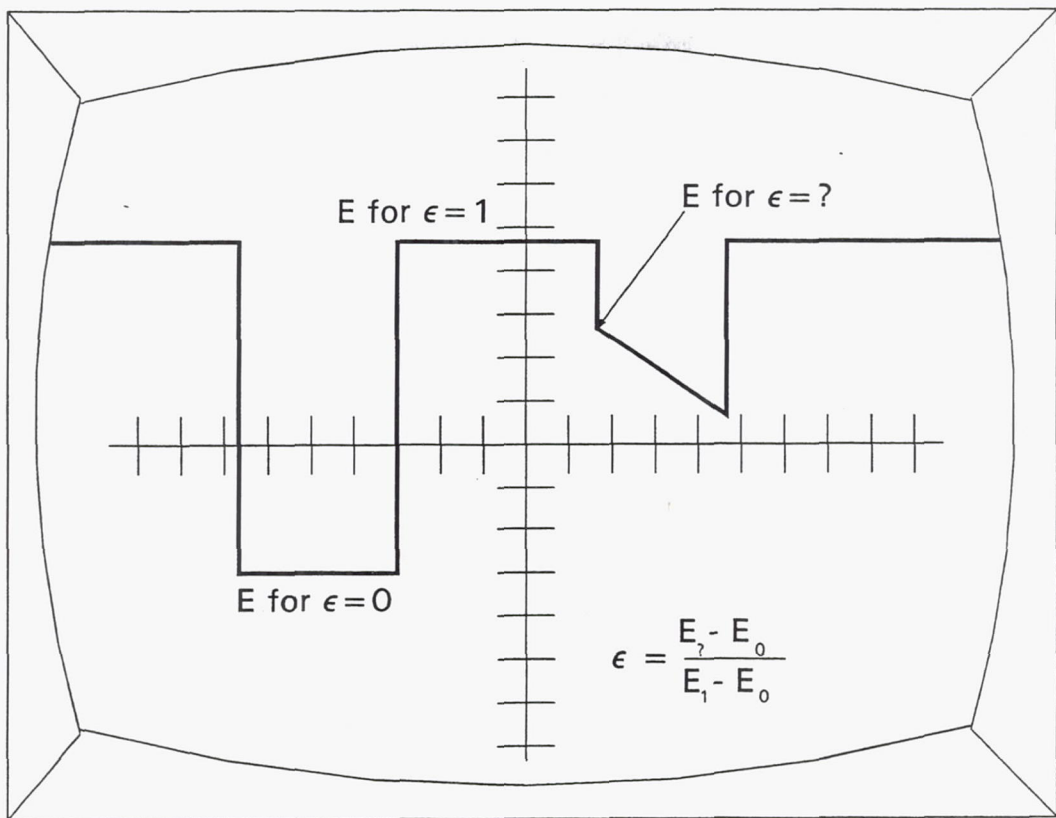


Figure 4 Emissometer Oscilloscope Trace

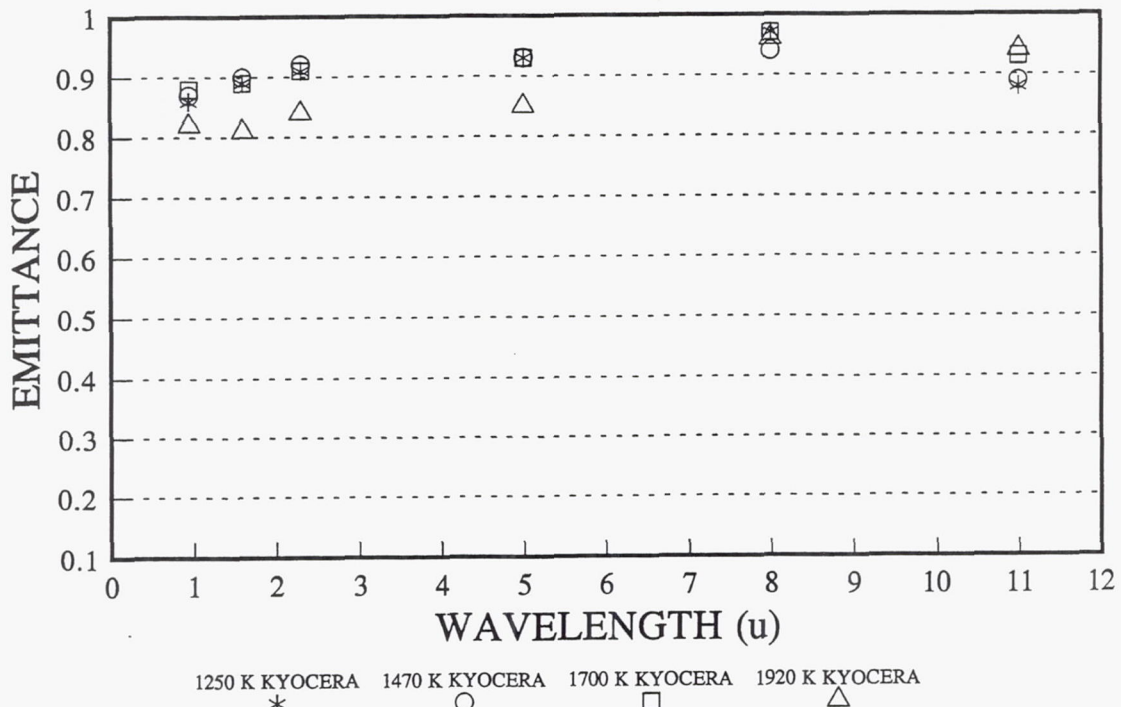


Figure 5 Measured Normal Spectral Emittance of Silicon Nitride

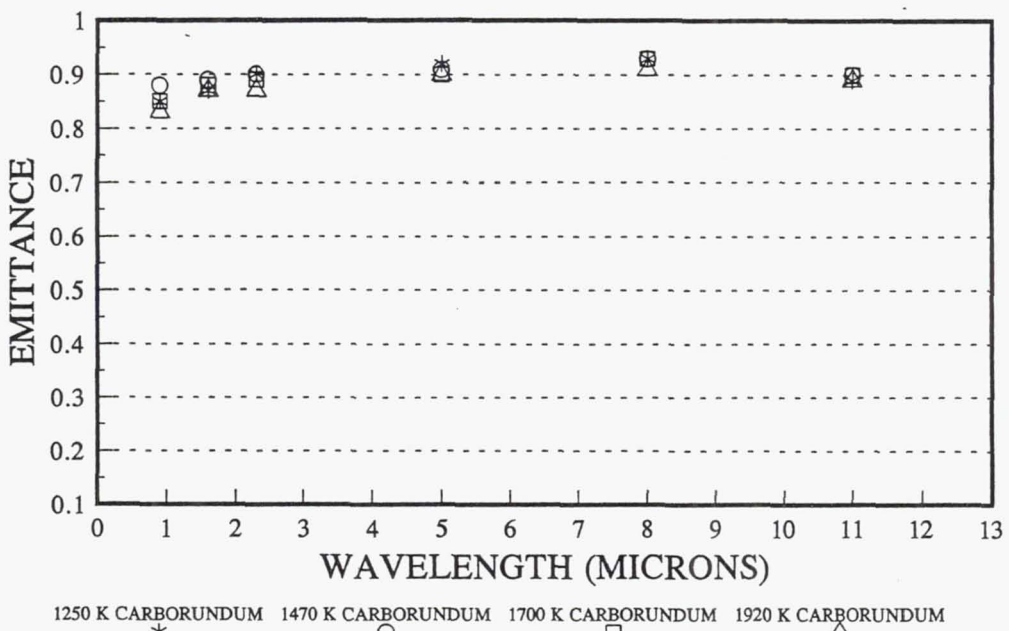


Figure 6 *Measured Normal Spectral Emittance of Silicon Carbide*

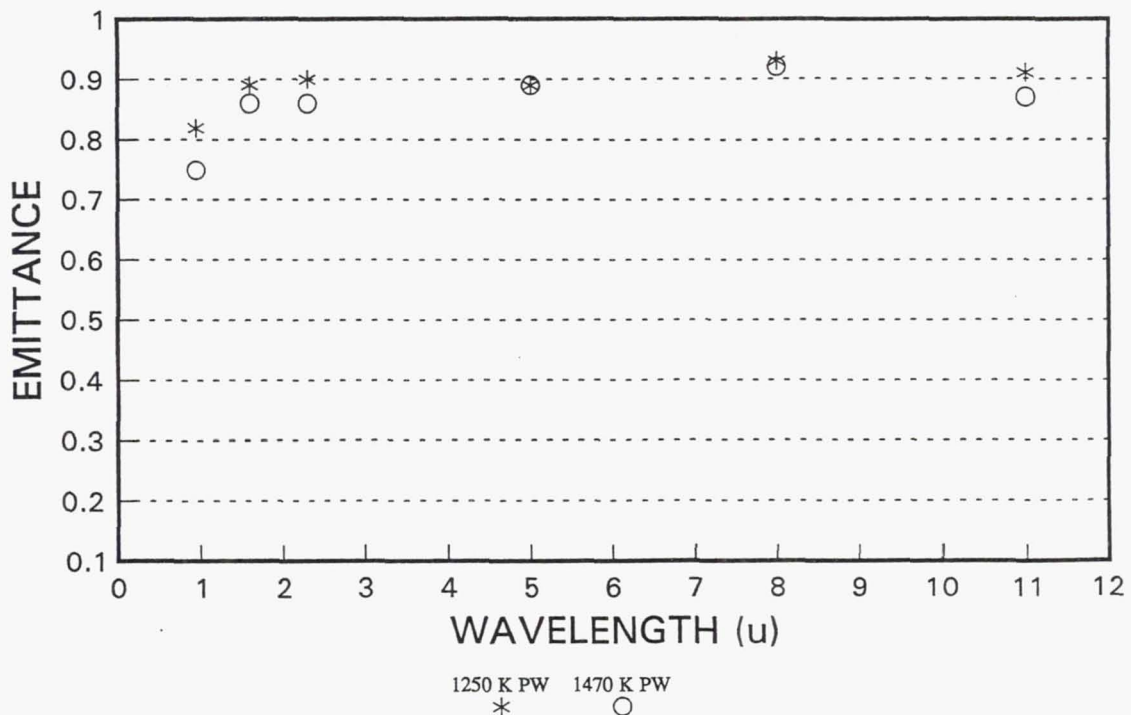


Figure 7 *Measured Normal Spectral Emittance of Compglas®*

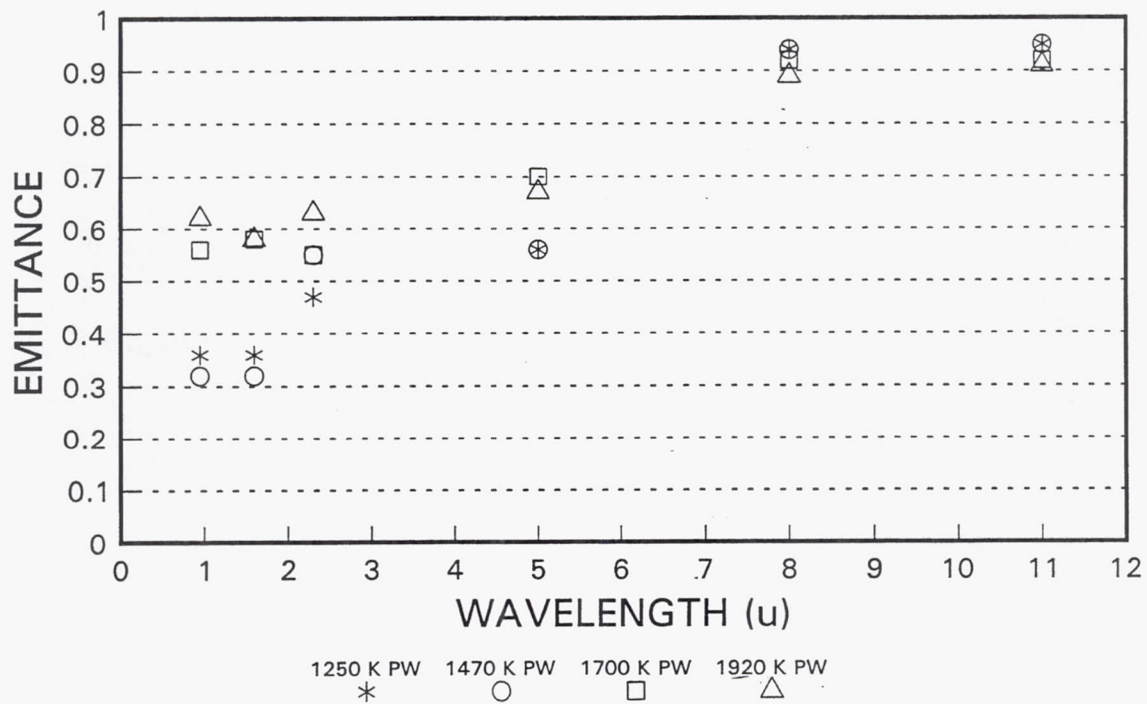


Figure 8 Measured Normal Spectral Emittance of 7% Yttria Stabilized Zirconia

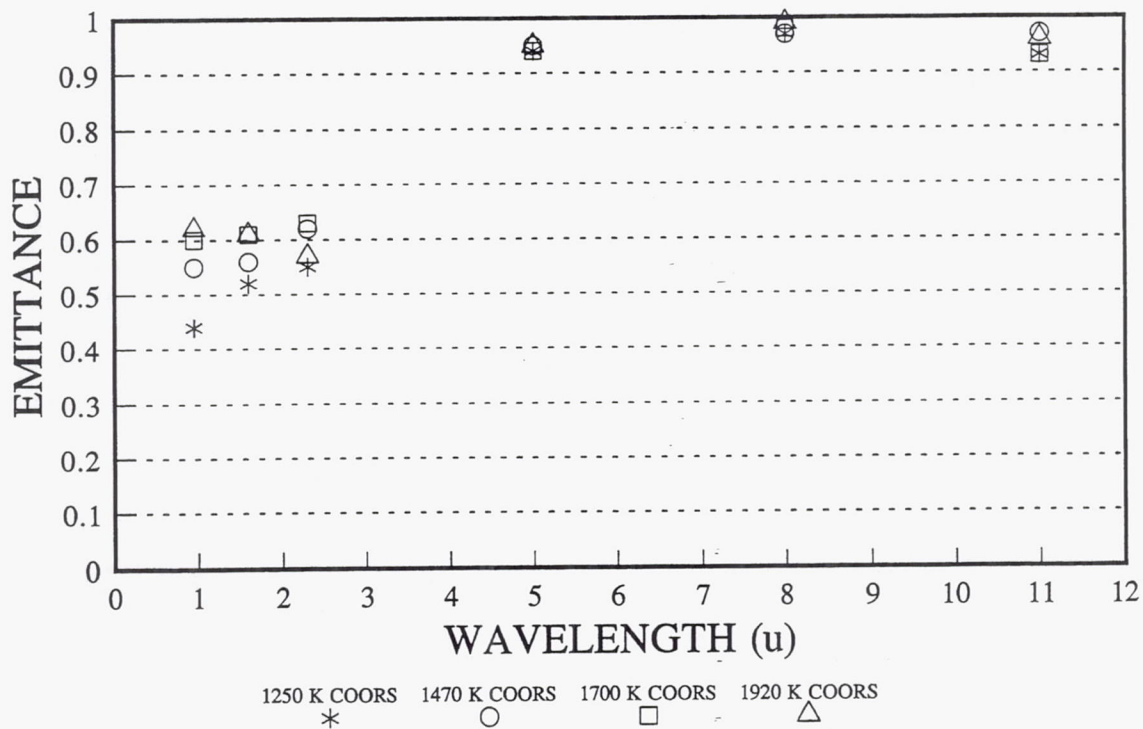


Figure 9 Measured Normal Spectral Emittance of Mullite

Table 1 Chemical Analysis of Tested Mullite and Si₃N₄

<u>Material</u>	<u>Pre-Test Composition</u>	<u>Post-Test Composition</u>
Mullite	100% single-phase orthorhombic mullite	50–45% orthorhombic mullite ($Al_6Si_2O_{13}$) 35–40% hexagonal alpha- Al_2O_3 alumina as corundum (white) 15% hexagonal alpha-SiC (black)
Silicon nitride	85% hexagonal Si ₃ N ₄ 15% tetragonal structure believed ($(Si_{(3-x)}Al_x)N_4$, an aluminum modification	60% hexagonal Si ₃ N ₄ 15–20% tetragonal ($Si_{(3-x)}Al_x)N_4$ 10% hexagonal SiC (black) 5% orthorhombic Al_2SiO_5 aluminum silicate as andalusite (white) 5% hexagonal ($Al_{(4-y)}SiY)C$ (black) 5% tetragonal SiO ₂ as stiskovite (white)

During the time period of the contract, additional emittance tests were performed at United Technologies Research Center (UTRC) for Pratt & Whitney under Independent Research and Development (IR&D) funding. The data were obtained using a spectrometer but, in principle, should have yielded identical results. The P&W data, UTRC data, and data obtained during the literature survey in Phase I of the contract are all combined and shown in Figures 11 through 15.

Overall, the emittance tests show that SiC and Si₃N₄ have emittances that are relatively high at all wavelengths and are stable with temperatures. However, the data obtained at UTRC indicates a lower emittance than the other sources. This has not yet been investigated further due to lack of funding. The emittance for Compglas® is also reasonably high and stable to 1475K. The results for zirconia and mullite are much more complex. The emittance data vary widely with wavelength, temperature, and materials source. In general, the data are most stable at longer wavelength.

Additional investigations were conducted to further clarify the wide range of variation observed in the emittance of 7% yttria stabilized zirconia at short wavelengths. Optical inspection of several materials purchased to the same P&W specification showed a wide range of variation in appearance at visible wavelengths (\approx 0.4 to 0.7 microns). Some specimens appeared pure white, some were bright yellow, and others were intermediate in appearance. Discussions with various people in the field indicated that very low level impurities (parts per billion) that have no effect on the structural characteristics of the material can have large effects on the short wavelength optical properties.

It was also observed that after emittance testing, the zirconia samples often appeared different (i.e., whiter) than before the test. Generally, during emittance testing, data were first obtained at the lowest temperature of interest. The data were then obtained in increasing temperature increments. A test was performed, under internal IR&D funding, where the low temperature emittance tests were repeated after high temperature testing. The results of that test program are given in Figure 16. It can be seen that the emittance data at short wavelengths after the sample has been taken to high temperatures is higher than initial short wavelength results but still lower than the high temperature data. This indicates some of the variation in emittance is due to material changes (bake-out of impurities, etc.), and that some of the variation is probably an intrinsic characteristic of the material.

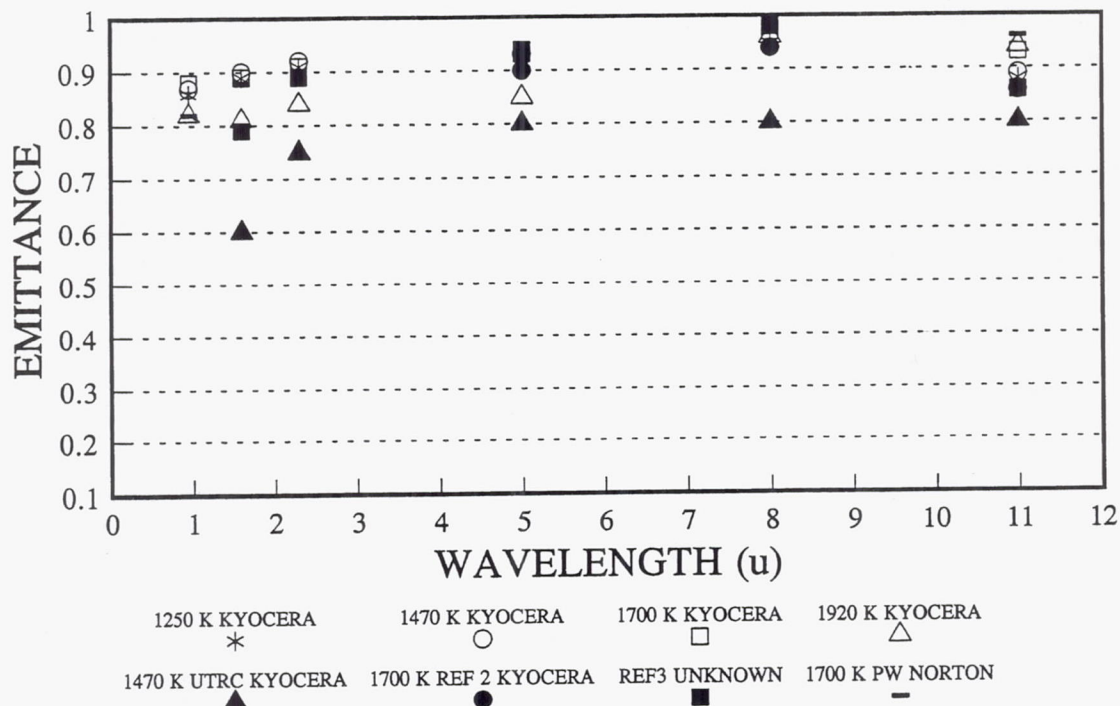


Figure 10 Compiled Normal Spectral Emittance of Silicon Nitride

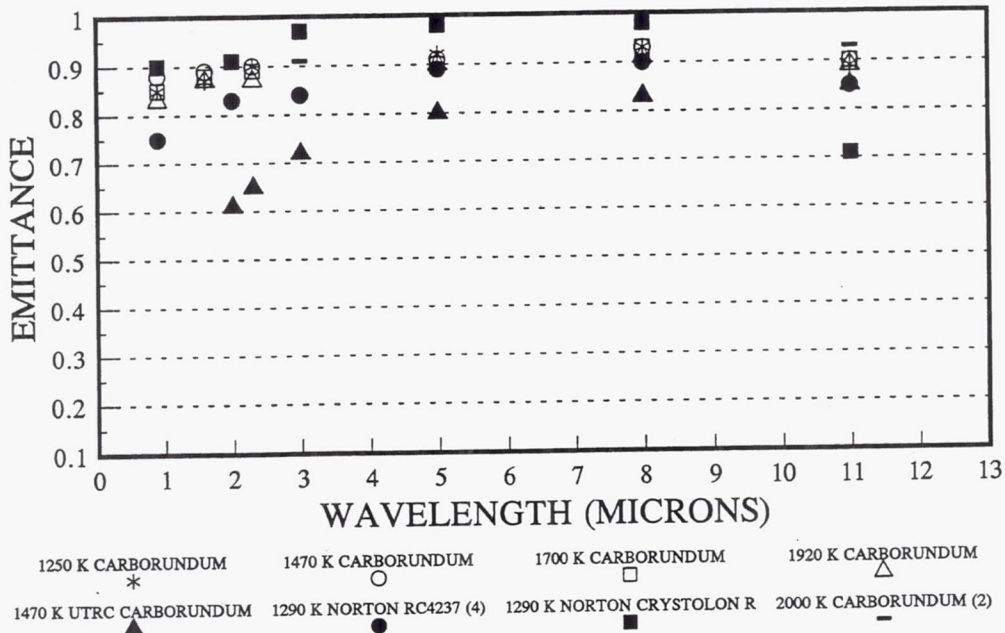


Figure 11 Compiled Normal Spectral Emittance of Silicon Carbide

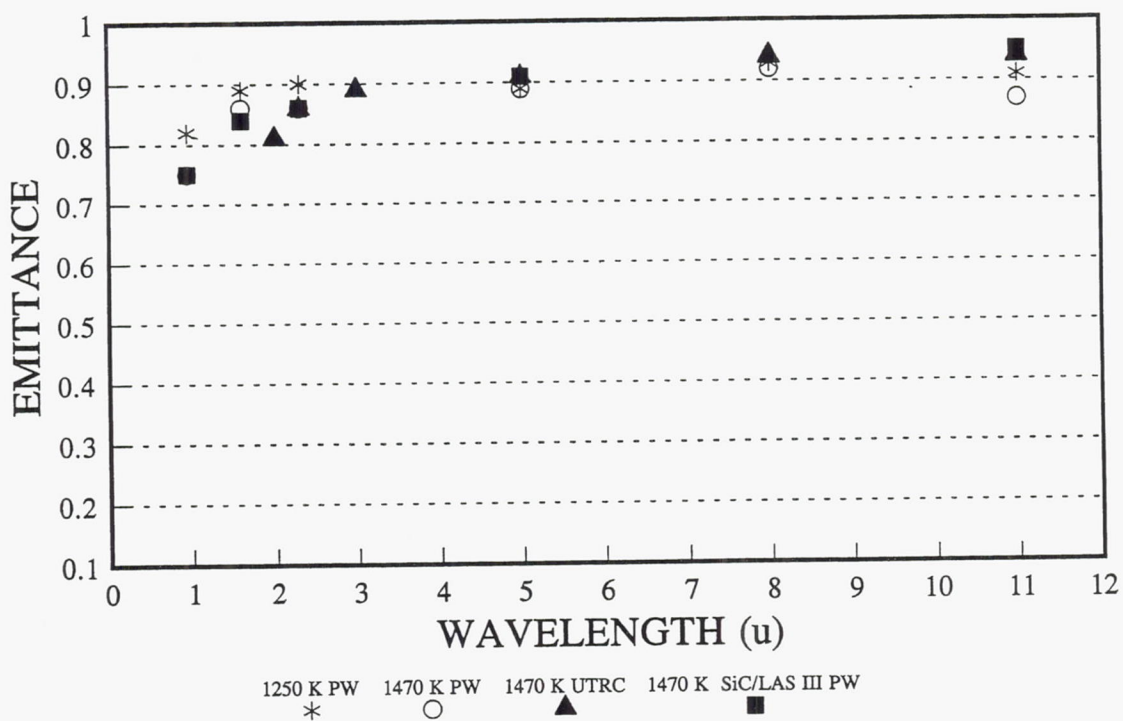


Figure 12 Compiled Normal Spectral Emittance of Compglas®

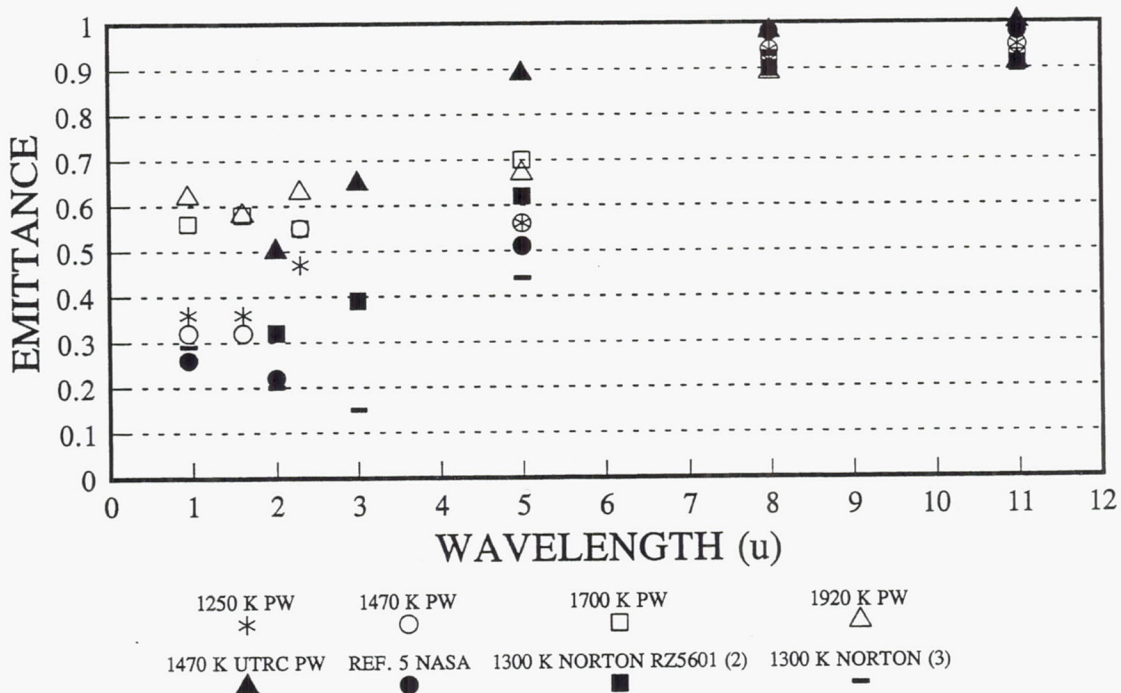


Figure 13 Compiled Normal Spectral Emittance of 7% Yttria Stabilized Zirconia

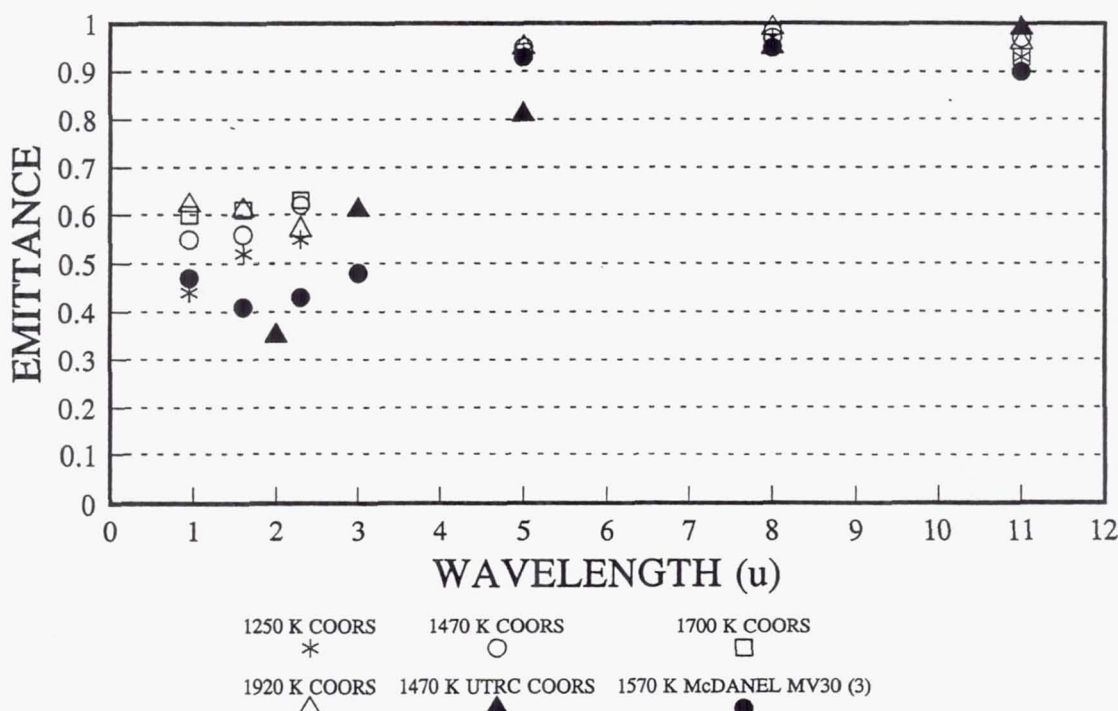


Figure 14 Compiled Normal Spectral Emittance of Mullite

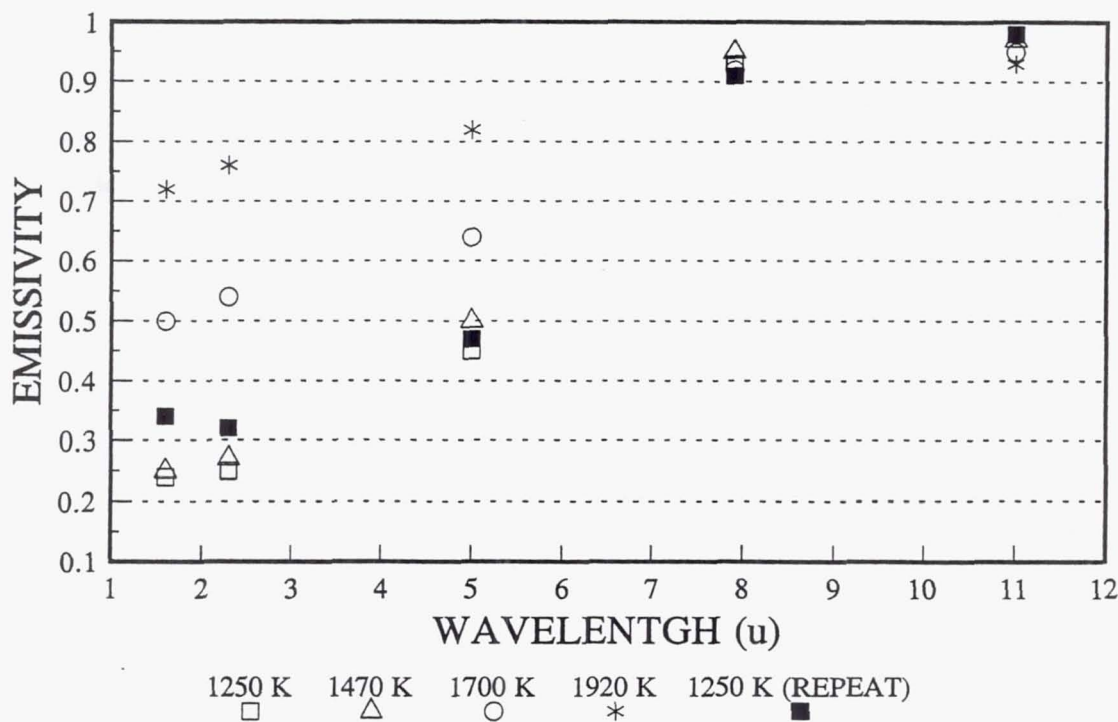


Figure 15 Results of Tests to Investigate the Variation of the Spectral Emittance of 7% Yttria Stabilized Zirconia

3.2 Pyrometry Uncertainty Analysis – Emittance Effects

The real concern with variation in surface emittance is the way it affects the accuracy of temperature data obtained with a pyrometer. The uncertainty of the pyrometer temperature measurement, as a result of emittance uncertainty, must be within acceptable bounds. It is also desirable that the correction in the pyrometer reading due to the surface emittance being less than one should not be too large.

To investigate the effect of emittance on temperature measurement, the monochromatic (single wavelength) emission power from Planck's law was used. The energy emitted by a surface is given by:

$$E_{T\lambda} = \varepsilon_{T\lambda} \frac{C_1 \lambda^{-5}}{e^{C_2/\lambda T} - 1} \quad (1)$$

where: $E_{T\lambda}$ is the energy at a given temperature and wavelength. $\varepsilon_{T\lambda}$ is the emittance of the material at that temperature and wavelength, λ is the wavelength, T is the temperature and C_1 and C_2 are constants.

An ideal black body surface would have an emittance of 1.0 at all temperatures and wavelengths. The energy emitted by a real surface is related to the energy emitted by a black body by:

$$E_{T\lambda} = \varepsilon_{T\lambda} E_{T_B\lambda} \quad (2)$$

This corresponds to the energy radiated by the surface at some lower temperature. Unless an emittance correction is made to the pyrometer, this is the lower indicated T_I that the pyrometer can read. Therefore:

$$E_{T\lambda} = \varepsilon_{T\lambda} E_{T_S\lambda} \quad (3)$$

where: T_I is the indicated temperature, and T_S is the true surface temperature.

Equations (1) and (3) may be combined to relate the indicated and the true surface temperatures. The result is:

$$\frac{C_1 \lambda^{-5}}{e^{C_2 T \lambda} - 1} = \varepsilon \left(\frac{C_1 \lambda^{-5}}{e^{C_2/T_S \lambda} - 1} \right) \quad (4)$$

Cross multiplying yields the following relationships:

$$e^{\frac{C_2}{T_S \lambda}} - 1 = \varepsilon \left(e^{\frac{C_2}{T_I \lambda}} - 1 \right) \quad (5)$$

and

$$\frac{C_2}{T_S \lambda} = \ln \left[\varepsilon \left(e^{\frac{C_2}{T_I \lambda}} - 1 \right) + 1 \right] \quad (6)$$

This can be rearranged to obtain T_S as a function of T_I :

$$T_S = \frac{C_2/\lambda}{\ln \left[\varepsilon \left(e^{\frac{C_2}{\lambda}} - 1 \right) + 1 \right]} \quad (7)$$

Similarly, T_I could be obtained as a function of T_S :

$$T_I = \frac{C_2/\lambda}{\ln \left[\frac{1}{\varepsilon} \left(e^{\frac{C_2}{\lambda}} - 1 \right) + 1 \right]} \quad (8)$$

The relationships above are strictly valid only at a single wavelength. For real pyrometer systems operating over relatively wide spectral bands, an integration must be performed where the variation in pyrometer sensitivity with wavelength is considered. The equations cannot be solved in closed form and numerical methods must be used. Since the radiometer wavelength bands used in the emittance tests were quite narrow, a monochromatic analysis near the middle of the pyrometer sensitivity band was used. This simplified and clarified the uncertainty analysis while giving close approximation to the actual uncertainties.

Figure 16 shows the typical types of variation in indicated temperature with emittance that can be obtained from the above analysis. It reflects the error in temperature indications as a function of emittance errors for various wavelength pyrometers. From the figure, it is clear that, all else being equal, shorter wavelength pyrometers will yield more accurate data. That is one of the primary reasons most high temperature pyrometry for metals is performed at short wavelengths. For those ceramics where emittance uncertainties are larger at shorter wavelengths, a closer look is required.

The uncertainty results for the materials tested under this contract are summarized in Table 2. For consistency, the data used for this analysis were limited to the Pratt & Whitney generated data shown in Figures 5 through 9. The average emittance at each wavelength is obtained by averaging the data. The uncertainty range was obtained from the high and low data readings.

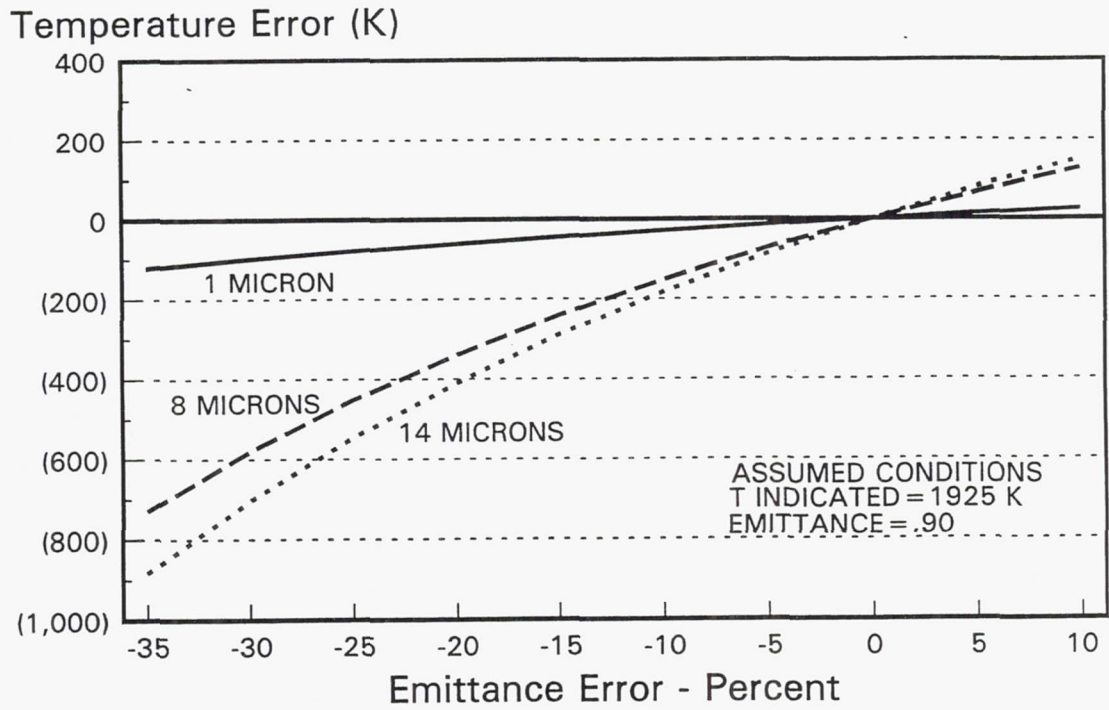


Figure 16 *Error in Indicated Temperature as a Function of Emittance Error*

Table 2 *Emittance Uncertainties*

Material	0.95 μ		1.6 μ		2.3 μ		5 μ		8 μ		11 μ	
	<i>High</i>		<i>High</i>		<i>High</i>		<i>High</i>		<i>High</i>		<i>High</i>	
	Avg.	—										
Silicon Nitride	0.88		0.90		0.92		0.93		0.97		0.91	
	0.86		0.87		0.90		0.91		0.96		0.94	
	0.82		0.81		0.84		0.85		0.94		0.88	
Silicon Carbide	0.88		0.89		0.90		0.92		0.93		0.895	
	0.85		0.88		0.89		0.91		0.92		0.91	
	0.83		0.87		0.87		0.90		0.91		0.89	
Comglas®	0.82		0.89		0.90		0.89		0.93		0.89	
	0.78		0.875		0.88		0.89		0.925		0.89	
	0.75		0.86		0.86		0.89		0.92		0.87	
Zirconia	0.62		0.58		0.63		0.70		0.94		0.95	
	0.46		0.46		0.55		0.62		0.92		0.93	
	0.32		0.32		0.47		0.56		0.89		0.91	
Mullite	0.62		0.61		0.63		0.95		0.99		0.97	
	0.55		0.58		0.59		0.945		0.98		0.95	
	0.44		0.52		0.55		0.94		0.97		0.93	

These emittance data were then used to predict the uncertainty characteristics of pyrometer systems operating at each of the wavelengths tested. The average emittance data were used to predict the nominal emittance correction that would have to be made to each pyrometer. The emittance uncertainty bounds were then used to predict the uncertainty in the final pyrometer measurement. For all materials with the exception of Compglas®, a true surface temperature of 1925K was chosen as an analysis point. For Compglas®, 1475K was used. The results of the analysis are summarized in Figures 17 through 31. There are three figures for each material. The first figure in each set shows the average emittance used at each wavelength and the uncertainty about that nominal value. The second figure in each set shows the average emittance correction that would be required at each wavelength. The third curve of each set shows the uncertainty bounds in the temperature measurement at each wavelength as a result of the emittance uncertainty. This third plot also indicates the ± 2 percent accuracy goals and ± 5 percent acceptable accuracy bounds for this contract.

The results for silicon nitride, silicon carbide, and Compglas® are similar to the results normally obtained on metals. In general, the emittance correction required to the pyrometer increases with increasing wavelength. For these materials, the pyrometer uncertainty is also smaller at short wavelength where the emittance effects are smallest. All the uncertainties due to emittance fall within the ± 5 percent contract limits; and, with the exception of the 5 and 11 micron data on silicon nitride, all uncertainties due to emittance fall within the ± 2 percent contract goals.

EMITTANCE

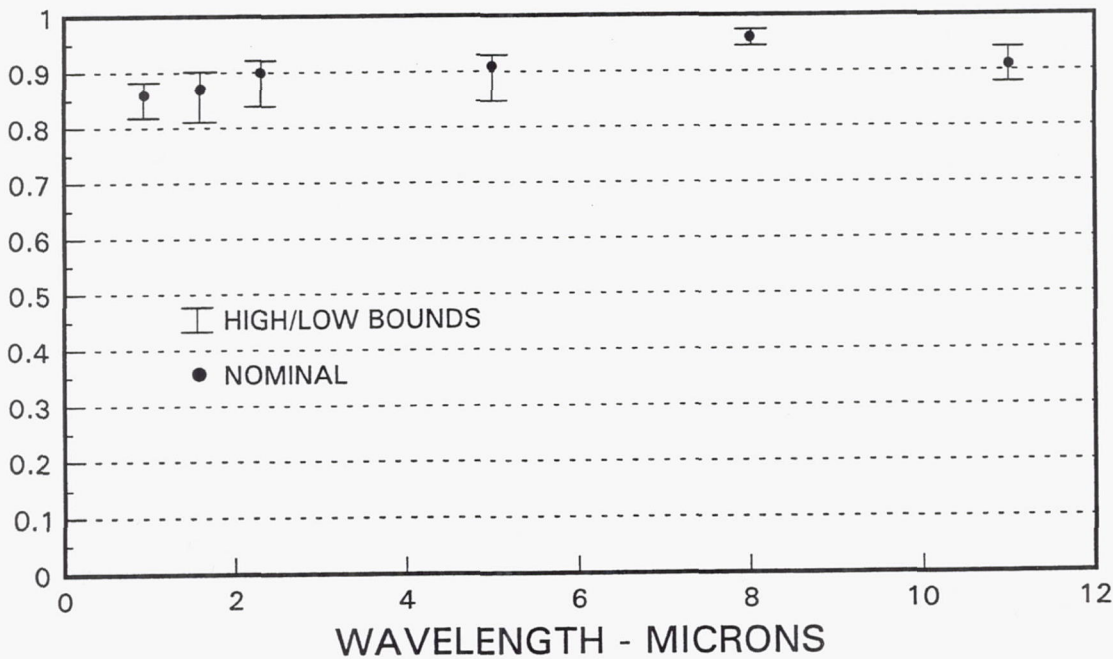


Figure 17 Summary of Pratt & Whitney Emittance Data on Silicon Nitride

PYROMETER CORRECTION K

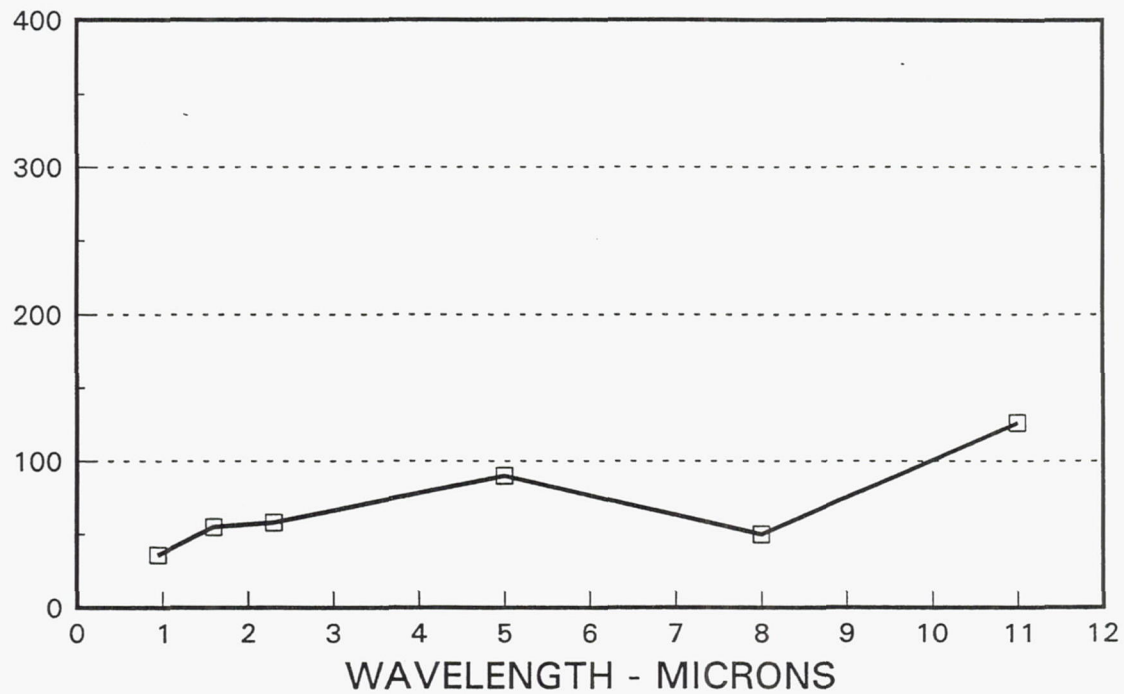


Figure 18 Nominal Pyrometer Corrections for Silicon Nitride at 1925K

TEMPERATURE UNCERTAINTY %

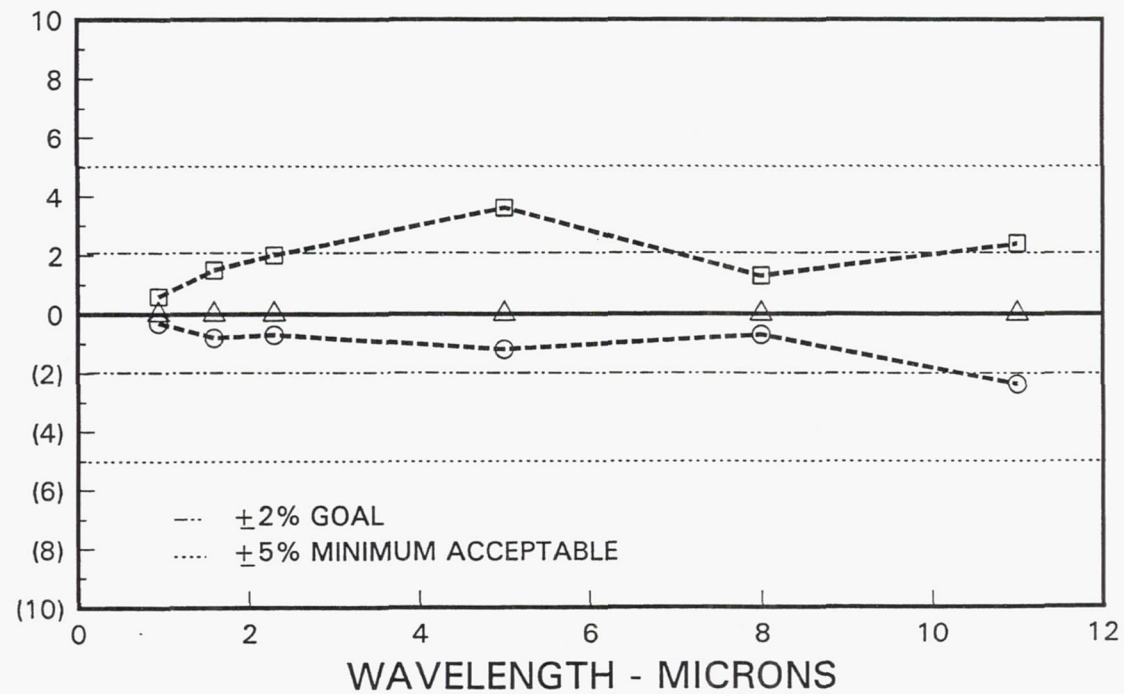


Figure 19 Indicated Temperature Uncertainty for Silicon Nitride at 1925K

EMITTANCE

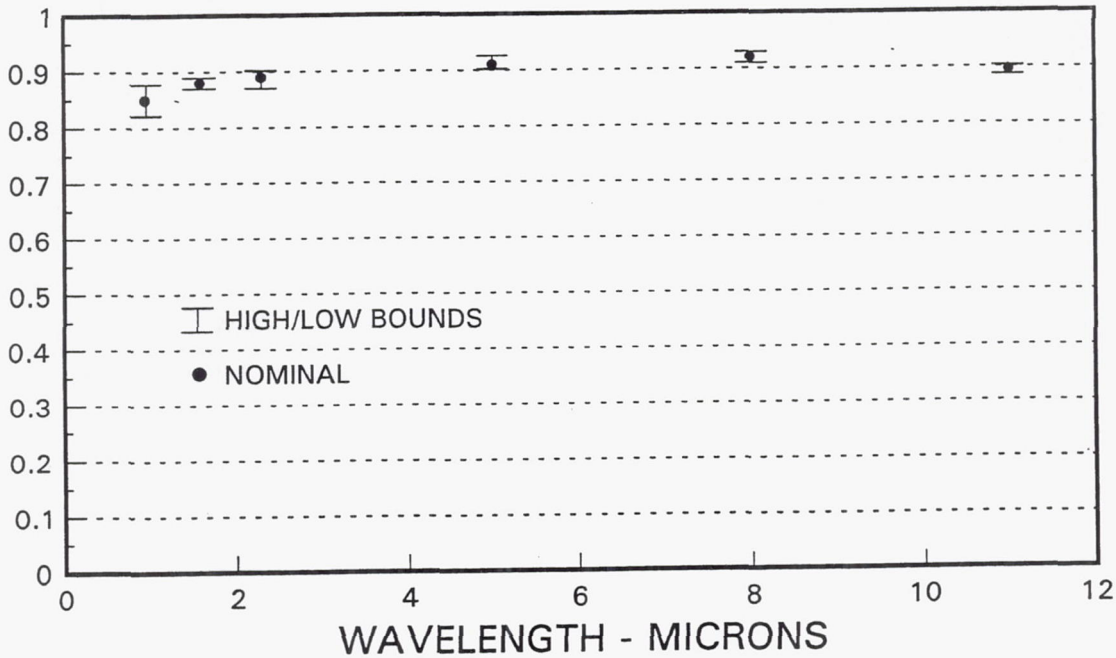


Figure 20 Summary of Pratt & Whitney Emittance Data on Silicon Carbide

PYROMETER CORRECTION K

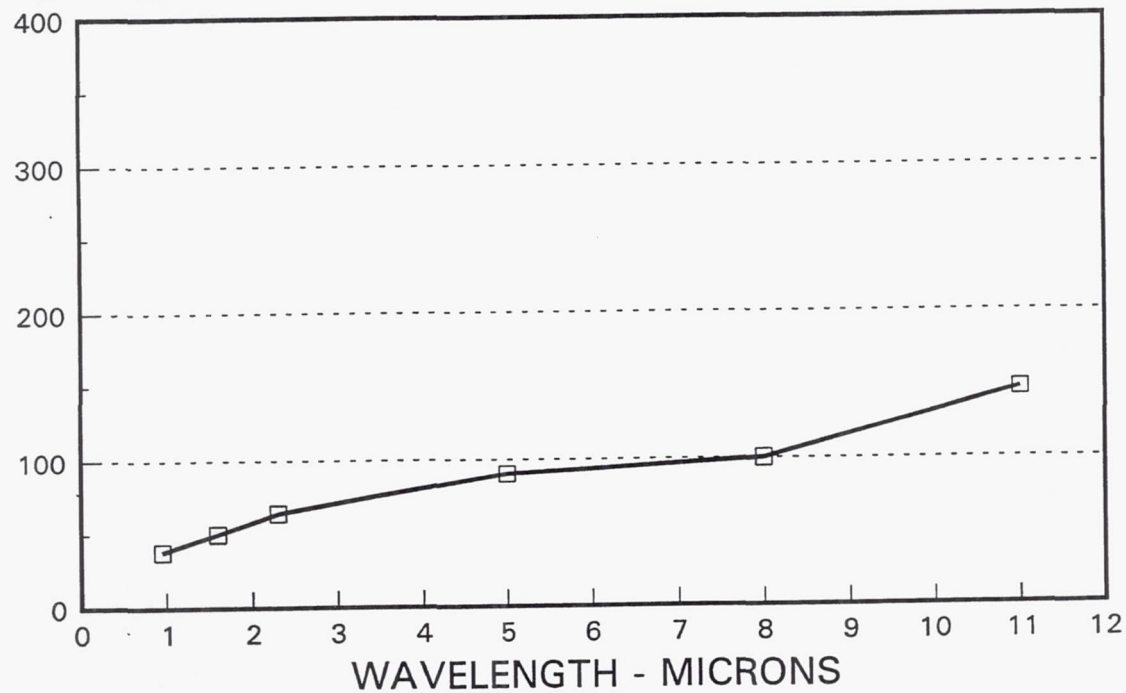


Figure 21 Nominal Pyrometer Corrections for Silicon Carbide at 1925K

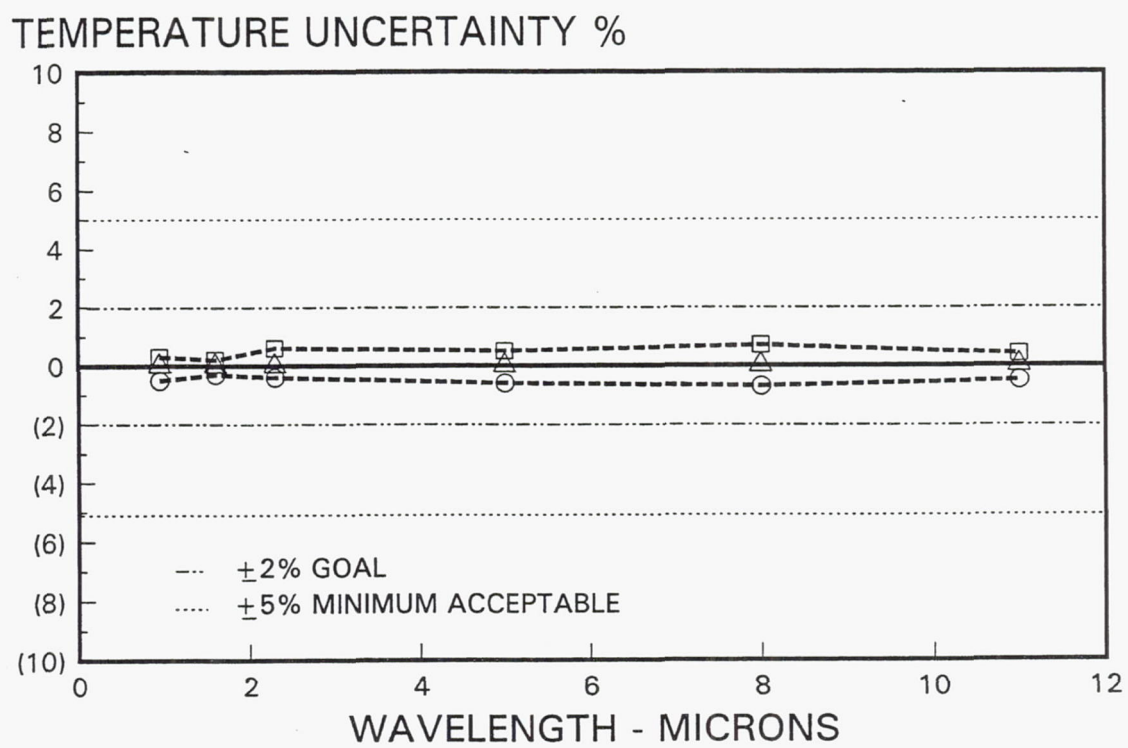


Figure 22 Indicated Temperature Uncertainty for Silicon Carbide at 1925K

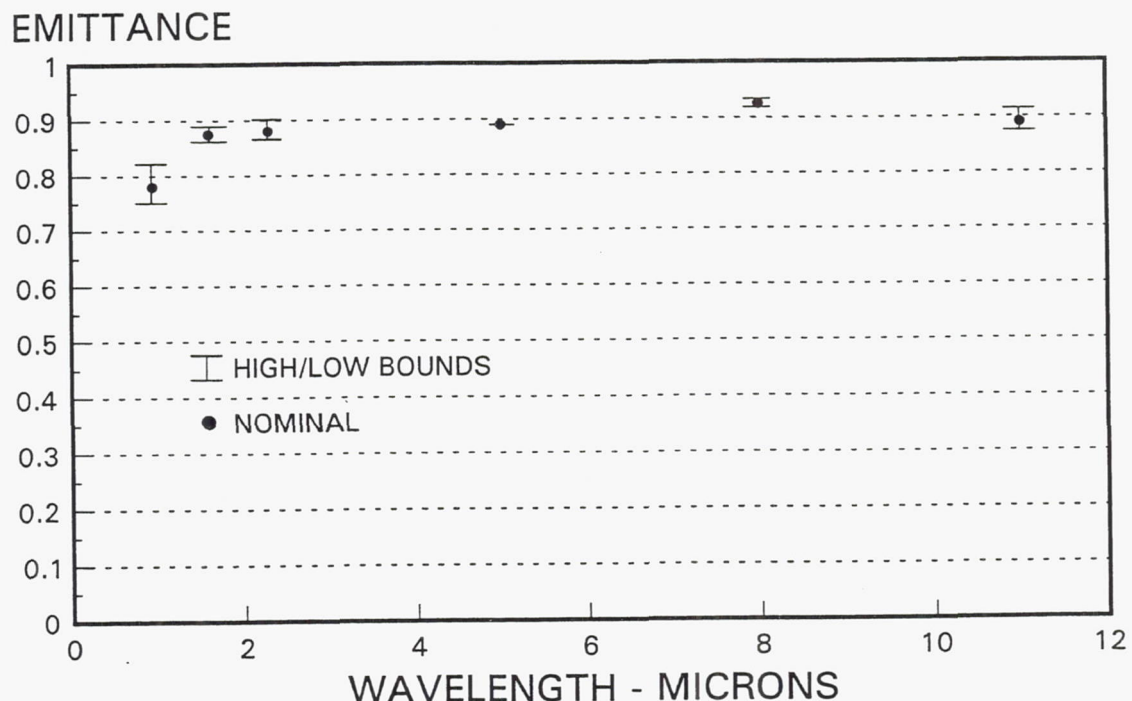


Figure 23 Summary of Pratt & Whitney Emittance Data on Compglas®

PYROMETER CORRECTION K

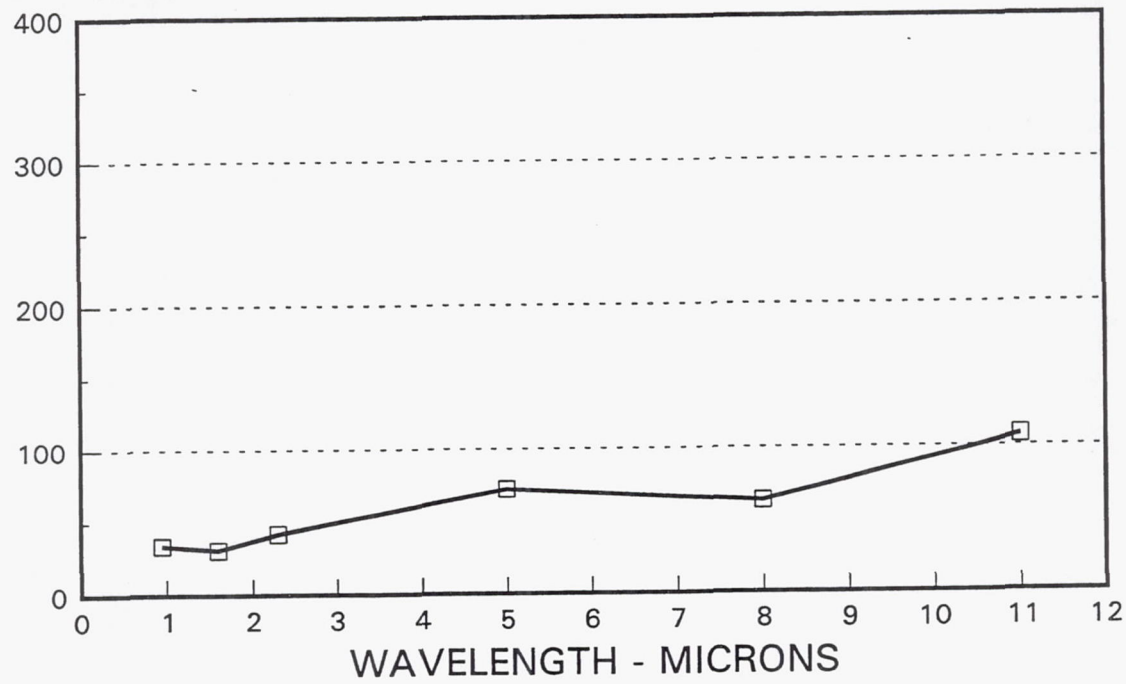


Figure 24 Nominal Pyrometer Corrections for Compglas® at 1925K

TEMPERATURE UNCERTAINTY %

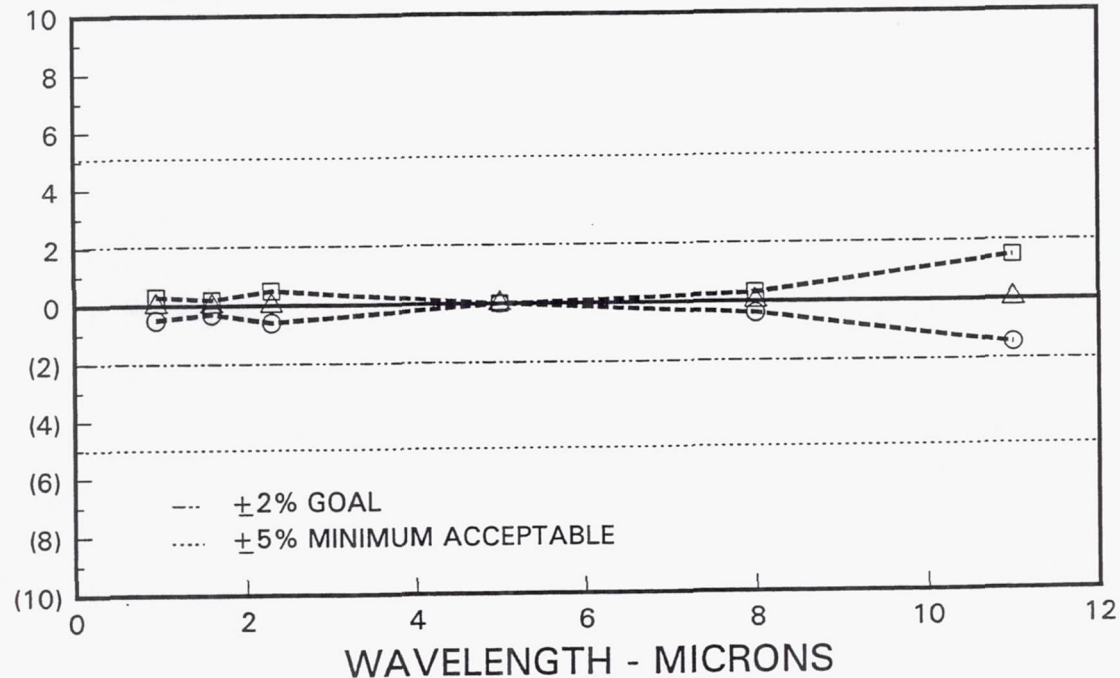


Figure 25 Indicated Temperature Uncertainty for Compglas® at 1925K

EMITTANCE

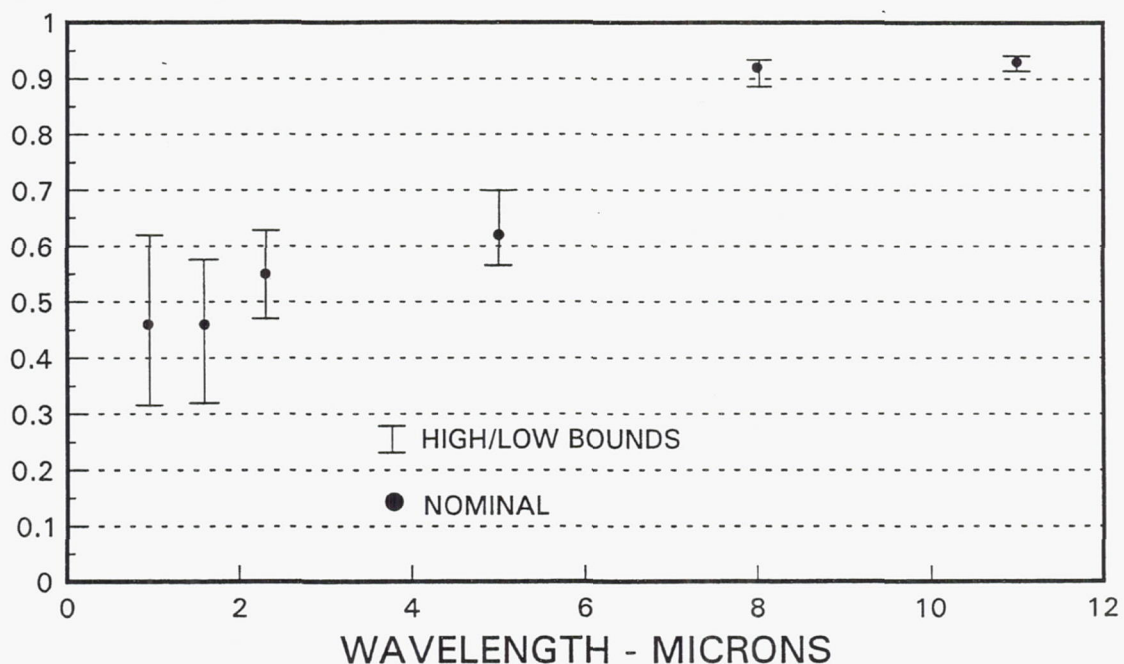


Figure 26 Summary of Pratt & Whitney Emittance Data on 7% Yttria Stabilized Zirconia

PYROMETER CORRECTION K

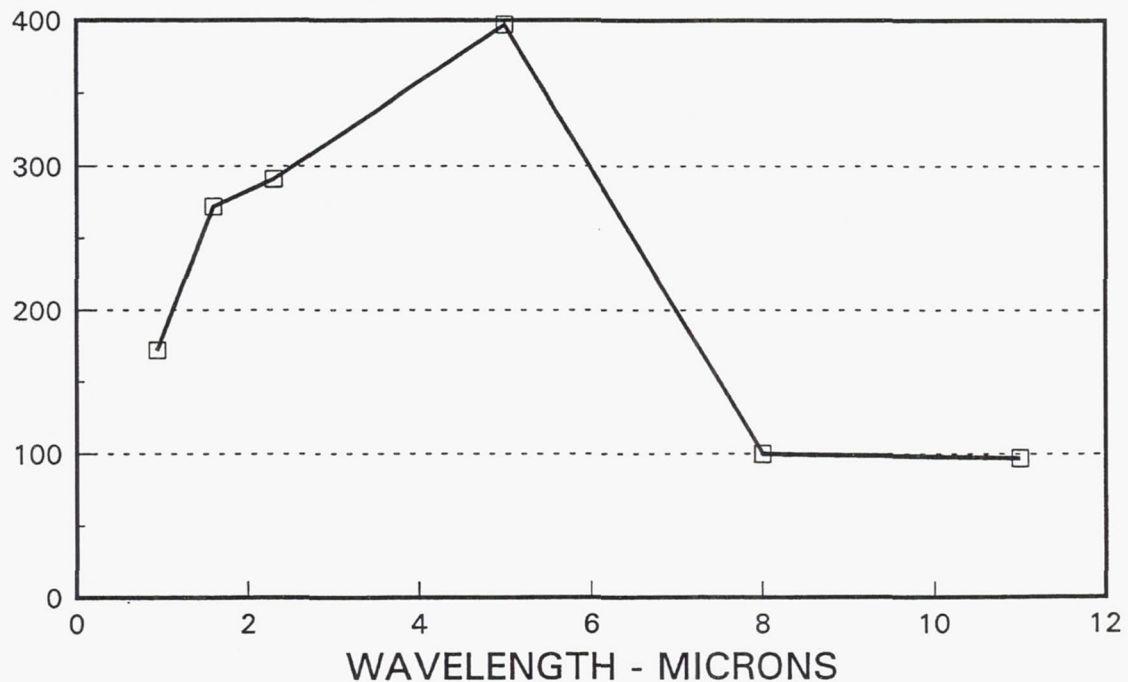


Figure 27 Nominal Pyrometer Corrections for 7% Yttria Stabilized Zirconia at 1925K

TEMPERATURE UNCERTAINTY %

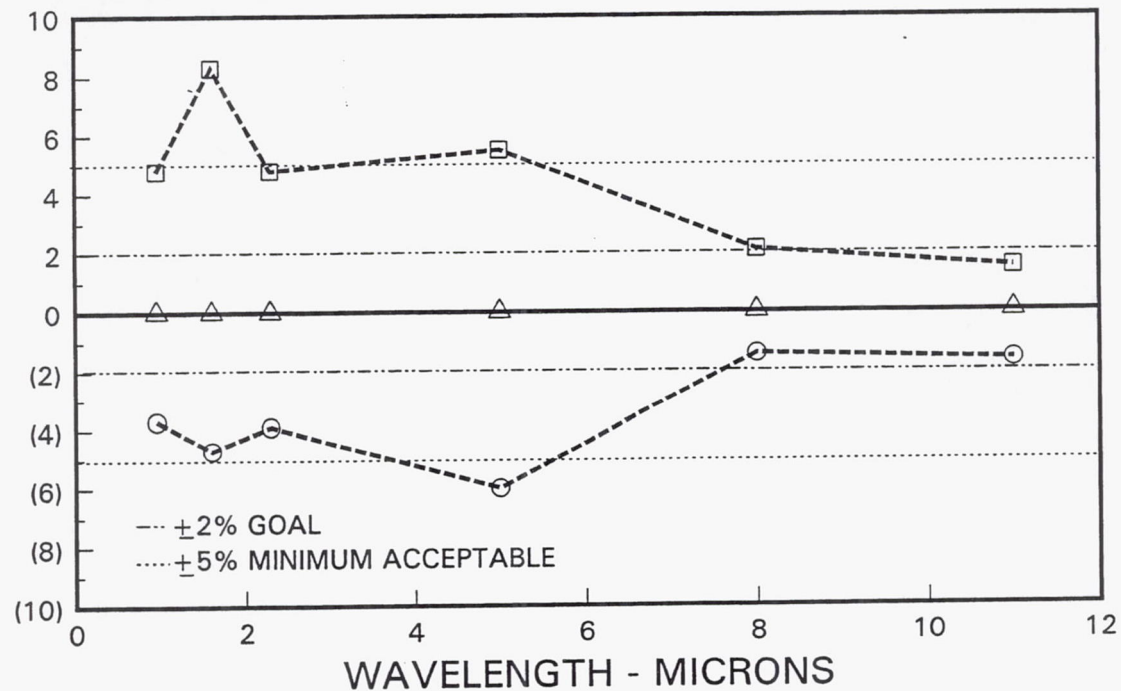


Figure 28 Indicated Temperature Uncertainty for 7% Yttria Stabilized Zirconia at 1925K

EMITTANCE

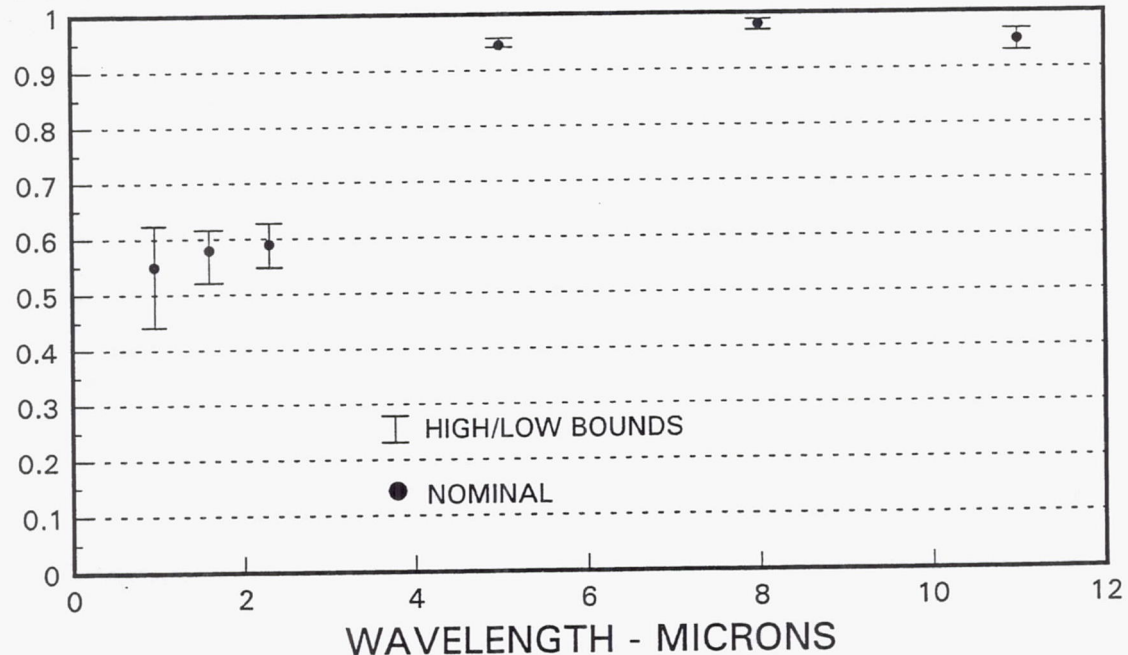


Figure 29 Summary of Pratt & Whitney Emittance Data on Mullite

PYROMETER CORRECTION K

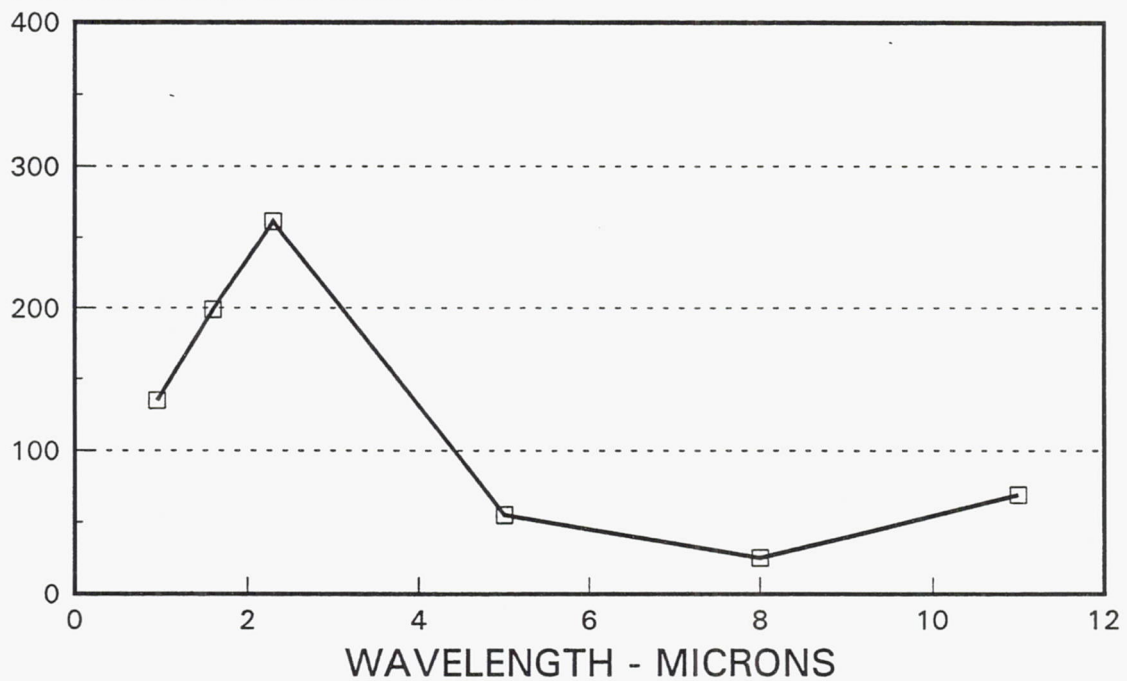


Figure 30 Nominal Pyrometer Corrections for Mullite at 1925K

TEMPERATURE UNCERTAINTY %

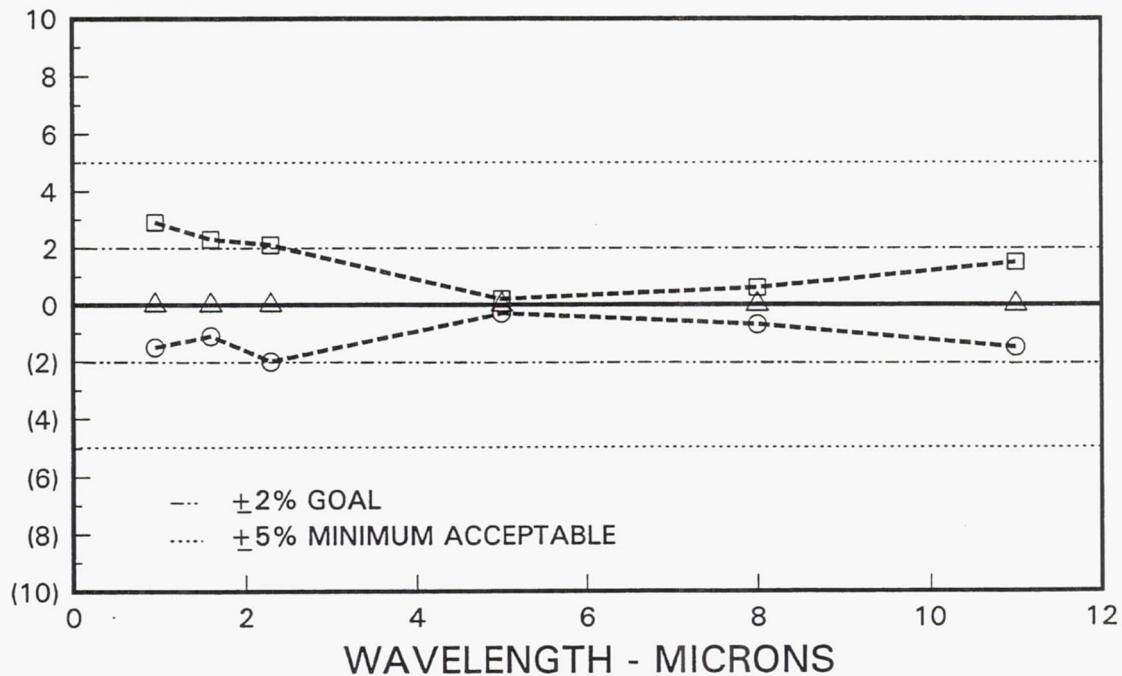


Figure 31 Indicated Temperature Uncertainty for Mullite at 1925K

For the yttria stabilized zirconia and mullite, the situation is quite different. The low variable emittance at short wavelengths yields large correction and high measurement uncertainty in the short wavelength range. For these two materials, the emittance correction to the pyrometer is relatively large at short wavelengths, increases still further at intermediate values, then decreases significantly at long wavelengths (\approx 8 microns). Similarly, the pyrometry uncertainty due to emittance uncertainty is minimized for these two materials at long wavelengths. For zirconia, the temperature measurement uncertainty is outside acceptable (\pm 5 percent) limits at short wavelength but attains the \pm 2 percent contract goals as the pyrometer wavelength increases to 8 microns or greater. Similarly for mullite, the uncertainty will be outside the \pm 2 percent goals for short wavelength pyrometers, but within the goals for larger wavelength units. Clearly, the usual guideline to use the shortest possible wavelength where there is enough energy to make the measurement does not apply to all ceramics. In addition to the emittance considerations, another factor that must be considered for ceramics is their possible optical transmission.

3.3 Translucency Testing

Some ceramics are transparent at some wavelengths and temperatures. Figure 32 shows typical data obtained from the literature for the transmittance of a mullite material. Attempts to measure surface temperature using pyrometers in wavelength bands where materials transmit energy can lead to large errors. The pyrometer will tend to "see into" the ceramic rather than measure the surface temperature. The possible errors are aggravated by the fact that, due to low thermal conductivity, the thermal gradients in the ceramics can be very large. Therefore, averaging the temperature over any significant depth into the ceramic can result in large errors in measured surface temperature.

To demonstrate the possible ceramic transmission problem at elevated temperatures, a short experimental test program was conducted. Figure 33 shows a schematic of that experiment. The apparatus used was a standard Thermogage two-cavity calibration black body furnace. Modifications included drilling a 1.30 cm diameter hole in the carbon wall separating the two black body cavities. A test specimen was then placed against the hole, and the black body was brought up to the required temperature. A high intensity pulsed light source (in this case, a photo strobe) was located on one side of the test specimen and a high speed detector (in this case, a silicon photodiode) was located on the other. When the strobe was pulsed, any energy that was transmitted through the sample under test and reaching the detector could be recorded. Since the heating of the sample by the strobe was negligible, the background energy due to sample luminescence as the result of its temperature, served only as a steady-state offset on the detector output and did not affect the test results.

The rig was initially checked out with no sample in place. This defined the "no absorption" condition. This level of energy transmission was assigned a value of 1.0. Tests were then run with a solid carbon disk as a sample. The purpose of this test was to investigate the possibility of scattered light reaching the detector by some route other than transmission through the specimen. Any such energy was less than the sensitivity of the detector (corresponding to a transmission of about 10^{-6}).

TRANSMITTANCE

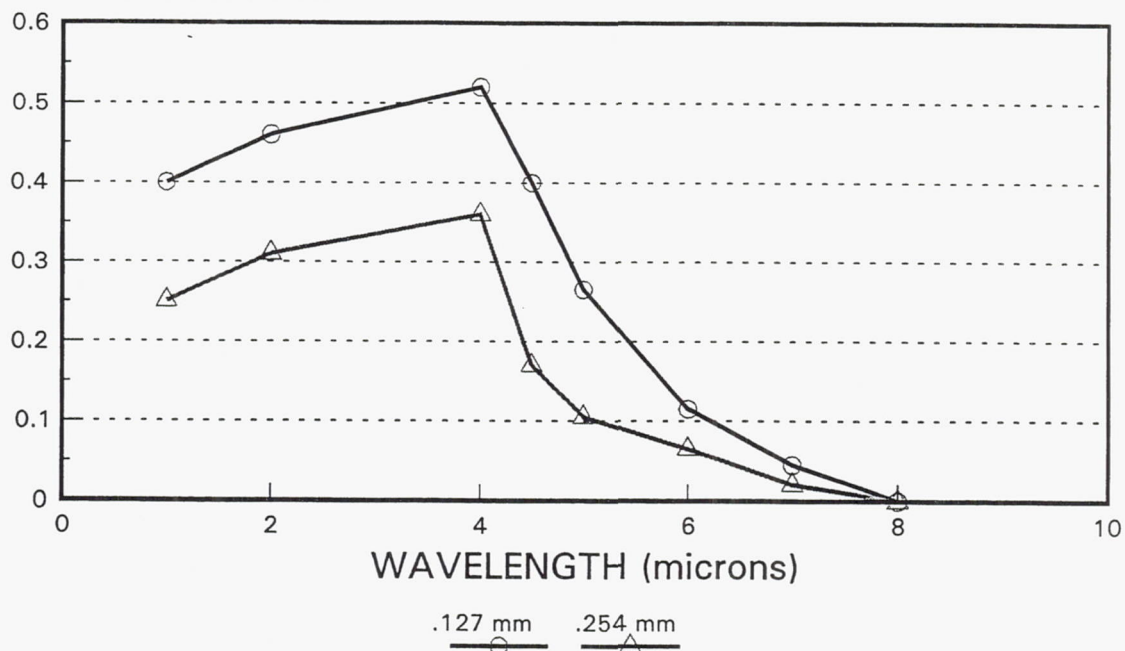


Figure 32 Normal Spectral Transmittance of McDaniel Mullite from Reference 3

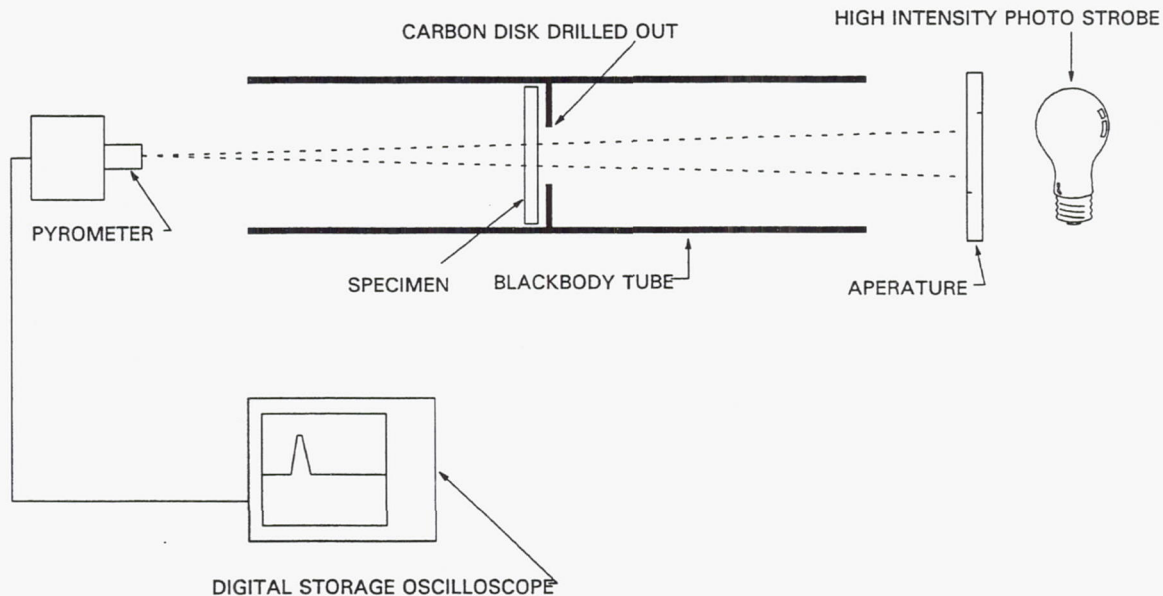


Figure 33 Schematic Diagram of Transmission Test

Five test specimens were prepared. The first was a polished, optical grade sapphire disk made to fit into the black body. The second sapphire sample was frosted on both surfaces to create an optical scatterer. Three more sapphire disks were prepared with 0.03 mm, 0.07 mm and 0.25 mm of yttria stabilized zirconia deposited on the sapphire. The test series on these samples is summarized in Figure 35 and discussed below.

After the rig checkout, the first step in testing was to mount the clear sapphire sample in the tube to demonstrate characteristics for a known material. As expected, the results indicated that almost all the energy from the photo strobe was transmitted through the disk with virtually no apparent scattering. In addition, it was observed that there was almost no self emission from the sapphire as the result of its temperature. This verified that sapphire was a suitable substrate for this test series.

The next set of tests was performed on the frosted sapphire disk. Inspection of the disk pretest showed that shadows and vague images could be seen through the disk despite the frosting. It was, therefore, expected that the disk would be less than a perfect Lambertian scatterer. As shown in Figure 36, a perfect Lambertian scatterer would yield a transmission:

$$T = \frac{d^2}{8x^2}$$

where d is the detector diameter, and x is the scatterer to detector distance.

For this test series:

$$d \approx 0.64\text{cm}$$

$$x \approx 24\text{cm}$$

$$\bar{T} \approx \frac{(0.64\text{cm})^2}{8x(21)^2} = 1.2 \times 10^{-4}$$

As shown in Figure 35, the frosted sapphire had a transmission of approximately 10^{-2} which is significantly higher than would be obtained from a perfect scatterer. This is in accordance with the pretest inspection results of the frosted sapphire disk.

Finally, the three zirconia coated disks were tested. Pretest inspection of the three samples showed that shadows and vague shapes could be seen through the 0.03 mm sample. This may be partially due to the nonuniformity of the very thin samples. The 0.07 mm and 0.25 mm samples appeared uniform and dense. As shown in Figure 35, when tested, the 0.03 mm thick sample yielded a transmission of $\approx 2 \times 10^{-2}$ (similar to frosted sapphire). The 0.07 mm and 0.25 mm samples yielded transmission of $\approx 10^{-4}$ which is in line with what was calculated above for a perfect nonabsorbing Lambertian scatterer.

Somewhat surprisingly, none of the test samples yield transmissions that varied strongly with temperature over the range tested. The data in Figure 9 show the emittance has a strong dependence on temperature at the short wavelengths, and it was anticipated that this effect would be evident in the transmission data as well.

This test series clearly shows that the optical transmission of ceramics must be carefully considered when choosing the wavelength of a pyrometer to be used for measuring ceramic temperature. Our data showed that even relatively thick (0.25 mm) samples of zirconia (7%YSZ) yield significant spectral transmission at 0.9 microns. The data are consistent with a perfectly scattering, nonabsorbing material. More work in this area is clearly required.

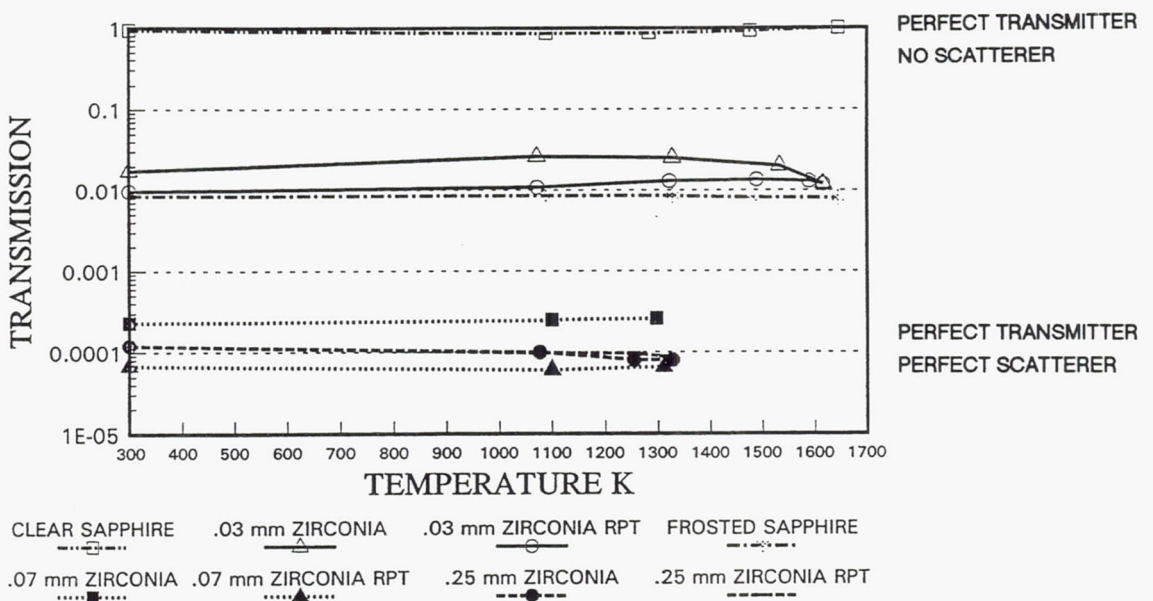
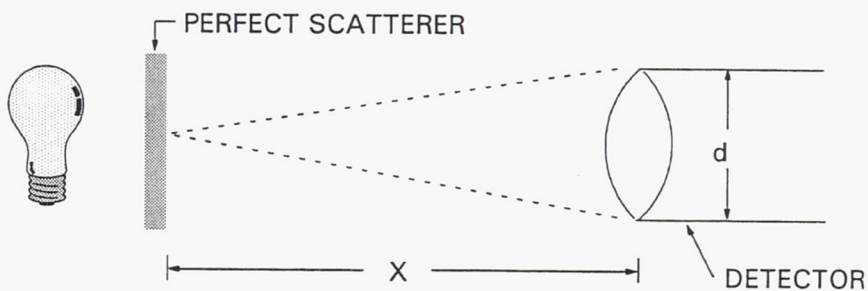


Figure 34 Measured Transmission Data for Sapphire and Zirconia at 0.9 Microns



$$\text{TRANSMISSION} \approx \frac{\text{DETECTOR AREA}}{\text{TOTAL HEMISPHERICAL AREA AT DETECTOR PLANE}} = \frac{\frac{\pi d^2}{4}}{2\pi X^2} = \frac{d^2}{8X^2}$$

Figure 35 Perfect Lambertian Scatterer

3.4 Results

Emissivity testing at Pratt & Whitney and UTRC indicates that for some ceramics, such as Si_3N_4 , SiC , and Compglas®, the conventional pyrometry guideline of running at as short a wavelength as possible to minimize emittance effects still works well. Other ceramics, such as zirconia and mullite, show large data scatter and/or low values at low wavelengths. At higher wavelengths, the data are better behaved and stable. This would tend to substantiate the use of long wavelength pyrometers to make surface measurements on these ceramic materials.

Data from the literature and a test series conducted under this contract also showed that ceramic translucency must be carefully considered. The proof-of-concept tests were performed at a wavelength of 0.9μ with a silicon detection system. This system showed that the zirconia was able to transmit energy through even a 0.25 mm thickness. Available data indicate that many ceramics became more opaque at longer wavelengths. This is another factor that indicates that long wavelength pyrometry may be the best choice for many ceramics.

In many pyrometry installations, fiber optics are used to transmit energy from the test location to the detector system. A concern for long wavelength pyrometry is the identification of suitable fiber systems. Figure 36 shows typical loss curves for three classes of fiber materials. Conventional silica glass currently used for short wavelength pyrometry work does not transmit energy beyond 2μ and is not suitable for long wavelength work. Fluoride glass extends the transmission to about 5μ but absorbs strongly at longer wavelengths. Current chalcogenide glasses transmit energy to longer wavelengths, but fiber lengths would have to be relatively short because of the large losses within the fiber. The field of infrared transmitting fibers is progressing rapidly. Refinement of existing materials, and development of new materials and unique concepts, e.g., hollow fiber infrared wave guides (Reference 6), are all being pursued. These will give increased flexibility in the development of the long wavelength pyrometer system for use on ceramics.

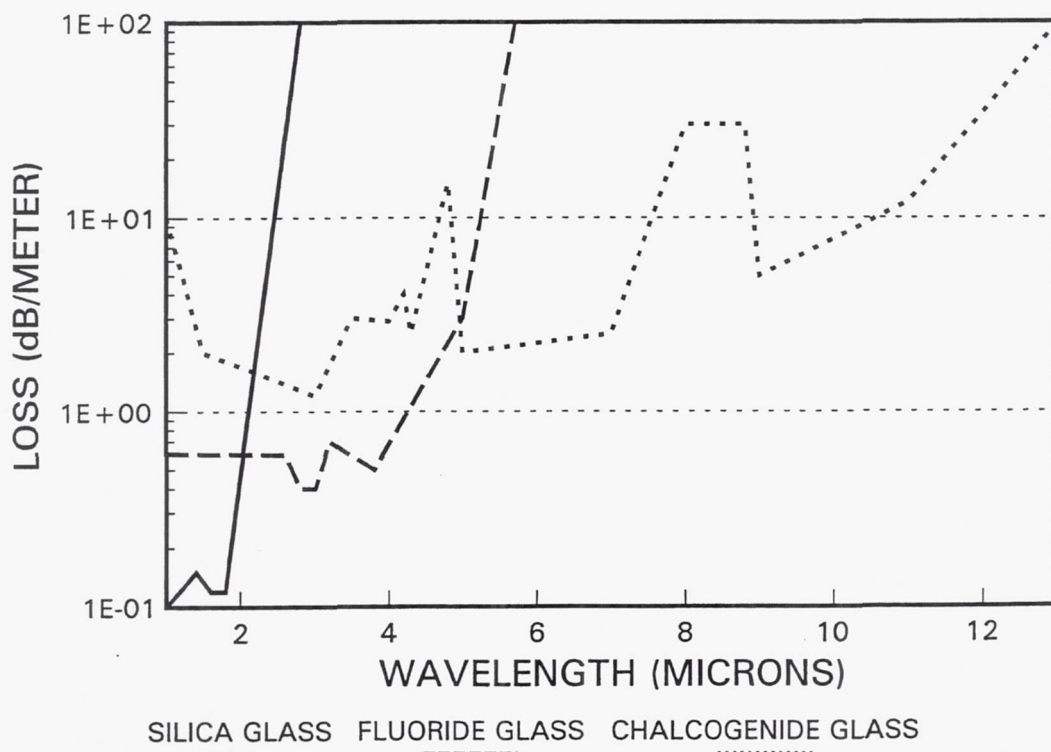


Figure 36 *Typical Loss Curves for Fiber Optic Materials*

3.5 Conclusions

Based on the results of the emissivity and translucency testing, short wavelength pyrometry is not recommended for materials like zirconia. The instability of the emissivity values at short wavelength, along with the translucency of these materials, would lead to significant errors in temperature measurements. These materials also have unstable emissivities, and probably transmissivity, which change as the materials cycle to temperature (i.e., oxidization, reduction of substrate, etc.).

At longer wavelengths, these problems seem to disappear. The emissivities become very stable and repeatable. This also leads one to believe that the materials are opaque at these wavelengths. Emittance measurements at these wavelengths become more critical for accurate temperature measurements, however. Small errors in emittance will now lead to large errors in surface temperature.

3.6 Recommendations

Care must be taken and individual ceramic characteristics must be considered when choosing a pyrometer. For some ceramics, the conventional wisdom of using short wavelengths works well; for others, it leads to a very poor selection. If a single system is to be chosen for use on a wide range of ceramics, a system operating at about 8μ seems to be the best choice. Emissivity testing should continue in order to expand the catalogue of existing as well as new materials and to investigate apparent differences between test facilities.

Additional translucency testing is recommended to further characterize the behavior of ceramic materials. A wide range of materials needs to be tested over extended wavelength bands. The limited proof-of-concept testing performed under this contract shows that this could be the limiting factor in the accuracy of pyrometry on ceramics.

Finally, systems integration work is required to investigate infrared transmitting fibers combined with long wavelength detectors to produce pyrometer systems for routine thermal measurements of advanced ceramics.

4. THIN-FILM SENSORS

4.1 Sample Preparation

The substrates to be used for thin-film samples were cut to size and then sent to United Technologies Research Center where they were lapped and polished to obtain the smoothest finish possible. Due to the difference in the physical makeup of the various ceramics and composites, each material had to be prepared in a different manner.

Si_3N_4 ceramics were first lapped on a diamond (μm grind) impregnated steel lapping plate to obtain a flat surface. They were cleaned thoroughly and transferred to a finer lapping plate consisting of a $12\mu\text{m}$ imbedded diamond to form a semi-polished surface. A final polish was obtained using a polishing cloth and a colloidal silica slurry.

Compglas® was processed in a similar manner. Compglas® could not be polished due to the makeup of the material. During the lapping process, the matrix of woven fibers would tear and break, creating a very rough surface. This problem was resolved by depositing Si_3N_4 , and giving a final polish with 1μ diamond paste on a polishing cloth.

The other materials were also prepared in the event that time and funding permitted. The silicon carbide and mullite samples were prepared using the same method as for the silicon nitride samples. The yttrium oxide samples were only lapped. The porosity of the substrate prevented obtaining a high polish. After the samples were polished, they were distributed to the various locations to have the thin-film thermocouples applied.

4.2 Application Methods

4.2.1 Ion Beam Etch Deposition

After the substrates were lapped and polished, the thermocouples were ready to be applied. The photoresist lift-off method was used to pattern the thermocouples. This method consisted of coating the substrate with positive photoresist, and baking at 350K to cure the photoresist. A photo mask was used to expose and develop away the resist where the thermocouples were to reside. The substrates were subsequently ion plated with the required metal to the proper thickness. The areas of photoresist that were covered with metal were then removed with acetone, leaving metal only at the electrode areas.

The contact printing exposure systems used would not allow us to contact print the photomask as supplied by Pratt & Whitney. The photomask alignment marks were outside the range of travel of the mask aligner. A composite mask was generated to include the Pt leg, center leg, and Rh leg to be used for alignment since it lay inside the range of travel of the mask aligner.

At the outset, Pt and Rh films were deposited directly onto the substrate surface. The adhesion of the film to the substrate was inadequate, and the thermocouple metal would peel off during the lift-off process. To overcome the adhesion problem, a thin layer of chrome was deposited prior to depositing the Pt and Rh films.

The final fabrication sequence was as follows:

1. Ultrasonic clean substrates after lapping and polishing
2. Deionized water rinse and dry with N_2 gas

3. Photoresist with HOECHST type 4620 photoresist
4. Oven cure at 350K for 30 minutes
5. Expose and develop composite mask pattern
6. Mount samples in ion beam vacuum system
7. Ion etch samples for 1 minute to clean surfaces
(200ma beam current, 1KV beam voltage)
8. Ion plate 1000Å of Cr on substrates
9. Mask off right electrode (Rh leg) up to junction overlap area
10. Place back in ion beam vacuum system
11. Ion beam etch exposed Cr to remove 500Å Cr
12. Ion beam deposit Pt to required thickness
13. Remove from vacuum system and lift off masking material in acetone
14. Reapply photoresist to the substrate; and cure, expose and develop composite mask
15. Mask off left and center electrode (Pt leg) up to overlap area
16. Place back in ion beam etch system
17. Ion etch exposed Cr to remove 500Å Cr
18. Ion deposit required Rh thickness
19. Remove from ion beam system and lift off masking with acetone
20. Thermocouple is now ready to have lead wires attached in preparation for testing.

The method outlined above resulted in the metal films having good adhesion to the substrates at room temperature. The exception to this was the yttria stabilized zirconia substrates. These substrates were very porous, and were very difficult to pattern because the photoresist soaked into the bulk of the substrate. Photos of these sensors on the different substrates are shown in Figures 38 through 42.

During temperature cycling testing, the thermocouples failed by lifting from the substrate. Possible causes of this problem were thermal coefficient mismatch, chrome layer diffusion, stress in the thin-films, outgassing of the substrate, or a combination of these factors. An attempt was made to address the adhesion problem of these sensors.

Two silicon nitride substrates were thermally cycled to stabilize the surface before the films were applied. The substrates were ramped up to 1275K at a rate of 10K/minute, held at 1275K for one hour, and cooled to room temperature at a rate of 10K/minute. The sensors (Figure 43) were then applied to the surface by ion beam etch deposition.

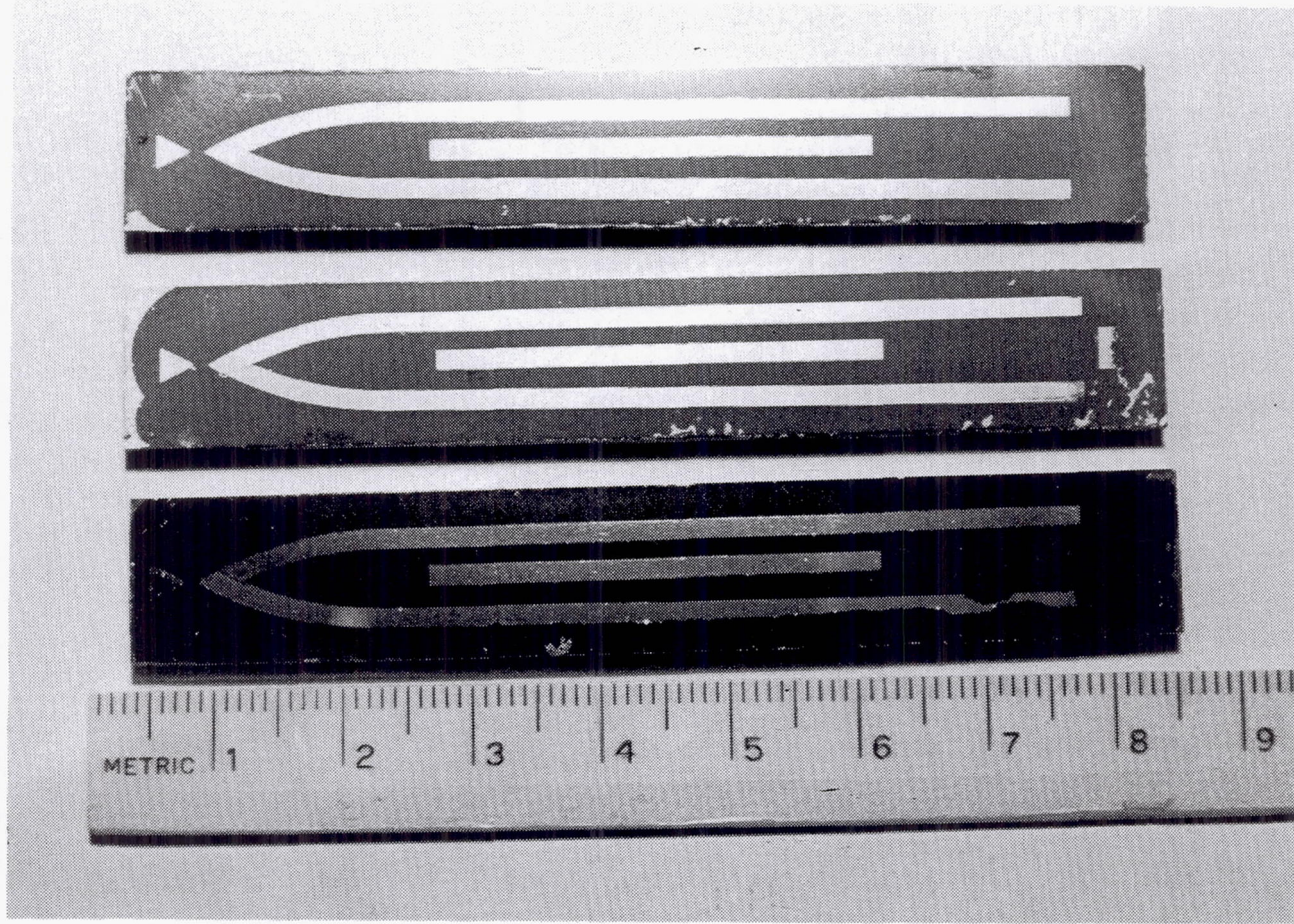


Figure 37 Ion Beam Etch Deposition Sensors Applied to Silicon Nitride

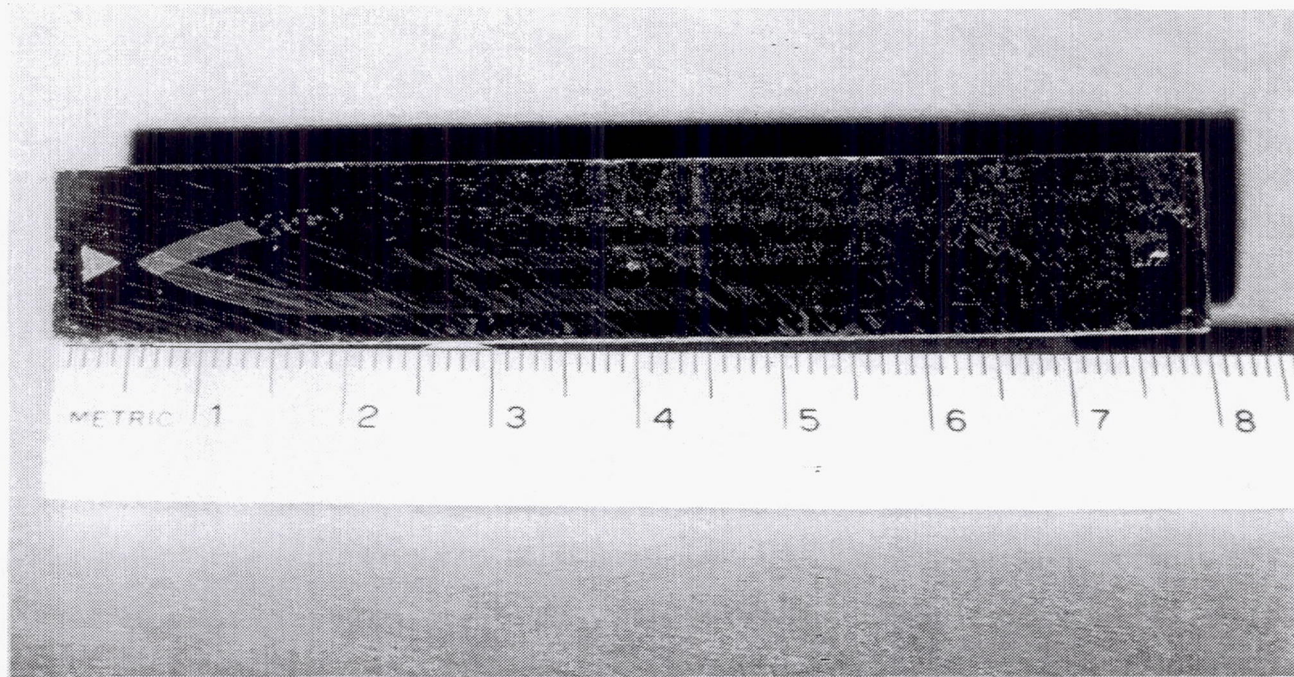


Figure 38 Ion Beam Etch Deposition Sensor Applied to Compglas®

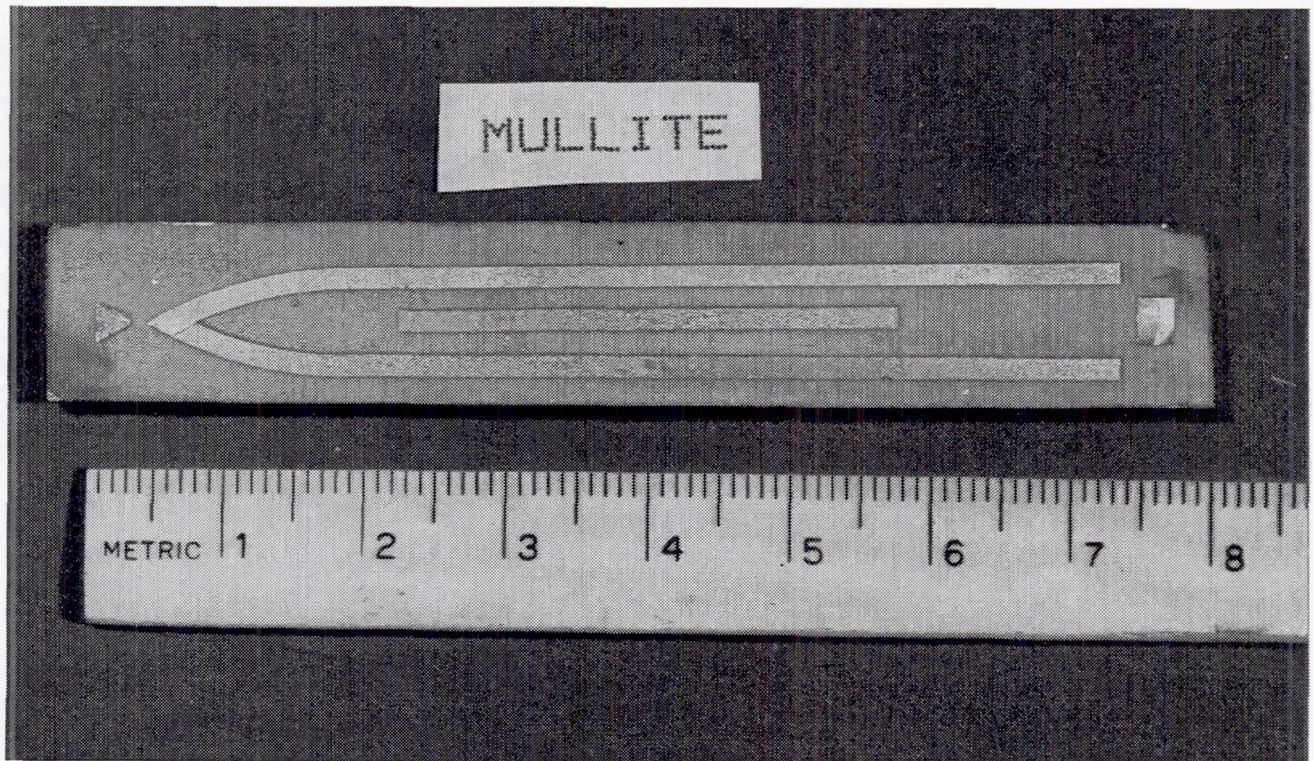


Figure 39 *Ion Beam Etch Deposition Sensor Applied to Mullite*

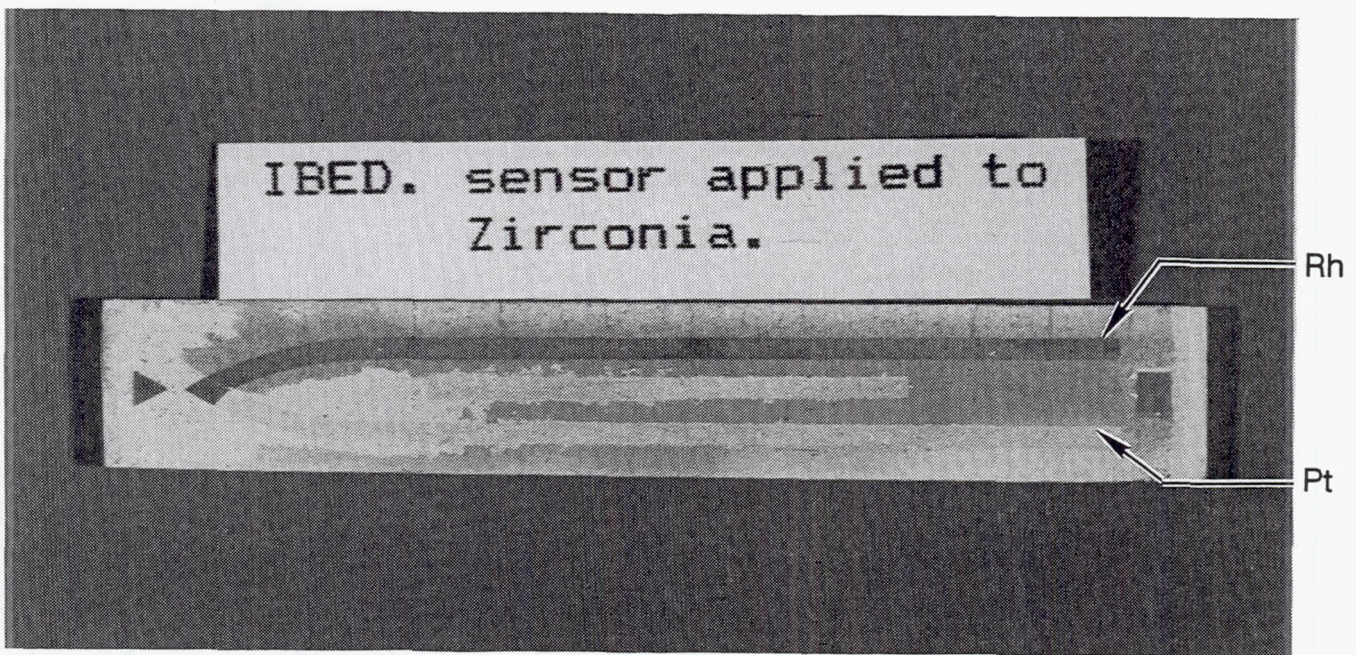


Figure 40 *Ion Beam Etch Deposition Sensor Applied to 7% Yttria Stabilized Zirconia*

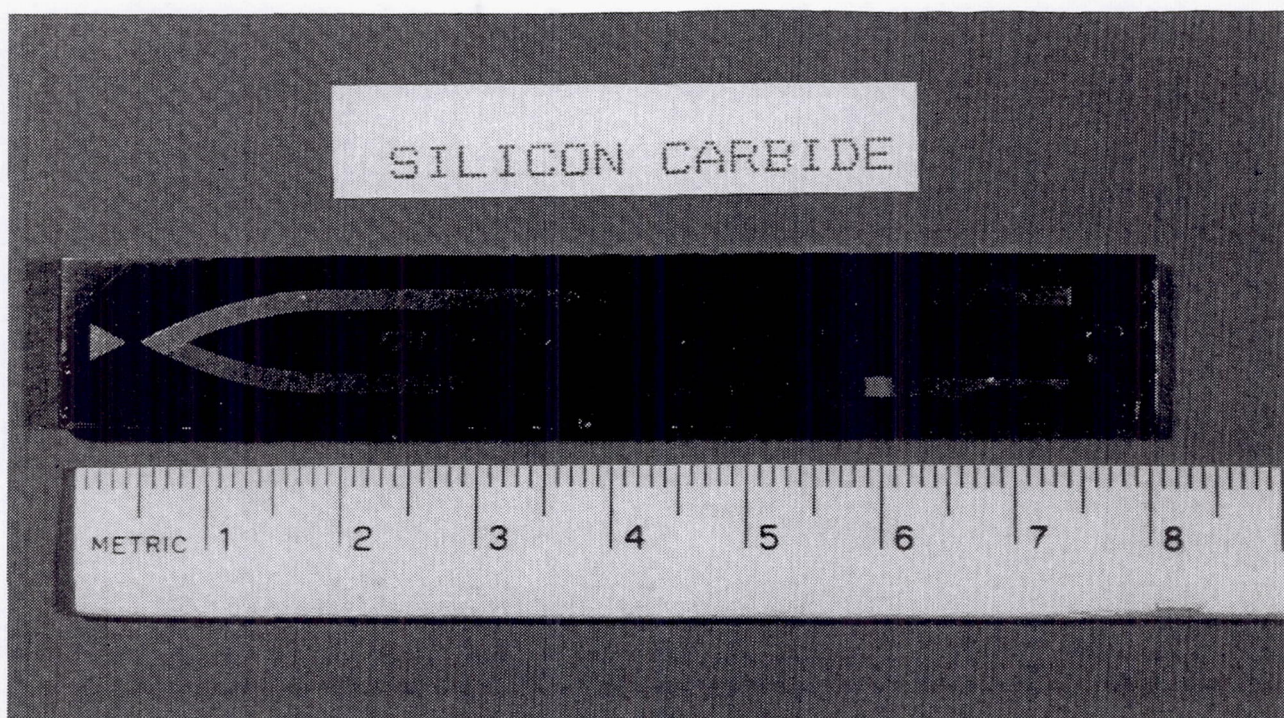


Figure 41 *Ion Beam Etch Deposition Sensor Applied to Silicon Carbide*

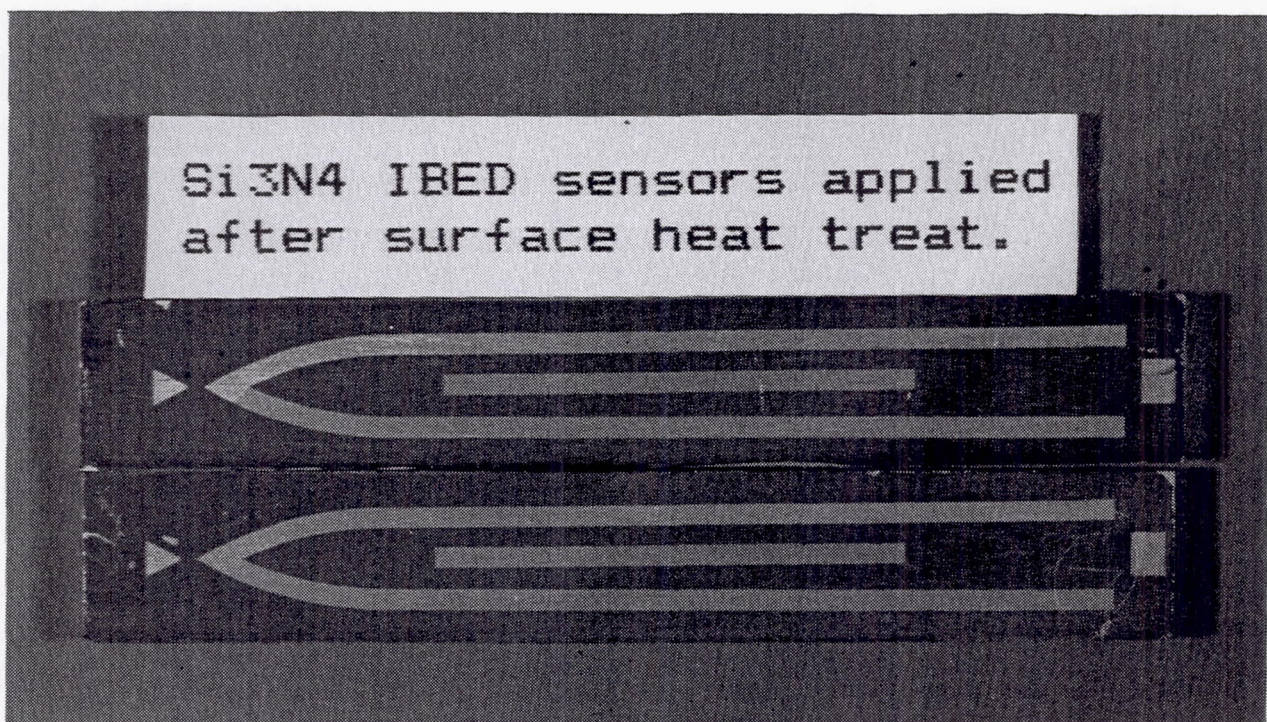


Figure 42 *Ion Beam Etch Deposition Sensors Applied to Silicon Nitride After the Substrate Was Heat Treated*

After the films were applied, one of the samples (Figure 43) was subjected to a second bake cycle at 1275K for one hour. The films remained intact, but the rhodium leg was noticeably darkened. The sensor resistance, measured with an ohmmeter, increased by a factor of 10. Limited funds prevented an investigation into what had physically occurred. One possibility is that the chrome interface layer may be diffusing into the films, thereby raising the resistance. Another possibility is oxidation of the rhodium film.

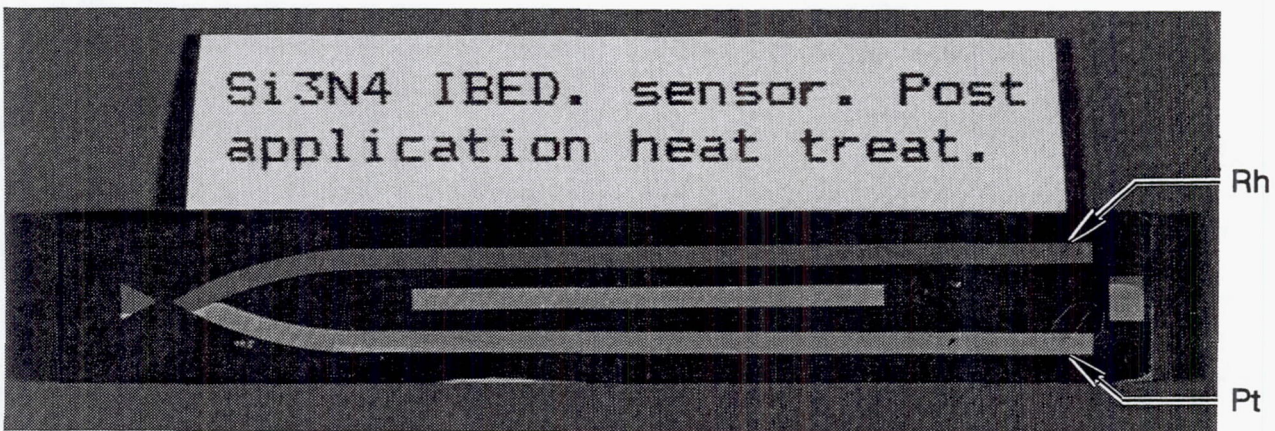


Figure 43 *Ion Beam Etch Deposition Sensor Applied to Silicon Nitride After Post Application Heat Treat*

4.2.2 Evaporation Plus Ion Implantation

For this phase of the task, the deposition of the thermocouple materials on the ceramic substrates was performed using a combination of electron beam (e-beam) evaporation and ion implantation. The rationale for this approach was that high-purity materials could be deposited using the inherently clean process of electron beam evaporation. Electron beam evaporation typically takes place at pressures of 10^{-6} pascals (10^{-8} torr). Due to the low background pressure, few contaminants are incorporated in the film during deposition. Consequently, it appeared that bulk value electrical properties could be expected from the thin-film thermocouples fabricated in this manner.

While it is generally recognized that electron beam evaporated material is high in purity, it is also generally agreed that e-beam deposited material does not adhere as well to the substrate as do materials deposited by other means (e.g., sputtering or ion beam deposition). To enhance the adhesion of the e-beam deposited material, ion implantation (using the concept of "knock-on" implantation) was used. In this technique, a thin film of the thermocouple material in question is deposited by e-beam evaporation. The shape of the thermocouple was defined using a stainless steel shadow mask which was held in intimate contact with the substrate. The thickness of the evaporated film was chosen to be about equal to the projected peak penetration of the implanted ion specie. To maximize the effectiveness of the "knock-on" technique, ions of the same material as the evaporated material were produced. That is, platinum ions were used to "knock-on" platinum, and rhodium ions were used to "knock-on" rhodium. The number of ions implanted was between 15 percent and 20 percent of the total number of atoms deposited in the thin e-beam evaporated layer. The desired result was that a graded junction would be produced between the substrate and the thin-film thermocouple. Following the implant step, a thicker layer of either platinum or rhodium was e-beam deposited to increase the total thickness of the thermocouple film.

In this phase of the program, three different varieties of the above concept were tried. For each variety, two samples were fabricated and tested. The first set of samples included silicon nitride

(Si_3N_4) substrates. In this group, layers of platinum 150Å thick and layers of rhodium 200Å thick were e-beam deposited on the Si_3N_4 substrates. The substrates were held at 675K during evaporation for all samples prepared during this phase of the program. Following evaporation, the samples were subsequently implanted with 200 key ions of either platinum or rhodium. The implanted dose was 2×10^{16} ions/cm². The substrates were at a temperature of approximately 300K during the implant. Following the implantation, platinum or rhodium was evaporated to increase the thickness of the metal on each leg to approximately 4μm.

The second set of samples in this phase of the task were fabricated on Compglas® substrates. Essentially, the same procedure was used to produce the initial thin films of platinum and rhodium and the subsequently implanted layers as was done in the previous samples. However, since it was observed that the thick (4μm) layers of rhodium had cracked during fabrication of one of the samples and the overlapped area of the sample under test had lifted after several thermal cycles, it was decided to reduce the total thickness of the thermocouple to 0.4μm. This set of samples showed no sign of cracks forming as a result of the fabrication process. The thermocouples performed very well under temperature testing until the rhodium leg oxidized to the point that the resistance became too high.

The third set of samples was silicon nitride. This time, alternating thin layers of evaporation and implants were used to increase adhesion. The electrode applications were conducted as follows:

For the platinum leg:

1. Three layers of 150Å platinum evaporation, followed by implant as described above
2. Two layers of 200Å evaporation and implant
3. Two layers of 250Å evaporation and implant
4. One layer of 300Å evaporation.

For the rhodium leg:

1. Two layers of 200Å evaporation and implant
2. Two layers of 300Å evaporation and implant
3. One layer of 400Å evaporation.

Two samples were prepared with this method. One was overcoated with silicon nitride. The other was left as is. This sample was not tested due to time and budget constraints.

4.2.3 Radio Frequency Sputtering

Samples prepared for sputtering went through the following processes. First, the samples were cleaned with a mixture of ethyl alcohol and ammonium hydroxide and rinsed with alcohol. Samples were then dried and baked at 380K. AZ1350 photoresist was applied; allowed to dry; and then underwent a prebake, expose, develop, dry, and bake cycle in order to complete masking.

For deposition, the samples were oxygen etched in the vacuum facility. This was pumped down to 1×10^{-6} torr and then backfilled to 5 millitorr with oxygen. Flow was set at 45 Sccm, with an aluminum oxide target in place. The facility had a forward power of 400w at 13.56 MHz and reflected power of 8w. Target and substrate voltages were 4kv and 300v, respectively. This process took 10 minutes.

The actual deposition of platinum and rhodium was performed in a vacuum of 1×10^{-6} torr backfilled to 5 millitorr of argon. Flow was set at 40 Sccm. Forward and reflected power were 400w and 8w, respectively. Target voltage was 4.5kv and substrate voltage was 30v. This process took 2.5 hours to deposit 4 μ m of platinum or 4.5 hours to deposit 8 μ m of rhodium.

4.3 Testing Procedure

Samples were tested using the tube furnace shown in Figure 44. The furnace was cycled to temperature while monitoring the EMF generated by the films. The facility consists of a 3.81 cm diameter by 20 cm long Inconel tube which is split in half lengthwise to facilitate sample installation. The ends of the heater tube are clamped in water-cooled electrodes which provide up to 900 amperes of AC power. Power to the furnace is controlled by a commercial closed loop controller and programmer. The programmer is adjusted to provide for constant temperature soaks at elevated temperatures and/or linear heating and cooling cycles at heating rates up to 250K/min.

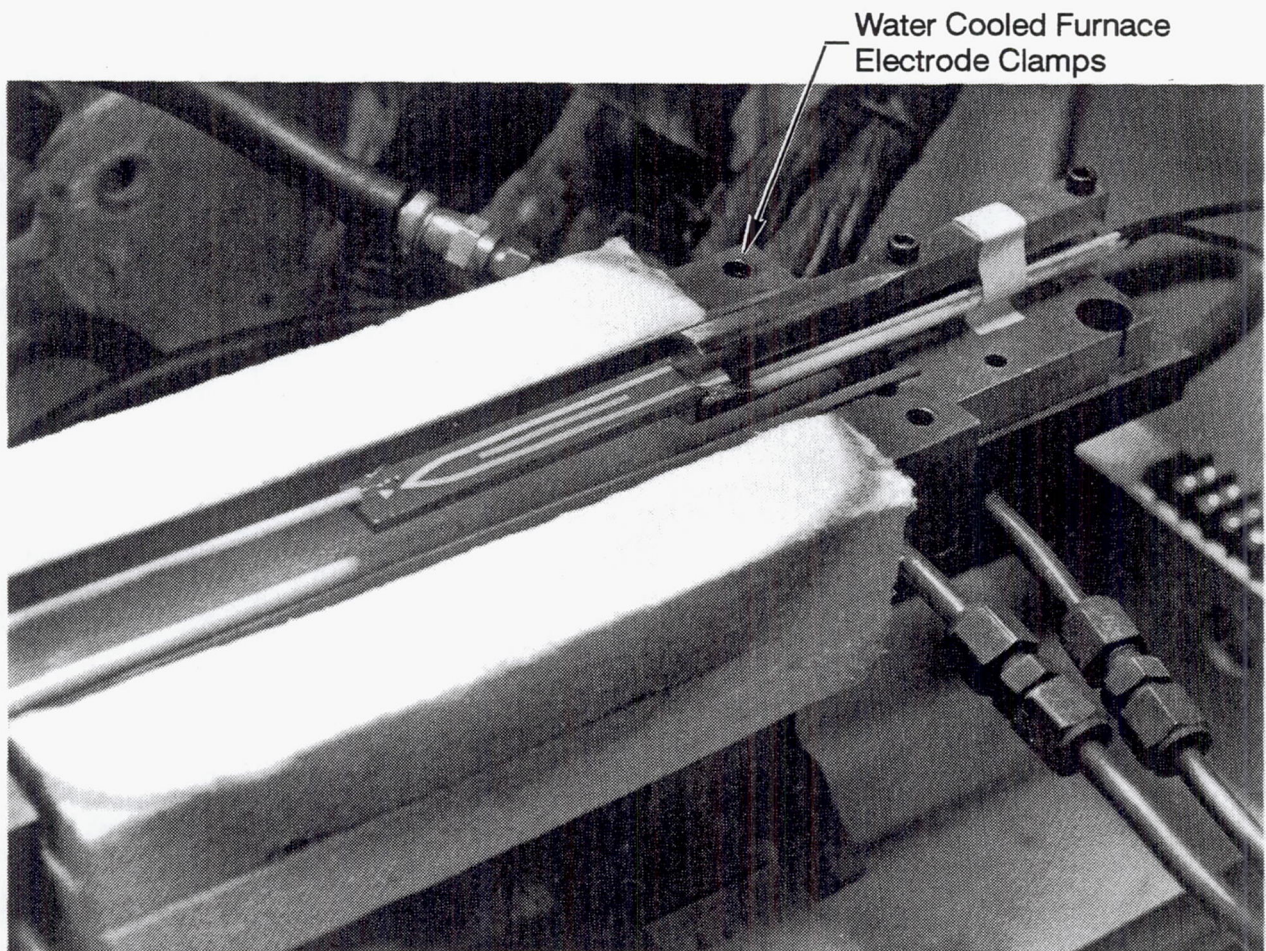


Figure 44 *Tube Furnace with Top Half Removed Showing Sample in Position for Thermal Testing*

A set of B-1900 superalloy clamping bars, which extended 5 cm into one end of the furnace, provided the clamping force for electrical contacts and physical support of the sample. Electrical contact with the thin-film leadfilms was made through 0.254 mm diameter platinum and rhodium leadwires clamped to the ends of the leadfilms and insulated from the B-1900 by an alumina plate. The temperature of the sample was measured by a 0.127 mm ANSI type S (Pt-Pt 10% Rh) thermocouple whose bead (junction) was in contact with the substrate adjacent to the thin-film junction.

A computer, voltmeter, programmable power supply, and a scanner were used to measure the resistance data and to store it on a floppy disk. The standard accuracy of the voltmeter was $20 \mu\text{V/V}$ (0.002% error) which was further improved to $4 \mu\text{V/V}$ (0.0004% error) by averaging five separate readings. A set of measurements was triggered by a wire thermocouple EMF change equivalent to $\pm 50\text{K}$.

The samples have a naming convention as follows: the first three letters indicate application technique (SCC-IBED; IIE-ION implant; RFS - sputtering); and the last two indicate substrate (S for silicon nitride; C for Compglas®) and sample number.

The first sample tested was an ion beam deposition sensor on silicon nitride, designated SCC-S5. This sample was also used to verify the test apparatus and data acquisition system. The sample was cycled to 800K twice, at a rate of 18K/minute. The EMF data (Figure 45) were much lower than the predicted value. Post-test examination revealed that both the platinum and rhodium films had spalled at the junction area. A photograph of this sample is shown in Figure 46.

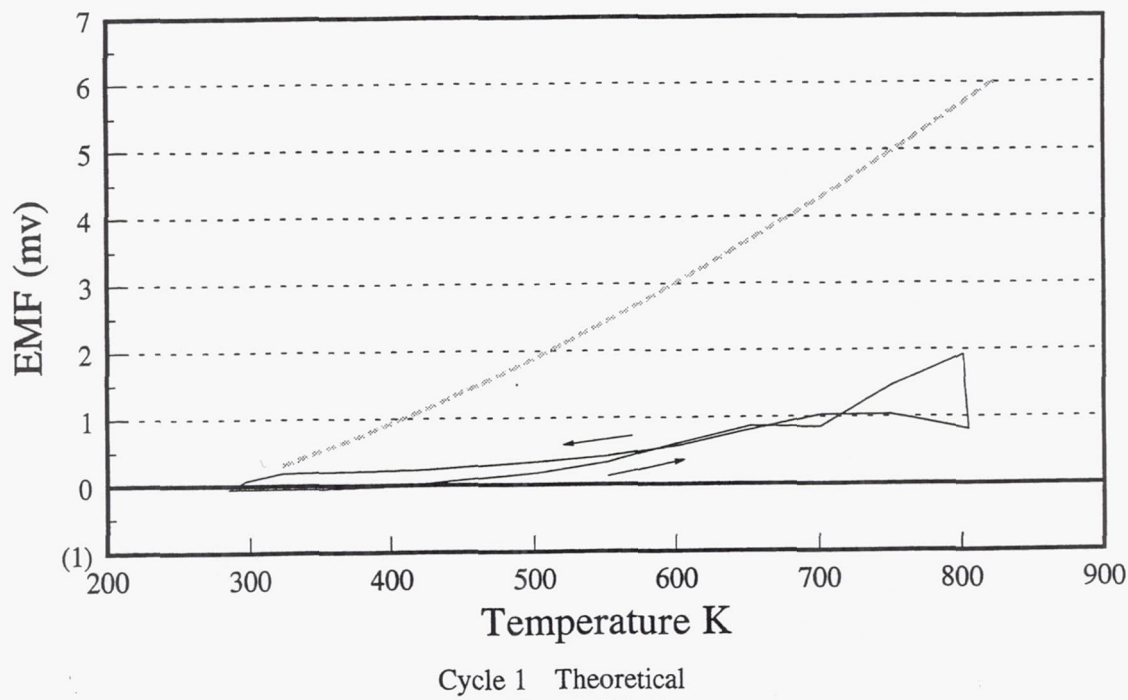


Figure 45 EMF Data from Sensor SCC-S5

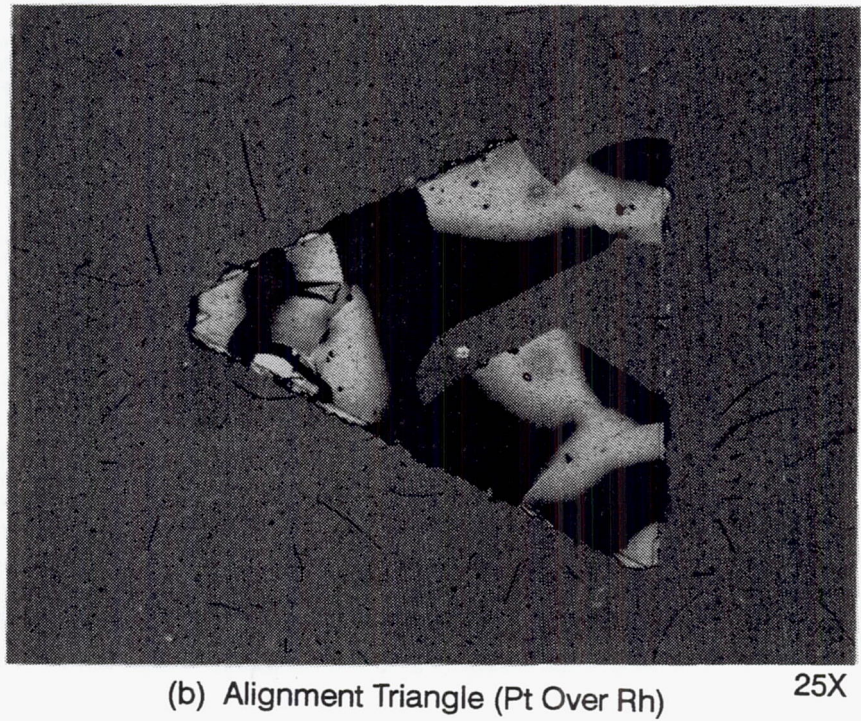
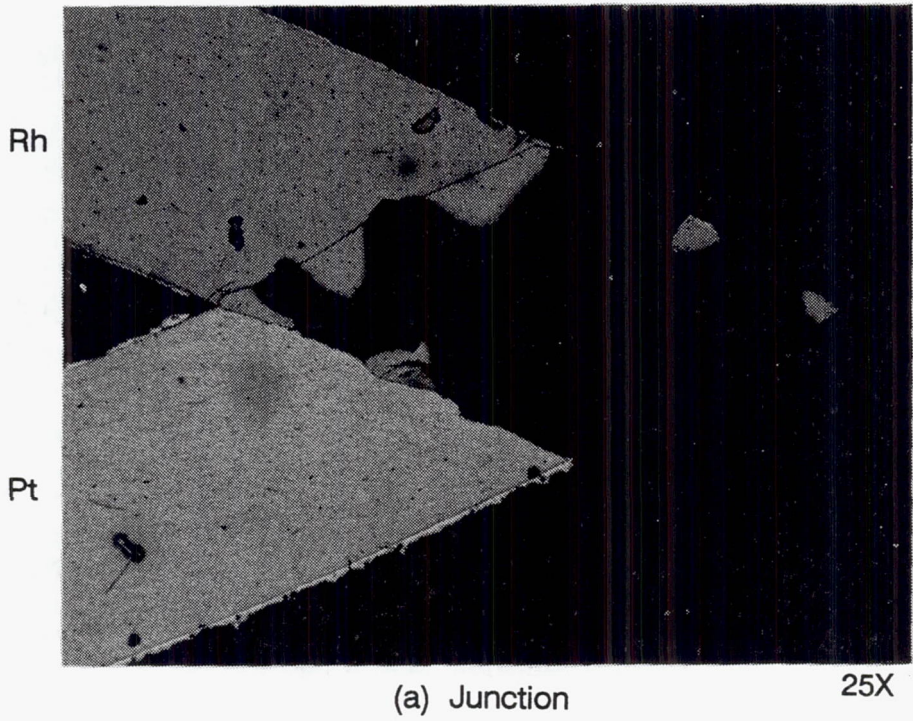


Figure 46 Photograph of Junction Area of Sample SCC-S5 After Two Cycles to 800K. Black regions are areas where the films have lifted from the silicon nitride.

Sample SCC-S3 was cycled once to 915K at 15K/minute. The EMF was approximately half the anticipated value, and the cool-down value did not track the heating as shown in Figure 47. The sensor became an open circuit on cool down. Post-test examination revealed that the platinum leg was wrinkled and cracked. The rhodium leg had apparently oxidized and darkened. This sensor is shown in Figures 48 through 51.

Sample SCC-S2 failed prior to testing, with the platinum leg delaminating from the surface.

Sample SCC-S4 was cycled to 920K at 16K/minute. The sample failed during the first cycle cool down. The output, shown in Figure 52, was again low and the cooling values did not repeat the heating values. Post-test inspection showed that the rhodium film had apparently oxidized and delaminated from the surface. The platinum film appeared good.

Sample SCC-S1 was cycled twice to 590K at 15K/minute. The output (Figure 53) was again low and exhibited an open loop between heating and cooling. On visual inspection, both films were bright and shiny after these cycles. One cycle to 915K was run with 30-minute holds at 590K, 770K and 915K, both on the heating and cooling portions of the cycle. As shown on Figure 54, all the holds on the heating cycle produced positive drifts, and the holds on cooling resulted in negative drifts. This indicates that given enough time, the output may stabilize at a discrete value. The reason for this behavior is unexplained. If the open loop behavior were caused only by a lack of thermal equilibrium of the sample in the oven, the 30 minute hold should have been sufficient time for the sample to reach equilibrium. The sample failed upon cooling to 350K. Visual examination after test indicated that the junction area had spalled. The platinum leg was shiny and wrinkled. The rhodium leg was darkened and also wrinkled.

The discrepancy between the measured EMF and the expected values was unexplained; therefore, a test was run to answer questions on the test technique. A platinum/rhodium thermocouple was produced from 1.27 mm wire. The thermocouple was installed on a piece of alumina that was the same size as the other test samples. Another piece of alumina was used to sandwich the thermocouple. The thermocouple was then clamped to the lead wires and inserted into the furnace. It was cycled to 920K in 30 minutes, which is faster than the heat rate used for the samples. The data (Figure 55) closely matched book values for pure metal thermocouples. The heating and cooling curves for this thermocouple were also very close in value. This test was run to determine if the low outputs were a function of the clamping method, stray EMFs or the data acquisition/reduction system. This test did not identify any cause for the low output. Testing on other samples was then resumed.

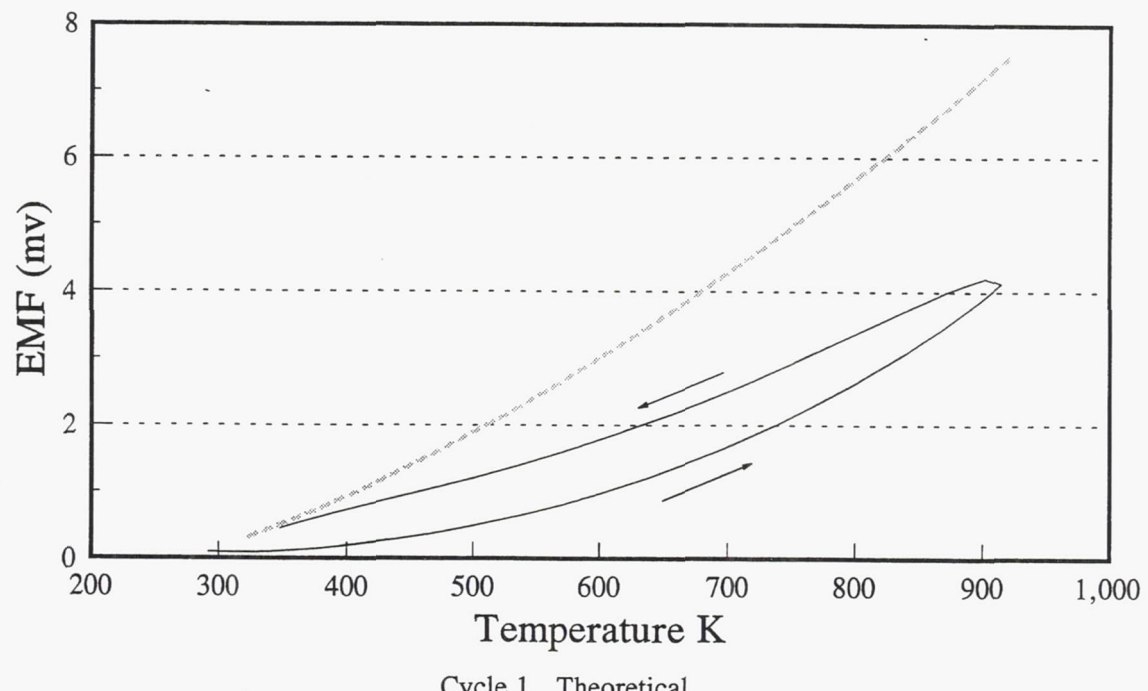


Figure 47 *EMF Data from Sensor SCC-S3*

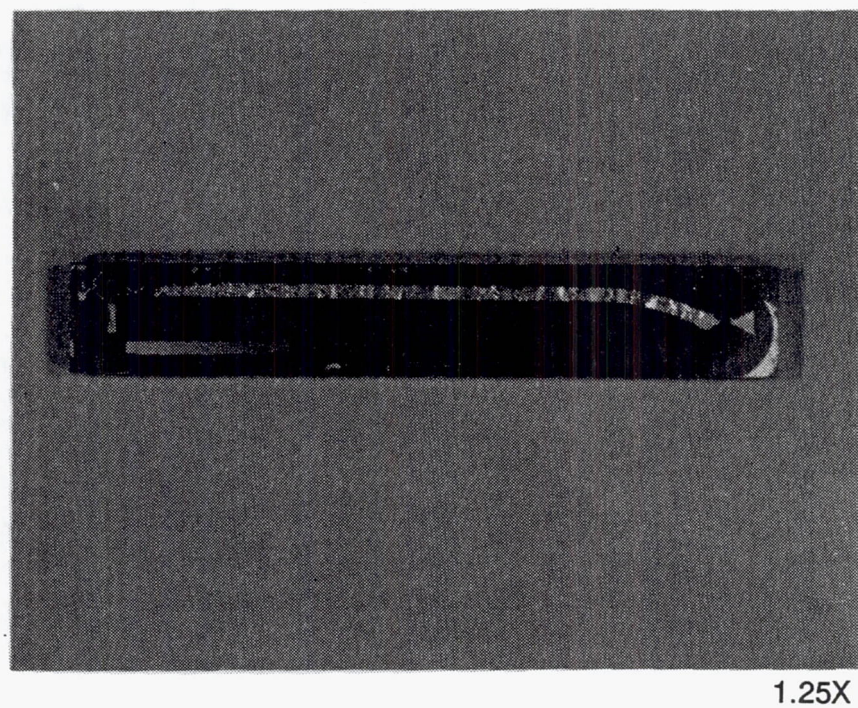
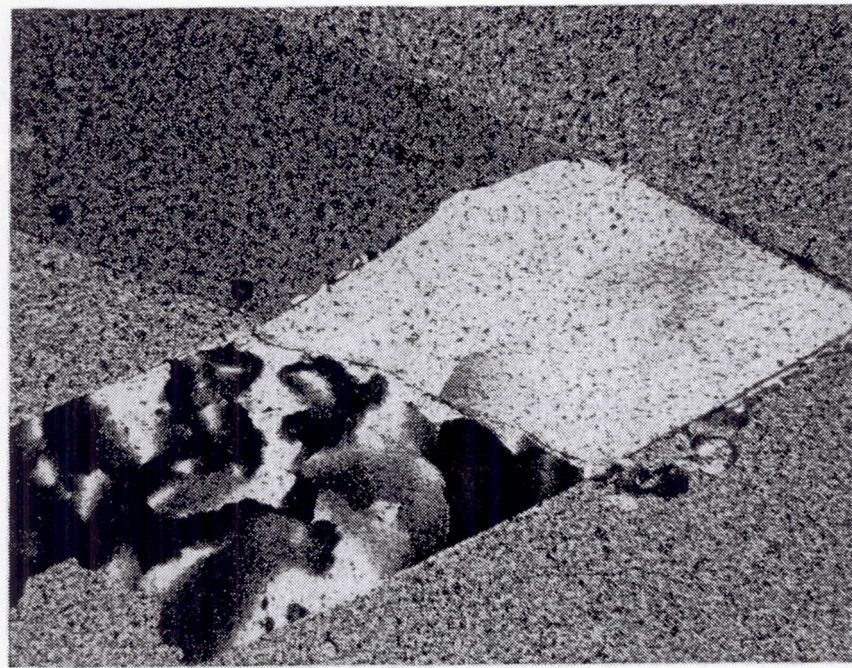
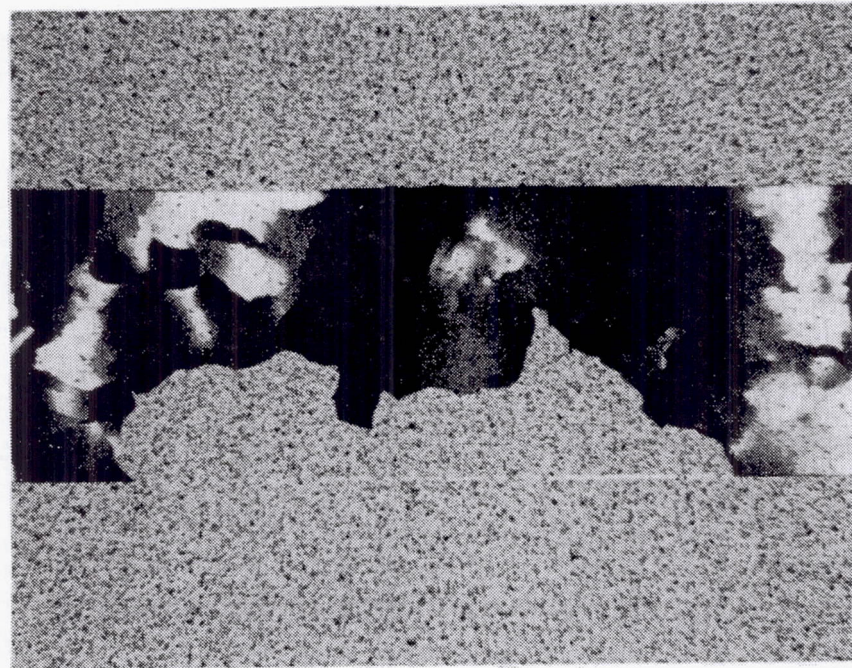


Figure 48 *Photograph of Sensor SCC-S3 After One Cycle to 915K*



25X

Figure 49 *Photograph of the Junction Area of Sensor SCC-S3 After One Cycle to 915K*



25X

Figure 50 *Photograph of Platinum Leg of Sensor SCC-S3 After One Cycle to 915K*

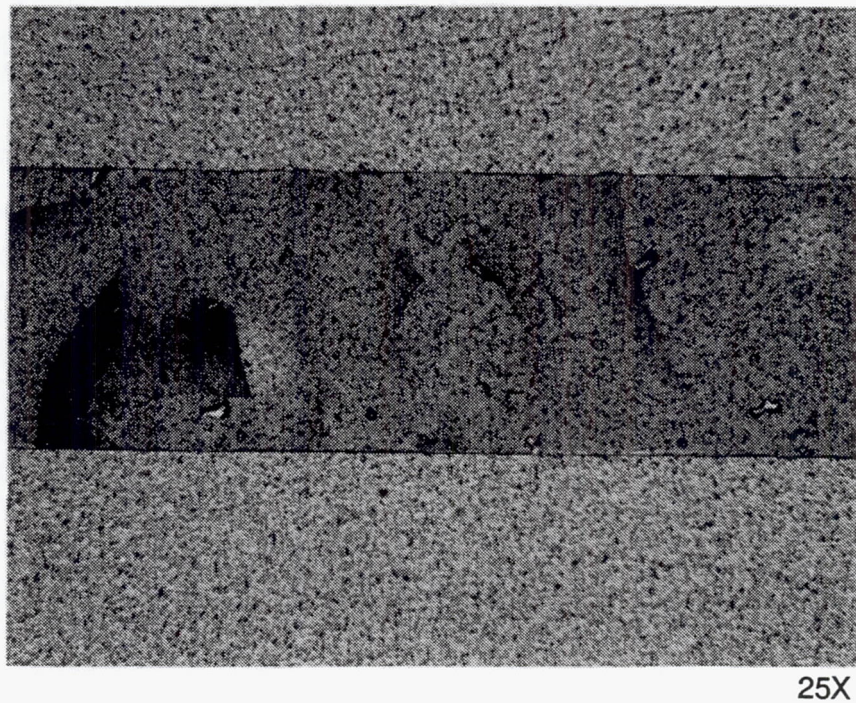


Figure 51 *Photograph of Rhodium Leg of Sensor SCC-S3 After One Cycle to 915K*

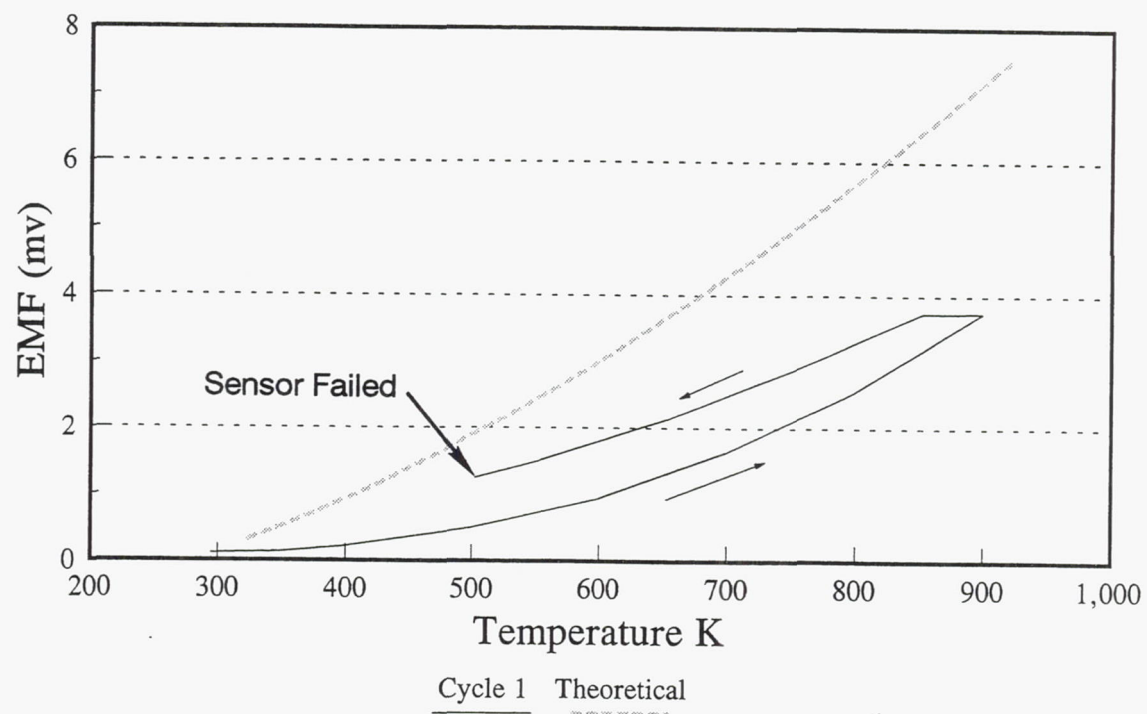


Figure 52 *EMF Data for Sensor SCC-S4*

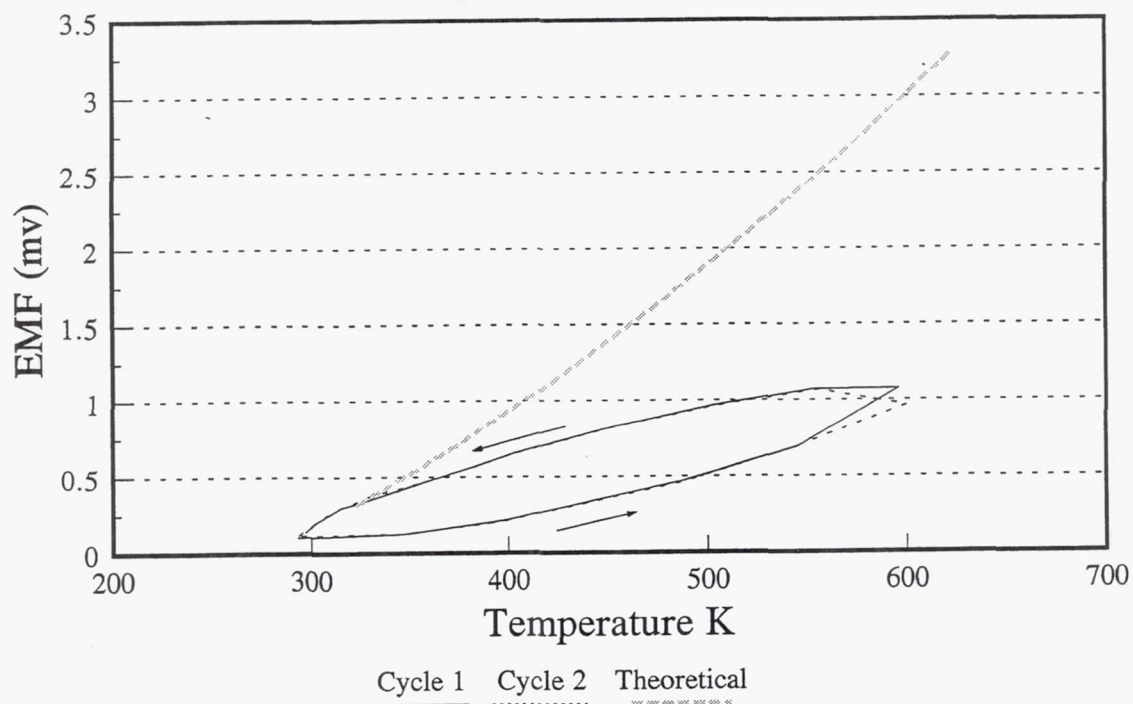


Figure 53 EMF Data for Sensor SCC-S1

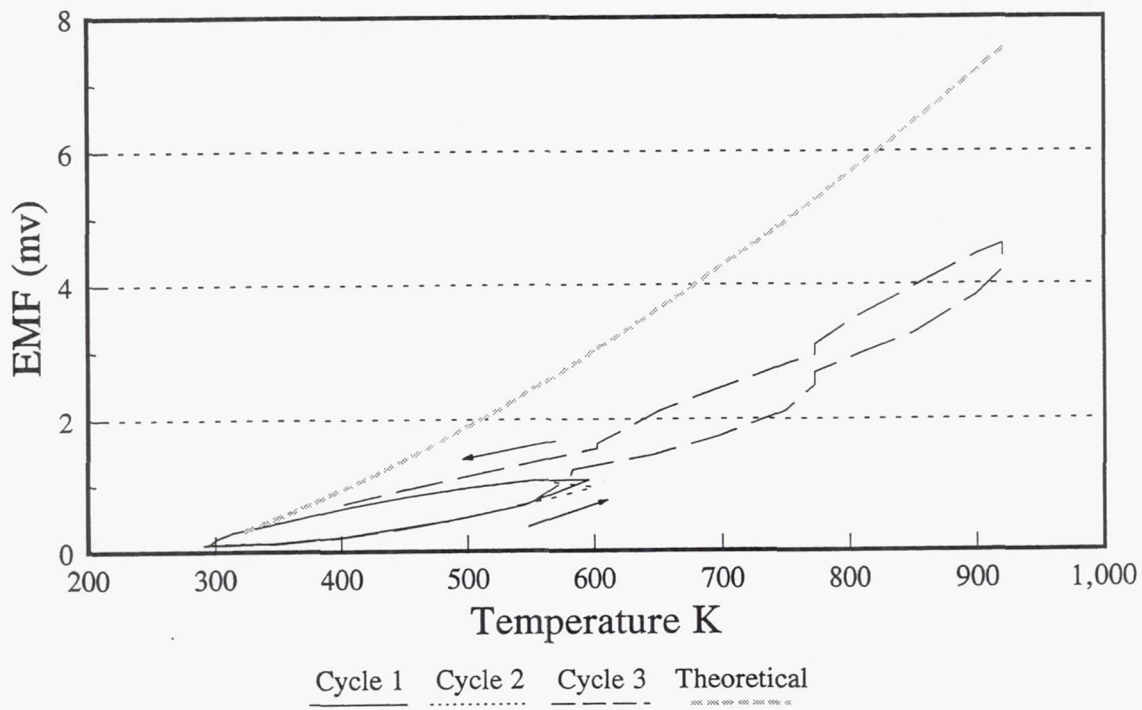


Figure 54 EMF Data for Sensor SCC-S1 with 30-Minute Holds at Each Temperature Level

**Experimental Pt - Rh Wire T.C. vs. Book
Value EMF for Rh vs Pt**

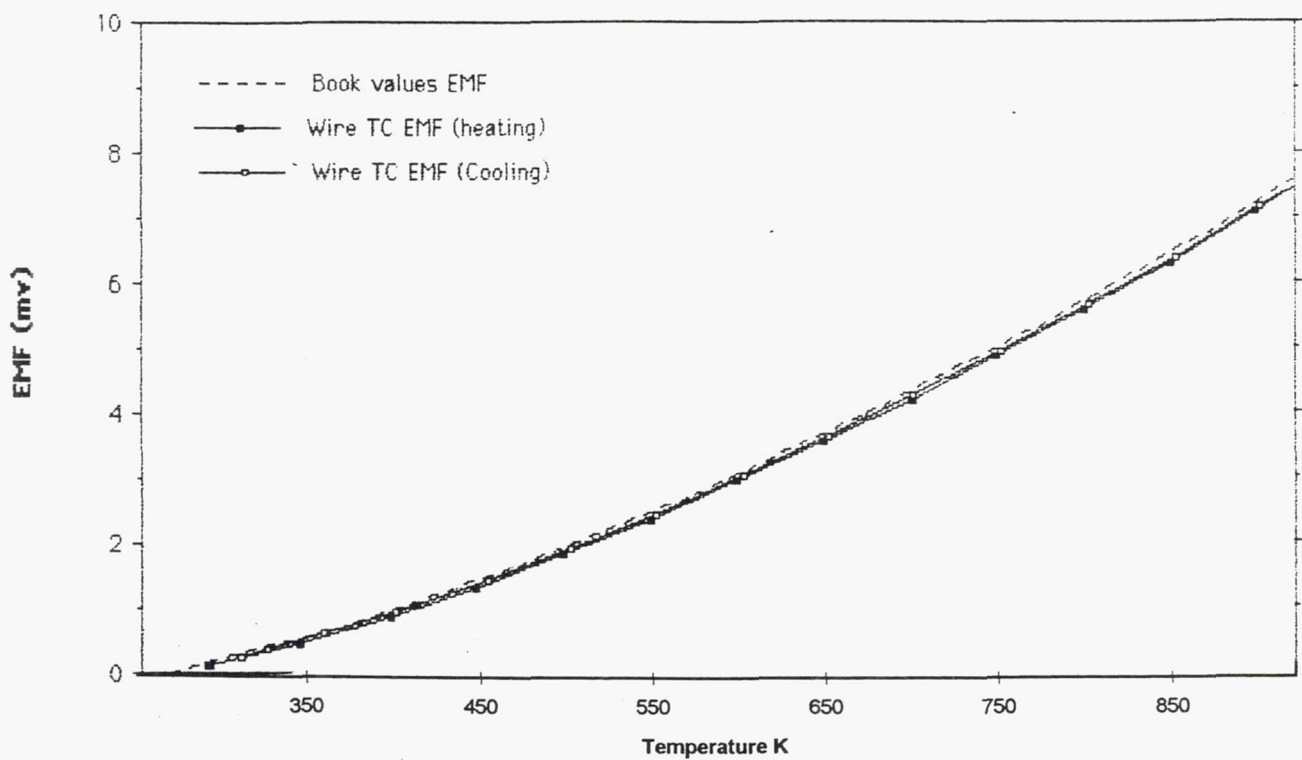


Figure 55 *Experimental Platinum Rhodium Wire Thermocouple Data Versus Book Values*

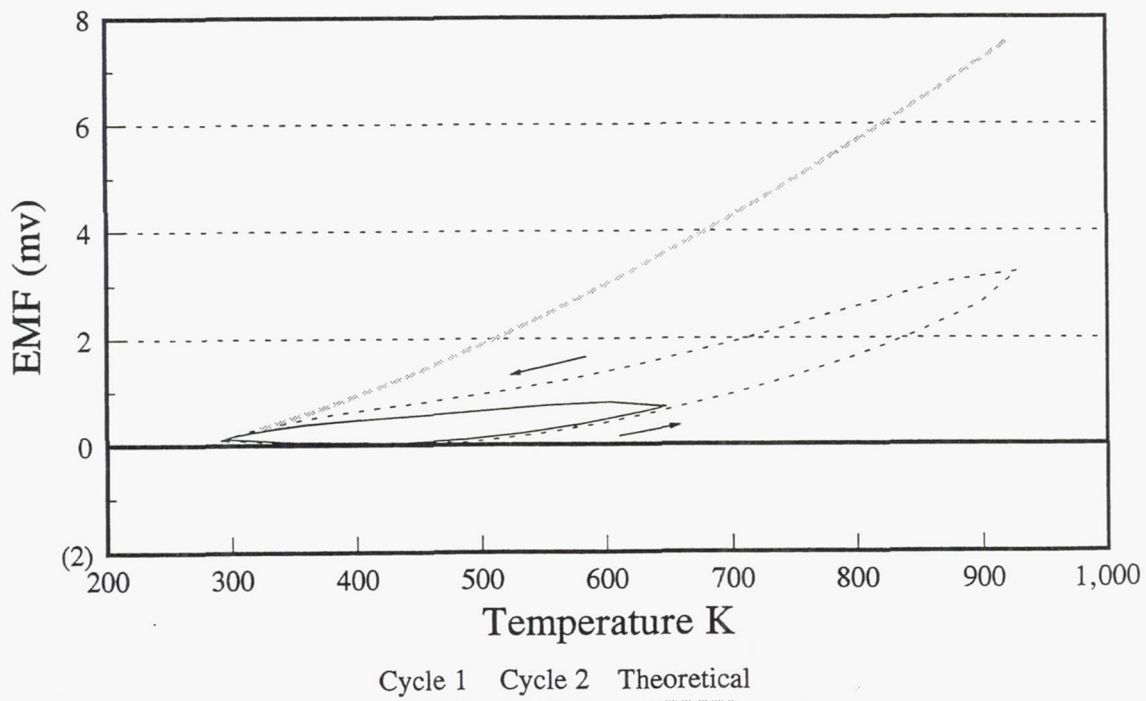


Figure 56 *EMF Data for Sensor SCC-C1*

The first of the Compglas® samples was tested next. Sample SCC-C1 was cycled twice to 644K at 12K/minute. The output was again low and had an open loop structure (Figure 56). Upon inspection, the platinum film had started to wrinkle, but otherwise, the sensor appeared good. The sensor was then cycled to 920K at 16K/minute. The output followed previous cycles, but the sample failed during cool down. The films were continuous but had lifted from the substrate.

The thin-film thermocouple on Sample SCC-C2 spalled prior to test and was used for microprobe work to determine the composition of the deposited films. The results, shown in Figures 57 and 58, indicate that there was no surface contamination on the films, and the films were either platinum or rhodium. The defracting crystal required to see light elements (e.g., oxygen) was not used in making these measurements. The EMF data was only slightly less than "theoretical" and showed some open loop behavior with the data on cooling again higher than that on heating.

The next samples tested were the ion implant and evaporation films applied to silicon nitride. Sample IIE-S1 was cycled twice to 590K at 18K/minute. The output more closely matched the expected values, and the heating and cooling values were very similar. The sample was then cycled twice to 920K at 11K/minute. The output (Figure 59) was again close to the expected values, and the heating and cooling curves were very similar. The sensor appeared good upon visual inspection. The sample was then cycled to 1144K at 15K/minute, and the EMF data continued to look good. Six more cycles to 1144K at a rate of 15K/minute were completed. The data (Figure 60) continued to look good with the exception of some scatter at room temperature. After these cycles, examination of this sensor revealed that the rhodium film was cracked at the edge of the junction area and the whole junction had lifted from the substrate. Figures 61 and 62 show the sample after one cycle to 1144K. Figures 63 through 66 show the appearance of the sample after seven cycles.

Sample IIE-S2 was cycled once to 920K at 3K/minute and once to 1144K at 4K/minute. The output (Figure 67) was close to the expected value and showed small differences between the heating and cooling values. The sample failed on cool-down from the 1144K cycle when the rhodium film delaminated from the substrate. Figures 68 through 71 show the sample as fabricated, and Figures 72 through 75 show the sample after test.

The samples prepared by ion implantation on Compglas® were tested next. Sample IIE-C1 was cycled once to 920K at 3K/minute and twice to 1144K at 29K/minute. The output, shown in Figure 76, was much lower than expected and the cool-down curve did not match the heating curve. Although the sample looked good by visual inspection and the films remained intact, the film resistance had risen to 32.5KΩ and the testing was discontinued. The sample after testing is shown in Figure 77.

Sample IIE-C2 was cycled five times to 1144K at 28K/minute. The data (Figure 78) are lower than expected, and there is a separation of the heating and cooling curves. The film resistance had risen to 15.6KΩ after the fifth cycle, and the testing was terminated. This sensor after test is shown in Figures 79 through 82.

The sputtered sensors were the next thermocouples tested. Two sensors were tested on what had been thought to be silicon nitride. RFS-S1 was cycled twice to 920K at 26K/minute. The output seemed to become insensitive to temperature between 865K and 920K. The samples looked good and cycling started to 1144K at 26K/minute. The sample was cycled seven times to 1144K. The output (Figure 83) tended to decrease at temperatures over 920K. The output had a peak of approximately 5mv at 865K and then decreased at higher temperatures. During one cycle, the EMF went negative. Although the sample looked good visually, the strange behavior made this sensor unusable as a temperature sensor and testing was stopped. The sensor is shown in Figures 84 through 86.

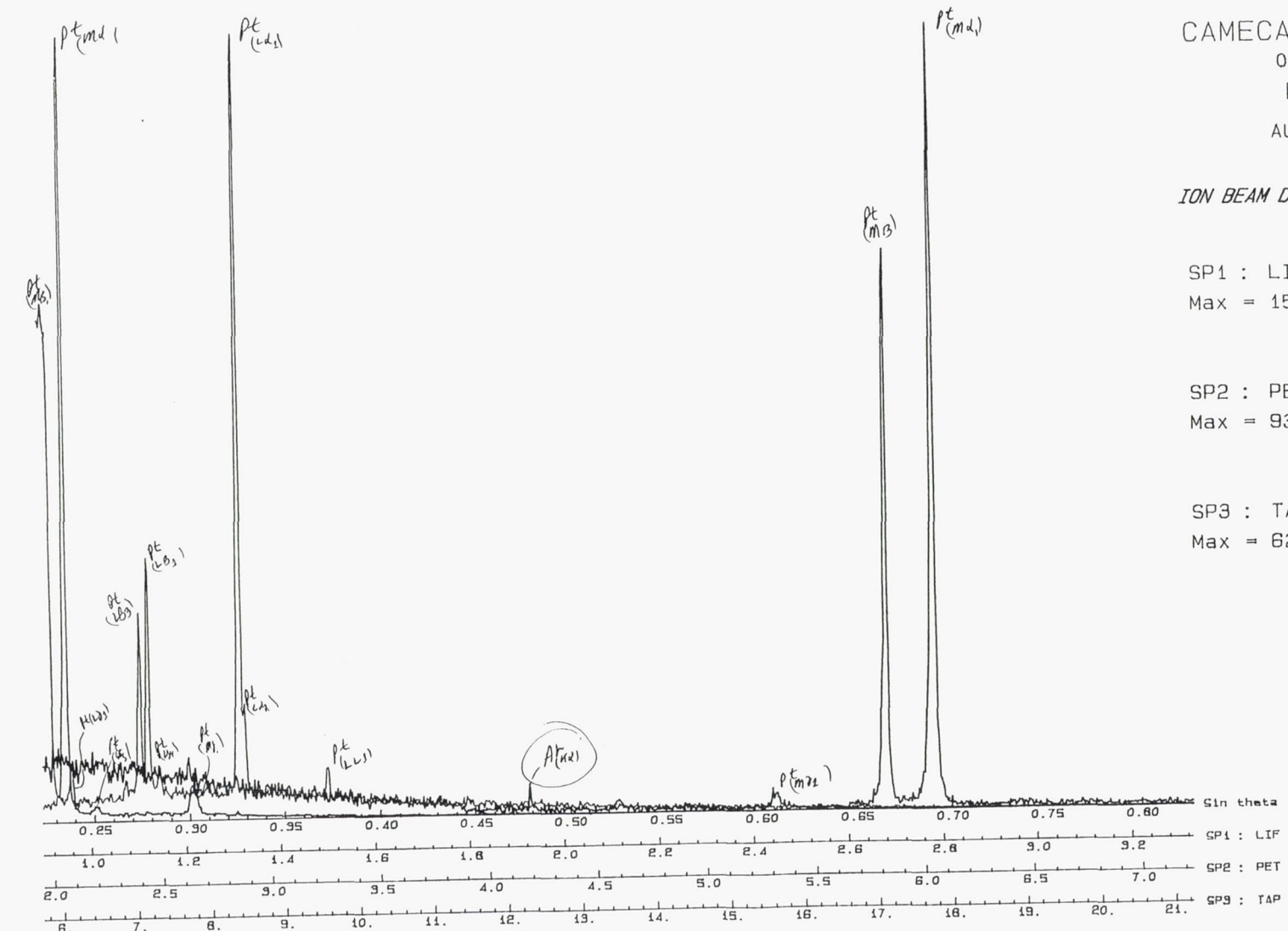


Figure 57 Cameca - Microbeam Spectrum of Platinum Leg on Sensor SCC-C2

Rh (ℓ_{21})

CAMECA-MICROBEAM

08-JUN-90

FULWDS

LINEAR SCALE

ION BEAM DEP. RH ON Si3N4

SP1 : LIF
Counts per Cm = 20

SP2 : PET
Counts per Cm = 76

SP3 : TAP
Counts per Cm = 20

49

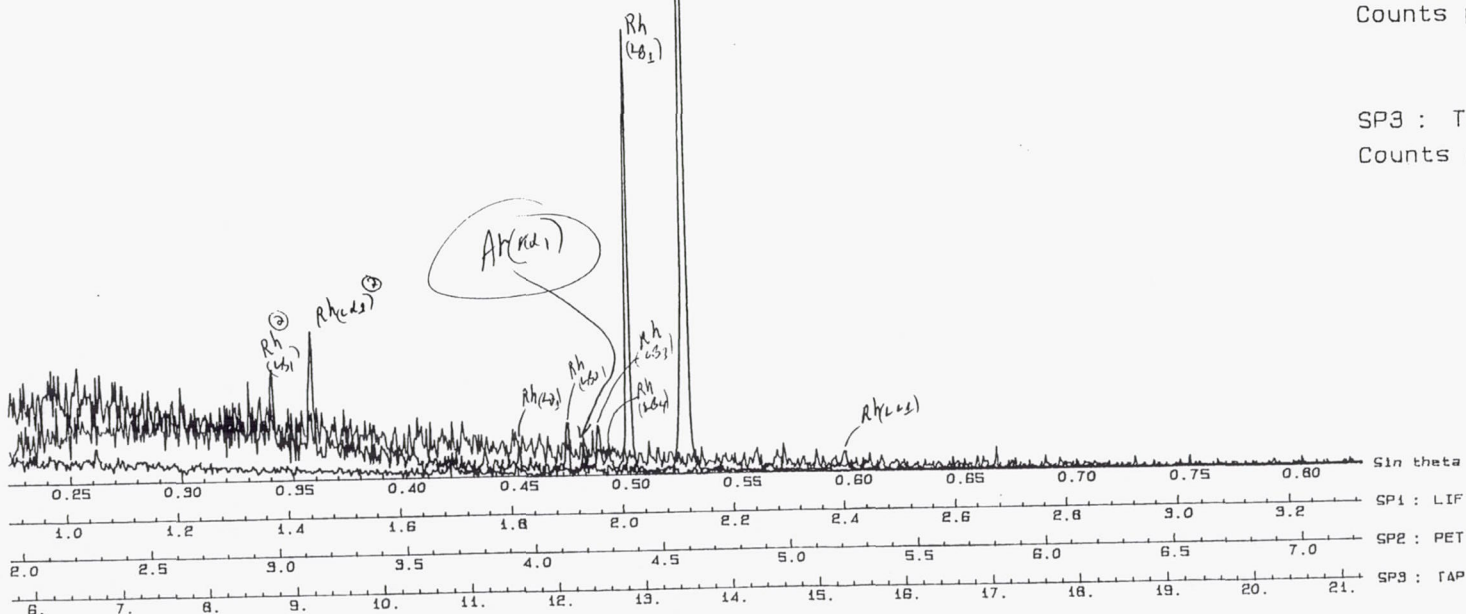


Figure 58 Cameca - Microbeam Spectrum of Rhodium Leg on Sensor SCC-C2

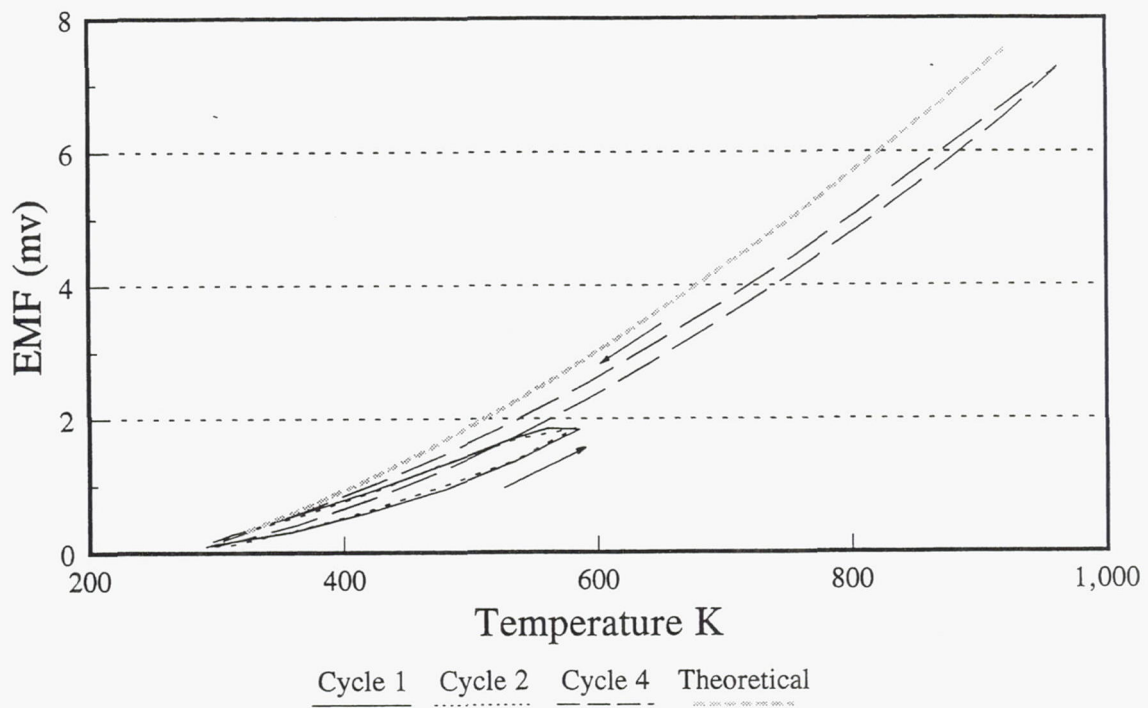


Figure 59 EMF Data on Sensor IIE-S1 – First Four Cycles

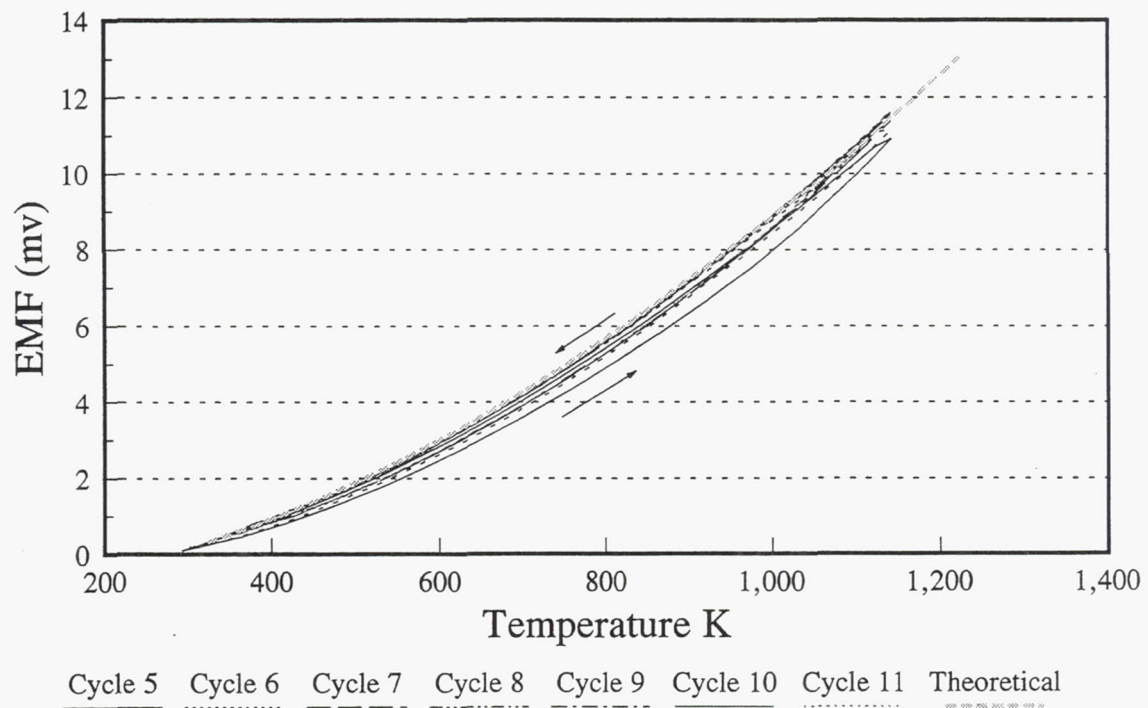
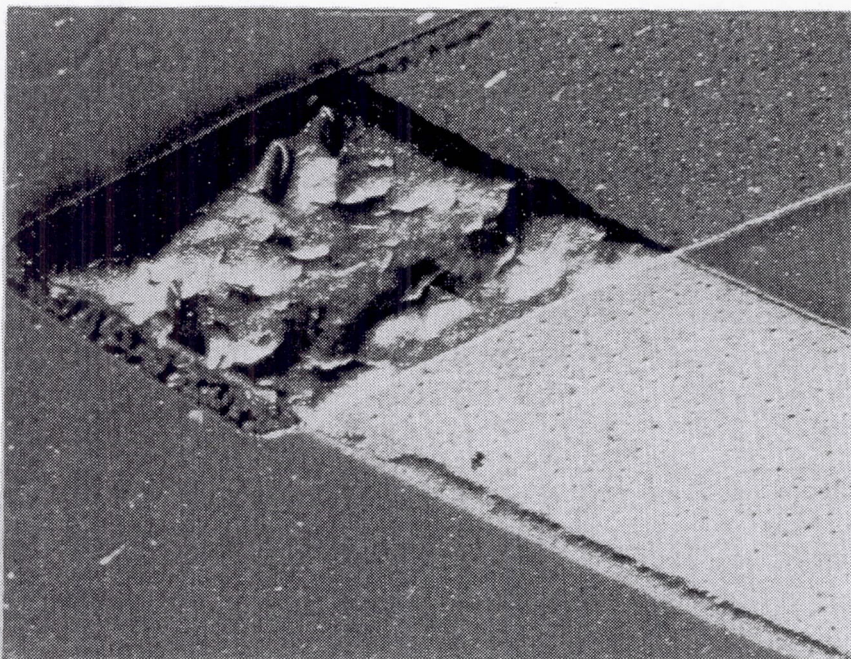
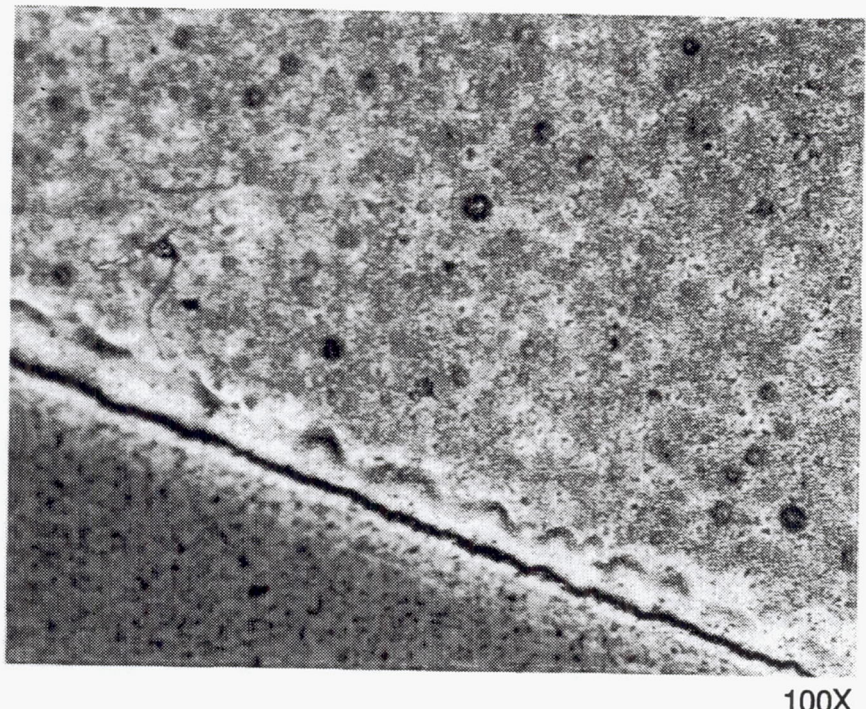


Figure 60 EMF Data on Sensor IIE-S1 – Last Seven Cycles

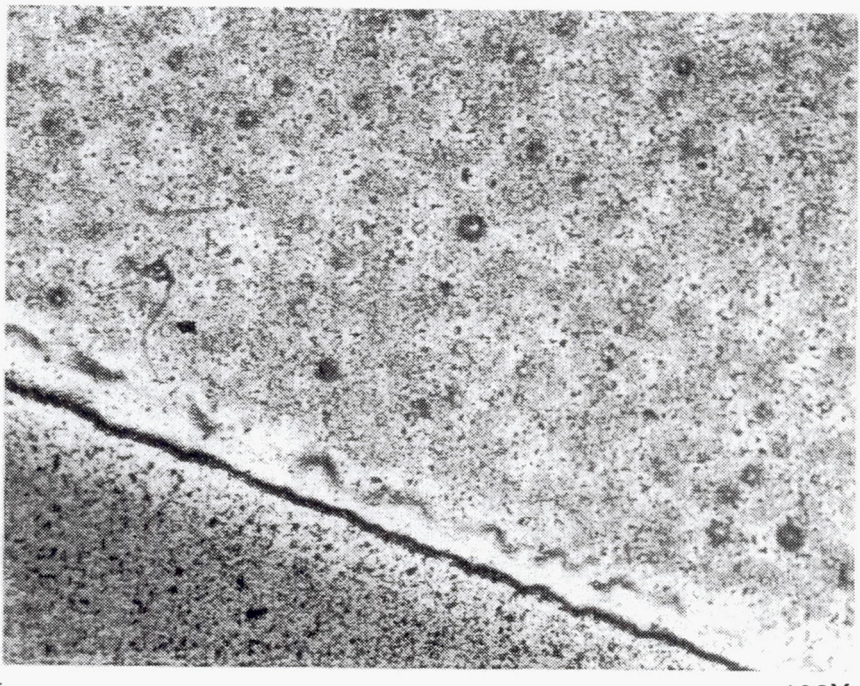


25X

Figure 61 *Photograph of Junction Area of Sensor IIE-S1 After One Cycle to 1144K*

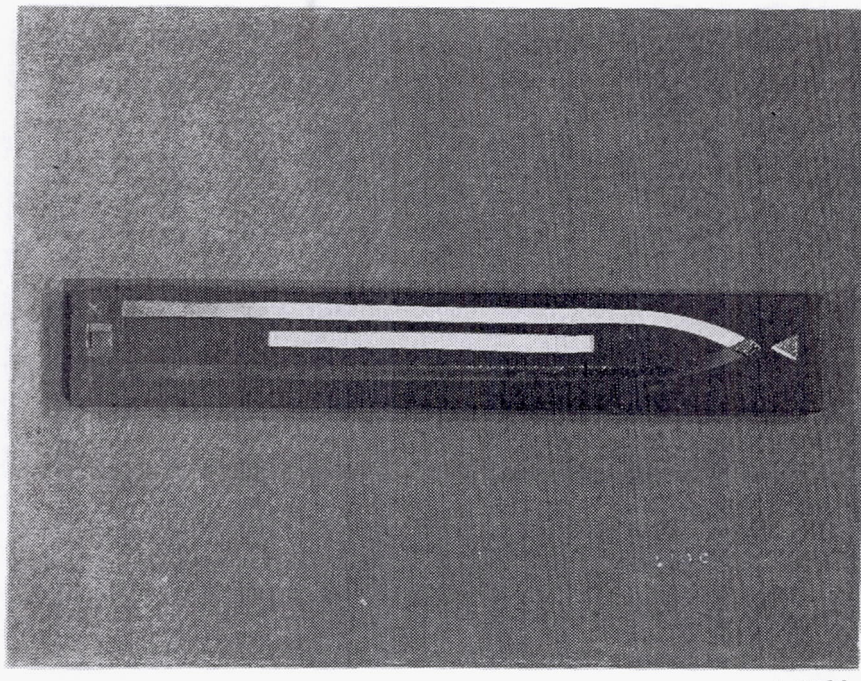


100X



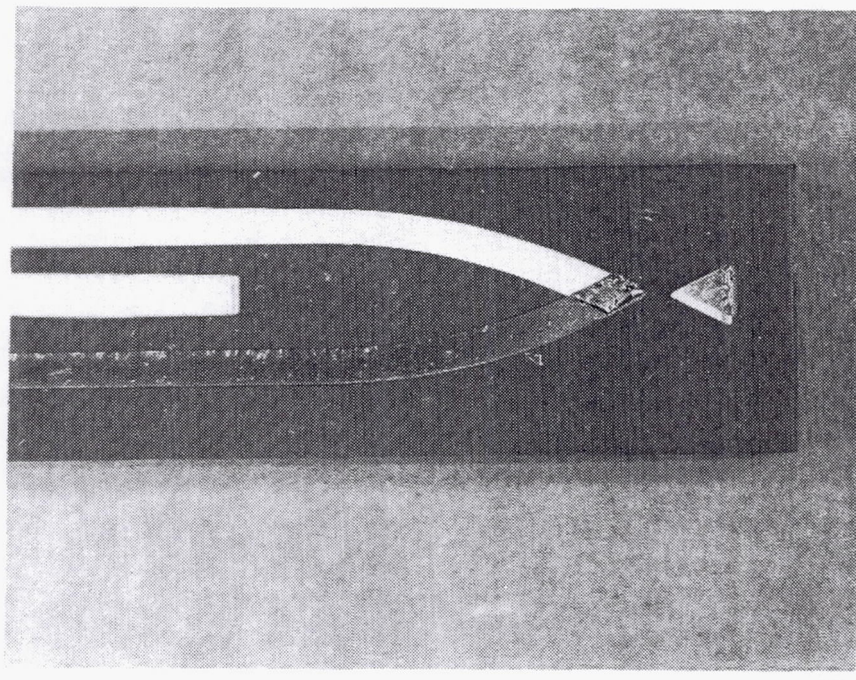
100X

Figure 62 *Photograph of Platinum Leg of Sensor IIE-S1 After One Cycle to 1144K Showing the Platinum Bubbled at the Edge*



1.25X

Figure 63 *Photograph of Entire Sample of Sensor IIE-S1 After Seven Cycles to 1144K*



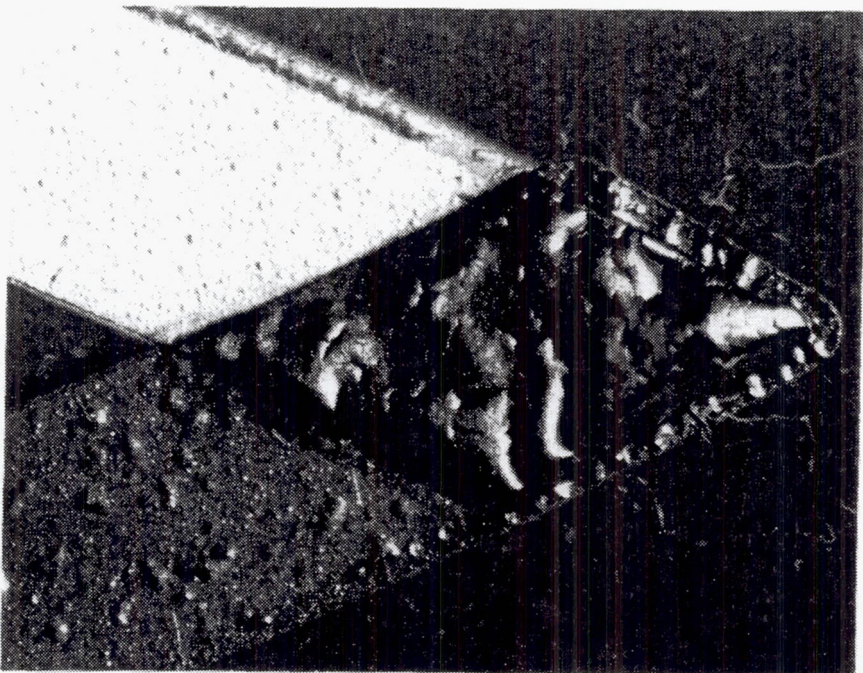
5X

Figure 64 *Photograph of Sensor IIE-S1 After Seven Cycles to 1144K*



25X

Figure 65 *Photograph of Rhodium Leg of Sensor IIE-S1 After Seven Cycles to 1144K*



25X

Figure 66 *Photograph of Junction Area of Sensor IIE-S1 After Seven Cycles to 1144K*

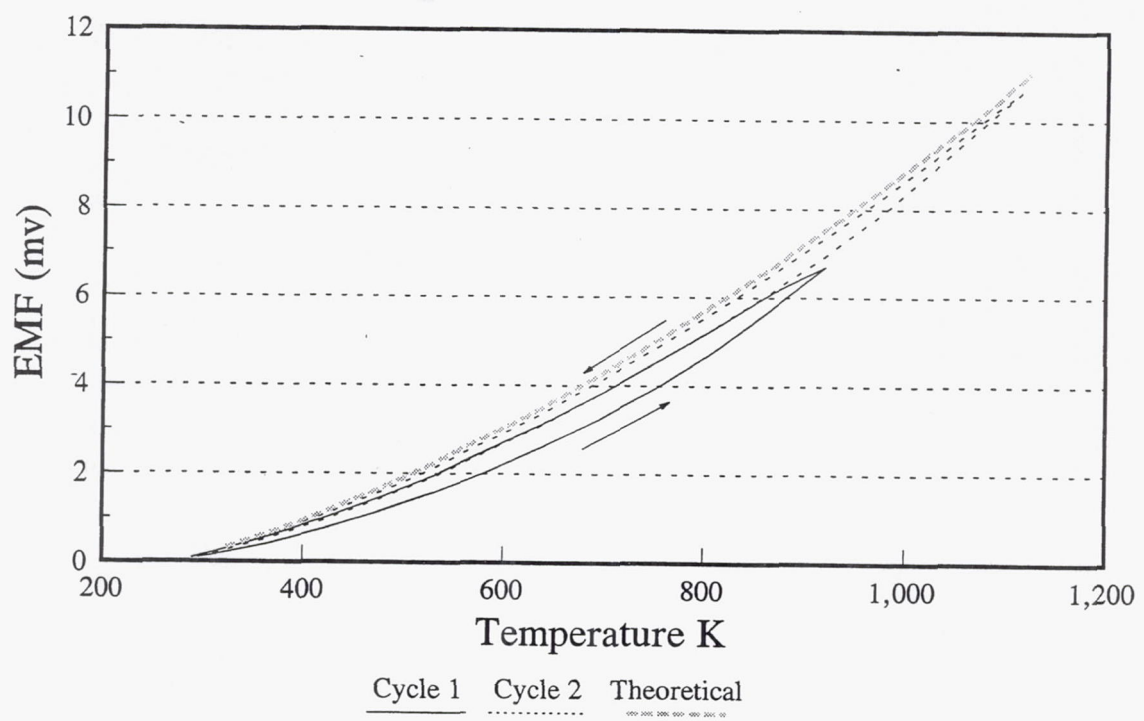


Figure 67 *EMF Data of Sensor IIE-S2*

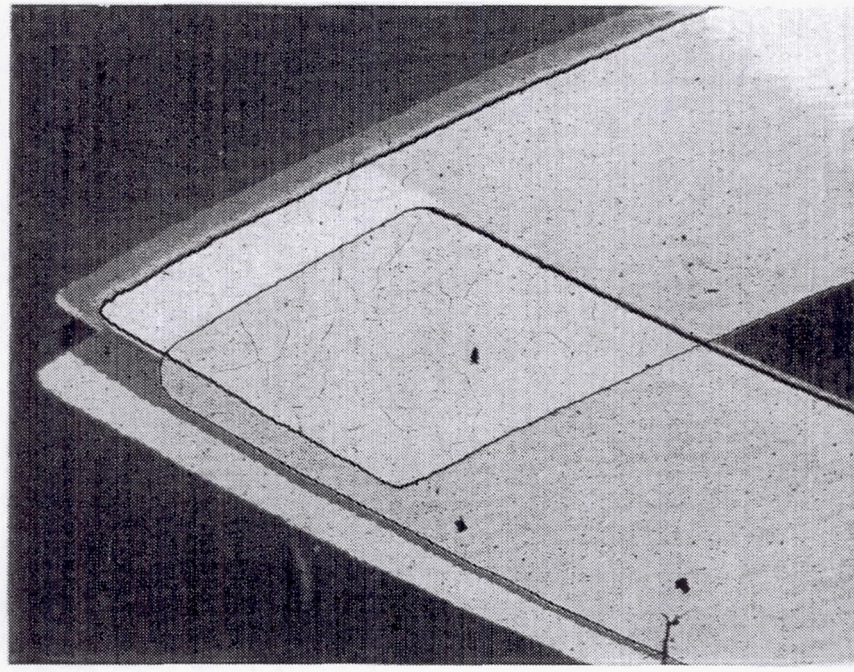
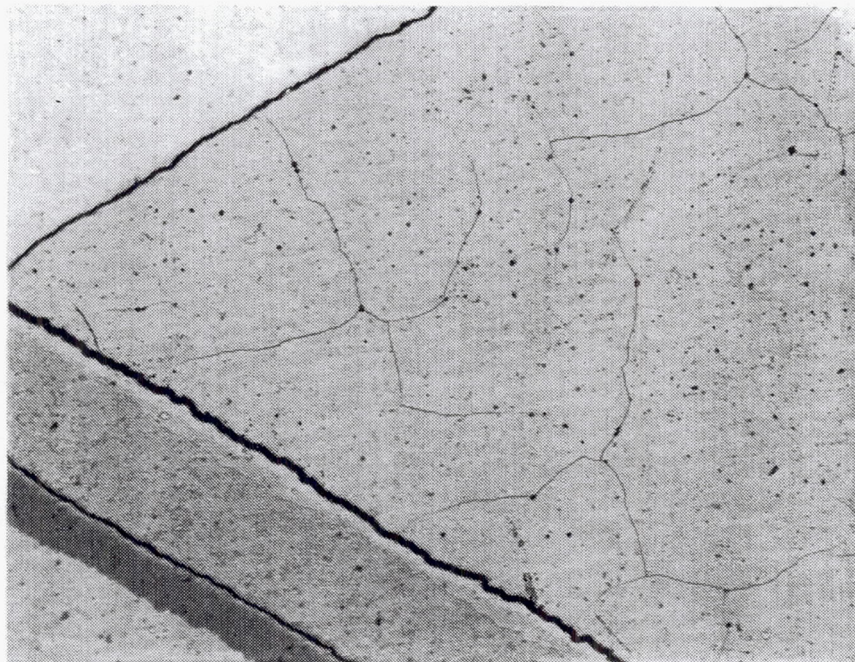
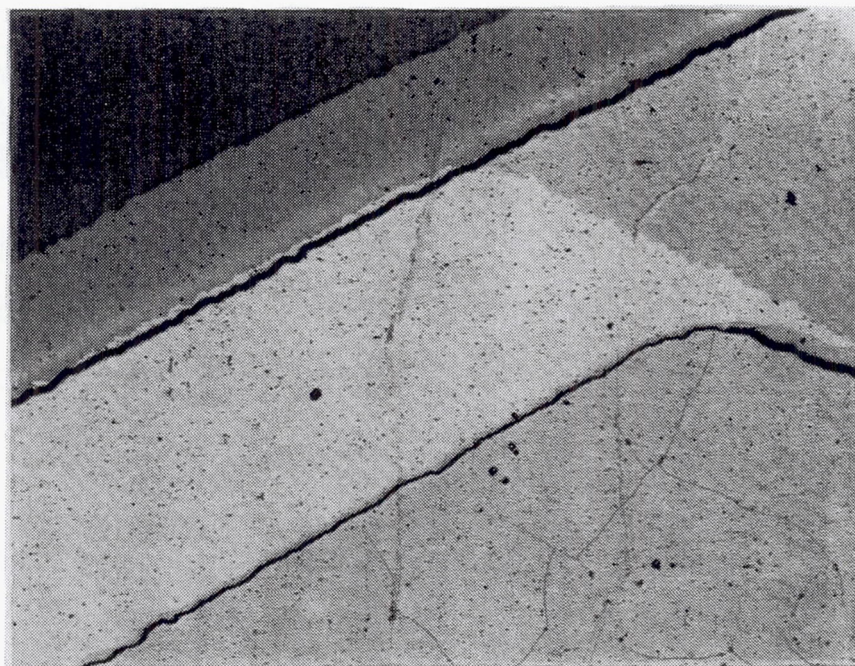


Figure 68 *Photograph of Junction Area of Sensor IIE-S2 As Fabricated*



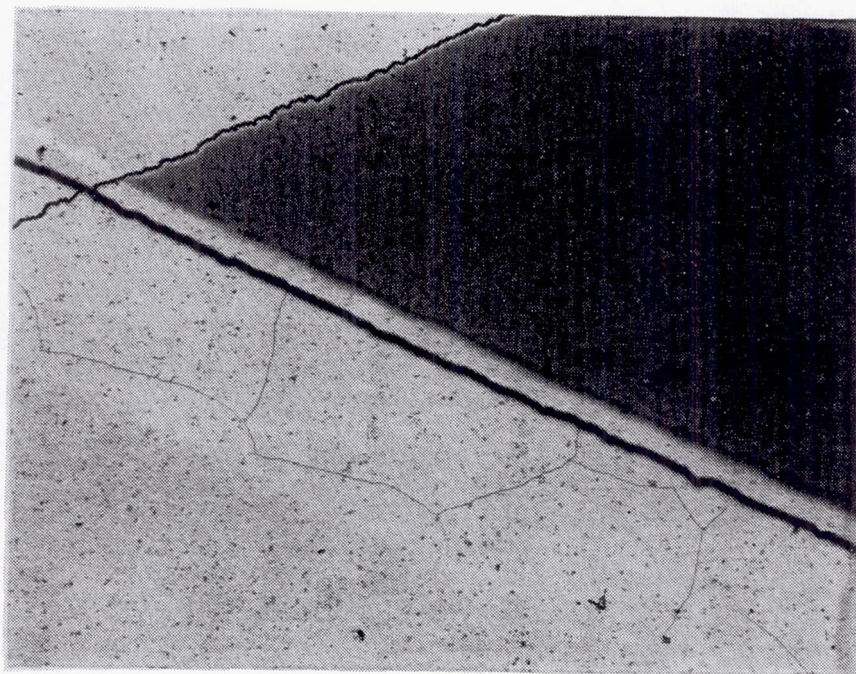
100X

Figure 69 Photograph of Sensor IIE-S2 As Fabricated Showing Cracks in the Overlap Area



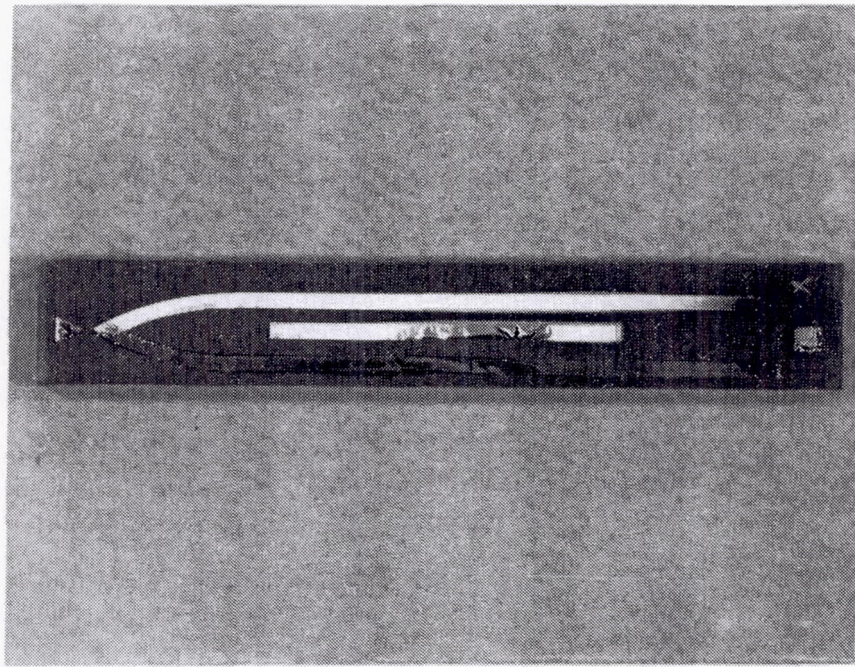
100X

Figure 70 Photograph of Platinum Leg of Sensor IIE-S2 As Fabricated



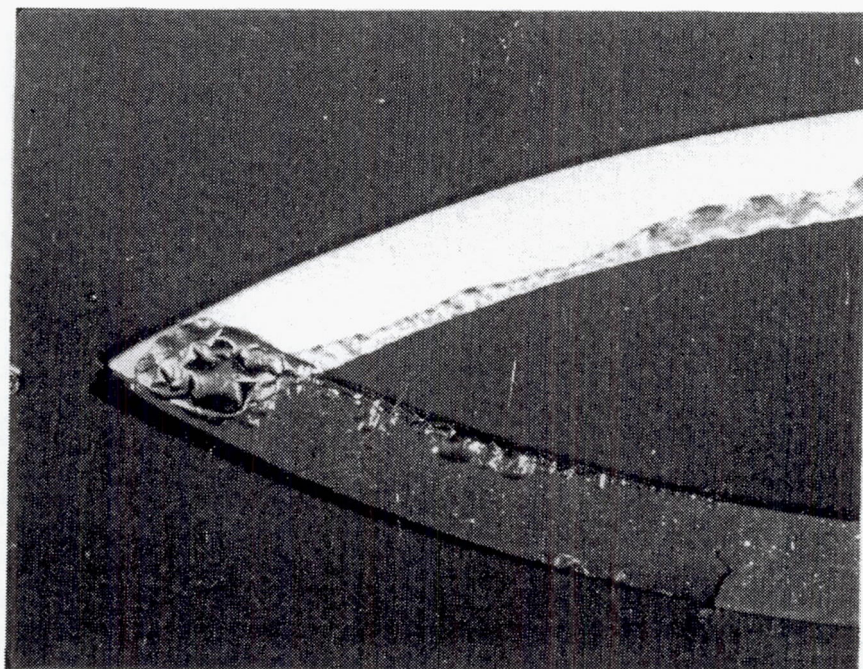
100X

Figure 71 *Photograph of Rhodium Leg of Sensor IIE-S2 As Fabricated*



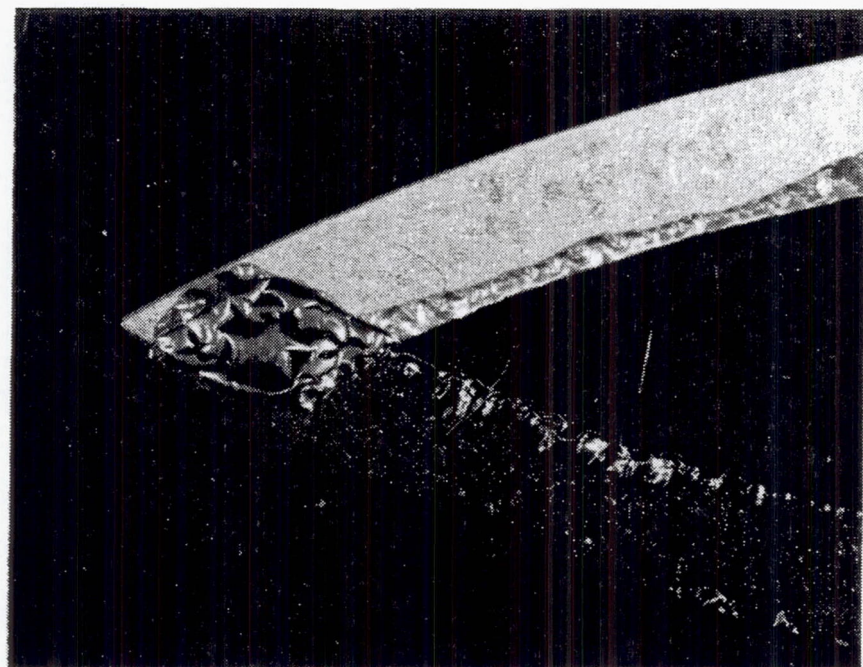
1.25X

Figure 72 *Photograph of Entire Sample of Sensor IIE-S2 After One Cycle to 1144K*



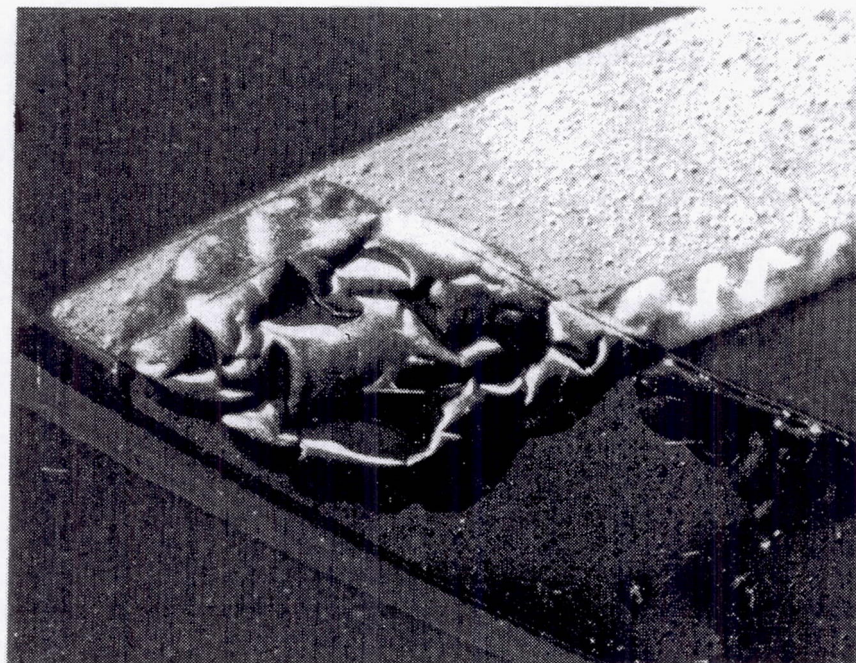
10X

Figure 73 *Photograph of Sensor IIE-S2 After One Cycle to 1144K*



10X

Figure 74 *Photograph of Junction Area of Sensor IIE-S2 After One Cycle to 1144K*



25X

Figure 75 *Photograph of Junction Area of Sensor IIE-S2 After One Cycle to 1144K*

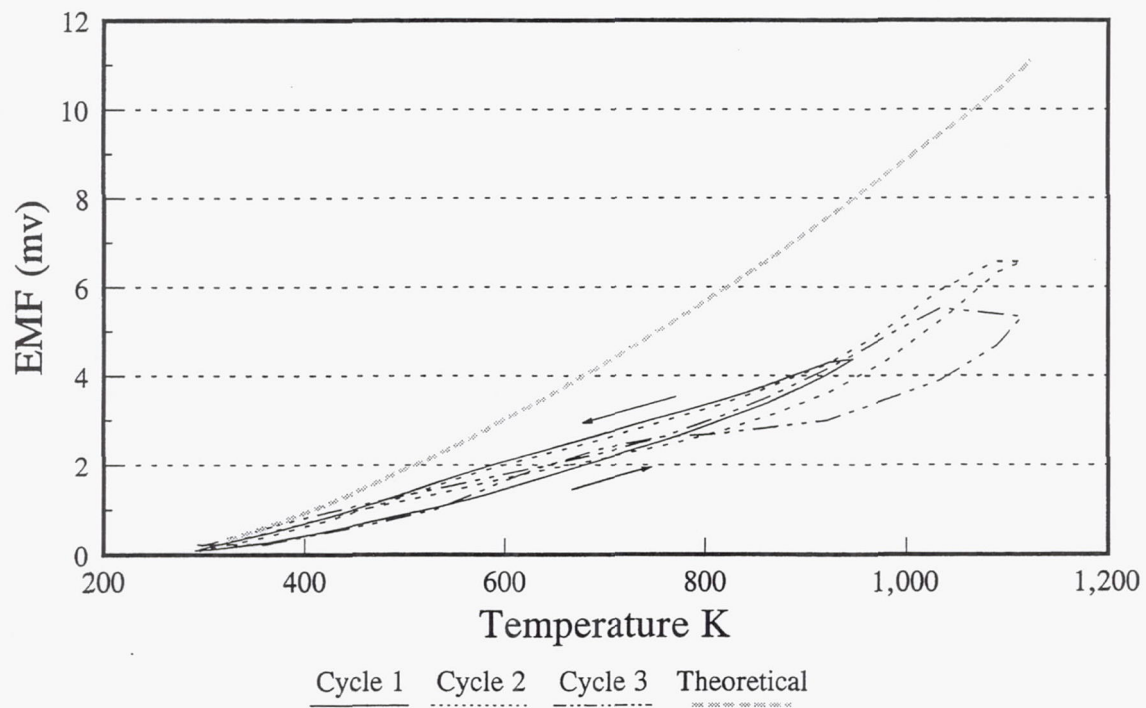


Figure 76 *EMF Data for Sensor IIE-C1*



25X

Figure 77 *Photograph of Junction Area of Sensor IIE-C1 After One Cycle to 1144K*

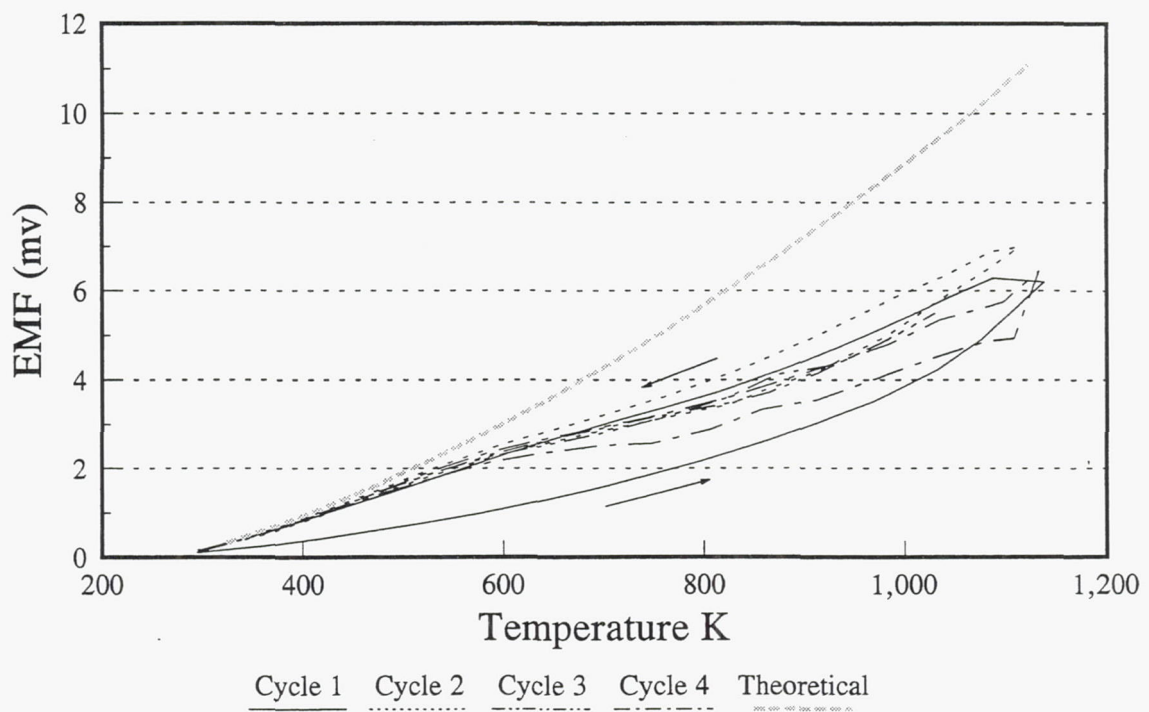
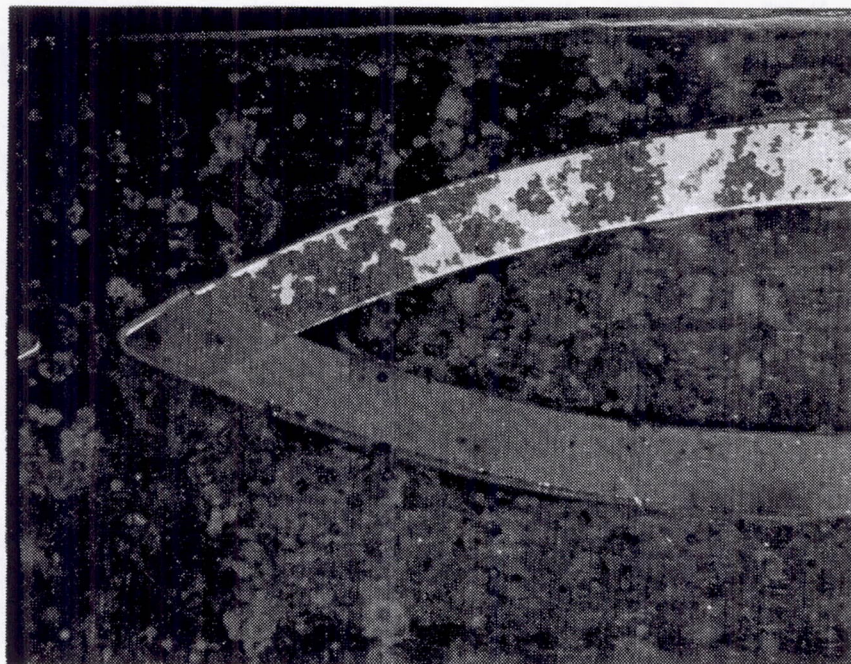


Figure 78 *EMF Data for Sensor IIE-C2*



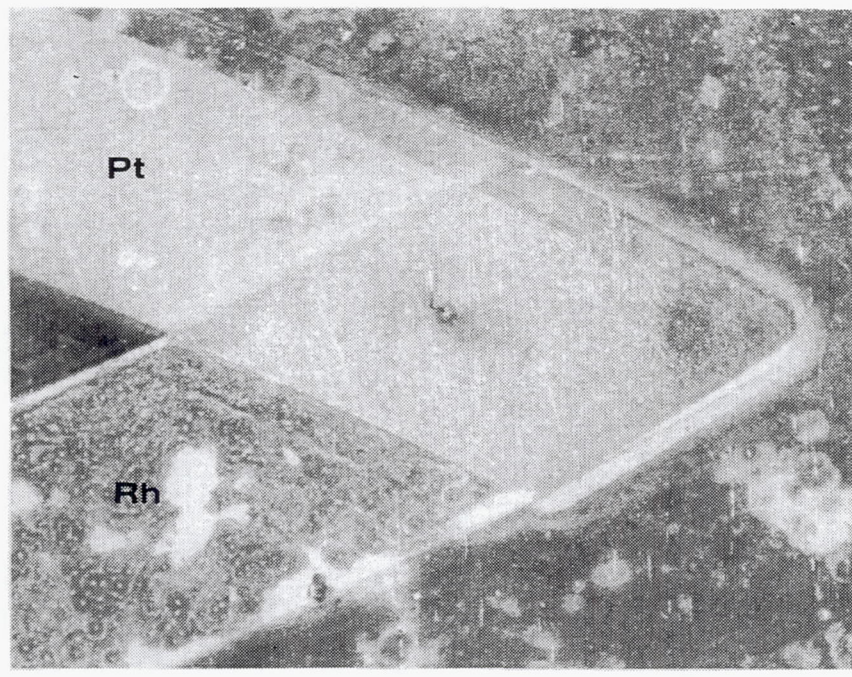
10X

Figure 79 *Photograph of Sensor IIE-C2 After Four Cycles to 1144K*



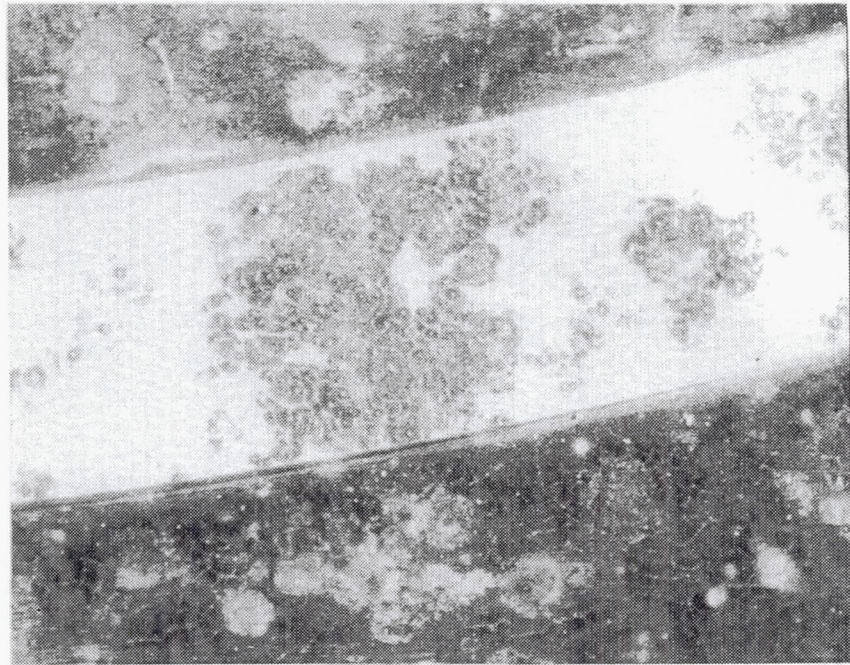
25X

Figure 80 *Photograph of Junction Area of Sensor IIE-C2 After Four Cycles to 1144K*



25X

Figure 81 Photograph of Junction Area of Sensor IIE-C2 After Four Cycles to 1144K



25X

Figure 82 Photograph of Platinum Leg of Sensor IIE-C2 After Four Cycles to 1144K

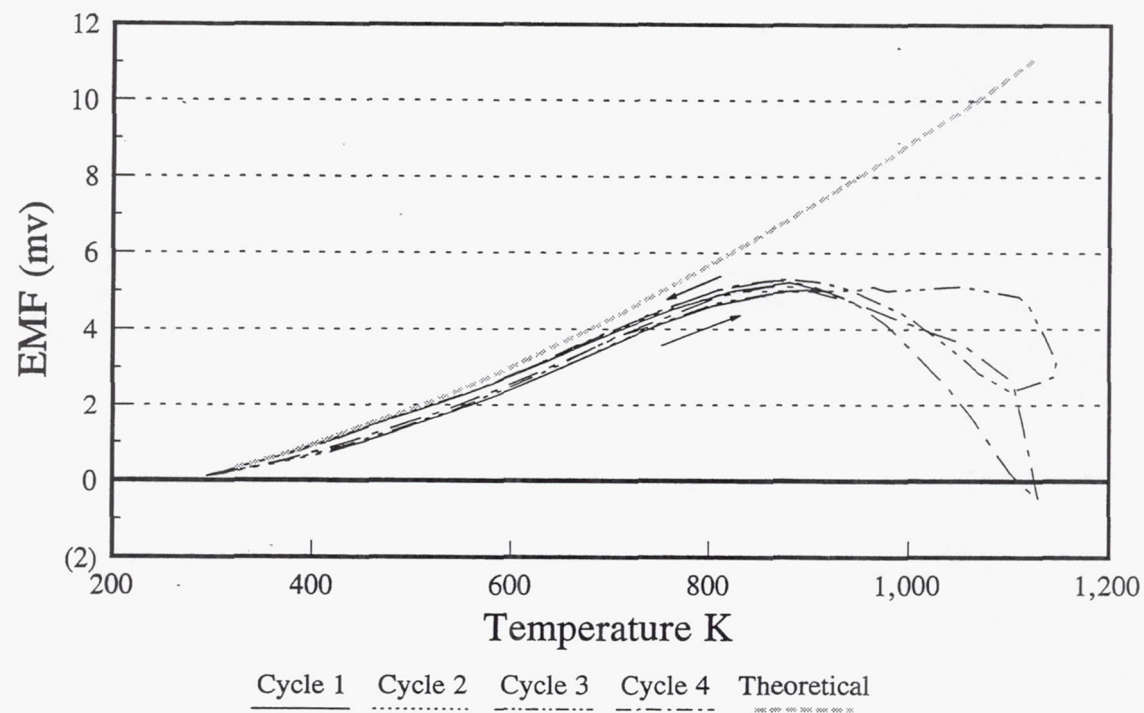


Figure 83 EMF Data for Sensor RFS-S1

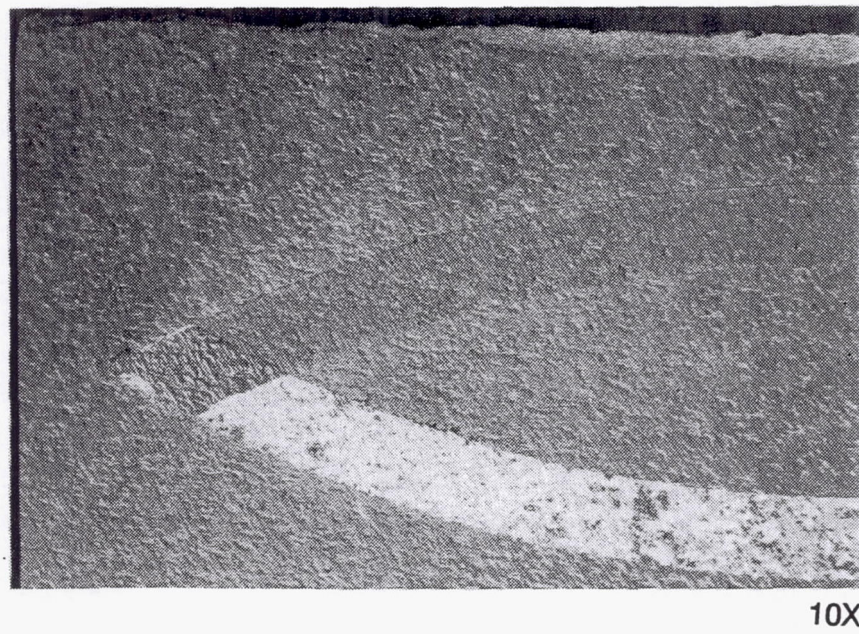
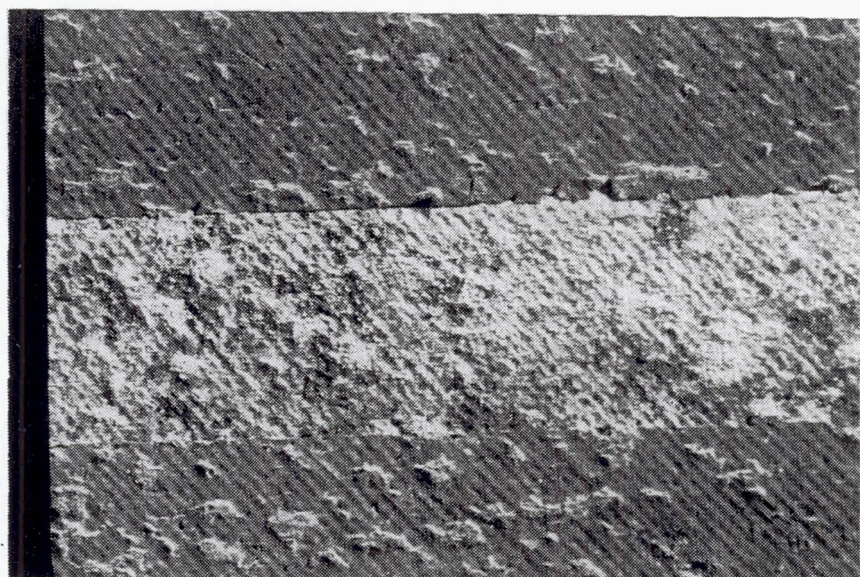


Figure 84 Photograph of Sensor RFS-S1 After Two Cycles to 1144K



25X

Figure 85 *Photograph of Junction Area of Sensor RFS-S1 After Two Cycles to 1144K*



25X

Figure 86 *Photograph of Platinum Leg of Sensor RFS-S1 After Two Cycles to 1144K*

Sample RFS-S2 was cycled once to 1144K at 24K/minute. The output, shown in Figure 87, became erratic above 920K and had a higher output than theoretical. This sample failed during the cool-down portion of the cycle. The rhodium leg was found to be cracked and open. This sample, as fabricated, is shown in Figures 88 and 89. The post-test appearance of the sample is shown in Figures 90 through 92.

The erratic results above 920K and the appearance of these sensors led to questioning the substrate material. The substrate did not look like the silicon nitride that was provided to be sputtered. Surface preparation can change visual appearance, but these samples appeared similar to the silicon carbide. Chemical analysis by X-ray diffraction showed that the substrate was indeed silicon carbide. Silicon carbide is electrically conductive at high temperatures which is one cause of the behavior exhibited by these sensors since there was no electrical insulation applied under the thermocouple films.

The last sample tested was a layered ion implant/evaporation sensor on silicon nitride with a silicon nitride overcoat, sample IIE-S3. The sample was cycled twice to 920K at 17K/minute. The output (Figure 93) was very erratic at temperatures below 500K and very high at 920K. Visually, the sensor looked good after these cycles. The sensor was cycled twice to 1144K at 2.8K/minute. The output repeated the previous cycles, and again was very high at the high temperatures. The film resistance had risen to over $20M\Omega$ and the testing was terminated. The Pt and Rh films deposited on this sample were very thin, totaling $0.16\mu m$ and $0.14\mu m$ for Pt and Rh, respectively. The conductive cross section was further reduced by driving the evaporated material into the substrate. The films were kept thin to prevent cracking.

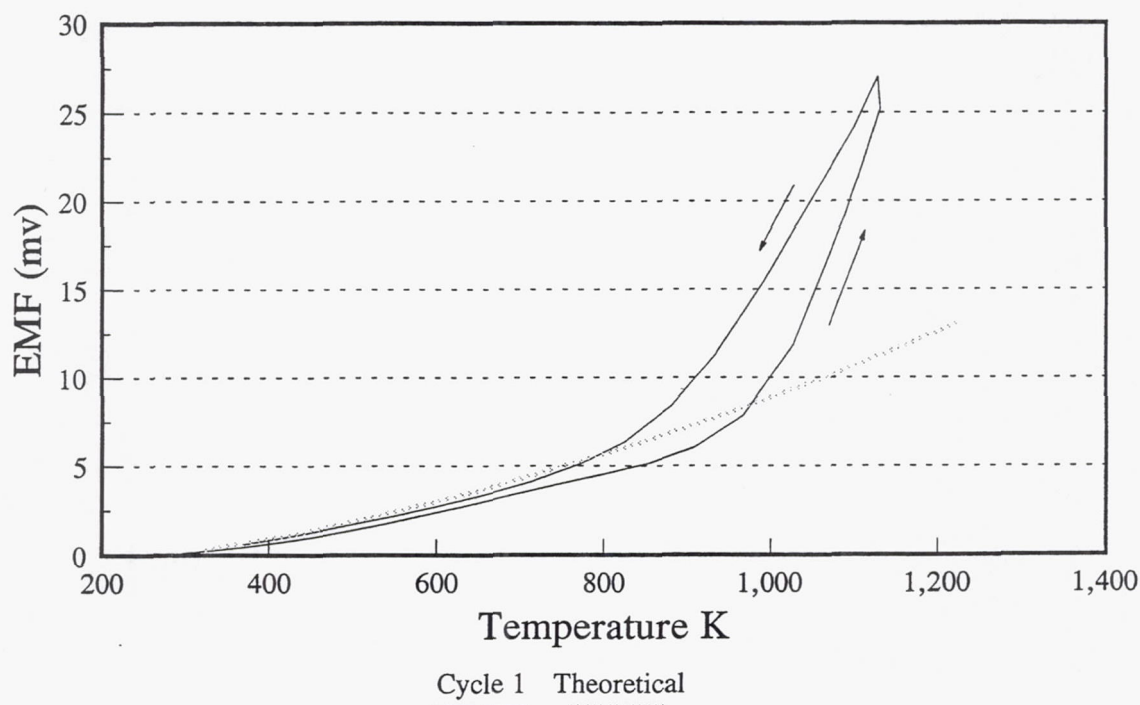


Figure 87 EMF Data for Sensor RFS-S2

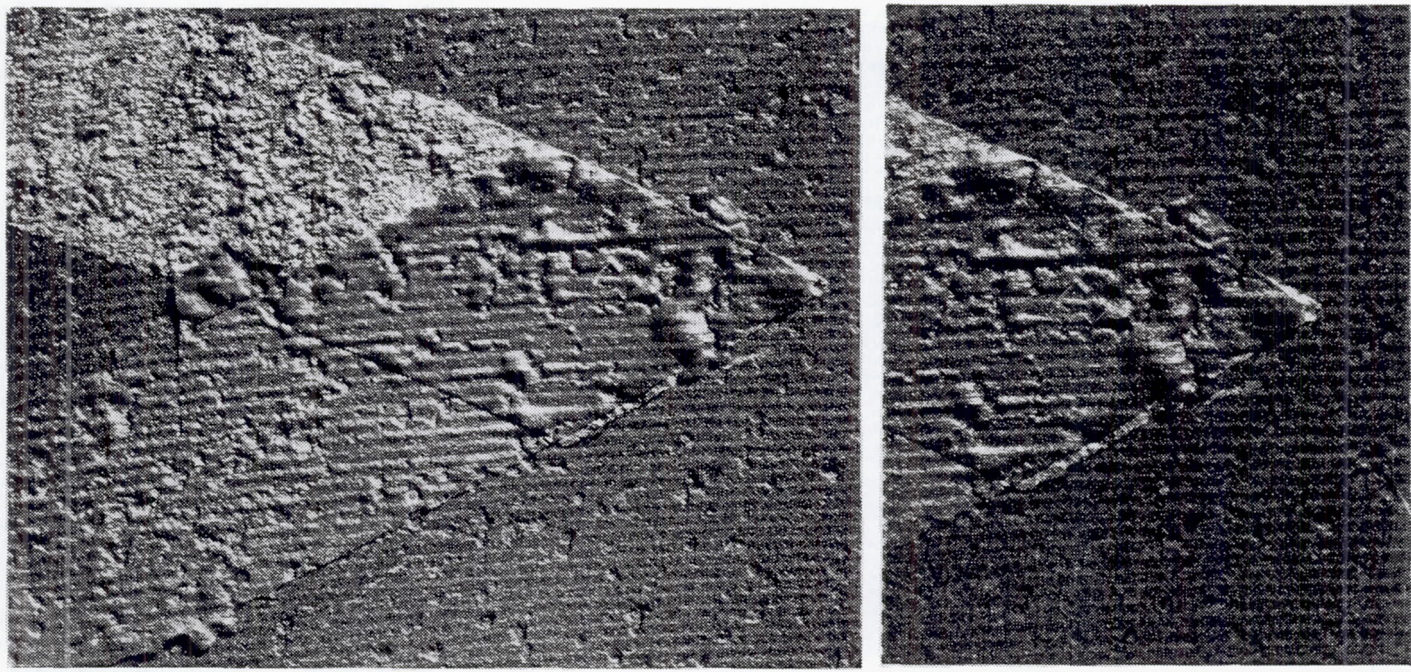


Figure 88 *Photograph of Junction Area of Sensor RFS-S2 As Fabricated*

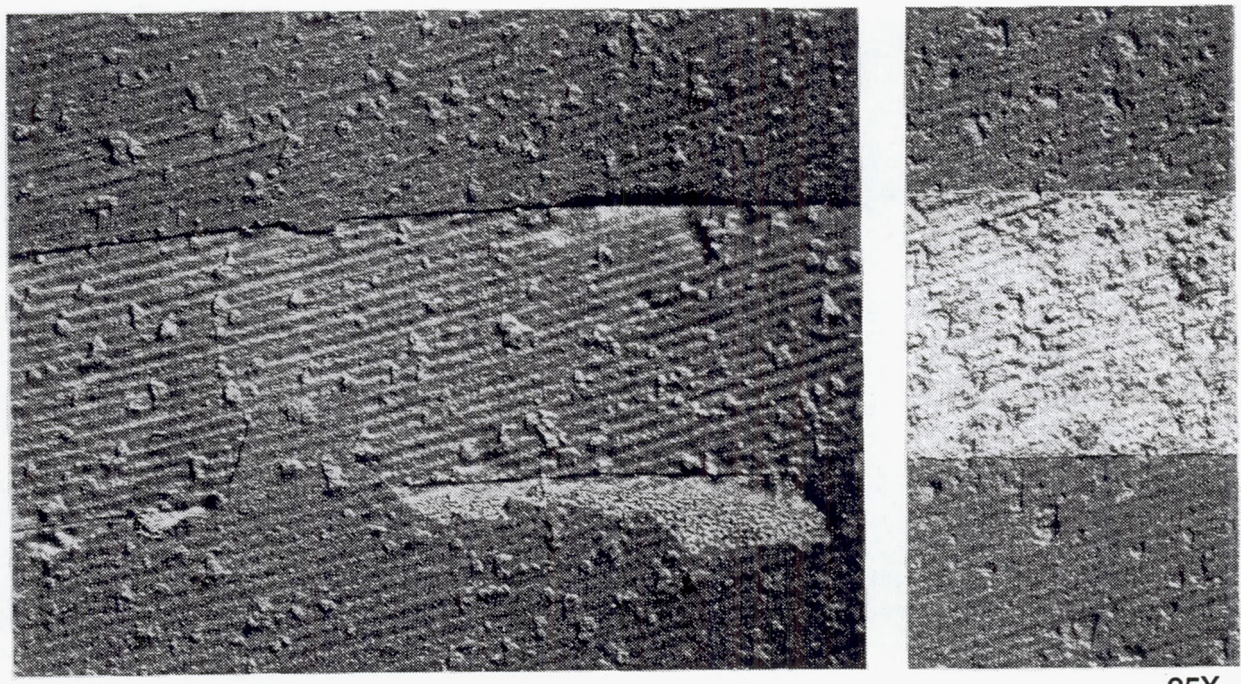
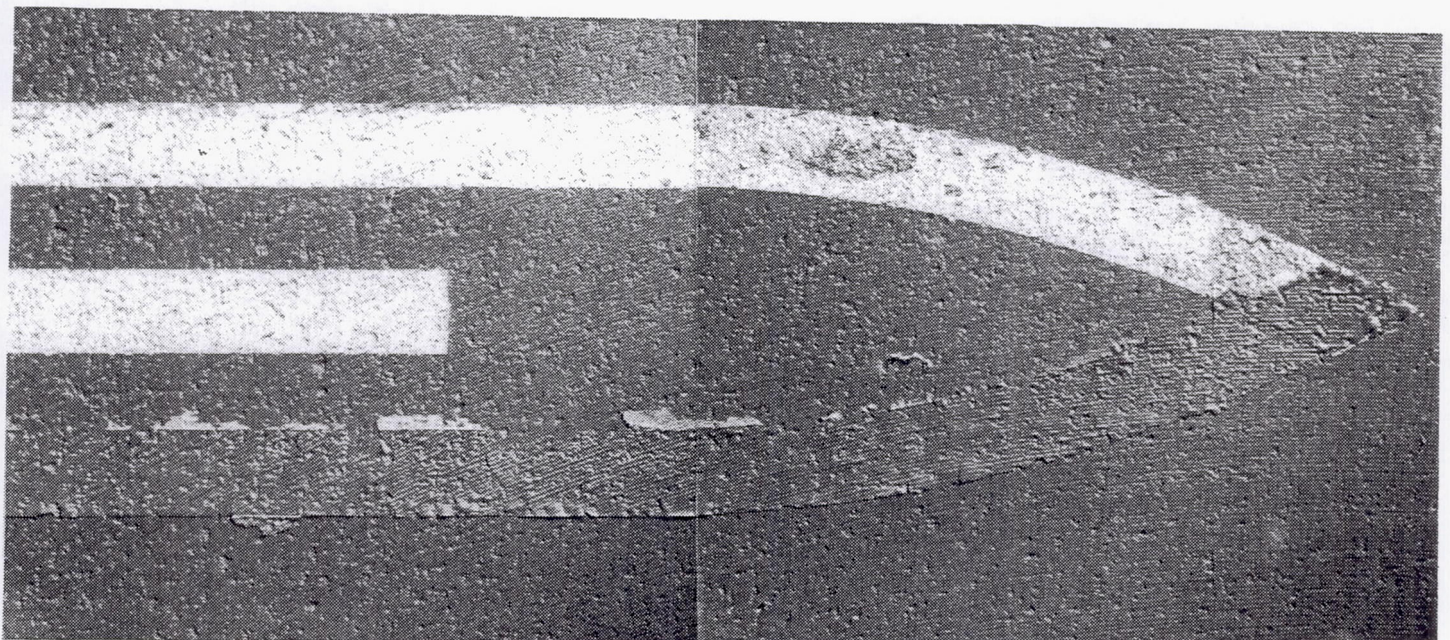


Figure 89 *Photograph of Rhodium Leg of Sensor RFS-S2 As Fabricated*



10X

Figure 90 *Photograph of Sensor RFS-S2 After One Cycle to 1144K*



25X

Figure 91 *Photograph of Junction Area of Sensor RFS-S2 After One Cycle to 1144K*



Figure 92 *Photograph of Rhodium Leg of Sensor RFS-S2 After One Cycle to 1144K*

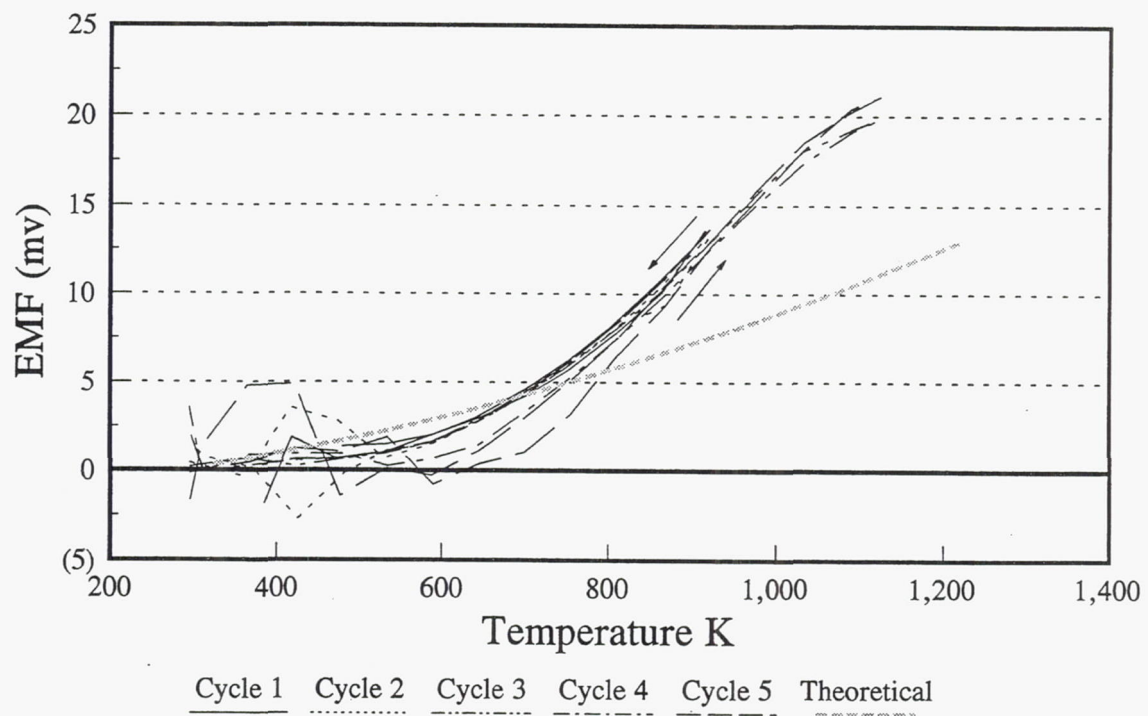


Figure 93 *EMF Data for Sensor IIE-S3*

4.4 Results

In this program, thin films were applied by three different methods as a form of screening tests of the techniques. Adherence was a major problem encountered with all three techniques, and was the dominant mode of failure. The test results are summarized in Table 3. The output of the thin-film thermocouples was generally much lower than the expected theoretical values. The reasons for this are unclear. To investigate this problem, a review was performed on the test data where the temperature of the clamp adjacent to the thin film-wire junctions was recorded. The data, shown in Figures 94 and 95, are not conclusive but do tend to indicate a stronger correlation between temperature calculated from sensor output and clamp temperature than between temperature calculated from sensor output and junction temperature as measured by the wire thermocouple. Another anomaly with the data was the difference between the heating and cool-down outputs. This also is unexplained, as the 30-minute holds at temperature reduced the size of the loops, but did not eliminate them. During these temperature holds, the clamp temperatures would also be expected to drift up or down, but at a much slower rate than the sample. This could be interpreted as showing that the clamp temperature had a strong influence on the output. Although the samples were not durable enough to conduct thermal soak tests, we did encounter several instances where the film resistance increased very rapidly. There could be several reasons for the increase; however, it is felt that the dominant cause would be oxidation of the rhodium film. The overcoating of the last sample we ran with silicon nitride was done both to improve adherence and to reduce oxidation effects. The sample resistance still increased rapidly. The EMF data generated for these sensors are presented in tabular form in Appendix A.

4.5 Conclusions

All three deposition methods have shown the ability to put films onto ceramic substrates. EMF stability and electrical insulation have been identified as potential problems on some substrates. More work is needed to address these problems as well as the problems of electrode adhesion.

4.6 Recommendations

A statistically designed experimental approach is recommended to identify the most significant variables in applying thin films to ceramic substrates. This might include, but not be limited to, addressing the role of stress and ways of minimizing stress while applying films, the role of an interface layer to improve adhesion and reduce thermal coefficient of expansion mismatch, the advantages of overcoating materials to prevent oxidation, the quality of the materials being applied, and the importance of various parameters in the application processes themselves.

Table 3 Thin-Film Sensors Test Result Summary

<u>Sample</u>	<u>Substrate</u>	<u>No. of Cycles</u>	<u>Temperature at Failure</u>	<u>Application Technique</u>	<u>Failure Mode</u>	<u>Comments</u>
SCC-S1	Silicon nitride	3	350–400K	IBED No Cr	Delamination	Junction spalled
SCC-S2	Silicon nitride	–	–	IBED	Delamination	Failed before testing; Pt spalled half its length
SCC-S3	Silicon nitride	1	348K	IBED No Cr	Delamination	Pt opened, Rh dark
SCC-S4	Silicon nitride	1	450–500K	IBED 1000Å Cr	Delamination	Rh spalled, Pt looked good
SCC-S5	Silicon nitride	2	800K	IBED 1000Å Cr	Delamination	Equipment shakedown test
SCC-C1	Compglas®	3	Room temp.	IBED 1000Å Cr	Delamination	Pt spalled at junction, Rh more adherent
SCC-C2	Compglas®	–	Room temp.	IBED 1000Å Cr	Delamination	Spalled prior to test
IIE-S1	Silicon nitride	7	915K	Ion implant	Delamination	Junction spalled
IIE-S2	Silicon nitride	2	360K	Ion implant	Delamination	Rh leg spalled
IIE-S3	Silicon nitride	–	–	Thin implants, no overcoat	–	Not tested
IIE-S4	Silicon nitride	–	–	Thin implants, no overcoat	–	–
IIE-C1	Compglas®	3	915K	Ion implant 4000Å films	High resistance	Rh oxidized, film resistance up to 30K ohms
IIE-C2	Compglas®	5	915K	Ion implant 4000Å films	High resistance	Resistance over 15K ohms
RFS-S1	Silicon carbide	3	–	RF sputter	Weird output	Film looked alright, but output is unusable
RFS-S2	Silicon carbide	1	321K	RF sputter	Open circuit	Film cracked

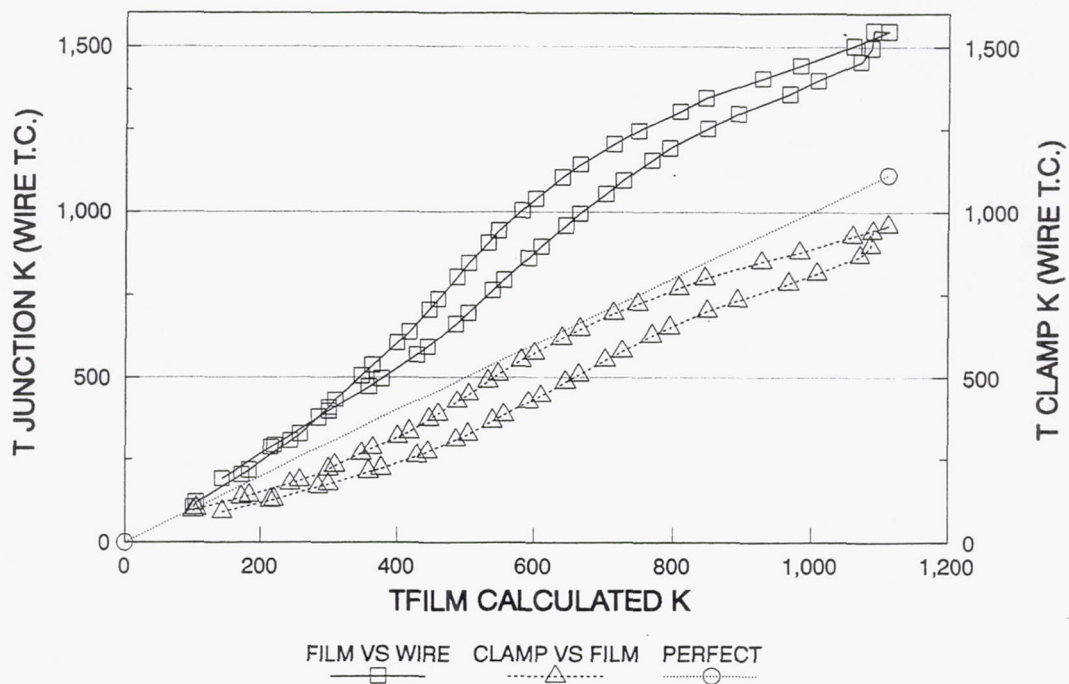


Figure 94 Plot of Film Versus Junction and Film Versus Clamp Temperatures for Sensor IIE-C1

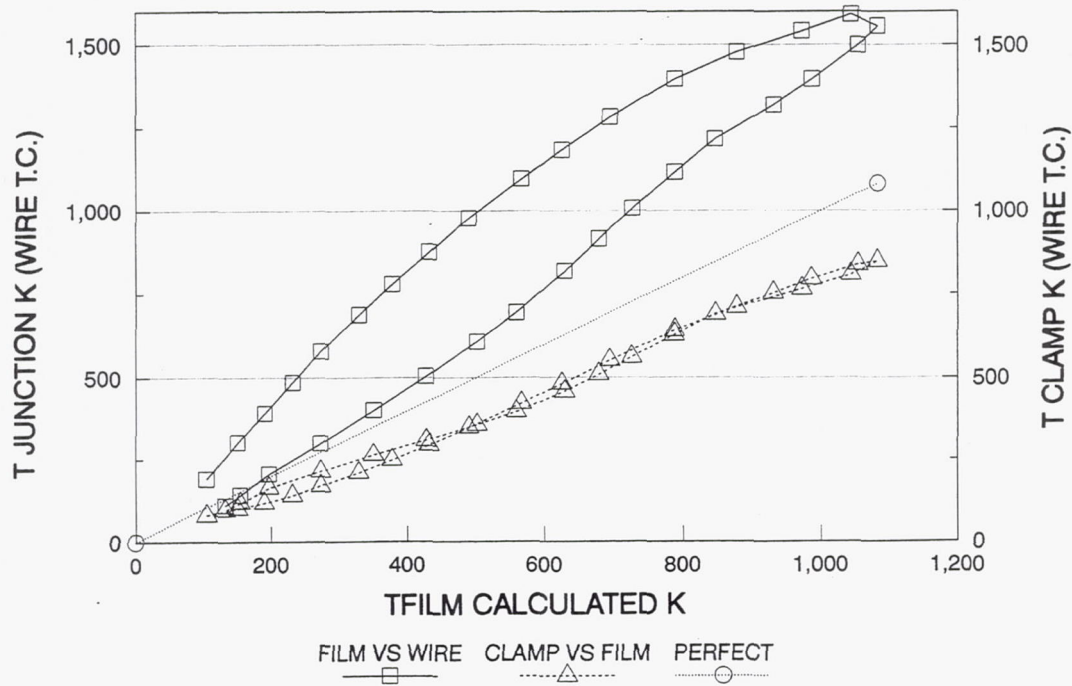


Figure 95 Plot of Film Versus Junction and Film Versus Clamp Temperatures for Sensor IIE-C2

5. THERMOGRAPHIC PHOSPHORS

5.1 Introduction

Thermographic phosphors are rare-earth doped ceramic materials whose thermally sensitive fluorescence lifetimes and amplitudes may be used to determine temperatures. A surface coating of a thermographic phosphor will fluoresce when irradiated by an appropriate ultraviolet light source. Fluorescence lifetimes and amplitudes obtained at known temperatures may be used as calibration standards. They may be compared to the fluorescence signals obtained from a phosphor coating in a test environment to determine surface temperature. Different phosphor systems have proven to be useful thermometers in ranges from 73K to 1773K.

Thermographic phosphors show promise for use as temperature measurement sensors for high-temperature applications. Phosphors have been shown to be effective in hazardous, noisy, even explosive environments. A well-operating system is immune to electrical interference, and being a noncontact technique, may be used on either static or dynamic surfaces in confined areas. This system may be ideal for some surface measurements in advanced propulsion systems.

This study was an initial investigation into the feasibility of utilizing thermographic phosphors for monitoring temperatures of ceramic components at temperatures above 1273K. Over the past five years, the Department of Energy (DoE) contractors, including Oak Ridge National Laboratory (ORNL), Los Alamos National Laboratory (LANL) and EG&G Santa Barbara, have conducted research and development work on thermographic phosphors under Air Force sponsorship. Oak Ridge National Laboratory has experience in developing thermographic phosphor techniques for monitoring and analyzing high temperatures in highly erosive environments inside turbomachinery (References 7 through 10). This work has included the screening of commercially available phosphors, manufacturing of special phosphors, calibration of various phosphors over a range of temperatures from 4K to 1673K, developing bonding techniques for bonding particular phosphors to a variety of substrates, and performing laboratory and field experiments utilizing the thermal phosphors.

In order to utilize the existing expertise in the field and to expand the technology, we chose to work with both the DoE personnel and UTRC in the thermographic phosphor tests. DoE coated the samples provided by Pratt & Whitney with thermographic phosphors. Samples of silicon nitride (Si_3N_4), silicon carbide (SiC), mullite, zirconia, and Complas® were coated. The coated samples were sent to UTRC for testing.

UTRC was responsible for performing both cyclic and endurance testing on the thermographic phosphor samples. Thermal cycle tests required that the samples be brought to a desired temperature, held at temperature to attain equilibrium, cooled to ambient conditions, and then brought back to temperature. This cycle was repeated 25 times. A second test, a steady-state thermal test or endurance test, required the sample to be held at temperature for a period of 10 hours with continuous testing for fluorescence.

After testing, the samples were sent to DoE for post-test analysis. This included scanning electron microscope (SEM), X-ray analysis, microprobe analysis, electron imaging, and X-ray photoelectron spectroscopy.

5.2 Sample Preparation

Phosphors come in a variety of compositions, based on their applications. Different dopant levels and fluorescence enhancing additives cause similar phosphors to possess different properties. Commercially available phosphors were used in this study. These phosphors are typically used as screen coatings for CRT displays. Choosing an appropriate phosphor system required the evaluation of the melting points and the temperature effective ranges of the candidate materials.

The two phosphors selected for this study were $\text{Y}_2\text{O}_3:\text{Eu}$ and $\text{Y}_3(\text{Al},\text{Ga})_5\text{O}_{12}:\text{Tb}$ (YAG:Tb). These phosphors were chosen because of their thermographic properties at elevated temperatures.

Figures 96 and 97 show the temperature dependency of these two phosphors as determined by the DoE (Reference 15). Both phosphors are commercially available and are sensitive to changes in temperature above 1273K. The Y₂O₃:Eu has been demonstrated to temperatures up to 1573K and the YAG:Tb to 1773K in lab tests.

The Y₂O₃:Eu phosphor exists as 6.8 mole percent Eu in the lattice. A strong fluorescence line occurs in the vicinity of 612 nm (temperature-sensitive), the ⁵D₀→⁷F₂ transition; while a second strong fluorescence signal may be recorded in the area of 587 nm (temperature insensitive), the ⁵D₁→⁷F₂ transition. The YAG:Tb phosphor has 0.12 mole percent terbium in the ceramic lattice. The ceramic lattice is actually a gallium-doped YAG – Y₃(Al,Ga)₅O₁₂. A strong fluorescence line occurs near 541 nm for this phosphor. Both lattices should withstand high-temperature testing quite easily – Y₂O₃ has a melting point of 2713K, while YAG melts at 2213K. The upper useable temperature is defined as the temperature at which the decay time becomes too short to measure reliably.

Prior to coating, each sample coupon was cleaned with acetone. The Si₃N₄ and SiC coupons were extremely smooth, making it difficult to adhere to the surface. A reverse sputtering process was used on each of the Si₃N₄ and SiC coupons to remove contaminants and roughen the surface prior to cleaning. This significantly improved the adherence and should be considered standard practice for all ceramic materials.

Two bonding techniques were used to apply Y₂O₃:Eu: electron beam deposition and RF sputtering. All the YAG:Tb samples were coated using the electron beam deposition technique. Seventy-three sample coupons were coated. Once the coupons were coated, a heat treatment was used to drive off contaminants, increase the relative intensity (signal level) of the phosphor coatings, and reestablish the typical fluorescent spectra. For each substrate material, coating process, and phosphor type, a single sample coupon was maintained as a control and the remaining samples were supplied to Pratt & Whitney for temperature cycling evaluation.

In working with the electron beam deposited and RF sputtered coatings for the nickel-based alloys, DoE determined that heat treating of the as-coated samples was required. The heat treating process served to drive off surface contamination, increase the signal intensity, and reestablish the fluorescent spectral signature of the phosphor in question. In order to determine if heat treating would be required, a fluorescent spectra was performed on each of the as-coated samples. The signal intensity and spectral structure of each of the samples was compared to that of a standard, hot-pressed pellet of the phosphor material. Both the electron beam and the RF sputtered as-deposited samples exhibited spectra which were significantly different than the pressed pellet. In addition, the signal intensity in most cases was down by a factor of more than 100. The sample coupons were then heat treated at 1220K for 3 hours and the fluorescent spectra were repeated. The surface chemistry analysis of an as-coated sample compared to a heat-treated sample showed that the heat treating causes a complete change in the surface morphology. The surface concentration of carbon dropped during the heat treating cycle. The heat treating process again served to drive off contaminants, increase the relative intensity and reestablish the typical fluorescent spectra. Figure 98 shows a typical spectra for a Y₂O₃:Eu standard hot-pressed pellet. Figure 99 shows a typical as-deposited and after heat treating spectra for electron beam deposited Y₂O₃:Eu. Figure 100 shows a typical spectra for a YAG:Tb standard hot-pressed pellet. Figure 101 gives a typical as-deposited and after heating spectra for an electron beam deposited YAG:Tb sample. In order to fully understand the heat treating process, additional time and funding would be required which is beyond the scope of this program. The columns in Table 4 labeled Relative Intensity, As Coated, and Heat Treated, refer to the relative intensity (signal level of the temperature dependent line of interest; in this case, the 611 nm line for Y₂O₃:Eu and 544 nm for the YAG:Tb) of the samples when compared to a standard hot-pressed pellet of the appropriate phosphor. As shown, the signal intensity is greatly increased by heat treating the samples. The last column in Table 4 gives the resulting relative intensity of several samples after temperature cycling.

Table 4

Sample Intensities

<u>Phosphor Coating</u>	<u>Coating Process</u>	<u>Substrate Material</u>	<u>Code Designation Standard</u>	<u>Relative Intensity</u>		
				<u>As Coated</u>	<u>Heat Treated</u>	<u>After Cycling</u>
<u><i>Y₂O₃:Eu</i></u>	<u>Electron- Beam Deposition</u>	<u>Zirconia</u>	<u>ZEB1</u>	<u>0.0101</u>	<u>0.10</u>	
				<u>ZEB2</u>	<u>0.0088</u>	<u>0.18</u>
				<u>ZEB3</u>	<u>0.0091</u>	<u>0.21</u>
				<u>ZEB4</u>	<u>0.0055</u>	<u>0.14</u>
				<u>ZEB5</u>	<u>0.0099</u>	<u>0.13</u>
			<u>Mullite</u>	<u>MEB1</u>	<u>0.0097</u>	<u>0.26</u>
				<u>MEB2</u>	<u>0.0091</u>	<u>0.25</u>
				<u>MEB3</u>	<u>0.0086</u>	<u>0.25</u>
				<u>MEB4</u>	<u>0.0065</u>	<u>0.26</u>
				<u>MEB5</u>	<u>0.0047</u>	<u>0.26</u>
<u>Compglas®</u>			<u>CGEB1</u>	<u>0.0080</u>	<u>0.15</u>	<u>0.039</u>
				<u>CGEB2</u>	<u>0.0040</u>	<u>0.10</u>
				<u>CGEB3</u>	<u>0.0040</u>	<u>0.07</u>
				<u>CGEB4</u>	<u>0.0036</u>	<u>0.11</u>
				<u>CGEB5</u>	<u>0.0042</u>	<u>0.14</u>
<u>Silicon Carbide</u>			<u>SCEB1</u>	<u>0.0040</u>	<u>0.11</u>	<u>0.214</u>
				<u>SCEB2</u>	<u>0.0044</u>	<u>0.16</u>
				<u>SCEB3</u>	<u>0.0032</u>	<u>0.13</u>
				<u>SCEB4</u>	<u>0.0041</u>	<u>0.14</u>
				<u>SCEB5</u>	<u>0.0040</u>	<u>0.15</u>
<u>Silicon Nitride</u>			<u>SNEB1</u>	<u>0.0038</u>	<u>0.17</u>	
				<u>SNEB2</u>	<u>0.0035</u>	<u>0.18</u>
				<u>SNEB3</u>	<u>0.0040</u>	<u>0.19</u>
				<u>SNEB4</u>	<u>0.0038</u>	<u>0.20</u>
				<u>SNEB5</u>	<u>0.0042</u>	<u>0.20</u>

Table 4 Sample Intensities (continued)

<i>Phosphor Coating</i>	<i>Coating Process</i>	<i>Substrate Material</i>	<i>Code Designation</i>	<i>Relative Intensity</i>		
				<i>As Coated</i>	<i>Heat Treated</i>	<i>After Cycling</i>
<i>Y₂O₃:Eu</i>	<i>RF Sputtering</i>	<i>Zirconia</i>	<i>ZRF1</i>	0.0001	0.0086	0.009
			<i>ZRF2</i>	0.0001	0.0112	
			<i>ZRF3</i>	0.0001	0.0073	
			<i>ZRF4</i>	0.0000	0.0	
			<i>ZRF5</i>	0.0003	0.0073	
		<i>Mullite</i>	<i>MRF1</i>	0.0000	0.012	
			<i>MRF2</i>	0.0000	0.012	
			<i>MRF3</i>	0.0000	0.014	
		<i>Compglas®</i>	<i>CGRF1</i>	0.0003	0.0094	
			<i>CGRF2</i>	0.0003	0.0086	
			<i>CGRF3</i>	0.0001	0.0086	
			<i>CGRF4</i>	0.0001	0.0077	
			<i>CGRF5</i>	0.0003	0.0094	
<i>Silicon Carbide</i>	<i>SCSPY</i>	<i>SCSPY01</i>	0.0003	0.0045		
			<i>SCSPY02</i>	0.0003	0.0062	0.014
			<i>SCSPY03</i>	0.0004	0.0049	
			<i>SCSPY04</i>	0.0003	0.0053	
			<i>SCSPY05</i>	0.0001	0.0058	
	<i>SNSPY</i>	<i>SNSPY01</i>	0.0004	0.0066		
			<i>SNSPY02</i>	0.0003	0.70	
			<i>SNSPY03</i>	0.0005	0.0062	0.013
			<i>SNSPY04</i>	0.0001	0.0070	
			<i>SNSPY05</i>	0.0003	0.0066	

Table 4 Sample Intensities (continued)

<u>Phosphor Coating</u> <u>YAG:Tb</u>	<u>Coating Process</u> --	<u>Substrate Material</u> --	<u>Code Designation</u> <u>Standard</u>	<u>Relative Intensity</u>		
				<u>As Coated</u> 1.0	<u>Heat Treated</u> 1.0	<u>After Cycling</u>
<i>Electron Beam Deposition</i>	<i>Zirconia</i>	<i>ZYT1</i>		0.0013	0.49	
			<i>ZYT2</i>	0.0007	0.54	
			<i>ZYT3</i>	0.0006	0.56	
			<i>ZYT4</i>	0.0005	0.54	0.021
			<i>ZYT5</i>	0.0006	0.50	
	<i>Mullite</i>	<i>MYT1</i>		0.0013	0.57	
			<i>MYT2</i>	0.0002	0.51	
			<i>MYT3</i>	0.0007	0.59	
			<i>MYT4</i>	0.0006	0.60	
			<i>MYT5</i>	0.0006	0.53	
<i>Compglas®</i>	<i>CYT1</i>			0.0013	0.28	
		<i>CYT2</i>		0.0013	0.38	
				0.0009	0.43	
			<i>CYT4</i>	0.0009	0.0049	
			<i>CYT5</i>	0.0003	0.06	
	<i>Silicon Carbide</i>	<i>SCYT1</i>		0.0031	0.37	
			<i>SCYT2</i>	0.0009	0.39	
			<i>SCYT3</i>	0.0009	0.25	
			<i>SCYT4</i>	0.0007	0.33	
			<i>SCYT5</i>	0.0008	0.42	
<i>Silicon Nitride</i>	<i>SNYT1</i>			0.0005	0.17	
		<i>SNYT2</i>		0.0006	0.47	0.006
				0.0005	0.22	0.012
			<i>SNYT4</i>	0.0005	0.18	
			<i>SNYT5</i>	0.0007	0.19	

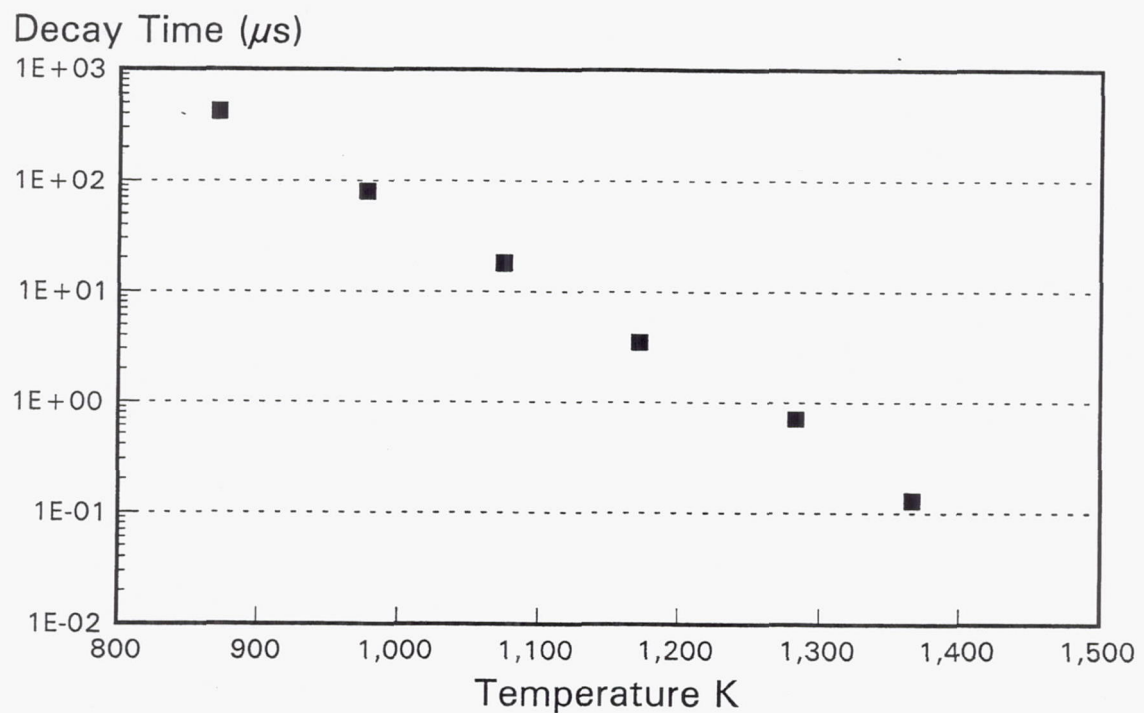


Figure 96 DoE Calibration for $Y_2O_3:Eu$ Phosphor

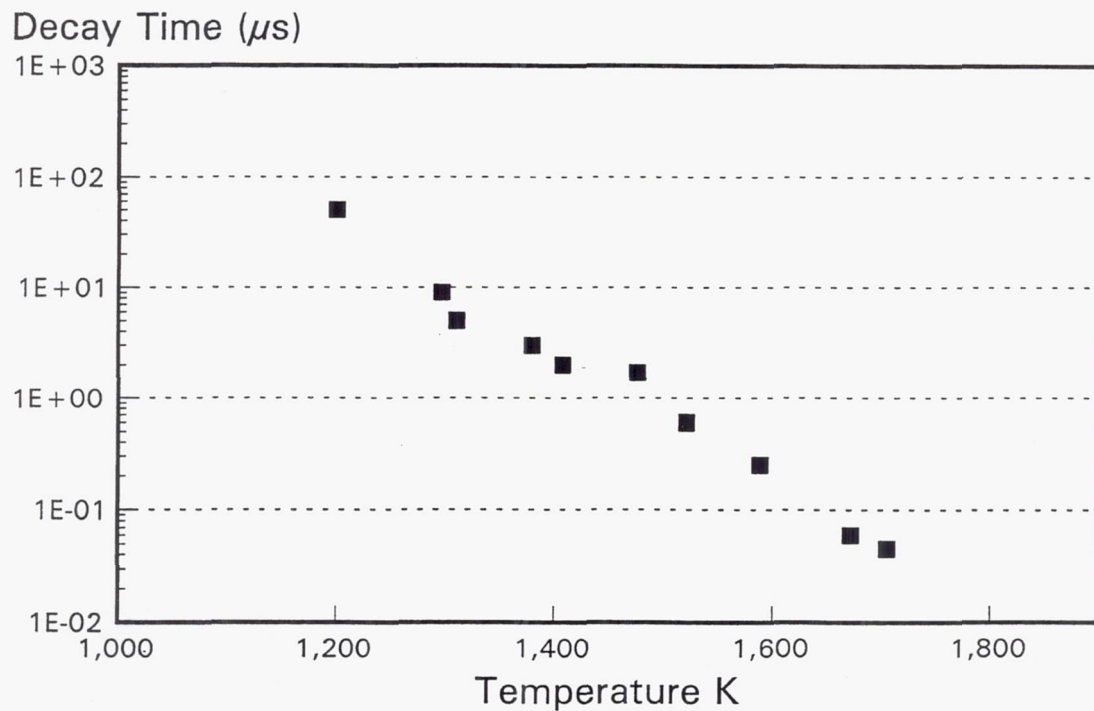


Figure 97 DoE Calibration for $YAG:Tb$ Phosphor

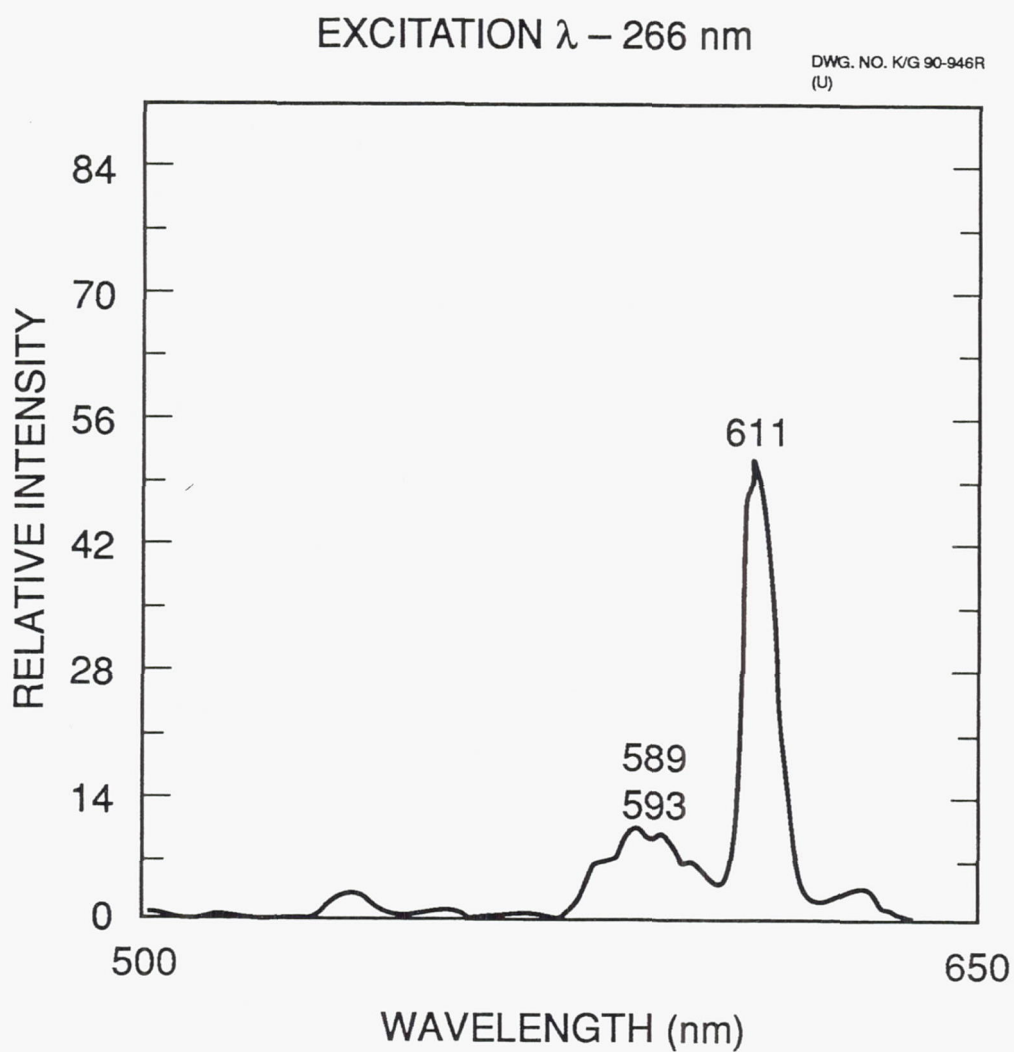


Figure 98 Emission Spectra for $Y_2O_3:Eu$ Pressed Pellet Standard

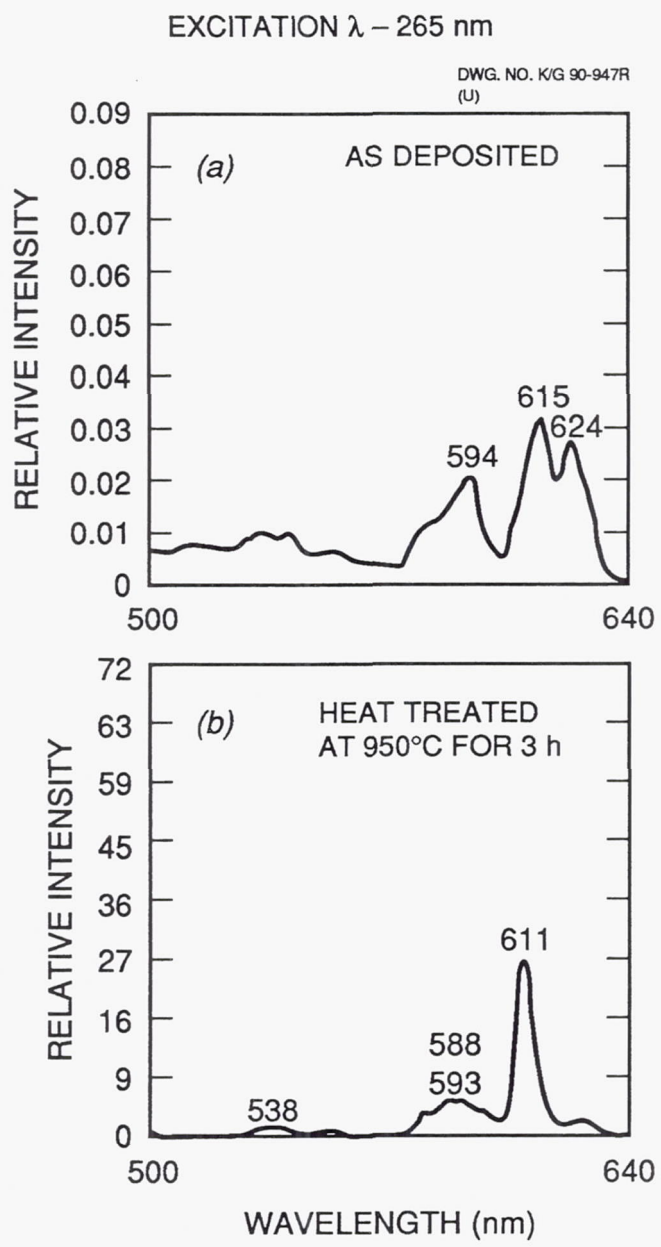


Figure 99 Emission Spectra for $\text{Y}_2\text{O}_3:\text{Eu}$ As Deposited and After Heat Treat

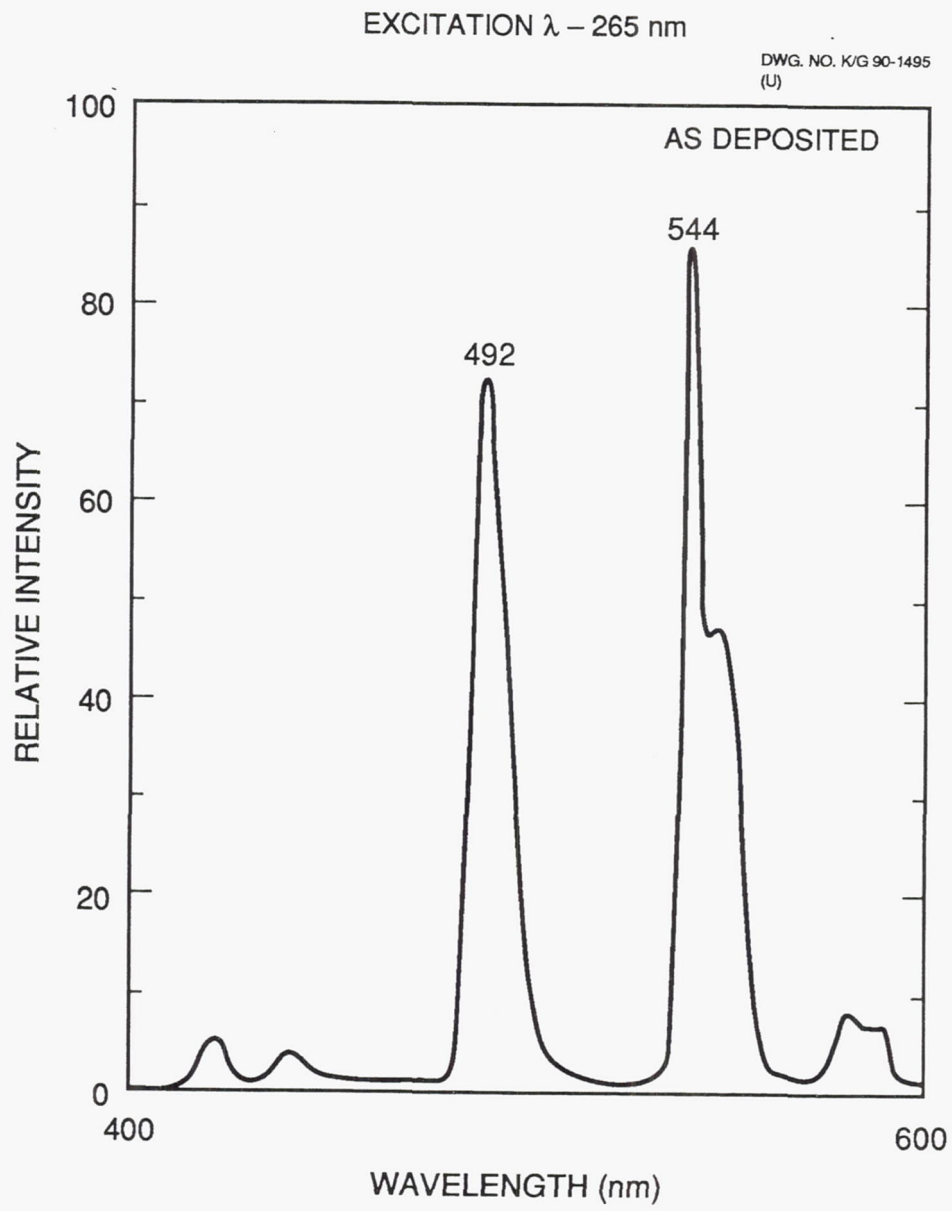


Figure 100 Emission Spectra for YAG:Tb Pressed Pellet Standard

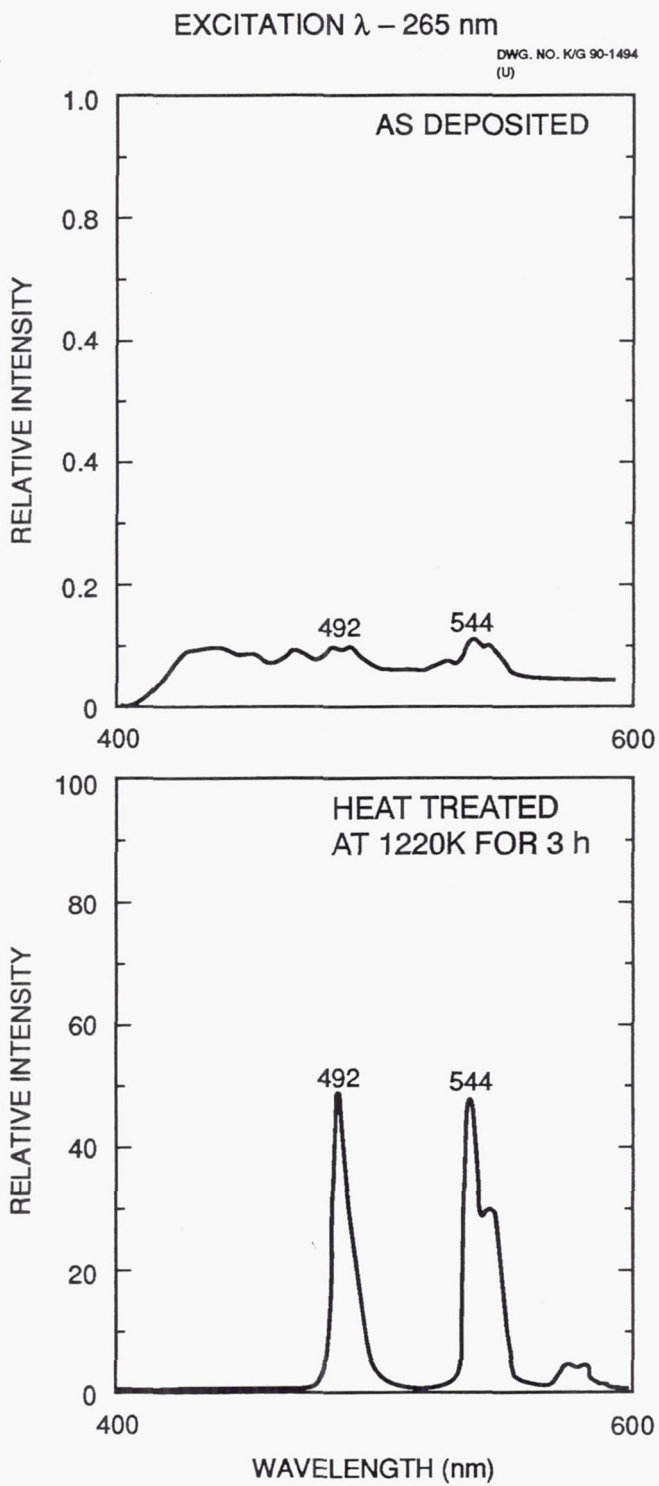


Figure 101 Emission Spectra for YAG:Tb As Deposited and After Heat Treat

5.3 Test Procedure

A Thermcraft tube furnace was used as the heat source for the temperature testing at UTRC. It has a maximum rated operating temperature of 1773K. The 2.54 cm x 2.54 cm sample coupons were placed upright into a mullite holder and positioned in the center of the tube furnace. A thermocouple was situated at the center of the furnace to record temperatures. The furnace was implemented with quartz windows to seal off the tube and provide optical access for laser introduction and analysis of the fluorescence.

The fourth harmonic output (266 nm) from a Nd:YAG laser was directed through a series of optics into the furnace. The laser spot interacted with the phosphor on the sample coupon, inducing a fluorescence signal. The fluorescence is captured with a lens and brought to a focus in the spectrometer. Decay rate measurements are made by concentrating on a single wavelength of the dispersed signal and measuring the rate of change of fluorescence signal intensity versus time. Figure 102 shows a schematic diagram of the test setup.

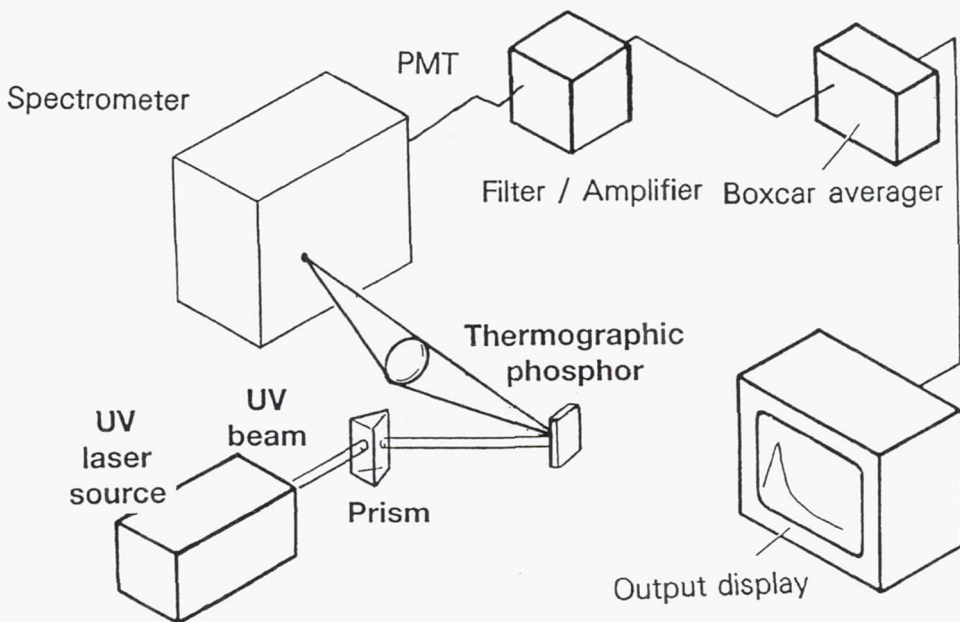


Figure 102 Schematic Diagram of UTRC Fluorescence Testing Setup

Each of the sample coupons was given a baseline room temperature emission and a room temperature excitation run when received. Emission runs spanned the region from 550 nm to 700 nm; excitation scans from 200 nm to 600 nm. Each sample was also subject to a room temperature emission and excitation run before a day's run if the sample had been previously tested at temperature. Additionally, room temperature emission and excitation runs were taken if a sample failed any of the heat tests.

For each sample, four target temperatures were desired: 1273K, 1473K, 1673K, and 1773K. Decay rate measurements were taken by concentrating on a single wavelength of the dispersed signal and measuring the rate of change of fluorescence signal intensity versus time.

Samples were thermal cycled to investigate degradation of the phosphors. Samples were cycled 25 times to each temperature setting. Each cycle consisted of placing the sample coupon at the target

temperature. Upon standing at temperature for 1 minute, the sample was removed to ambient for 1 minute. On every fifth heat cycle, the sample was allowed to remain at temperature, whereby a fluorescence signal was obtained. Due to the thermal conductivity of the ceramic test samples, the sample was given ample time to equilibrate to the target temperature before a fluorescent measurement was made. Typically, the fluorescence signal was obtained after a 10 to 15 minute equilibration period.

A candidate sample coupon from each sample set was chosen and cycled at the first temperature. If the coupon survived at temperature, a calibration run (room temperature emission and excitation spectra) was taken before testing the coupon at the next highest temperature. The process continued until either the sample failed to produce a reliable fluorescence signal or the high-temperature limit for the phosphor was reached. If a sample failed, a calibration run was made. A second sample coupon from the same sample set would then be evaluated starting at the last temperature at which the prior sample had been successfully tested. The target temperatures would be raised until the sample produced an unreliable fluorescence signal or the high-temperature limit of the furnace was reached.

In addition to the heat cycle testing, sample sets were tested for their ability to withstand long periods of time at temperature. In these durability tests, samples were placed at a target temperature for a 10-hour period. The $\text{Y}_2\text{O}_3:\text{Eu}$ samples were heated to 1473K, the YAG:Tb samples to 1773K. At regular intervals during the 10-hour run, fluorescence spectra were obtained. If a sample failed to give a reliable signal at any point in the testing, it was allowed to remain at temperature for another hour, at which time another fluorescence signal was taken. Calibration spectra were taken the day after these durability tests.

Due to time constraints in the test program, some sample sets were subject to a quick heat-up test. For these tests, a sample was placed at an initial temperature and the fluorescence signal recorded. The temperature was then increased in 100 degree increments and fluorescence spectra taken at each new temperature. In addition, several of the sample sets were subject to a "modified durability test." For these tests, the samples were placed at the desired temperature for a 10-hour period. No fluorescence spectra of the samples were taken during this period. Calibration spectra were taken the day after the run to investigate any possible chemical changes.

5.4 Results

Overall, the phosphor/substrate systems survived reasonably well for a first attempt at coating ceramic-based materials. The phosphor adherence was good on a majority of the samples. In most cases, the phosphor performed as well as or better than the substrate materials. In cases where the phosphor performance was poor, substrate degradation seemed to be the cause. The electron beamed coatings appeared very uniform in spectral structure. The sputtered $\text{Y}_2\text{O}_3:\text{Eu}$ showed more inconsistency of spectral structure from sample to sample. This was evidenced by the discrepancy in the location of emission peaks in the pre-test calibration. Figures 103 and 104 show the calibration data generated by UTRC used to transform decay rate to temperature for $\text{Y}_2\text{O}_3:\text{Eu}$ and YAG:Tb, respectively.

For electron beam deposited $\text{Y}_2\text{O}_3:\text{Eu}$, strong fluorescence signals were observed for temperatures below 1473K. At this temperature, fluorescence levels were still very high even for periods of 12 hours. Testing at 1573K for a 2-hour period resulted in little loss of signal intensity. At 1673K, short tests (0.5 hour) resulted in little change in signal intensity; long runs (4 hours) caused complete loss of spectral identification. Physical changes were apparent after testing at 1673K. A Compglas® sample subjected to this temperature melted and bubbled in its holder. As a result, no more Compglas® samples were tested to this temperature. The phosphors on both the silicon nitride and silicon carbide samples showed a greater contrast to their respective substrate materials after 1673K testing. Both the zirconia and mullite samples appeared unchanged.

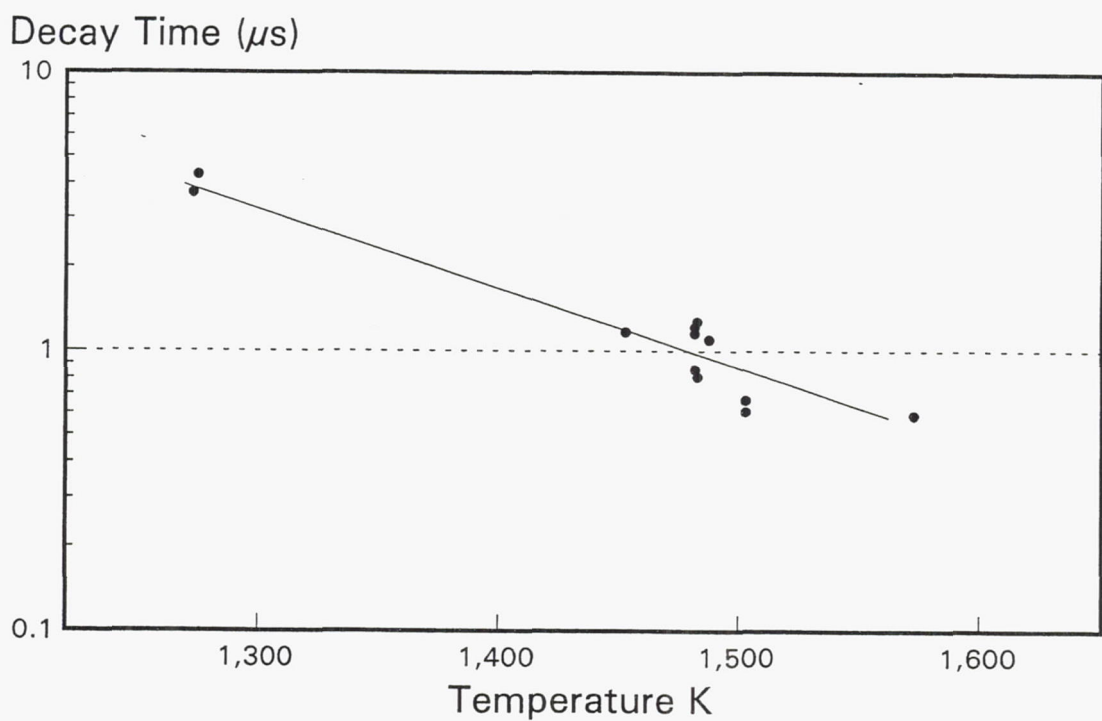


Figure 103 UTRC Calibration Data for $Y_2O_3:Eu$ Phosphor

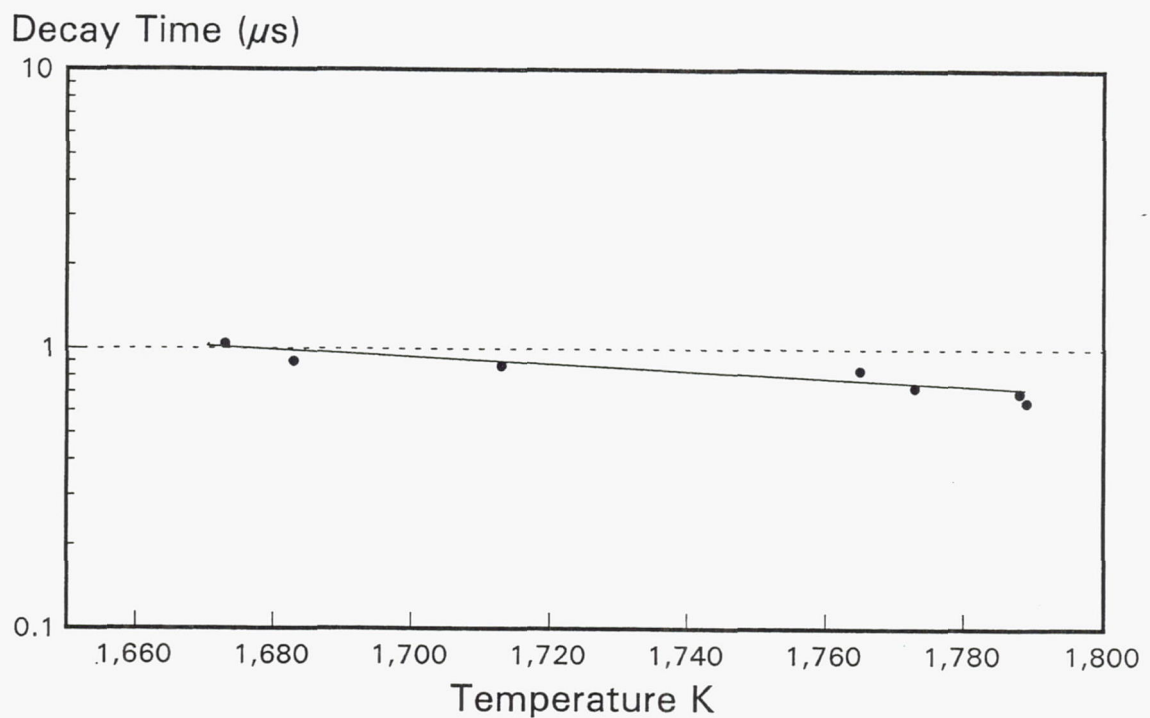


Figure 104 UTRC Calibration Data for $YAG:Tb$ Phosphor

Figure 105 shows a temperature comparison between the fluorescence decay time measured temperature and that measured in the calibration furnace with a thermocouple. There is very good correlation between the measurements for this case of a $\text{Y}_2\text{O}_3:\text{Eu}$ phosphor electron-beamed on a zirconia substrate for temperatures at 1473K for this 10-hour durability test. Fluorescence temperatures fell within 2 percent of the thermocouple values at all points, with the exception of the initial measurement point (4 percent deviation).

The results for a thermal cycle test of a sample from the same sample set are shown in Figure 106. The temperature measurements agreed to within 3 percent in this trial.

Silicon nitride was the substrate for a durability test of the same phosphor, and the results are presented in Figure 107. The temperatures agreed to within 2.5 percent at all points, with the exception of the initial measurement point (8 percent deviation).

Good fluorescence was obtained from samples with sputtered $\text{Y}_2\text{O}_3:\text{Eu}$ up to 1473K for periods up to 12 hours. The silicon nitride sample completed 12.5 hours at 1473K with some structural change. A silicon carbide sample retained strong signal levels at 1673K for a period of 2 hours.

Physically, the silicon nitride and silicon carbide samples both emerged with a higher white-to-dark phosphor contrast ratio than they had originally. A corner of a zirconia sample broke off resulting in a deep, red clay hued discoloration at the corner.

Figure 108 presents the results from a durability test for a $\text{Y}_2\text{O}_3:\text{Eu}$ phosphor RF-sputtered on the zirconia. In this case, the fluorescence temperatures were consistently lower than those recorded by the thermocouple. At the worst case (325 minutes into the test), there was a 10 percent deviation.

The results of a durability test of this phosphor RF-sputtered on a silicon nitride sample (Figure 109) showed a similar trend. Aside from the initial point, fluorescence temperatures were consistently lower than the thermocouple measurements. The greatest deviation, occurring at 360 minutes after heatup, showed an 8 percent difference.

Initial testing of electron-beamed YAG:Tb samples showed strong fluorescence signals at 1673K and 1773K. A half-hour trial at 1613K resulted in strong fluorescence. At 1673K, a diminished signal was recorded after only half an hour. Calibration spectra revealed that after 2 hours, major changes had occurred indicating a chemical change. At 1773K, a test of two-thirds of an hour resulted in structural changes; by 4 hours, major changes; by 10 hours, total deterioration of fluorescence signal. Of the substrates, the zirconia samples showed only minor changes after 4 hours at 1773K; major changes after 8 hours based on calibration data.

The zirconia samples tended to crack during thermal cycling. The phosphors coated on the silicon carbide samples tended to change from a uniform, white, powdery coating to globules of crystalline to milky white deposits on various surfaces of the coupon. The phosphors coated on the silicon nitride samples did the same as their silicon carbide counterparts (i.e., uniform, white coating to crystalline, milky pockets of material on all surfaces). As with the carbide samples, bubbling occurred at 1773K.

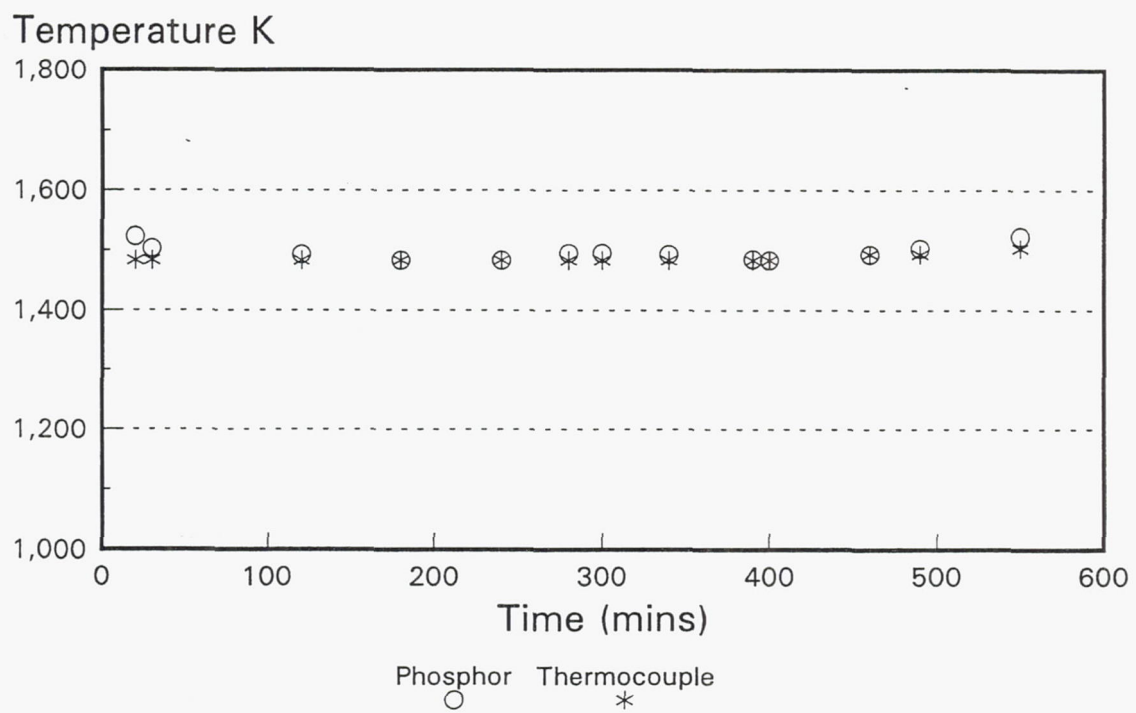


Figure 105 Durability Test of $Y_2O_3:Eu$ Electron Beam Deposited on 7% Yttria Stabilized Zirconia

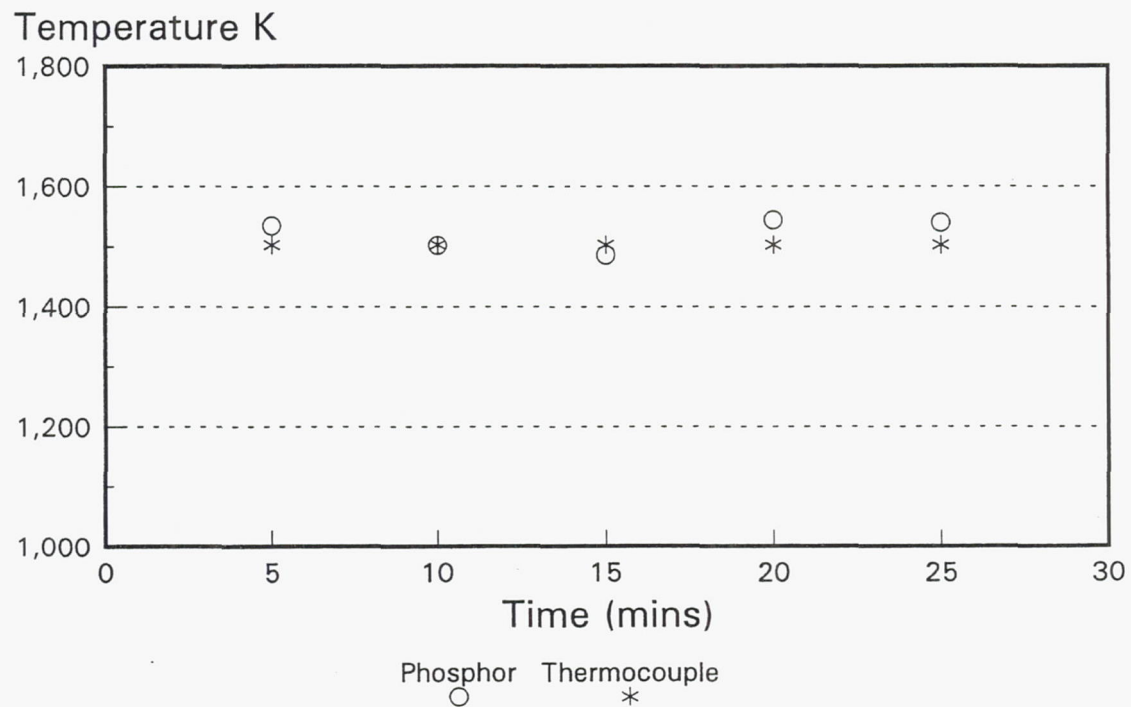


Figure 106 Thermal Cycling Test of $Y_2O_3:Eu$ Electron Beam Deposited on 7% Yttria Stabilized Zirconia

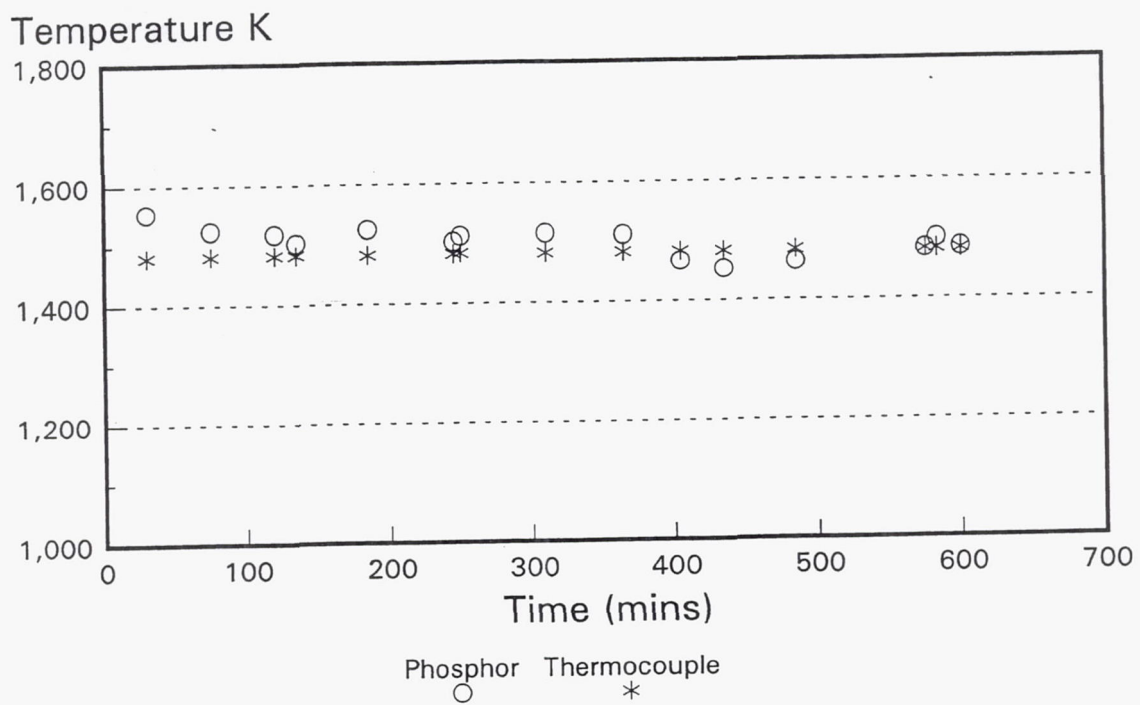


Figure 107 Durability Test of $\text{Y}_2\text{O}_3:\text{Eu}$ Electron Beam Deposited on Silicon Nitride

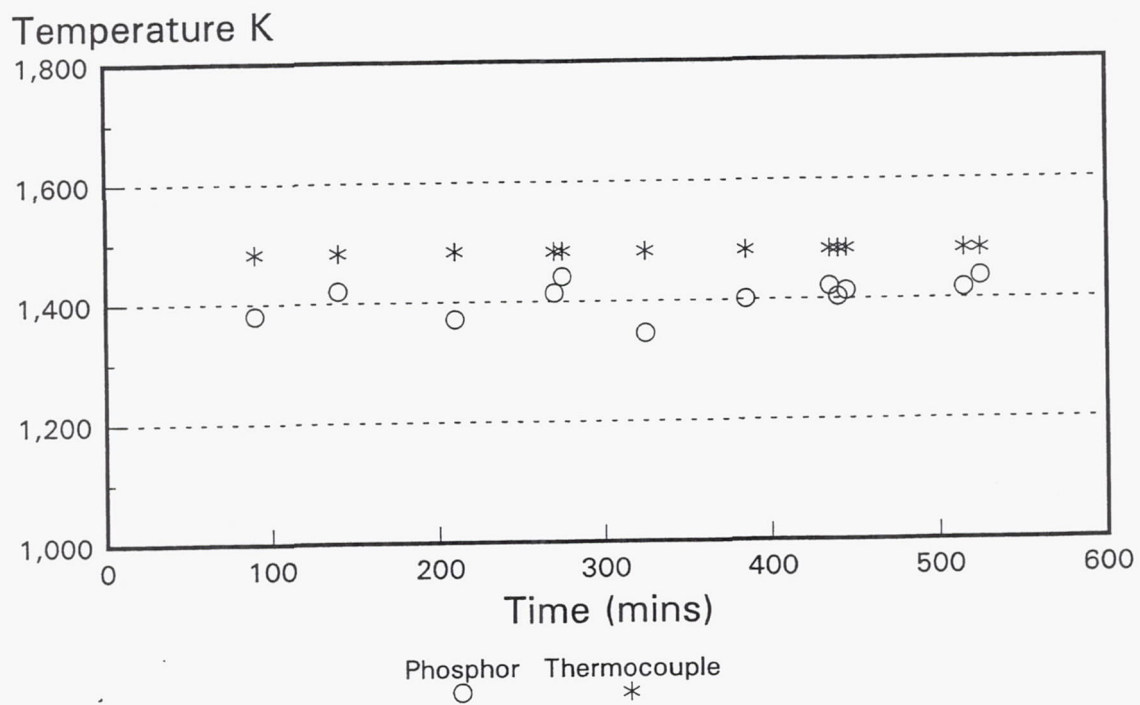


Figure 108 Durability Test of $\text{Y}_2\text{O}_3:\text{Eu}$ RF Sputtered on 7% Yttria Stabilized Zirconia

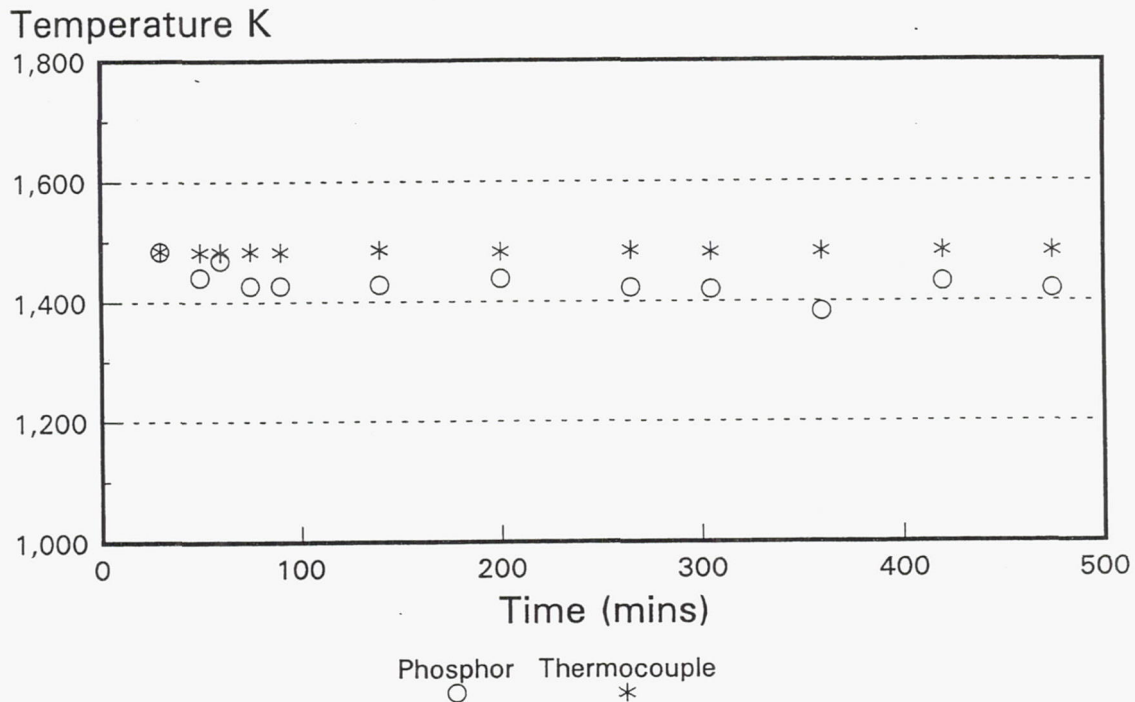


Figure 109 Durability Test of $Y_2O_3:Eu$ RF Sputtered on Silicon Nitride

Figure 110 displays the results from a durability test of YAG:Tb electron beam deposited on a zirconia test piece. The sample was tested at 1773K. The temperature measurements made during the first two hours of this run agreed quite well with the thermocouple measurements. Fluorescence spectra obtained after the two hour mark were noisier and resulted in larger deviations from the thermocouple measurements. After four hours, the noise on the fluorescence spectra made the results difficult to interpret. Chemical changes are apparently occurring after the phosphor has been exposed to the high temperatures for extended periods.

Figure 111 shows a thermal cycle test of a YAG:Tb phosphor electron-beamed on zirconia at approximately 1773K. For the 25 cycles of this test, the fluorescence temperatures measured were consistently lower than those recorded by the thermocouple. There was an increasing disparity between the temperature measurements as a function of cycle number (time).

Appendix B contains a test history for each test sample.

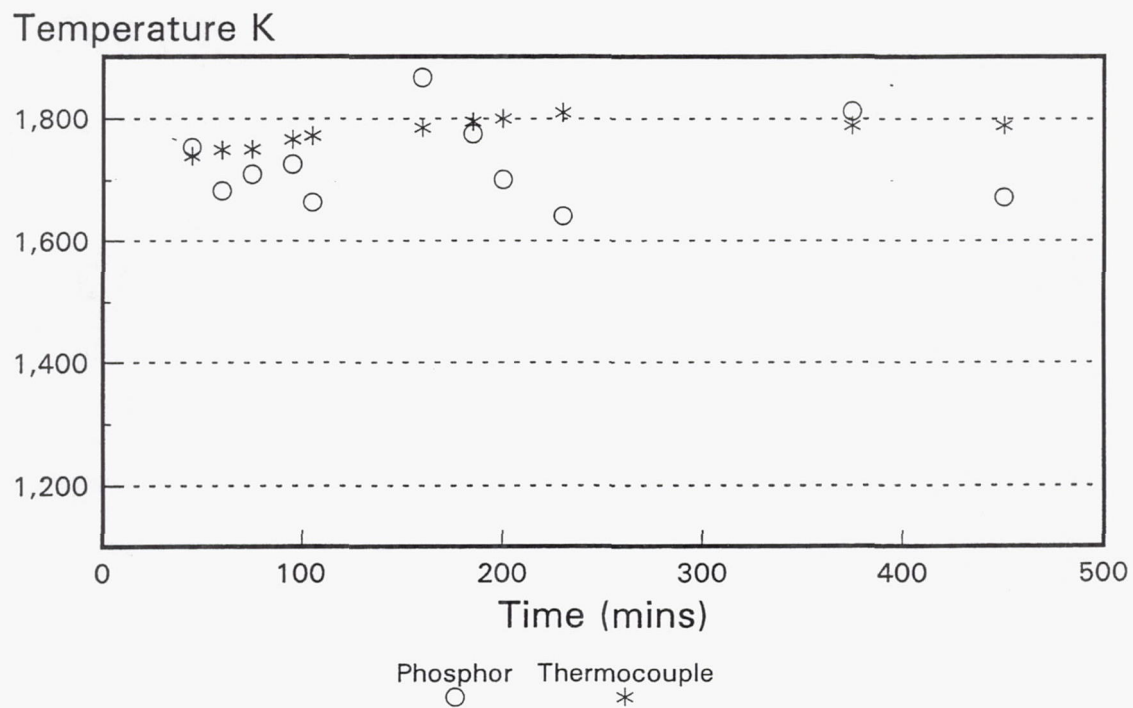


Figure 110 Durability Test of YAG:Tb Electron Beam Deposited on 7% Yttria Stabilized Zirconia

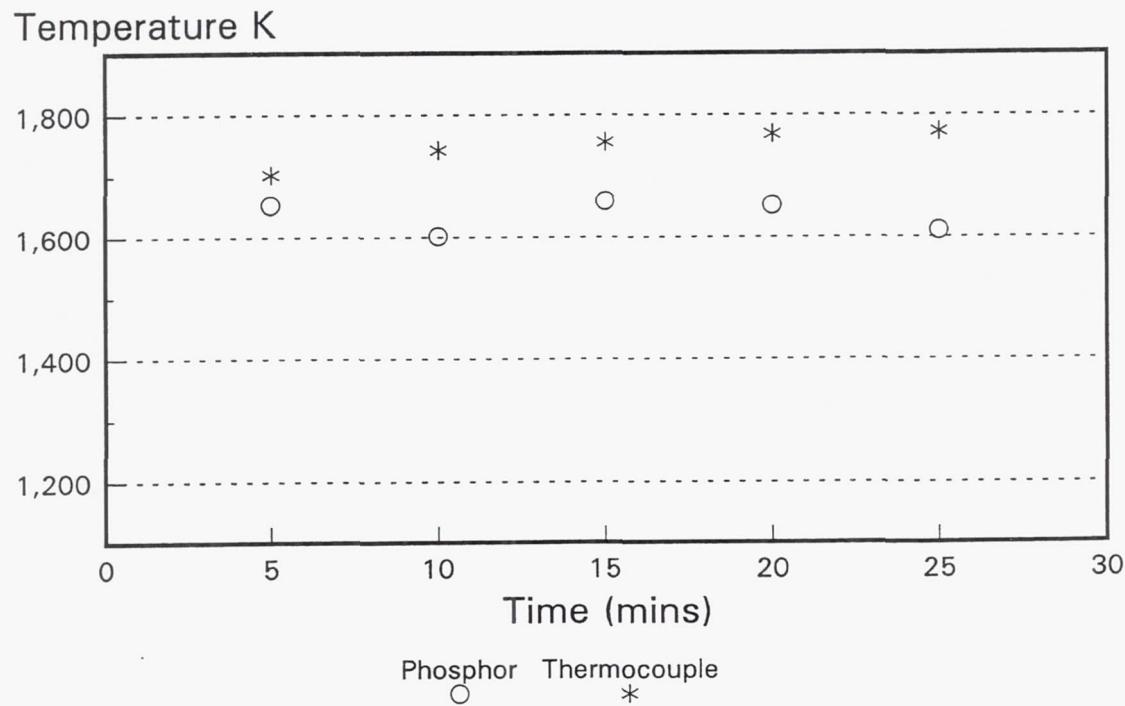


Figure 111 Thermal Cycling Test of YAG:Tb Electron Beam Deposited on 7% Yttria Stabilized Zirconia

5.5 Data Analysis

Calibration data were obtained for each phosphor system by measuring the decay rate at each target temperature. The data are then used to generate a look-up table to convert decay time to temperature. The DoE and UTRC calibrations and temperature measurement techniques are different and thus, resulted in different calibration data. This is shown in Figures 112 and 113.

Typically, the DoE does a simple averaging of a number of sample signals. Then the background noise (environmental and system electrical noise) is subtracted out, resulting in a signal containing only data from the phosphor. A portion of the decay curve is extracted. This is typically on the order of 80 percent to 30 percent of peak intensity. The natural logarithm of the data is then taken and a straight line is fitted using a least squares method. The slope of this line indicates measured decay time (slope = $-1/\tau$).

United Technologies Research Center used a different approach to measuring decay time. Each fluorescence measurement required five minutes to complete. In this approach, UTRC used a boxcar averager with a variable delay gate to generate a fluorescence decay curve. Figure 114 illustrates this approach. A 100 ns window is moved in time along the measured signal by a delay gate. The delay is set for scanning between 0 seconds and 8 μ s of the measured signal. Five minutes were required to scan the whole signal, so the window is moving at a rate of 27 ns/sec. The laser is pulsed at 10 hz. A total of 100 pulses are averaged in the boxcar averager which provides an exponential moving average. The average data are then used to build a new fluorescence signal. Fluorescence intensities at 90 percent and 10 percent of the peak signal intensity are plotted against time to determine decay rate. A linear best fit was used to determine the decay time which was calculated the same way as that of the DoE.

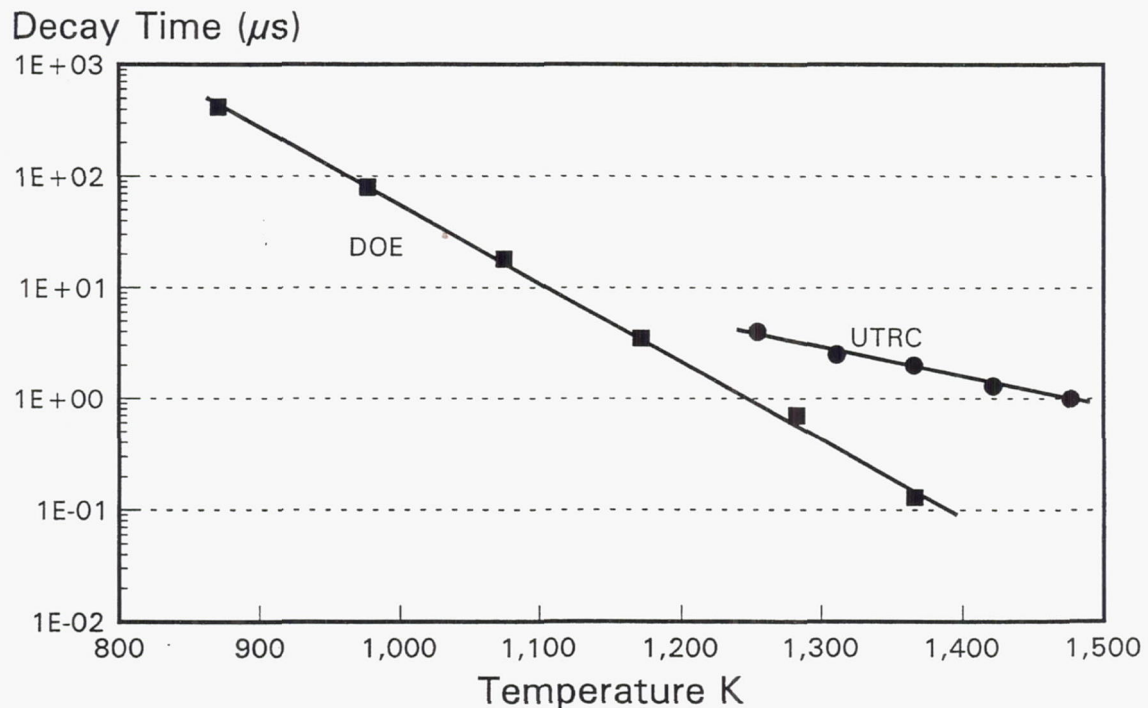


Figure 112 Comparison Between DoE and UTRC Calibrations for $Y_2O_3:Eu$

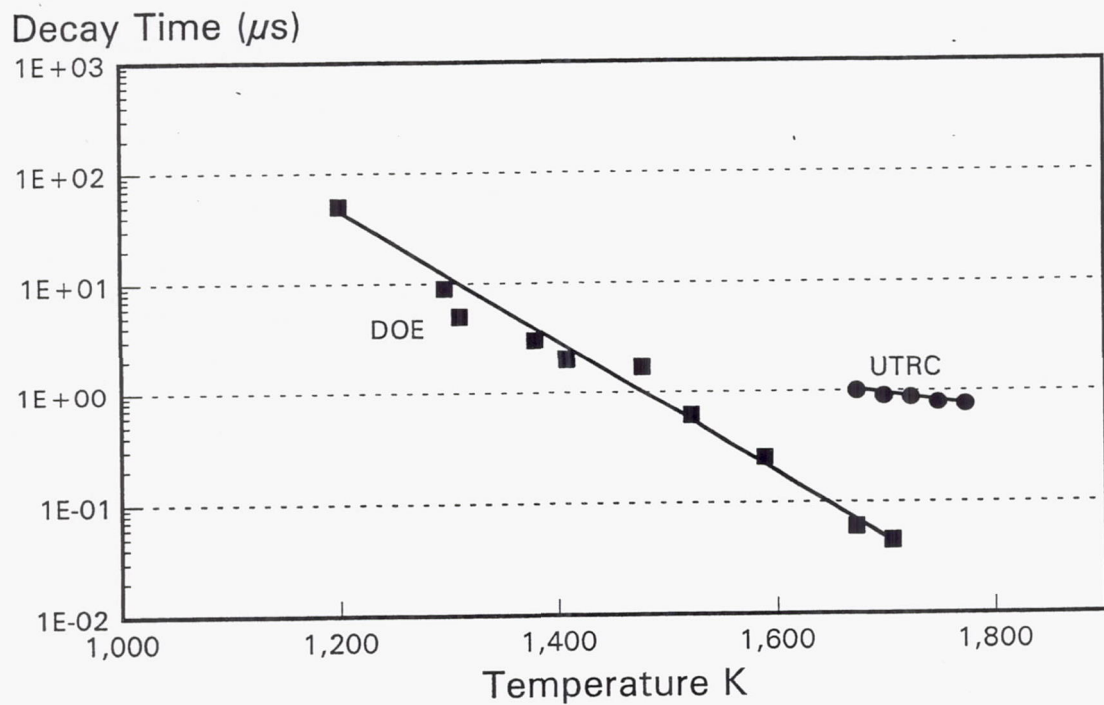


Figure 113 Comparison Between DoE and UTRC Calibrations for YAG:Tb

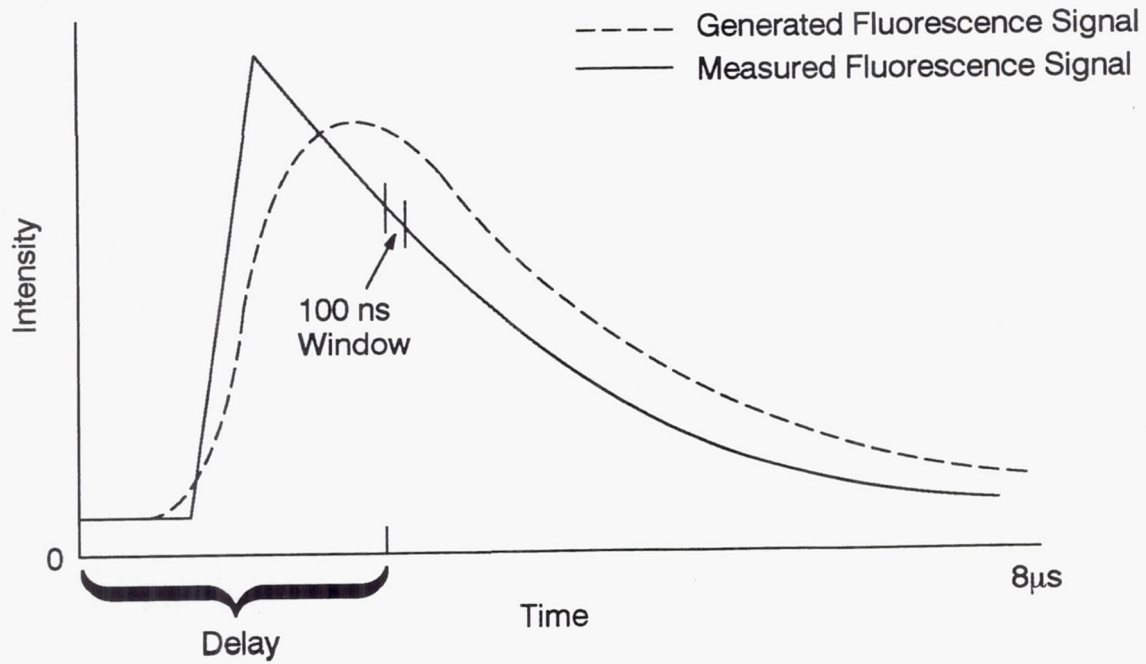


Figure 114 UTRC Data Reduction Method

A representative sample of the raw data is located in Appendix C. The data shapes were not what had been expected. The rise times were long as were the decay times. A computer simulation of the UTRC data system was used to attempt to explain the raw data and the differences in the calibration curves. The analysis was run with decay times set to 100 ns, 250 ns, 500 ns, 1 μ s, 1.5 μ s, and 2 μ s. These data (Figures 115 through 120) show a driving function simulating the phosphor signal at different temperatures and decay times and the signal as constructed by a model of the UTRC data analysis system. The results of this model indicate that the data analysis method should be valid for decay times of 500 ns or longer. This is summarized in Table 5.

Table 5 Summary of Fluorescence Modeling Results

<i>Driving Function Decay Time</i>	<i>Constructed Signal Decay Time</i>	<i>Difference (%)</i>
100 ns	277 ns	177
250 ns	348 ns	39
500 ns	551 ns	10.2
1 μ s	1.019 μ s	1.9
1.5 μ s	1.513 μ s	0.9
2 μ s	2.0009 μ s	0.5

While this model verifies the measurement technique, there are still questions surrounding the UTRC data. The calibration curves differ in slope from the DoE curves, and the rise time in the test data is approximately 1.5 times slower than the model predicts. The reason for this is not clearly understood at this time, and further evaluation is being performed.

5.6 Sample Analyses

After the cyclic and endurance testing were completed, the samples were sent back to the DoE for evaluation. Table 4 shows the results of this evaluation. The most dramatic effect was seen on the YAG:Tb samples. The relative fluorescence intensities were substantially reduced after thermal testing. A more in-depth analysis was needed, and surface characterization tests were performed.

Funding levels only allowed a small amount of surface characterization to be performed. Surface characterization was performed using the scanning electron microscope (SEM), energy-dispersive X-ray analysis (EDS), electron microprobe analysis, backscattered electron imaging (BSE), and X-ray photoelectron spectroscopy (XPS).

The surface characterization was performed on four samples. The samples chosen were all coated with YAG:Tb phosphor using electron beam deposition. The first set of samples selected were Si₃N₄ substrates (the control sample which was coated and heat treated and no additional temperature cycling performed, and one of the four samples which was temperature cycled to 1773K by UTRC). The second set of samples chosen were zirconia (ZrO₂) substrates (the control sample which was coated and heat treated at 1223K and no additional temperature cycling performed, and one of the four samples which was temperature cycled to 1773K by UTRC).

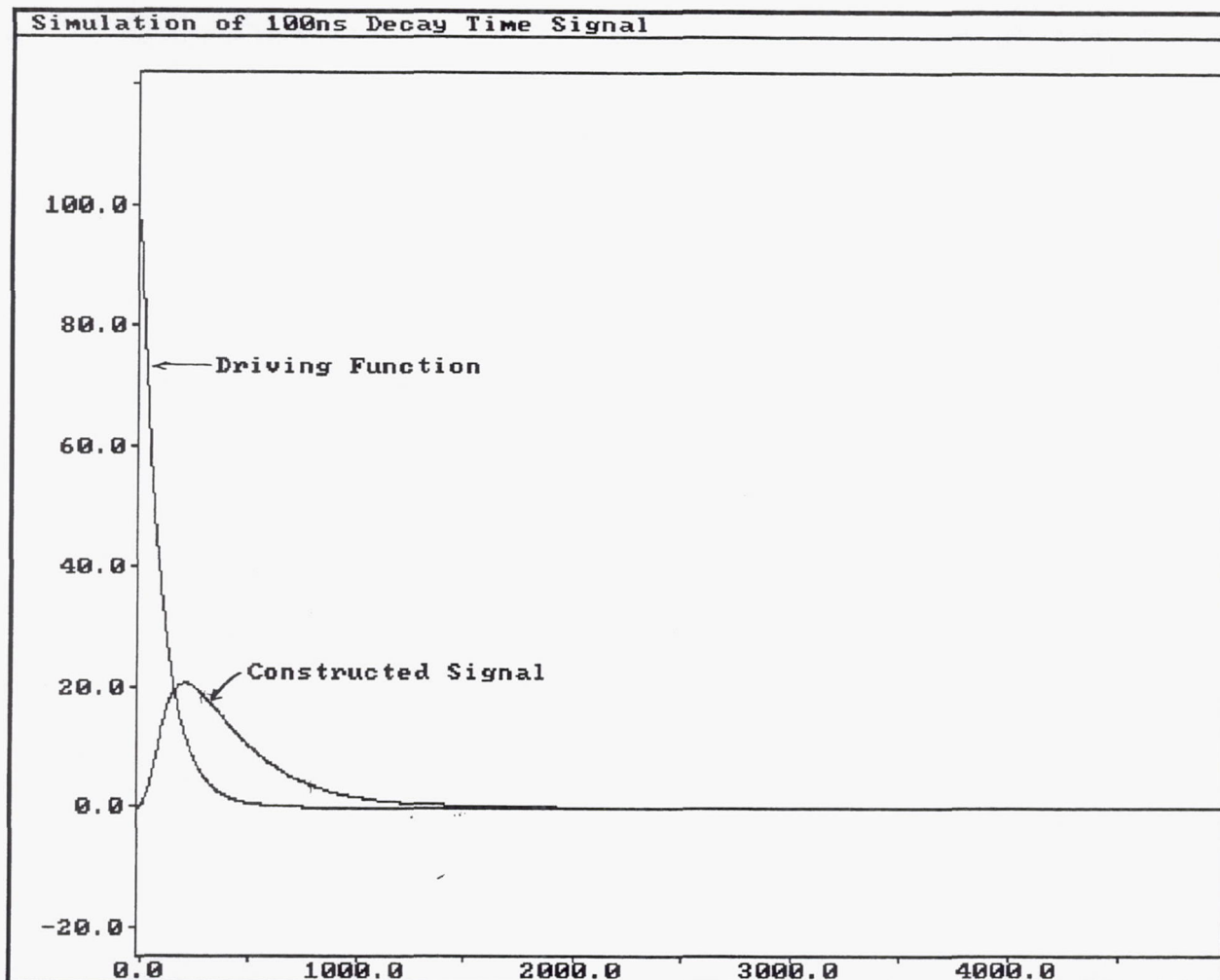


Figure 115 Simulation of UTRC Data System 100 Nanosecond Decay Time

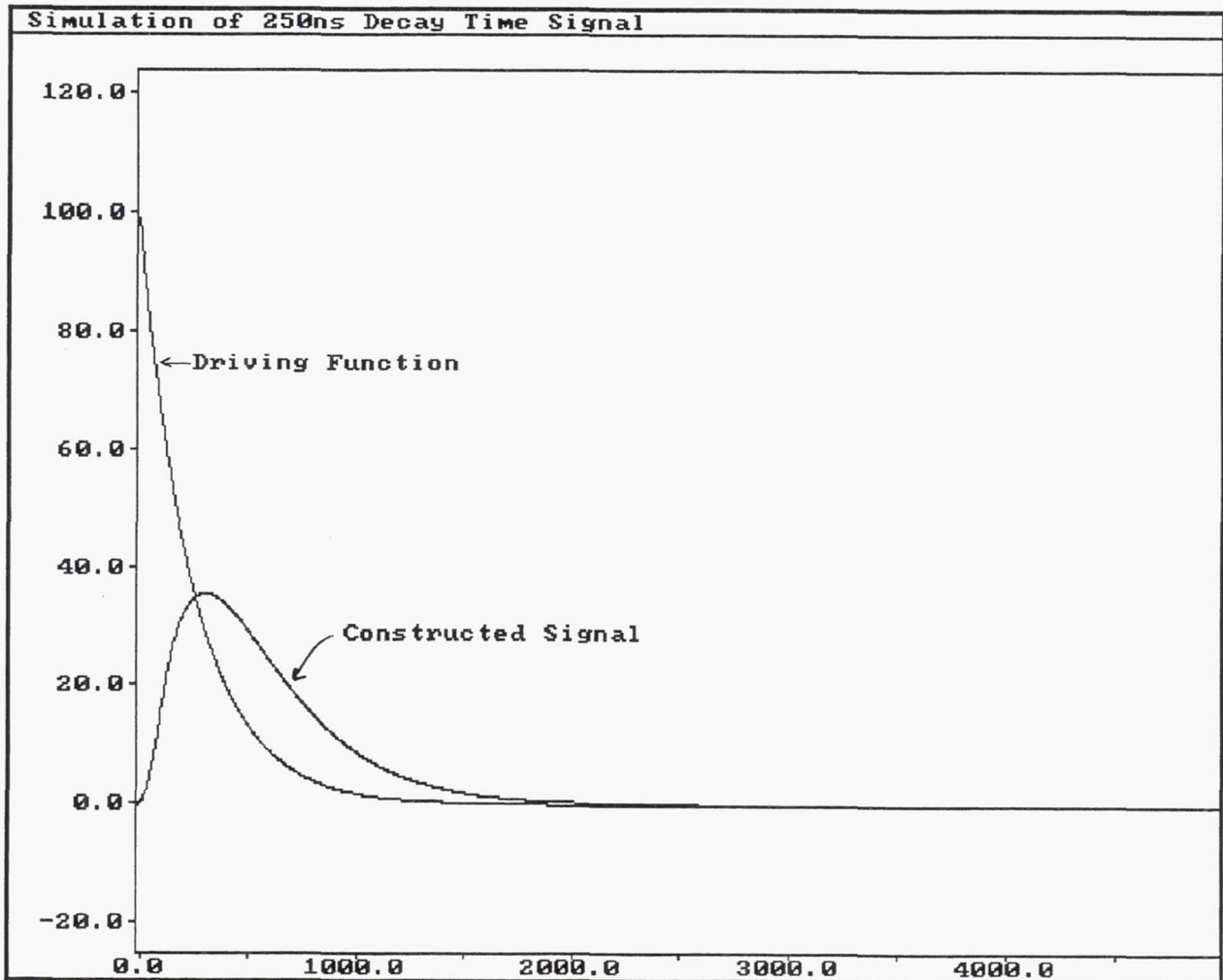


Figure 116 *Simulation of UTRC Data System 250 Nanosecond Decay Time*

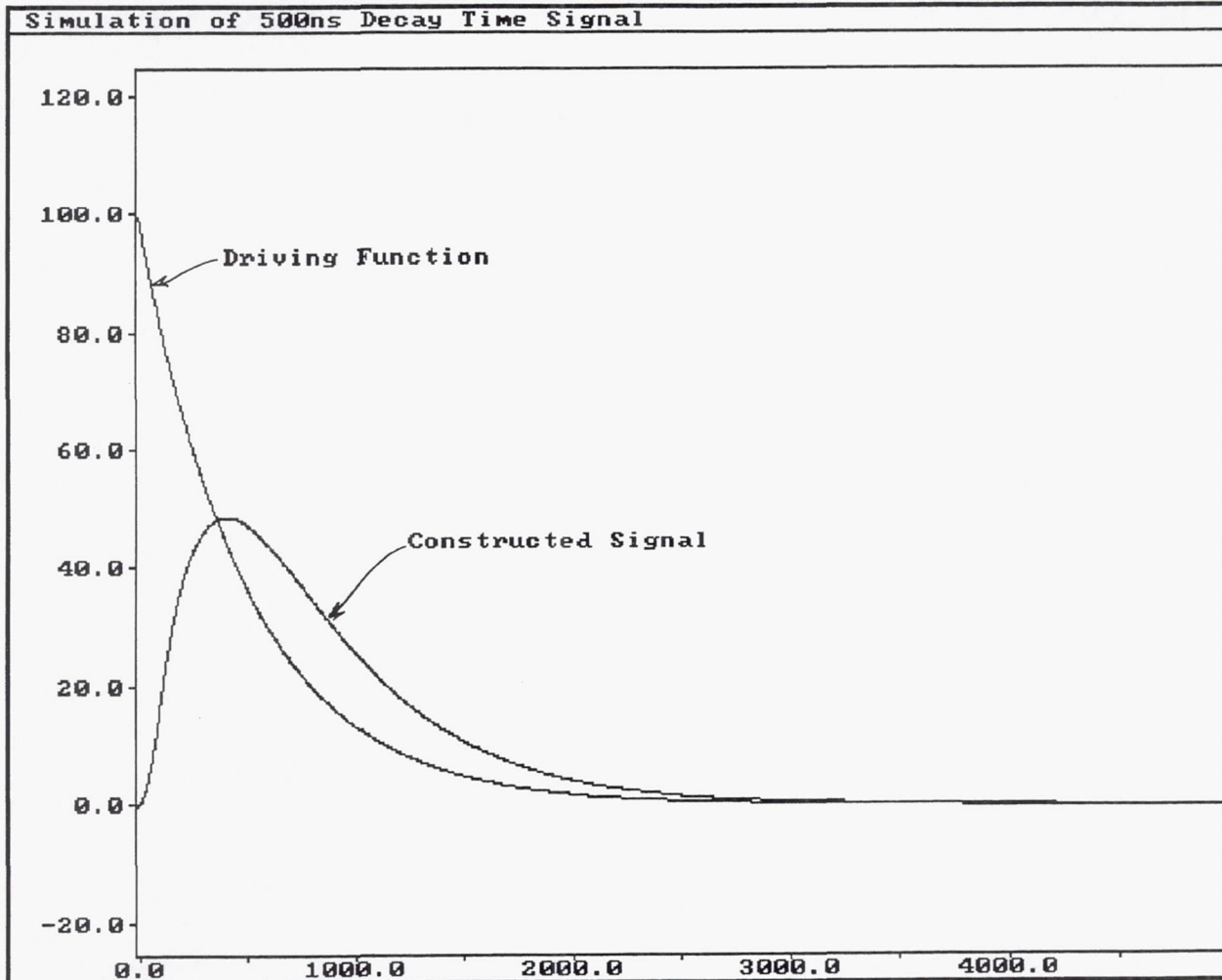


Figure 117 Simulation of UTRC Data System 500 Nanosecond Decay Time

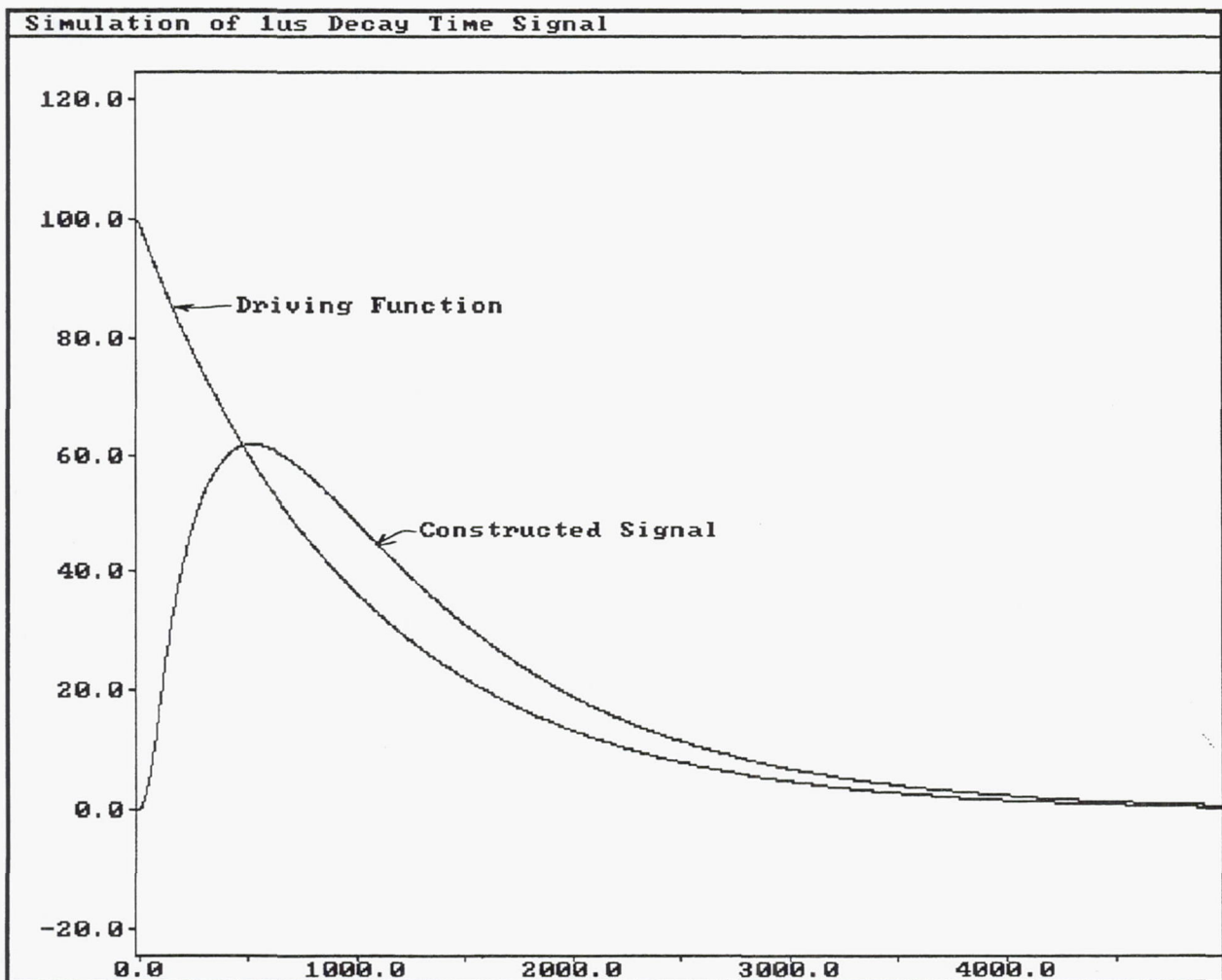


Figure 118 *Simulation of UTRC Data System 1 Microsecond Decay Time*

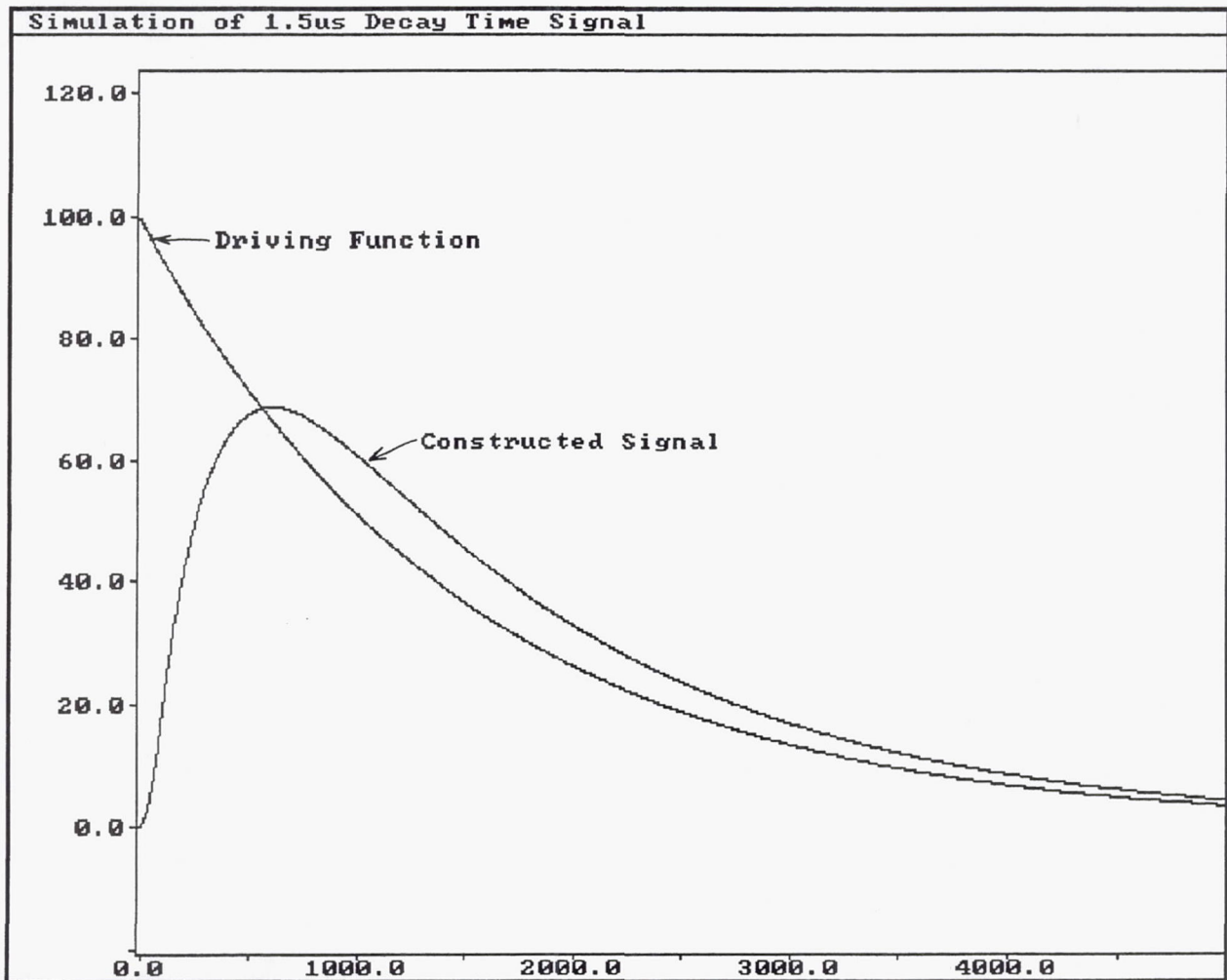


Figure 119 Simulation of UTRC Data System 1.5 Microsecond Decay Time

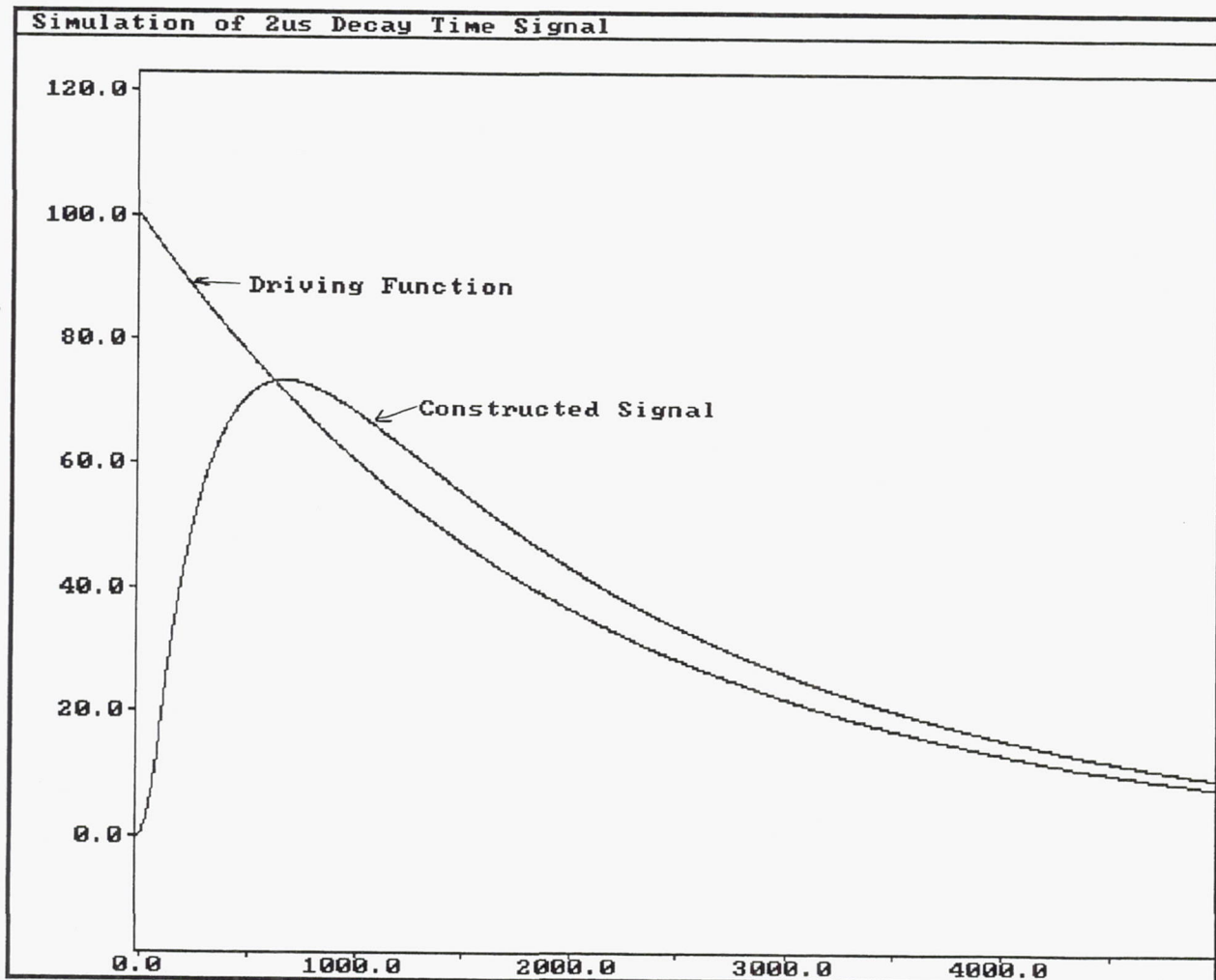


Figure 120 Simulation of UTRC Data System 2 Microsecond Decay Time

5.6.1 YAG:Tb Electron Beam Deposited on Si₃N₄ Substrate – Analysis Results

The fluorescence intensity of the coating dropped by an order of magnitude after thermal cycling to 1773K (see Table 4). The thermal cycled coupon showed obvious morphological damage (Figure 121).

Figure 122 compares the coated surface after heat treatment at 1223K with a similar surface after thermal cycling. The heat-treated surface was covered with a network of thermal cracks, with some regions beginning to show signs of flaking. After thermal cycling, two discrete surfaces were observed. The center of the Si₃N₄ coupon contained a thick region of bubbled coating, while the coupon edges were bare Si₃N₄ substrate. The original coating structure was destroyed during cycling, apparently due to the substrate Si diffusing to the surface and creating a puddling of the phosphor coating.

EDS analysis of the material present at the center of the coupon after thermal cycling is presented in Figure 123. Y, Al, Ga, and Tb are still present in the coating. The coating contains Si as its major constituent. The surface is very irregular.

Electron microprobe examination (Figure 124) of the thermally cycled coupon shows the coating components restricted to the surface. There is no evidence of any phosphor components diffusing into the substrate. However, the coating was confirmed to contain large amounts of Si indicating that the Si did diffuse into the phosphor coating. The resultant coating microstructure is shown in Figure 125. Backscattered electron imaging of the substrate indicates the presence of many metal particulates such as tungsten, iron and nickel.

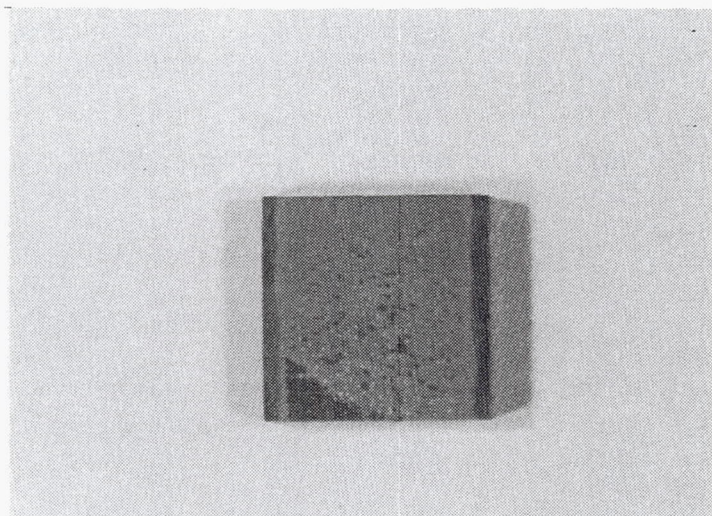
In summary, substrate Si was incorporated into the phosphor coating with subsequent melting.

5.6.2 YAG:Tb Electron Beam Deposited on a ZrO₂ Substrate – Analysis Results

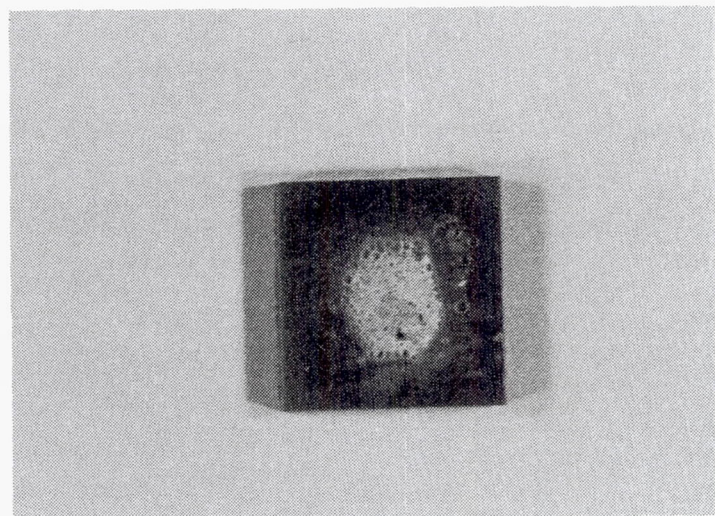
This thermal cycled coating/substrate system showed less evident of damage than the YAG:Tb/Si₃N₄ system (Figure 126). The fluorescent intensity again decreased by an order of magnitude after thermal cycling, as indicated in Table 4.

Coating surfaces of the YAG:Tb/ZrO₂ system are compared in Figure 127 before and after the thermal cycle. Some surface texture appears to have developed during cycling. EDS analysis of these surfaces indicates a loss of surface Tb (as well as Cr coating contamination) during cycling (Figure 128). This is confirmed by XPS surface (top 50 Å) analyses displayed in Figures 129 and 130. While only very small amounts of Tb are present in the top 50 Å before thermal cycling, none is detectable afterward. Intensity ratios for the YAG components (Y:Al:Ga) were 6:1:3 after heat treatment and 3:1:6 after thermal cycling, showing preferential diffusion into the substrate. The surface depletion of the fluorescent component of the phosphor has been observed on both electron beam and sputtered coatings. Correlation of elemental distribution within the coatings with fluorescent performance could potentially offer significant performance improvement.

Electron microprobe scanning images (Figures 131 and 132) demonstrate how the coating components have diffused into the zirconia substrate. Both the Tb and the Y diffusion is evident; Ga remains in the coating. It appears that the incorporation of a diffusion barrier into the phosphor/substrate system may expand the useful range of this phosphor system.



HEAT TREATED AT 1223K

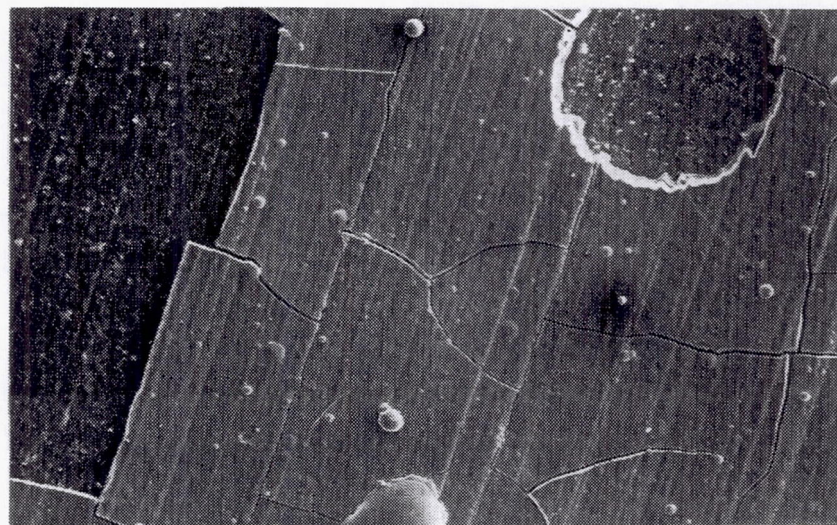


THERMALLY CYCLED AT 1773K

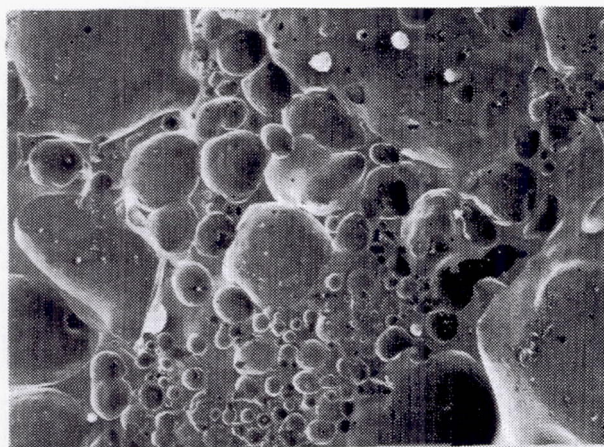
Figure 121 *YAG:Tb Electron Beam Deposited on Silicon Nitride After Heat Treating and After Thermal Testing*

SCANNING ELECTRON MICROSCOPY – 100X

1223K HEAT TREATMENT



AFTER THERMAL CYCLING
TO 1773K
CENTER REGION

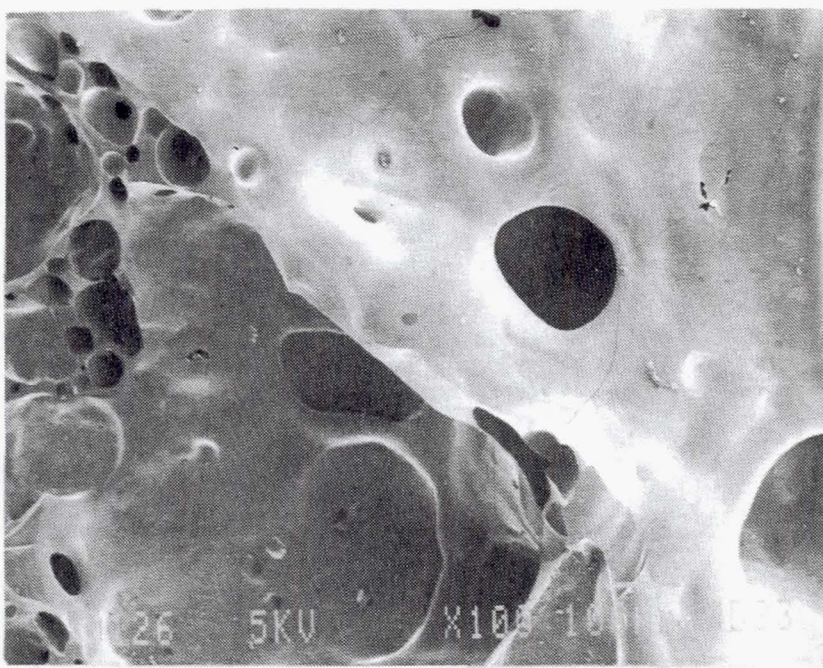


AFTER THERMAL CYCLING
TO 1773K
EDGE REGION

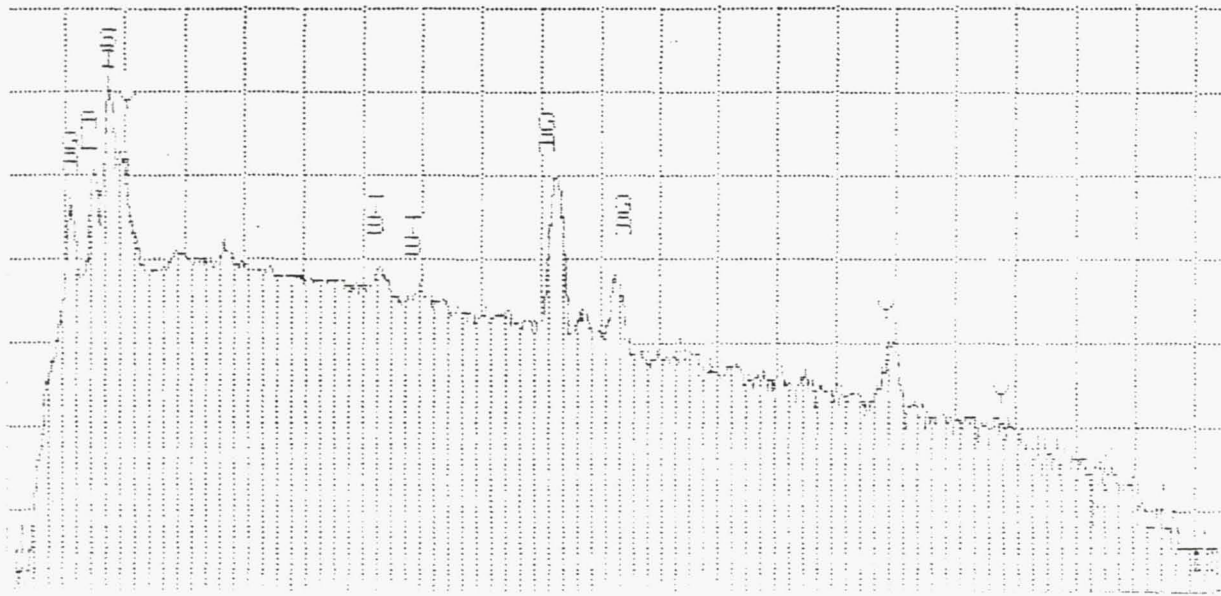


Coating morphology altered dramatically during thermal cycling

Figure 122 SEM Analysis of YAG:Tb Electron Beam Deposited on Silicon Nitride



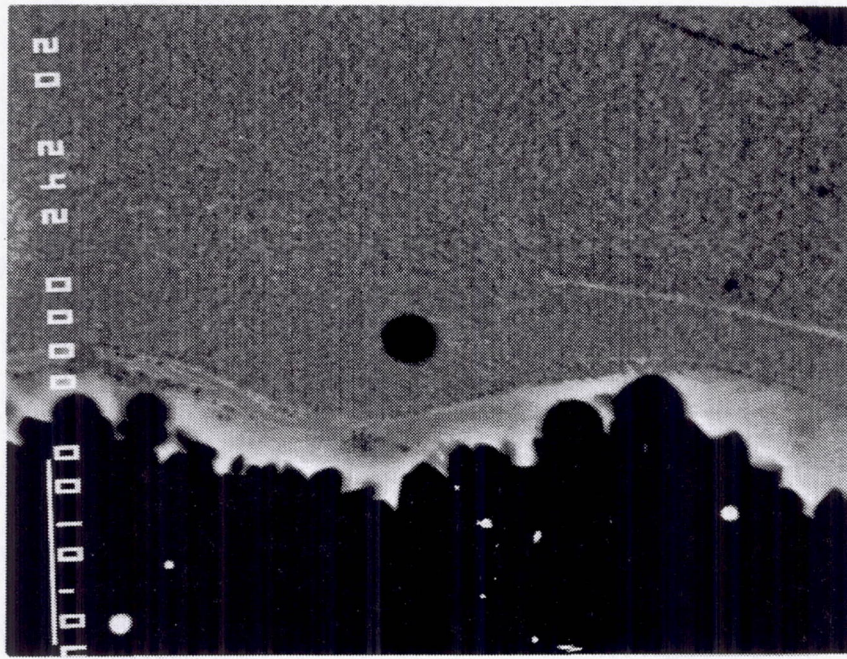
SURFACE MORPHOLOGY (SEM - 100X)



ENERGY - DISPERSIVE X-RAY ANALYSIS OF SURFACE

Surface morphology and chemistry have been altered during cycling

Figure 123 EDS Analysis of YAG:Tb Electron Beam Deposited on Silicon Nitride

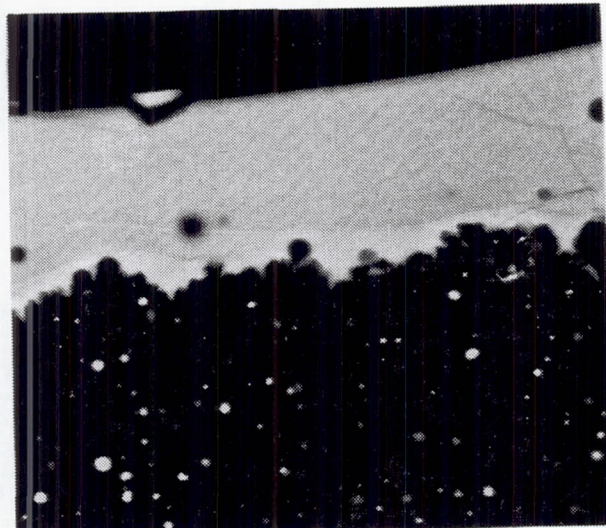


2400X

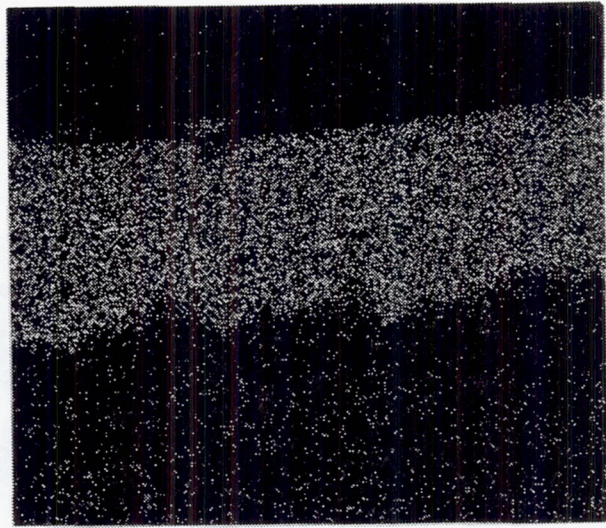
*After thermal cycling, considerable microstructure has been developed in the coating.
The reaction zone is prominent.*

Figure 124 *Electron Microprobe Scanning Image of Coating of YAG:Tb Electron Beam Deposited on Silicon Nitride After Thermal Cycling to 1773K*

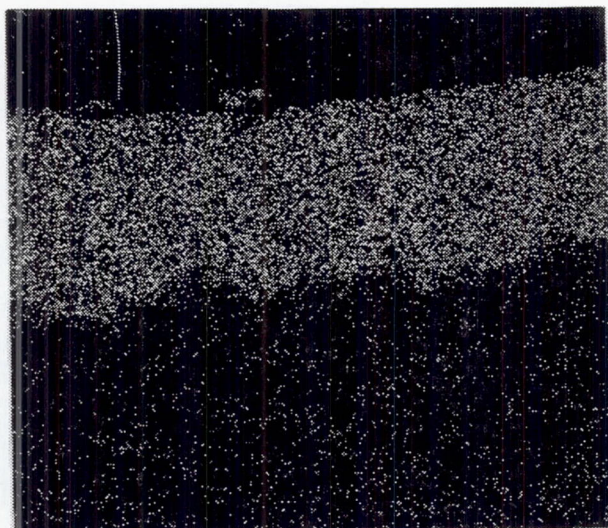
ELECTRON MICROPROBE SCANNING IMAGES – 860X



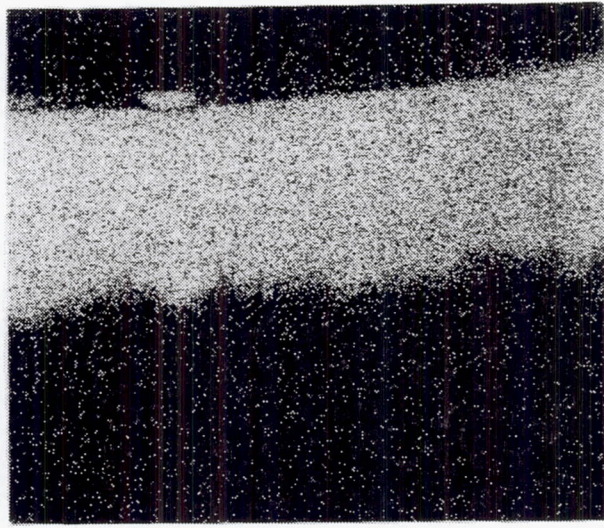
BACKSCATTERED ELECTRON



Tb L α



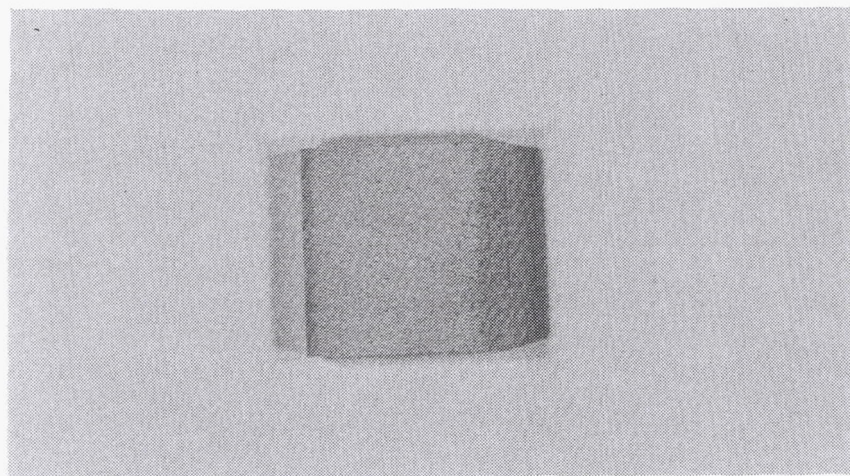
Y L α



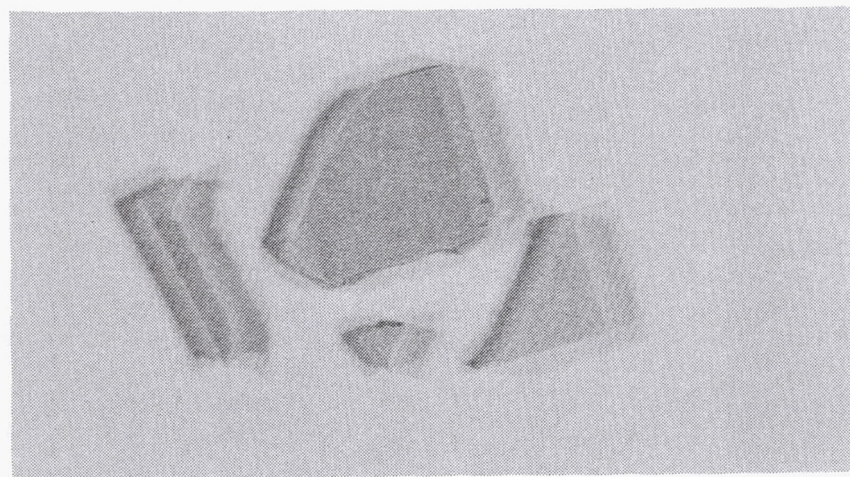
Ga K α

A reaction zone at the coating–substrate interface is seen, and the coating itself contained high amounts of silicon. No indications of coating diffusion into the substrate were observed.

Figure 125 Electron Microprobe Scanning Image of Coating/Substrate Interface of YAG:Tb Electron Beam Deposited on Silicon Nitride After Thermal Cycling to 1773K



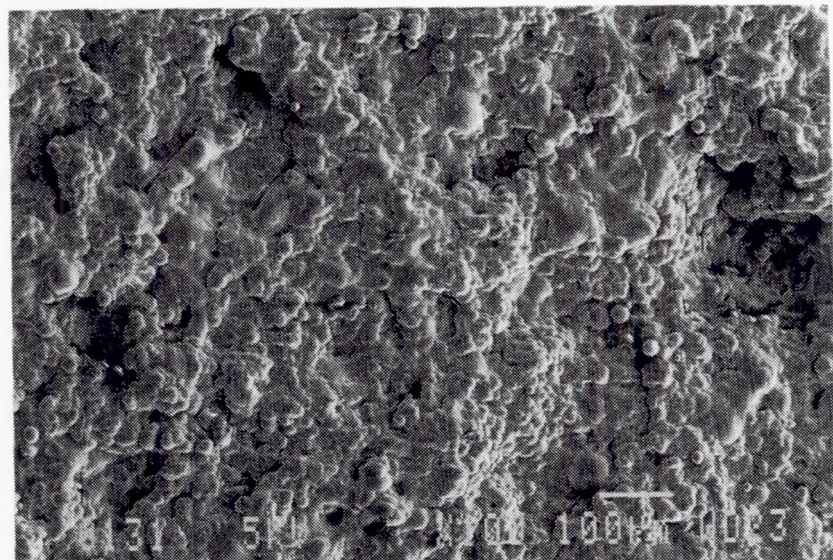
HEAT TREATED AT 1223K



THERMALLY CYCLED 1773K

Figure 126 *YAG:Tb Electron Beam Deposited on Zirconia After Heat Treating and After Thermal Testing*

SCANNING ELECTRON MICROSCOPY – 100X



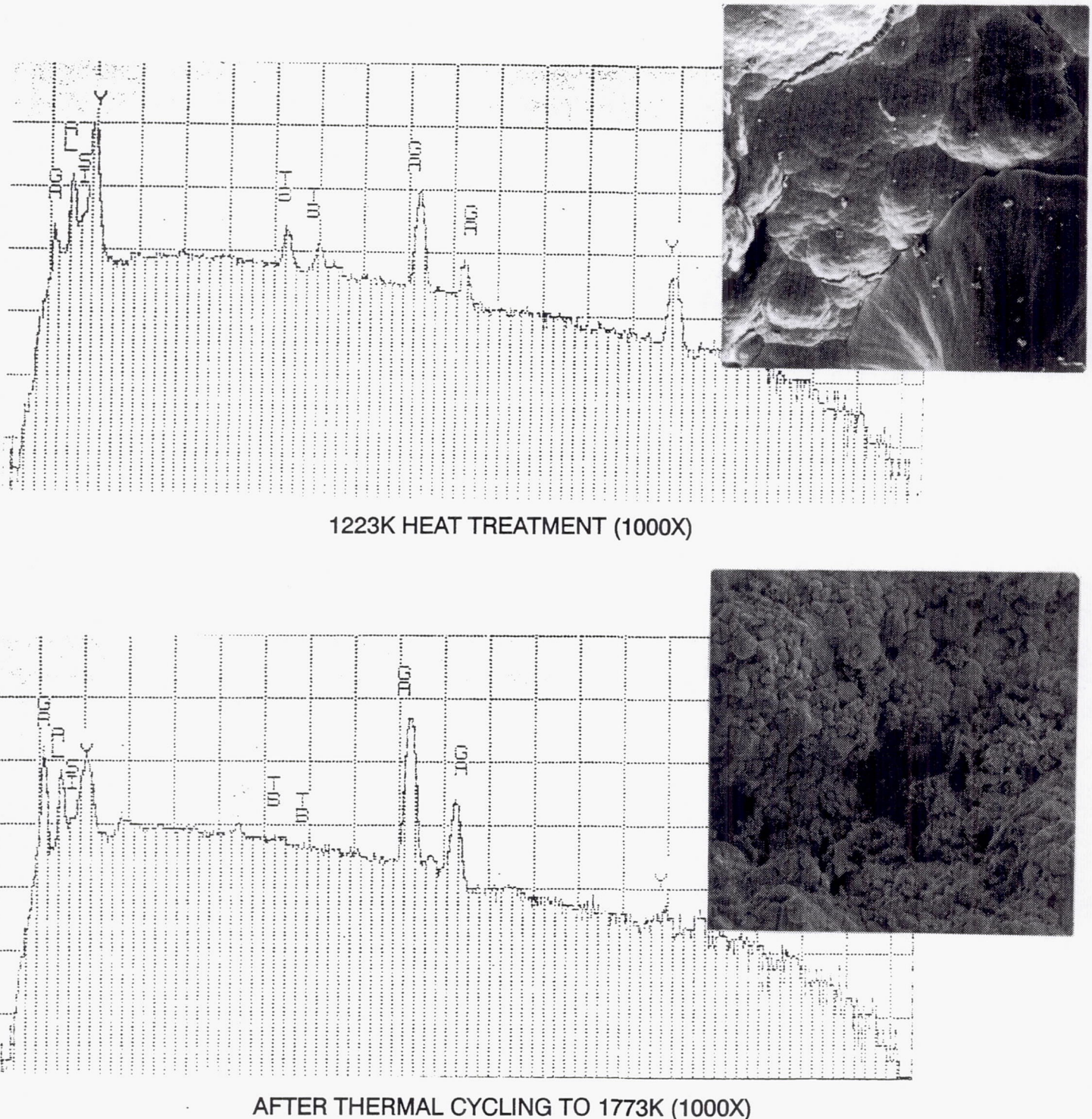
1223K HEAT TREATMENT



AFTER THERMALLY CYCLING TO 1773K

Changes may be seen in the coating surface texture

Figure 127 SEM Analysis of YAG:Tb Electron Beam Deposited on 7% Yttria Stabilized Zirconia



Reduction in surface Tb as well as traces of Cr are seen after thermal cycling

Figure 128 EDS Analysis of YAG:Tb Electron Beam Deposited on 7% Yttria Stabilized Zirconia

ESCA SURVEY 6/26/90 ANGLE= 45 deg ACQ TIME=28.02 min
FILE: 90.030.7 Zirconium; YAG Tb HT 950C
SCALE FACTOR, OFFSET: SCAN 1= 29.218, 14.770 k c/s PASS ENERGY=178.950 eV
SCAN 2= 7.304, 3.692 k c/s Al 400 W

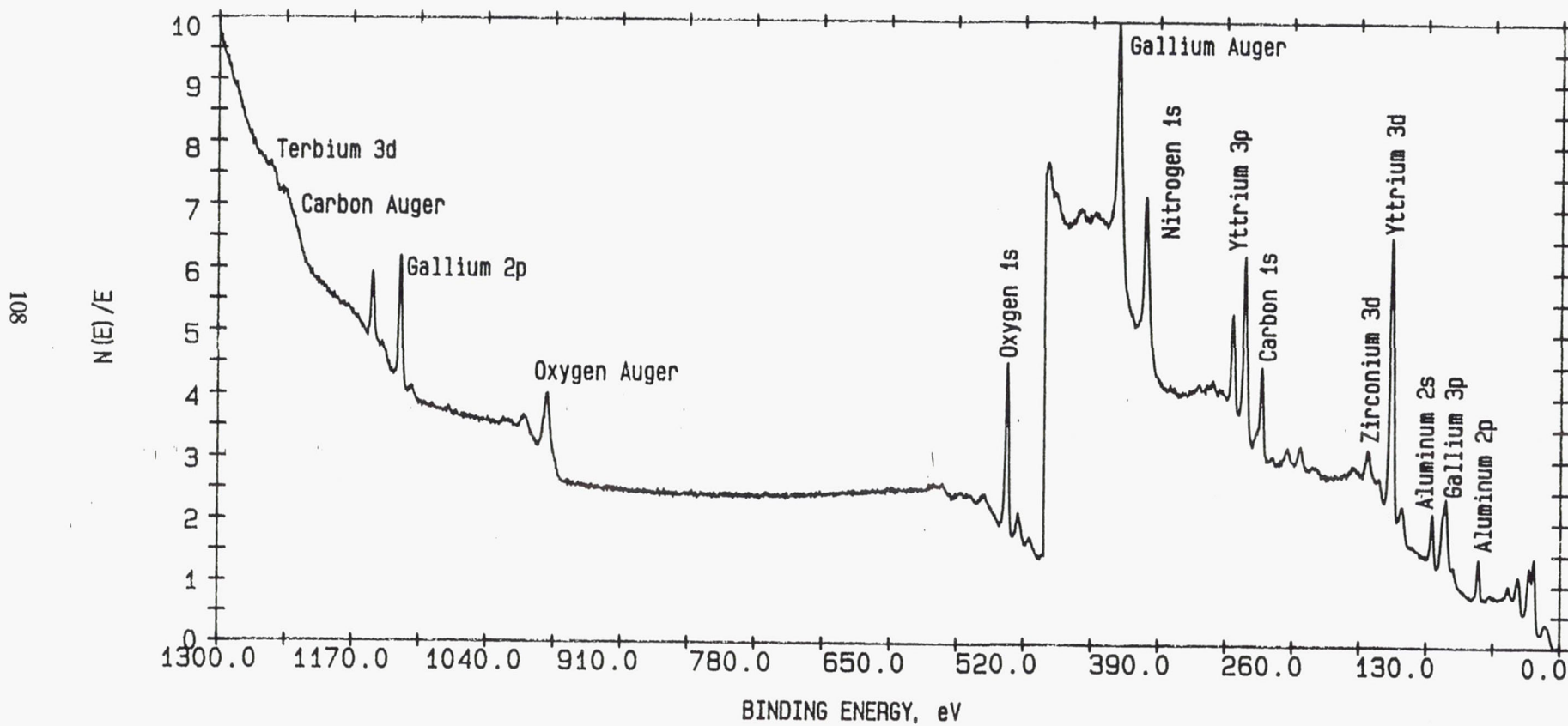


Figure 129 XPS Surface Analysis of YAG:Tb Electron Beam Deposited on 7% Yttria Stabilized Zirconia

ESCA SURVEY 6/25/90 ANGLE= 45 deg ACQ TIME=28.02 min
FILE: 90.030.5 Zirconium; YAG Tb 1500C
SCALE FACTOR, OFFSET: SCAN 1= 34.310, 13.590 k c/s PASS ENERGY=178.950 eV
SCAN 2= 8.578, 3.397 k c/s Al 400 W

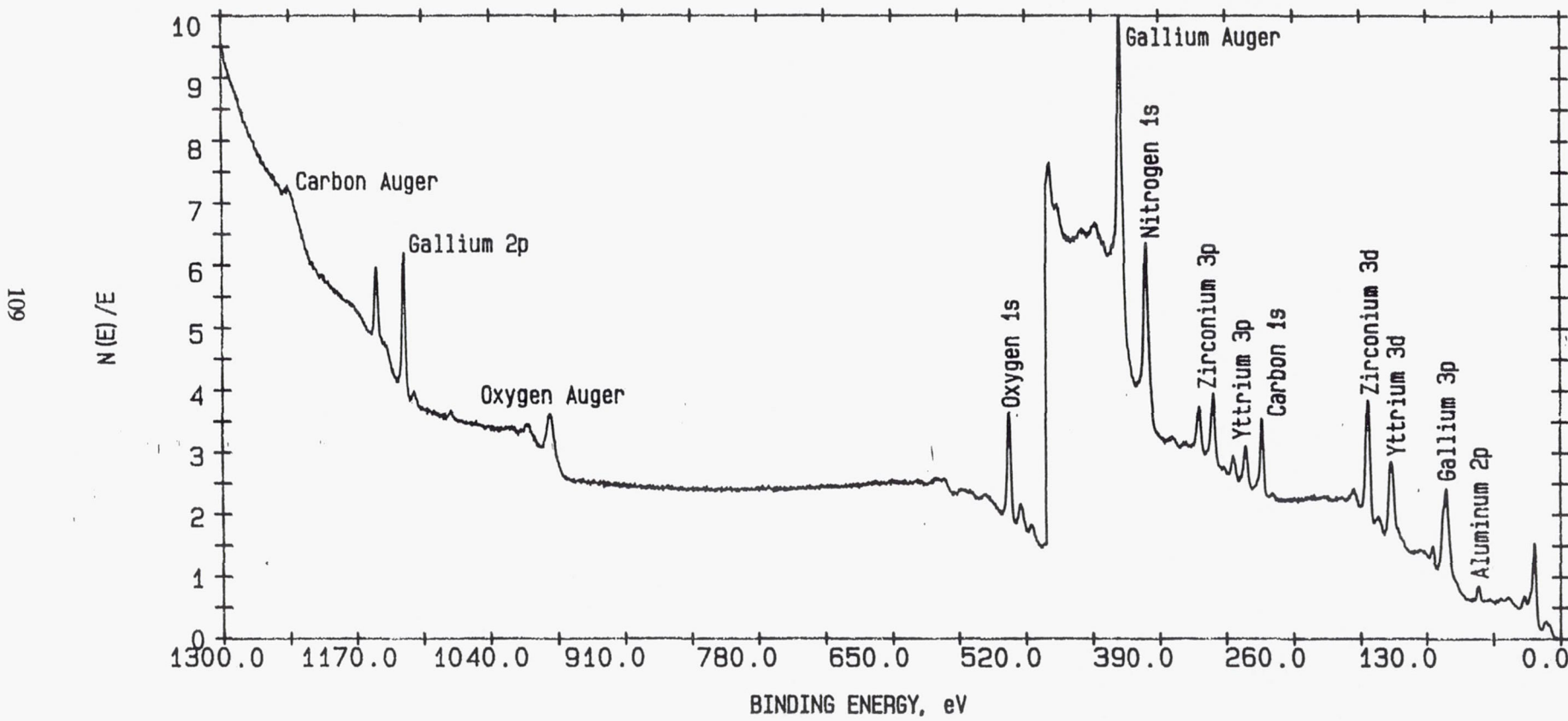
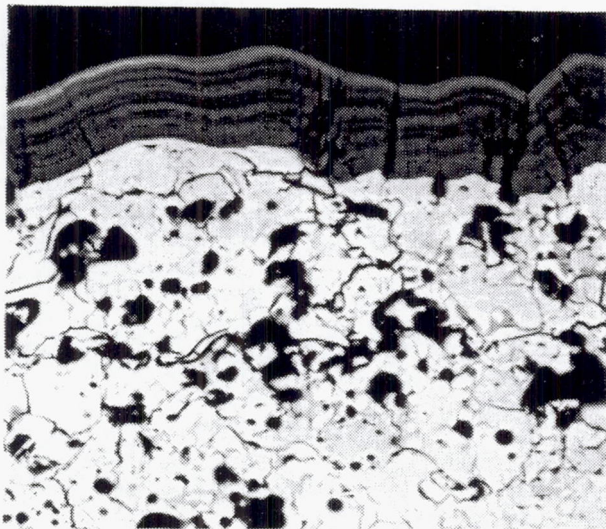
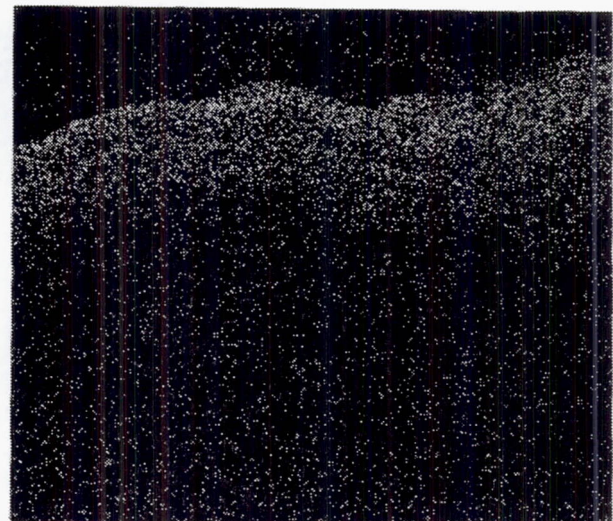


Figure 130 XPS Surface Analysis of YAG:Tb Electron Beam Deposited on 7% Yttria Stabilized Zirconia After Thermal Testing

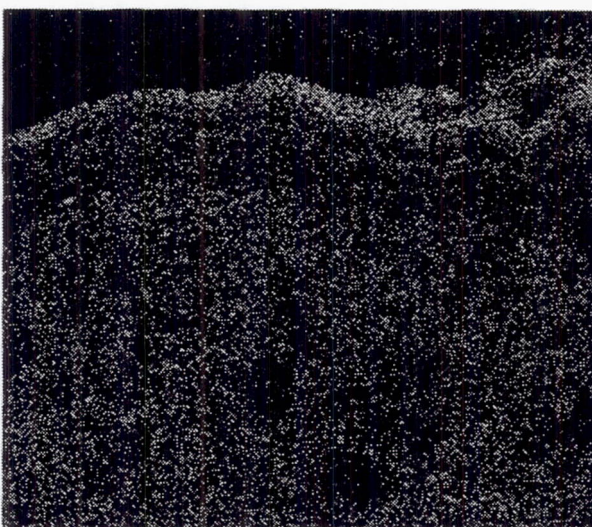
ELECTRON MICROPROBE SCANNING IMAGES – 600X



BACKSCATTERED ELECTRON



Tb L α



Y L α

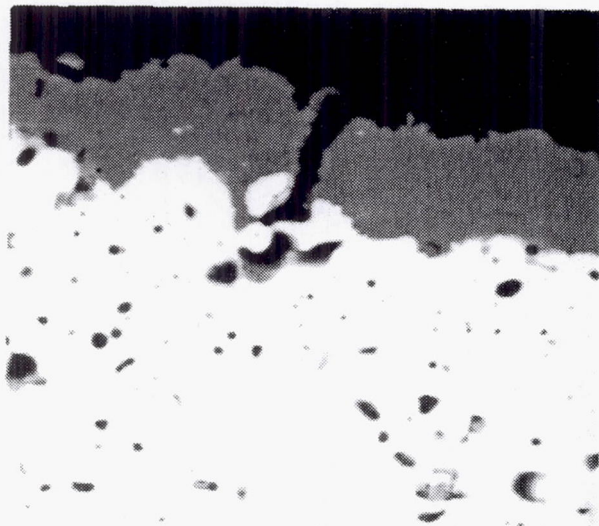


Ga K α

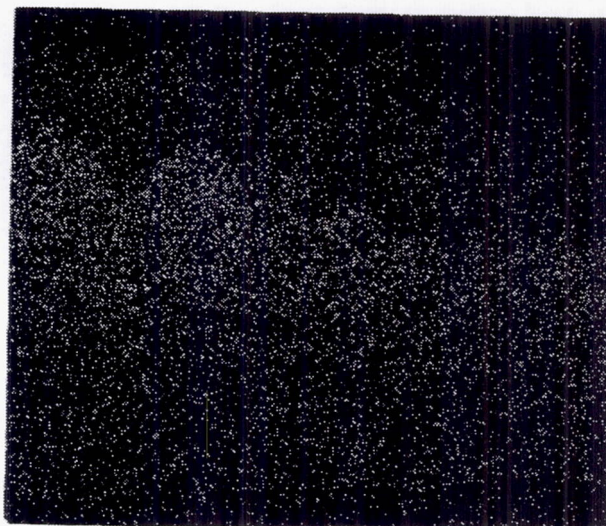
The layered surface typical of electron deposition is seen

Figure 131 Electron Microprobe Scanning Image of YAG:Tb/Zirconia Interface of YAG:Tb Deposited on 7% Yttria Stabilized Zirconia After Heat Treat

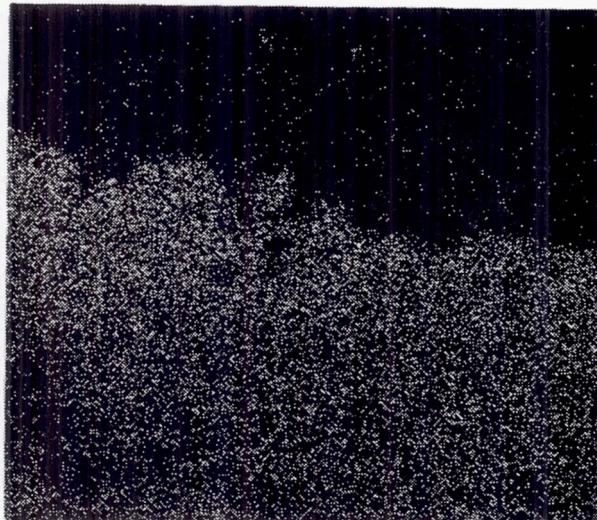
ELECTRON MICROPROBE SCANNING IMAGES - 860X



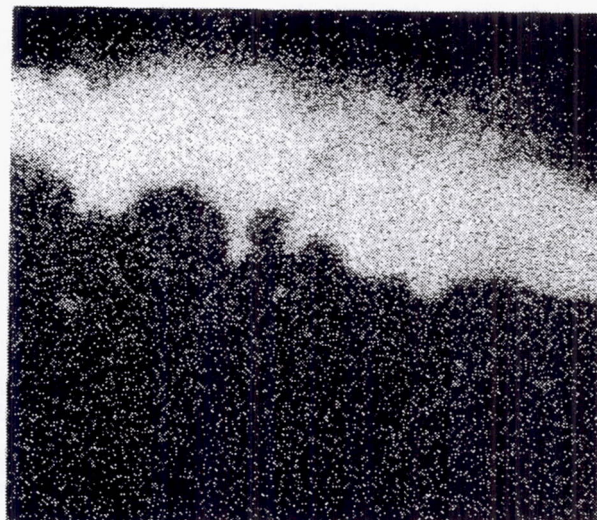
BACKSCATTERED ELECTRON



Tb L α



Y L α



Ga K α

Coating-substrate diffusion has occurred

Figure 132 Electron Microprobe Scanning Image of YAG:Tb/Zirconia Interface of YAG:Tb Deposited on 7% Yttria Stabilized Zirconia After Thermal Testing

5.7 Conclusions

Although the phosphor intensities or signal levels decreased by an order of magnitude after thermal testing, they still remained at a level adequate to perform thermal diagnostics. This method has been proven as feasible for the ceramic materials for high-temperature applications. $\text{Y}_2\text{O}_3:\text{Eu}$ is a potential thermometry agent up to 1573K and YAG:Tb to 1773K. More testing is required to determine maximum operating time at temperature.

YAG:Tb fluorescence signals, recorded at 1773K for the zirconia samples, retained strength for a longer duration than the other substrates. Major changes were seen when YAG:Tb samples were held at 1773K for extended periods. This may be more diffusion of substrate or phosphor constituents than failure of the phosphor itself.

5.8 Recommendations

More work is required to evaluate the applicability of thermographic phosphor systems for high-temperature ceramic thermometry as indicated by these preliminary measurements. Evaluation of alternative systems and coating techniques may prove valuable in identifying the optimal system. A repeatable and reliable technique to allow for consistent temperature monitoring is a high priority in future studies.

Phosphor life expectancy at a given temperature needs to be further investigated. The adherence of the phosphor to the substrate material is another issue of concern. A next step to improve phosphor/substrate systems should include the following. A diffusion barrier should be used to prevent diffusion of components of the substrate into the phosphor as well as the phosphor components into the substrate. A reverse sputtering step during cleaning and preparation of the sample should improve adherence. Optimization of deposition parameters for various substrates would maximize coating durability and fluorescence intensity. The substrate surface and interface regions should be evaluated for contamination. This can alter both fluorescence and adherence characteristics. Surface analysis of substrate and coating surfaces could offer valuable information for describing and monitoring process steps.

Improved instrumentation will allow for resolution of faster decay rates than were observed in this study. The use of a higher-temperature furnace for future studies will allow for the upper temperature limit for phosphor use to be found. Research is needed to qualify new candidate phosphors for applications above 1773K. Included would be theoretical considerations of phosphor fluorescence mechanisms as well as calibration of materials. Variation of the concentration of the phosphor dopant levels may be another method of optimizing the fluorescence signal by reducing background quenching effects. Determining the effect of surface depletion of phosphor components on signal level performance may be accomplished by correlating the elemental distribution of the phosphor constituents with coating performance.

Finally, work must be performed to refine and standardize the data acquisition and reduction techniques. Different methods may also be developed, such as a two-color spectral ratioing approach which can be used for an imaging system.

APPENDIX A

TABULAR DATA FROM THE THIN-FILM THERMOCOUPLE TESTING

PLATINUM VERSUS RHODIUM THERMOCOUPLE
EMF Book Values

TEMPERATURE C	TEMPERATURE K	EMF MILLIVOLTS
50	323	0.314
100	373	0.696
150	423	1.127
200	473	1.608
250	523	2.128
300	573	2.687
350	623	3.282
400	673	3.918
450	723	4.580
500	773	5.281
550	823	6.010
600	873	6.772
650	923	7.568
700	973	8.398
750	1023	9.262
800	1073	10.108
850	1123	11.083
900	1173	12.033
950	1223	13.034
1000	1273	14.050
1050	1323	15.106
1100	1373	16.181
1150	1423	17.292
1200	1473	18.423

PLATINUM/RHODIUM WIRE THERMOCOUPLE DATA

TEMPERATURE K	EMF MILLIVOLTS	TIME MINUTES
295	0.114	0
295	0.112	2.01
295	0.111	4.01
295	0.110	6.02
347	0.455	7.43
398	0.849	8.57
448	1.296	9.76
500	1.804	11.00
550	2.339	12.24
598	2.900	13.48
649	3.529	14.81
699	4.167	16.11
749	4.849	17.46
799	5.564	18.83
849	6.295	20.18
898	7.063	21.57
949	7.876	23.00
923	7.483	25.01
902	7.146	25.64
852	6.368	27.08
802	5.632	28.48
751	4.911	29.89
701	4.230	31.27
651	3.586	32.64
602	2.982	33.97
552	2.400	35.37
502	1.867	36.94
454	1.388	38.95
418	1.059	40.95
402	0.918	42.09
379	0.726	44.10
361	0.586	46.10
348	0.481	48.10
337	0.402	50.11
328	0.341	52.12
322	0.294	54.13
317	0.258	56.14
312	0.228	58.15

SENSOR SCC-C1
 Ion Beam Deposited Sensor on Compglas
 Three Cycles

First Cycle			Second Cycle			Third Cycle		
TEMP K	EMF MV	TIME MIN	TEMP K	EMF MV	TIME MIN	TEMP K	EMF MV	TIME MIN
297	0.127	0	294	0.103	0			
297	0.126	0.10	294	0.104	0.12			
297	0.126	2.10	294	0.100	2.12			
297	0.125	4.10	294	0.101	4.12			
296	0.123	6.11	294	0.100	6.13			
296	0.123	8.11	345	0.032	7.79			
296	0.121	10.12	396	-0.009	9.79			
296	0.121	12.12	447	0.002	11.80			
345	0.060	13.45	493	0.064	13.81			
390	0.03	15.45	505	0.089	14.37			
436	0.039	17.46	546	0.208	16.37			
448	0.049	18.02	586	0.353	18.38			
487	0.105	20.02	597	0.402	19.00			
497	0.125	20.53	633	0.572	21.00			
533	0.221	22.53	647	0.645	21.78			
548	0.271	23.42	682	0.841	23.79			
582	0.397	25.42	698	0.931	24.65			
598	0.464	26.38	731	1.151	26.66			
630	0.615	28.39	747	1.258	27.59			
648	0.713	29.57	780	1.498	29.59			
622	0.789	31.58	797	1.633	30.64			
603	0.794	32.70	829	1.919	32.65			
569	0.765	34.71	848	2.097	33.78			
553	0.739	35.66	879	2.433	35.79			
519	0.678	37.67	898	2.629	36.92			
504	0.648	38.59	927	2.983	38.92			
468	0.582	40.60	928	3.232	40.93			
453	0.557	41.42	904	3.192	42.43			
418	0.501	43.43	871	3.041	44.43			
404	0.479	44.34	853	2.938	45.49			
379	0.431	46.35	823	2.732	47.50			
359	0.387	48.35	802	2.600	48.66			
345	0.346	50.36	770	2.378	50.66			
334	0.310	52.36	752	2.258	51.74			
325	0.28	54.37	719	2.041	53.75			
319	0.255	56.38	703	1.942	54.68			
313	0.233	58.39	669	1.738	56.69			
309	0.213	60.40	653	1.650	57.58			
306	0.197	62.41	617	1.458	59.59			
303	0.183	64.41	603	1.387	60.38			
301	0.173	66.42	567	1.216	62.39			
299	0.161	68.43	554	1.161	63.05			
298	0.153	70.44	516	1.005	65.05			
297	0.145	72.44	503	0.959	65.69			
296	0.138	74.45	463	0.826	67.69			
295	0.133	76.46	452	0.793	68.23			
294	0.127	78.47	416	0.688	70.24			
294	0.123	80.48	404	0.653	71.00			
293	0.119	82.48	379	0.571	73.01			
293	0.115	84.49	360	0.499	75.02			
293	0.112	86.50	346	0.438	77.03			
292	0.109	88.50	335	0.383	79.03			
292	0.106	90.51	326	0.338	81.04			
292	0.104	92.52	320	0.303	83.05			
292	0.102	94.52	314	0.270	85.05			
291	0.100	96.53	310	0.252	87.06			
			307	0.218	89.07			
			304	0.199	91.08			
			302	0.193	93.09			
			300	0.182	95.10			
			298	0.158	97.10			
			297	0.151	99.11			
			296	0.156	101.20			
			295	0.131	103.20			

SENSOR SCC-S1

Ion Beam Deposited Sensor on Silicon Nitride

Three Cycles

First Cycle			Second Cycle			Third Cycle		
TEMP K	EMF MV	TIME MIN	TEMP K	EMF MV	TIME MIN	TEMP K	EMF MV	TIME MIN
294	0.109	0	324	0.242	0	293	0.104	0
294	0.107	2.00	313	0.229	2.00	293	0.101	2.00
293	0.104	4.01	306	0.210	4.01	293	0.099	4.01
312	0.101	6.02	302	0.189	6.02	303	0.094	6.01
346	0.126	8.03	299	0.170	8.02	335	0.104	8.02
389	0.193	10.03	297	0.153	10.03	348	0.116	8.78
400	0.218	10.62	295	0.141	0.00	382	0.171	10.79
444	0.330	12.62	296	0.137	0.55	398	0.203	11.67
489	0.473	14.62	295	0.126	2.56	435	0.298	13.68
499	0.509	15.07	295	0.118	4.57	449	0.339	14.41
545	0.689	17.07	313	0.109	6.57	488	0.470	16.42
591	0.910	19.07	345	0.126	8.58	500	0.512	17.00
596	1.076	21.07	386	0.184	10.59	540	0.668	19.01
565	1.087	23.07	398	0.210	11.23	550	0.725	19.54
553	1.072	23.77	442	0.317	13.23	572	0.885	21.54
515	0.997	25.78	487	0.459	15.23	578	0.994	23.55
503	0.966	26.45	500	0.506	15.79	580	1.066	25.55
465	0.861	28.45	546	0.696	17.80	581	1.114	27.56
452	0.822	29.16	591	0.919	19.81	582	1.148	29.56
419	0.714	31.17	600	0.965	20.19	582	1.170	31.57
403	0.654	32.39	588	1.079	22.20	582	1.187	33.58
380	0.563	34.39	555	1.069	24.21	582	1.198	35.59
362	0.485	36.39	518	0.100	26.22	582	1.207	37.60
351	0.432	37.95	503	0.960	27.08	583	1.213	39.60
337	0.379	39.95	465	0.857	29.09	583	1.217	41.61
323	0.337	41.95	453	0.822	29.76	583	1.222	43.61
315	0.295	43.95	420	0.714	31.77	582	1.224	45.62
309	0.257	45.95	402	0.648	33.09	583	1.227	47.62
304	0.226	47.96	379	0.558	35.09	583	1.230	49.63
302	0.199	49.96	361	0.481	37.09	583	1.231	51.63
302	0.177	51.97	348	0.415	39.09	583	1.233	53.64
300	0.162	53.97	329	0.369	41.09	583	1.233	55.64
299	0.149	55.98	328	0.368	41.16	583	1.234	57.65
297	0.139	57.99	318	0.322	43.17	583	1.235	59.65
			312	0.277	45.18	583	1.235	61.66
			307	0.241	47.19	583	1.237	63.66
			303	0.211	49.19	583	1.238	65.67
			302	0.187	51.20	583	1.238	67.67
			301	0.169	53.20	591	1.254	69.68
			299	0.156	55.21	622	1.345	71.68
			298	0.144	57.21	648	1.455	73.15
			297	0.135	59.22	686	1.661	75.16
			296	0.127	61.22	698	1.739	75.80
			295	0.120	63.23	736	2.015	77.81
			294	0.115	65.24	749	2.118	78.50
			293	0.109	67.24	770	2.370	80.50
			293	0.105	69.25	772	2.491	82.51
			292	0.101	71.26	772	2.557	84.51
			292	0.099	73.26	772	2.599	86.52
			292	0.098	73.33	772	2.625	88.53
			292	0.096	75.33	772	2.642	90.54
			291	0.093	77.34	772	2.653	92.55
						772	2.662	94.55
						772	2.669	95.56
						772	2.674	98.57
						772	2.678	100.60
						772	2.680	102.60
						772	2.683	104.60
						772	2.685	106.60
						772	2.689	108.60
						772	2.689	110.60
						772	2.691	112.60
						772	2.691	114.60
						778	2.720	116.60

SENSOR SCC-S1
 Ion Beam Deposited Sensor on Silicon Nitride
 Three Cycles

Third Cycle (Continued)			Third Cycle (Continued)		
TEMP K	EMF MV	TIME MIN	TEMP K	EMF MV	TIME MIN
799	2.840	117.90	552	1.361	238.30
833	3.110	119.90	517	1.212	240.40
849	3.252	120.70	503	1.151	241.20
885	3.646	122.80	467	1.000	243.20
899	3.826	123.60	453	0.939	244.00
919	4.193	125.70	422	0.806	246.00
920	4.331	127.70	402	0.716	247.50
920	4.410	129.70			
920	4.455	131.70			
920	4.487	133.70			
920	4.510	135.70			
920	4.528	137.70			
920	4.542	139.70			
920	4.553	141.70			
920	4.564	143.70			
920	4.572	145.70			
920	4.580	147.70			
920	4.587	149.70			
920	4.592	151.70			
920	4.597	153.70			
912	4.540	155.70			
902	4.458	156.40			
874	4.190	158.40			
851	3.963	159.90			
822	3.666	162.00			
801	3.462	163.40			
776	3.199	165.40			
772	3.088	167.40			
772	3.032	169.40			
772	2.999	171.40			
772	2.979	173.40			
772	2.967	175.40			
772	2.958	177.40			
772	2.953	179.40			
772	2.948	181.40			
772	2.945	183.40			
772	2.943	185.40			
772	2.940	187.40			
772	2.938	189.40			
772	2.937	191.40			
772	2.937	193.40			
767	2.914	195.40			
751	2.820	196.50			
720	2.607	198.60			
702	2.482	199.70			
670	2.257	201.70			
652	2.129	202.80			
620	1.195	204.80			
608	1.773	206.80			
604	1.695	208.80			
603	1.647	210.80			
602	1.616	212.80			
602	1.595	214.80			
602	1.580	216.80			
602	1.570	218.80			
602	1.563	220.80			
602	1.558	222.80			
602	1.554	224.80			
602	1.551	226.80			
602	1.548	228.80			
602	1.546	230.80			
602	1.544	232.80			
602	1.543	234.80			
579	1.467	236.80			

SENSOR SCC-S2
 Ion Beam Deposited on Silicon Nitride
 One Cycle

First Cycle

TEMP K	EMF MV	TIME MIN
313	0.097	0
316	0.101	1.01
316	0.108	2.01
314	0.114	3.02
312	0.119	4.03
310	0.122	5.03
308	0.123	6.04
307	0.125	7.04
325	0.125	8.05
343	0.134	9.05
359	0.150	10.06
376	0.174	11.07
392	0.205	12.07
413	0.244	13.08
414	0.248	13.15
431	0.291	14.16
448	0.340	15.16
464	0.396	16.16
482	0.455	17.17
492	0.514	18.18
495	0.564	19.18
484	0.597	20.19
466	0.609	21.20
464	0.609	21.28
453	0.607	21.90
435	0.595	22.90
434	0.593	22.97
418	0.572	23.98
404	0.546	24.99
391	0.517	26.00
380	0.487	27.01
369	0.458	28.02
354	0.432	28.78
334	0.394	29.79
321	0.356	30.80
312	0.319	31.81
310	0.288	32.82
309	0.261	33.83
309	0.241	34.84
308	0.224	35.84
306	0.209	36.85
305	0.197	37.86
304	0.185	38.87
302	0.176	39.88
301	0.167	40.89
300	0.160	41.90
299	0.153	42.90
299	0.147	43.91
298	0.141	44.91
298	0.137	45.92
297	0.132	46.93
297	0.128	47.93
296	0.125	48.94
296	0.121	49.95
295	0.118	50.96
295	0.116	51.97
294	0.113	52.98
295	0.112	53.99
294	0.110	54.99
294	0.107	56.00
294	0.106	57.01

First Cycle (Continued)

TEMP K	EMF MV	TIME MIN
294	0.105	58.02
294	0.103	59.03
293	0.102	60.03
293	0.101	61.04
293	0.100	62.05
293	0.099	63.06
293	0.097	64.07
293	0.097	65.07
293	0.097	66.08
293	0.096	67.09
293	0.096	68.10
293	0.095	69.11
292	0.094	70.12
293	0.094	71.13
292	0.093	72.14
292	0.094	73.15
292	0.093	74.16
292	0.093	75.17
292	0.092	76.17
292	0.093	77.18
292	0.091	78.18
292	0.091	79.19
292	0.091	80.20
292	0.090	81.21
292	0.090	82.22
292	0.090	83.23
292	0.090	84.24
292	0.090	85.24
292	0.090	86.25
292	0.090	87.25
292	0.090	88.26
292	0.089	89.27
292	0.089	90.28
292	0.090	91.29
292	0.090	92.30
292	0.090	93.31
292	0.090	94.32
292	0.089	95.33
292	0.090	96.33
292	0.089	97.34
292	0.089	98.34
292	0.089	99.35
292	0.088	100.40
292	0.087	101.40
292	0.087	102.40
292	0.087	103.40
292	0.087	104.40
292	0.087	105.40
292	0.087	106.40
292	0.086	107.40
292	0.086	108.40
292	0.086	109.40
292	0.087	110.40
292	0.086	111.40
292	0.086	112.40
292	0.087	113.40
292	0.086	114.40
292	0.087	115.40
292	0.087	116.40
292	0.087	117.40
292	0.088	118.40
292	0.088	119.40

SENSOR SCC-S3
 Ion Beam Deposited Sensor on Silicon Nitride
 One Cycle

First Cycle			First Cycle (Continued)		
TEMP K	EMF MV	TIME MIN	TEMP K	EMF MV	TIME MIN
292	0.096	0	668	2.251	57.43
292	0.094	1.01	653	2.140	58.30
292	0.092	2.01	636	2.017	59.30
292	0.091	3.02	618	1.898	60.31
291	0.09	4.03	604	1.801	61.17
291	0.089	5.03	586	1.690	62.17
291	0.087	6.04	569	1.584	63.18
290	0.086	7.04	567	1.574	63.25
290	0.085	8.05	553	1.490	64.12
306	0.082	9.05	536	1.574	65.12
323	0.085	10.06	519	1.297	66.13
340	0.096	11.07	504	1.221	66.98
358	0.115	12.07	486	1.135	67.99
376	0.142	13.08	469	1.052	69.00
394	0.178	14.09	454	0.980	69.92
413	0.219	15.10	438	0.906	70.93
432	0.269	16.11	423	0.836	71.93
447	0.311	16.88	409	0.770	72.94
467	0.371	17.88	399	0.722	73.74
487	0.440	18.89	388	0.666	74.75
499	0.486	19.52	379	0.615	75.75
519	0.564	20.53	378	0.611	75.83
539	0.651	21.54	369	0.566	76.83
549	0.695	22.02	361	0.524	77.84
569	0.795	23.03	355	0.485	78.85
589	0.902	24.03	348	0.450	79.86
598	0.955	24.49			
617	1.075	25.50			
638	1.021	26.51			
648	1.279	27.07			
667	1.420	28.08			
687	1.571	29.09			
698	1.658	29.66			
717	1.819	30.66			
736	1.985	31.67			
748	2.105	32.37			
767	2.285	33.38			
785	2.473	34.39			
799	2.618	35.13			
800	2.636	35.20			
802	2.655	35.30			
819	2.861	36.31			
838	3.071	37.31			
847	3.187	37.84			
865	3.413	38.84			
883	3.648	39.85			
898	3.868	40.77			
915	4.118	41.78			
911	4.218	42.79			
902	4.196	43.39			
887	4.110	44.39			
871	3.994	45.40			
854	3.855	46.41			
837	3.708	47.41			
820	3.556	48.42			
803	3.402	49.43			
786	3.246	50.44			
769	3.093	51.45			
768	3.080	51.52			
752	2.938	52.49			
735	2.789	53.50			
718	2.647	54.50			
702	2.519	55.42			
685	2.384	56.43			

SENSOR SCC-S4
Ion Beam Deposited on Silicon Nitride
One Cycle

First Cycle

TEMP K	EMF MV	TIME MIN
295	0.112	0
295	0.112	0.68
295	0.109	5.68
347	0.131	8.95
349	0.132	9.02
351	0.133	9.12
397	0.212	11.70
398	0.216	11.77
399	0.220	11.87
449	0.341	14.41
499	0.498	16.93
550	0.696	19.52
599	0.934	22.02
649	1.254	24.76
699	1.631	27.44
749	2.067	30.14
799	2.553	32.79
849	3.111	35.50
899	3.741	38.31
867	3.855	43.31
852	3.735	44.24
802	3.315	47.20
751	2.881	50.22
702	2.487	53.11
653	2.128	55.98
602	1.798	58.89
553	1.505	61.80
502	1.243	64.70

SENSOR SCC-S5
Ion Beam Deposited Sensor on Silicon Nitride
Two Cycles

First Cycle			Second Cycle		
TEMP K	EMF MV	TIME MIN	TEMP K	EMF MV	TIME MIN
285	-0.050	0			
285	-0.050	2.01			
302	-0.053	2.84			
348	-0.051	4.20			
401	-0.020	5.64			
452	0.084	6.95			
502	0.181	8.18			
552	0.334	9.34			
601	0.608	10.40			
652	0.869	11.45			
701	0.854	12.45			
752	1.473	13.50			
801	1.923	14.53			
804	0.809	16.55			
750	1.033	18.11			
700	1.025	19.43			
649	0.804	20.77			
601	0.573	22.09			
551	0.418	23.52			
503	0.343	25.19			
458	0.297	27.21			
423	0.236	29.23			
353	0.214	30.96			
324	0.193	32.98			
309	0.146	35.00			
300	0.109	37.02			
297	0.078	39.04			
294	0.053	41.05			
292	0.037	43.07			
292	0.021	45.09			
293	0.006	47.11			

SENSOR IIE-C1
 Ion Implanted Sensor on Compglas
 Three cycles

First Cycle			Second Cycle			Second Cycle (Continued)		
TEMP K	EMF MV	TIME MIN	TEMP K	EMF MV	TIME MIN	TEMP K	EMF MV	TIME MIN
297	0.116	0	292	0.094	0	294	0.111	481.50
297	0.116	0.11	292	0.094	10.00	294	0.102	482.30
293	0.100	10.12	292	0.094	20.01	293	0.112	492.30
292	0.094	20.13	306	0.139	30.02	292	0.041	502.30
292	0.114	30.14	362	0.402	39.25	292	0.116	512.30
307	0.116	35.41	415	0.709	49.26	292	0.077	522.30
307	0.115	35.51	419	0.732	50.03	292	-0.032	532.30
362	0.270	44.84	465	1.048	60.03			
410	0.462	54.85	475	1.121	62.30			
418	0.499	56.68	518	1.431	72.31			
459	0.693	66.69	531	1.527	75.22			
476	0.778	70.92	572	1.820	85.23			
511	0.951	80.93	585	1.911	88.52			
530	1.045	85.77	623	2.152	98.52			
564	1.236	95.78	641	2.263	102.80			
586	1.368	102.30	679	2.486	112.80			
616	1.569	112.30	697	2.590	117.40			
641	1.730	119.80	733	2.820	127.40			
671	1.944	129.90	753	2.939	132.40			
696	2.116	137.60	788	3.173	142.50			
724	2.324	147.60	808	3.302	147.50			
752	2.520	156.70	842	3.568	157.50			
781	2.730	166.70	864	3.742	163.30			
807	2.931	176.00	899	4.044	173.40			
837	3.171	186.00	919	4.230	178.40			
863	3.400	194.70	952	4.636	188.40			
891	3.687	204.80	977	4.983	195.20			
920	4.005	214.70	1010	5.571	205.20			
947	4.372	224.70	1032	5.902	211.10			
925	4.310	234.10	1064	6.430	221.20			
897	4.077	244.10	1087	6.567	227.10			
870	3.851	253.80	1115	6.588	235.50			
842	3.632	263.80	1114	6.777	245.50			
814	3.443	272.70	1091	6.339	252.30			
785	3.250	282.80	1058	5.696	262.40			
759	3.077	292.10	1035	5.256	268.30			
729	2.896	302.20	1003	4.614	278.40			
703	2.737	310.70	980	4.332	284.30			
674	2.559	320.70	948	3.900	294.30			
648	2.395	329.10	925	3.650	300.20			
617	2.193	339.20	892	3.308	310.30			
592	2.036	346.60	869	3.137	316.10			
559	1.802	356.70	833	2.881	326.20			
536	1.630	363.60	814	2.753	331.30			
503	1.378	373.60	779	2.540	341.40			
481	1.224	379.30	759	2.449	346.40			
442	0.954	389.40	725	2.273	356.40			
426	0.848	393.50	701	2.166	362.20			
383	0.584	403.50	665	2.000	372.20			
370	0.511	406.40	647	1.921	376.30			
325	0.280	416.50	610	1.751	386.40			
315	0.225	420.10	592	1.653	390.50			
304	0.167	426.20	554	1.458	400.60			
296	0.124	436.20	536	1.374	404.70			
293	0.106	446.20	495	1.171	414.80			
292	0.096	456.20	481	1.121	417.80			
292	0.092	466.20	438	0.916	427.90			
292	0.091	476.20	426	0.847	430.60			
			377	0.573	440.60			
			369	0.523	442.20			
			323	0.264	452.30			
			315	0.239	455.00			
			304	0.140	461.40			
			296	0.015	471.50			

SENSOR IIE-C1
 Ion Implanted Sensor on Compglas
 Three cycles

Third Cycle

TEMP K	EMF MV	TIME MIN
294	0.149	0
295	0.230	0.35
310	0.048	0.79
362	0.239	2.17
419	0.484	4.89
476	0.722	6.34
531	1.007	7.74
591	1.562	9.34
642	1.997	10.83
697	2.381	12.52
755	2.644	14.39
810	2.705	16.27
866	2.850	18.23
921	2.995	20.22
980	3.469	22.38
1033	3.888	24.30
1089	4.675	26.37
1115	5.325	27.36
1090	6.217	30.25
1034	5.518	32.30
979	4.865	34.27
922	4.154	36.33
867	3.563	38.28
814	3.062	40.22
757	2.640	42.20
702	2.301	44.13
646	2.013	46.03
591	1.740	47.90
534	1.475	49.79
480	1.230	51.85
423	0.944	54.82
369	0.641	59.41
338	0.439	64.42
319	0.312	69.43
314	0.296	71.67
305	0.254	76.68
301	0.125	81.69
298	0.210	86.69

SENSOR IIE-C2
 Implanted Sensor On Compglas
 Five Cycles

First Cycle			Second Cycle			Third Cycle		
TEMP K	EMF MV	TIME MIN	TEMP K	EMF MV	TIME MIN	TEMP K	EMF MV	TIME MIN
294	0.104	0	295	0.112	0	294	0.111	0
294	0.103	0.09	295	0.112	0.38	295	0.140	3.75
304	0.120	4.47	309	0.164	4.65	308	0.180	4.60
361	0.253	5.97	364	0.462	6.33	365	0.533	6.77
424	0.434	7.42	421	0.805	7.85	419	0.937	8.37
473	0.602	8.53	698	3.327	0	477	1.432	10.14
525	0.789	9.76	644	2.932	0.95	526	1.816	11.63
578	0.991	11.09	588	2.517	2.19	589	2.248	13.38
638	1.274	12.77	534	2.064	3.73	648	2.601	15.28
689	1.531	14.29	480	1.574	5.73	687	2.804	16.66
743	1.838	16.04	439	1.207	7.74	743	3.066	18.50
799	2.176	17.88	423	1.062	8.75	824	3.439	20.02
865	2.653	20.20	395	0.835	10.76	859	3.761	21.03
914	3.040	21.93	374	0.671	12.77	914	4.193	22.77
969	3.515	23.87	367	0.613	13.64	984	5.014	25.20
1032	4.222	26.17	352	0.504	15.64	1025	5.650	26.59
1077	4.920	27.88	340	0.422	17.65	1085	6.504	28.80
1112	5.611	29.14	331	0.356	19.66	1114	6.995	29.86
1139	6.192	30.16	324	0.306	21.67	1086	6.885	31.68
1120	6.526	31.97	318	0.268	23.68	1042	6.351	33.30
1089	6.281	33.10	313	0.236	25.69	986	5.808	35.22
1032	5.725	35.14	310	0.212	27.70	923	5.104	37.49
989	5.277	36.68	307	0.193	29.71	867	4.533	39.49
932	4.713	38.70	306	0.177	31.72	823	4.125	41.01
876	4.219	40.65	304	0.164	33.73	764	3.653	43.04
815	3.737	42.92	303	0.154	35.74	710	3.275	44.92
764	3.402	44.72	301	0.147	37.74	655	2.912	46.81
710	3.068	46.57	300	0.141	39.75	599	2.546	48.68
641	2.608	48.90	299	0.135	41.76	534	2.020	51.07
594	2.253	50.50	298	0.131	43.77	484	1.588	53.04
536	1.810	52.39	297	0.126	45.77	425	1.073	56.09
479	1.390	54.41	297	0.126	47.78	371	0.631	60.67
423	0.986	57.09	297	0.123	49.79	319	0.288	70.67
370	0.604	61.32	296	0.120	51.80	312	0.242	73.65
335	0.376	66.33	295	0.118	53.81	303	0.176	80.97
317	0.259	71.33	295	0.118	55.81	298	0.159	90.98
302	0.168	76.33	295	0.117	57.81	295	0.160	101.00
297	0.134	81.34	294	0.116	59.82	295	0.134	111.00
296	0.123	86.34						

SENSOR IIE-C2
 Implanted Sensor On Compglas
 Five Cycles

Fourth Cycle

TEMP K	EMF MV	TIME MIN
331	0.331	0
320	0.253	10.00
312	0.204	13.37
300	0.144	21.83
307	0.183	27.68
364	0.551	30.11
417	0.959	31.73
476	1.468	33.48
532	1.902	35.21
586	2.291	36.87
641	2.628	38.64
691	2.880	40.28
748	3.154	42.15
817	3.439	44.42
865	3.722	46.04
915	4.168	47.72
973	4.793	49.74
1030	5.503	51.79
988	4.966	57.43
931	4.343	59.54
872	4.110	61.67
819	3.568	63.64
764	3.186	65.66
701	2.817	67.96
645	2.540	70.08
589	2.272	72.23
534	1.922	74.36
478	1.484	76.54
422	1.022	79.44
366	0.592	84.15
317	0.260	94.15
310	0.216	97.62
301	0.158	106.50
297	0.136	116.50

Fifth Cycle

TEMP K	EMF MV	TIME MIN
294	0.103	0
297	0.149	3.79
307	0.201	4.15
364	0.600	5.79
421	1.031	7.24
477	1.432	8.64
532	1.797	10.08
588	2.140	11.64
644	2.358	13.30
699	2.524	15.04
749	2.572	16.71
806	2.889	18.61
858	3.334	20.39
911	3.545	22.23
976	4.059	24.51
1022	4.443	26.13
1081	4.866	28.23
1109	4.938	29.30
1134	6.443	30.33
1128	6.160	30.64
1099	5.757	31.63
1035	5.356	33.98
985	4.817	35.78
923	4.322	37.94
875	3.958	39.66
814	3.545	41.77
757	3.220	43.78
700	2.949	45.77
645	2.688	47.69
590	2.387	49.54
535	1.979	51.50
479	1.502	53.62
425	1.037	56.33
370	0.600	60.90
318	0.269	70.91
312	0.248	72.82
303	0.185	80.03
297	0.152	90.04
294	0.135	100.10
294	0.163	110.10

SENSOR IIE-S1
 Implanted Sensor on Silicon Nitride
 Eleven Cycles

First Cycle

TEMP K	EMF MV	TIME MIN
295	0.118	0
295	0.117	0.09
352	0.247	5.10
359	0.305	5.63
415	0.575	8.23
480	0.945	10.92
534	1.355	13.35
585	1.834	15.91
560	1.849	20.92
531	1.677	22.30
479	1.312	25.17
425	0.939	28.41
367	0.589	33.24
333	0.396	38.24
314	0.281	43.25
304	0.213	48.26
297	0.174	53.27

Second Cycle

TEMP K	EMF MV	TIME MIN
299	0.108	0
299	0.103	0.12
311	0.119	3.56
360	0.320	6.00
416	0.602	8.59
475	0.971	11.23
534	1.375	13.53
582	1.852	16.06
536	1.688	22.37
476	1.312	25.31
429	0.943	28.50
372	0.586	33.37
311	0.248	45.18
300	0.177	51.97

Third Cycle

TEMP K	EMF MV	TIME MIN
410	0.620	0
368	0.487	4.54
317	0.244	0
307	0.223	1.63
368	0.352	8.89
423	0.649	11.63
480	0.979	13.96
534	1.391	16.36
583	1.870	18.88
534	1.695	25.11
476	1.318	28.02
429	0.948	31.21
368	0.603	36.05
311	0.244	47.69
299	0.180	54.20

SENSOR IIE-S1
 Implanted Sensor on Silicon Nitride
 Eleven Cycles

Fourth Cycle			Fifth Cycle			Sixth Cycle		
TEMP K	EMF MV	TIME MIN	TEMP K	EMF MV	TIME MIN	TEMP K	EMF MV	TIME MIN
293	0.099	0	291	0.089	0	292	0.100	0
293	0.096	5.01	292	0.096	5.01	293	0.100	5.00
297	0.111	9.88	307	0.144	7.43	309	0.163	6.61
363	0.159	10.40	364	0.452	10.49	365	0.488	7.81
419	0.449	14.25	420	0.836	13.34	421	0.898	8.76
294	0.105	0	475	1.272	15.97	477	1.378	9.63
294	0.105	0.70	532	1.784	18.77	536	1.940	10.44
293	0.100	5.70	587	2.336	21.63	589	2.509	11.16
306	0.132	9.52	642	2.932	24.66	644	3.139	12.59
363	0.413	13.11	698	3.582	27.88	700	3.830	13.39
420	0.780	16.73	753	4.273	31.28	759	4.616	14.15
476	1.211	20.22	809	5.022	34.85	812	5.375	14.96
533	1.708	23.85	865	5.802	38.44	865	6.178	15.84
587	2.246	27.68	921	6.653	42.23	977	8.015	16.78
642	2.824	31.68	976	7.521	45.91	1033	9.004	17.74
699	3.481	36.12	1033	8.572	49.93	1090	10.057	18.73
752	4.150	40.52	1087	9.689	53.66	1116	10.587	19.22
808	4.887	45.30	1117	10.332	55.70	1142	11.134	19.89
865	5.677	50.19	1143	10.916	57.60	1130	11.121	24.90
920	6.524	55.19	1123	10.701	62.60	1114	10.825	25.22
962	7.264	60.20	1116	10.617	62.99	1089	10.344	25.70
925	6.765	63.54	1091	10.120	64.91	1032	9.312	26.74
869	5.964	68.52	1034	9.124	68.85	977	8.348	27.75
812	5.180	73.49	980	8.189	72.70	921	7.418	28.76
757	4.463	78.26	923	7.270	76.62	867	6.555	29.74
702	3.770	83.01	868	6.410	80.37	810	5.686	30.77
646	3.125	87.67	812	5.584	84.12	756	4.918	31.75
591	2.524	92.19	756	4.806	87.81	701	4.165	32.79
534	1.960	96.65	701	4.074	91.41	644	3.453	33.94
480	1.475	100.70	645	3.365	95.07	591	2.814	35.26
425	1.031	104.80	591	2.732	98.48	534	2.182	37.05
370	0.622	109.90	535	2.129	101.90	480	1.622	39.36
338	0.407	114.90	480	1.581	105.20	423	1.125	41.10
321	0.290	119.90	424	1.077	108.80	369	0.676	44.02
315	0.249	122.60	370	0.643	113.80			
307	0.198	127.60	340	0.425	118.80			
303	0.165	132.60	324	0.309	123.80			
299	0.143	137.60	314	0.241	128.70			
297	0.128	142.60	304	0.198	133.80			
295	0.118	147.60	301	0.171	138.80			
294	0.110	152.60	299	0.152	143.80			
294	0.105	157.60	297	0.139	148.80			
293	0.101	162.60	296	0.125	153.80			
293	0.098	167.60	295	0.119	158.80			
292	0.096	172.60	295	0.114	163.80			
291	0.093	177.60	294	0.111	168.80			
			294	0.108	173.80			
			294	0.105	178.80			

SENSOR IIE-S1
 Implanted Sensor on Silicon Nitride
 Eleven Cycles

Seventh Cycle			Eighth Cycle			Ninth Cycle		
TEMP K	EMF MV	TIME MIN	TEMP K	EMF MV	TIME MIN	TEMP K	EMF MV	TIME MIN
369	0.676	44.02	334	0.402	87.93	337	0.424	129.20
401	0.840	49.02	364	0.566	89.35	364	0.571	130.30
477	1.462	50.46	422	0.978	90.57	421	0.978	131.50
534	1.995	51.32	477	1.451	91.52	478	1.462	132.50
590	2.592	52.12	535	2.000	92.37	532	1.984	133.30
648	3.265	52.90	590	2.585	93.13	589	2.590	134.10
701	3.930	53.61	645	3.222	93.86	644	3.227	134.80
756	4.662	54.36	701	3.924	94.60	702	3.947	135.60
812	5.456	55.16	810	5.435	96.14	755	4.654	136.30
866	6.272	55.98	865	6.258	96.96	812	5.471	137.10
923	7.175	56.87	922	7.172	97.86	866	6.292	138.00
977	8.098	57.77	979	8.140	98.80	922	7.200	138.90
1034	9.123	58.74	1034	9.163	99.74	977	8.126	139.80
1089	10.246	59.72	1089	10.346	100.70	1033	9.191	140.70
1117	10.836	60.22	1117	10.946	101.20	1090	10.458	141.70
1142	11.380	60.84	1142	11.504	101.90	1117	11.018	142.20
1133	22.279	65.85	1133	11.334	106.90	1142	11.572	142.90
1118	10.996	66.15	1117	11.036	107.20	1133	11.373	147.90
1089	10.438	66.70	1090	10.496	107.70	1117	11.068	148.20
1032	9.385	67.74	1034	9.443	108.70	1089	10.521	148.70
975	8.366	68.79	979	8.460	109.70	1035	9.501	149.70
921	7.459	69.76	923	7.508	110.70	977	8.463	150.70
867	6.573	70.75	866	6.588	111.80	922	7.512	151.70
811	5.721	71.75	812	5.729	112.80	867	6.608	152.70
754	4.897	72.79	755	4.914	113.80	812	5.761	153.70
700	4.164	73.80	701	4.180	114.80	755	4.926	154.80
645	3.463	74.93	645	3.467	115.90	697	4.140	155.80
590	2.800	76.31	590	2.801	117.30	644	3.453	156.90
536	2.200	78.02	535	2.190	119.00	591	2.817	158.30
480	1.626	80.37	480	1.621	121.40	536	2.205	160.00
425	1.179	81.30	424	1.163	122.40	480	1.628	162.30
369	0.706	82.92	369	0.697	124.20	424	1.160	163.40
334	0.402	87.93	338	0.425	129.20	369	0.698	165.30
						339	0.433	170.30

SENSOR IIE-S1
 Implanted Sensor on Silicon Nitride
 Eleven Cycles

Tenth Cycle			Eleventh Cycle		
TEMP K	EMF MV	TIME MIN	TEMP K	EMF MV	TIME MIN
339	0.433	170.30	342	0.450	211.50
366	0.583	171.30	363	0.570	212.20
421	0.980	172.50	476	1.456	214.50
479	1.471	173.50	533	1.998	215.30
536	2.026	174.40	589	2.587	216.10
590	2.604	175.10	644	3.233	216.80
701	3.939	176.60	701	3.948	217.60
756	4.676	177.30	756	4.693	218.40
810	5.452	178.10	810	5.465	219.10
870	6.351	179.00	871	6.380	220.00
922	7.196	179.80	922	7.214	221.80
977	8.159	180.80	978	8.176	222.70
1033	9.219	181.70	1032	9.244	223.70
1089	10.489	182.70	1089	10.538	224.90
1142	11.620	183.90	1142	11.666	229.90
1133	11.404	188.90	1118	11.139	230.20
1117	11.094	189.20	1089	10.559	230.70
1085	10.466	189.80	1035	9.532	231.70
1030	9.436	190.80	977	8.496	232.70
977	8.474	191.70	923	7.555	233.70
921	7.519	192.80	866	6.629	234.80
866	6.605	193.80	811	5.762	235.70
807	5.689	194.80	752	4.894	236.80
756	4.946	195.70	701	4.187	237.80
645	3.474	197.90	644	3.463	238.90
590	2.808	199.30	589	2.795	240.30
535	2.187	201.00	534	2.185	242.00
480	1.624	203.30	479	1.618	244.40
423	1.150	204.50	422	1.136	245.60
369	0.687	206.50	367	0.679	247.60
343	0.450	211.50	341	0.444	252.60
			327	0.328	257.60
			315	0.251	262.60
			308	0.201	267.60
			303	0.149	272.60
			299	0.132	277.60
			297	0.124	282.60
			294	0.100	287.60
			293	0.077	292.60
			292	0.141	297.60
			291	0.152	302.60
			291	0.098	307.60
			290	0.145	312.60
			290	0.182	317.60
			290	0.007	322.60
			290	0.080	327.60
			290	0.085	332.60
			290	-0.054	337.60
			290	0.053	342.60
			290	0.181	347.60
			289	0.033	352.60
			289	-0.005	357.60

SENSOR IIE-S2
Implanted Sensor on Silicon Nitride
Two Cycles

First Cycle			Second Cycle		
TEMP K	EMF MV	TIME MIN	TEMP K	EMF MV	TIME MIN
294	0.107	0	291	0.087	0
294	0.106	0.32	290	0.083	20.00
291	0.089	20.33	295	0.104	27.05
296	0.098	32.36	307	0.168	29.40
306	0.131	34.62	363	0.510	41.24
364	0.404	49.48	419	0.923	53.32
420	0.738	64.49	476	1.401	65.85
475	1.125	80.20	531	1.931	78.71
531	1.565	96.30	587	2.507	91.67
586	2.064	113.50	641	3.122	105.00
642	2.614	131.00	697	3.802	119.20
697	3.237	149.40	752	4.510	133.30
753	3.948	167.90	809	5.272	148.10
809	4.758	187.10	864	6.078	163.30
864	5.681	206.60	920	6.937	178.10
920	6.700	226.40	976	7.899	193.30
920	6.869	246.50	1032	9.001	209.40
869	6.116	264.90	1087	10.125	225.70
812	5.315	284.70	1115	10.658	233.20
757	4.578	303.40	1090	10.255	250.00
702	3.870	322.30	1034	9.258	266.00
646	3.192	341.00	980	8.337	280.60
591	2.571	359.00	924	7.400	297.20
536	2.006	376.40	869	6.543	310.90
480	1.475	393.50	813	5.706	327.30
425	1.008	409.70	757	4.901	342.00
369	0.592	425.70	701	4.153	356.30
314	0.235	442.60	646	3.443	370.30
303	0.166	449.90	591	2.790	384.40
293	0.101	469.90	536	2.167	398.50
290	0.086	489.90	480	1.593	413.00
290	0.081	509.90	425	1.091	425.10
289	0.079	529.90	368	0.625	438.70

SENSOR IIE-S3
 Implanted Sensor on Silicon Nitride
 Five Cycles

First Cycle			Second Cycle			Third Cycle		
TEMP K	EMF MV	TIME MIN	TEMP K	EMF MV	TIME MIN	TEMP K	EMF MV	TIME MIN
295	0.157	0	295	0.505	0	295	0.237	0
295	0.083	0.09	295	0.478	0.14	295	0.416	10.00
640	2.881	0	295	0.007	10.15	294	0.248	20.02
624	2.646	1.01	295	2.046	20.16	295	0.191	30.04
590	2.055	1.99	295	0.412	30.16	302	0.389	40.05
554	1.641	3.00	306	0.302	39.39	310	0.202	41.89
534	1.388	3.62	344	0.548	49.40	349	0.520	51.91
504	1.168	4.62	362	-0.378	54.21	365	0.651	56.16
480	0.995	5.56	400	-0.819	64.22	404	0.724	66.18
457	0.903	6.57	418	3.558	69.09	422	0.225	70.99
437	0.688	7.58	454	4.163	79.09	457	0.483	80.99
424	0.065	8.37	475	2.777	85.10	477	0.602	87.08
409	0.783	9.37	509	0.864	95.11	512	0.771	97.10
395	-0.981	10.38	531	0.675	101.70	533	0.944	104.00
384	-2.217	11.39	562	1.390	111.80	565	1.272	114.00
375	3.691	12.40	585	1.425	119.20	588	1.591	121.50
385	-1.822	13.41	615	2.061	129.30	617	2.170	131.50
398	1.883	14.42	641	2.674	138.00	644	2.876	140.10
400	2.897	15.42	670	3.313	148.00	673	3.622	150.10
403	2.794	16.42	696	4.137	156.90	699	4.398	158.90
405	-1.639	17.43	724	4.996	167.00	727	5.286	169.00
405	2.626	18.44	751	5.956	176.60	755	6.220	178.50
412	-0.318	19.45	778	6.807	186.60	782	7.189	188.60
419	1.853	19.89	806	7.933	196.60	810	8.318	198.30
443	0.332	20.90	808	8.036	197.00	837	9.431	208.30
471	0.640	21.91	834	9.042	207.00	865	10.748	218.30
503	0.754	22.92	861	10.347	217.00	892	12.137	228.30
532	1.007	23.77	863	10.372	217.60	918	13.523	238.30
554	1.412	24.78	890	11.617	227.70	922	13.777	329.70
565	1.548	25.79	917	13.210	237.70	903	12.618	249.80
570	1.652	26.79	919	13.192	238.30	877	11.316	259.80
574	1.728	27.79	896	11.882	248.30	867	10.832	263.00
588	1.998	28.57	869	10.549	258.00	840	9.563	273.00
613	2.411	29.57	843	9.397	268.00	812	8.395	283.00
642	3.014	30.58	816	8.227	278.00	784	7.267	293.00
673	3.842	31.59	814	8.173	278.60	757	6.315	303.00
700	4.566	32.43	788	7.186	288.70	729	5.354	313.00
731	5.490	33.44	760	6.14	298.70	701	4.438	323.00
745	5.904	34.45	759	6.167	298.90	673	3.639	333.00
748	6.017	35.45	732	5.263	309.00	645	2.832	342.50
752	6.238	36.46	704	4.350	319.00	616	2.150	352.60
776	7.032	37.47	702	4.518	319.30	589	1.633	361.50
804	8.163	38.48	674	3.479	329.30	560	1.236	371.50
832	9.345	39.48	648	2.910	338.80	534	1.079	379.70
861	10.696	40.49	619	2.093	348.80	502	0.957	389.80
864	10.858	40.62	592	1.537	358.00	479	0.612	397.20
892	12.325	41.62	562	1.395	368.00	445	0.456	407.30
912	13.344	42.63	537	1.176	376.30	422	0.607	413.60
915	13.375	43.64	506	0.636	386.40	388	0.880	423.70
915	13.295	44.65	481	-0.161	394.20	366	0.116	429.50
915	13.356	45.66	448	0.659	404.20	330	0.079	439.50
915	13.367	46.67	426	-2.712	410.50	311	0.086	446.60
915	13.593	47.67	392	0.730	420.60	300	0.492	456.70
915	13.303	48.68	371	0.132	426.20	297	-0.142	466.70
915	13.319	49.69	334	0.776	436.30	295	-0.144	476.70
904	12.450	50.69	315	0.702	442.80	295	0.405	486.70
864	10.086	51.21	305	0.032	450.30	295	-0.170	496.70
809	7.755	51.85	299	1.172	460.40	295	-0.033	506.70
755	5.773	52.54	297	1.171	470.40	295	0.410	516.70
699	4.154	53.37	296	-0.694	480.40	295	-0.213	526.70
644	2.962	54.35	295	1.168	490.40	295	-0.199	536.70
599	2.220	55.35	295	1.306	496.80			
590	2.025	55.56	295	1.468	506.90			
552	1.671	56.57						
534	1.479	57.13						
505	1.287	58.14						
480	1.354	59.15						

SENSOR IIE-S3

Implanted Sensor on Silicon Nitride

Five Cycles

Fourth Cycle			Fifth Cycle			Fifth Cycle (Continued)		
TEMP K	EMF MV	TIME MIN	TEMP K	EMF MV	TIME MIN	TEMP K	EMF MV	TIME MIN
295	0.025	0	296	-0.691	0	296	-2.671	600.10
295	-0.171	10.02	295	1.022	10.02	295	-3.032	610.10
295	0.514	20.03	295	0.278	20.03	295	0.724	620.10
295	-0.154	30.05	295	-1.641	30.05	294	2.391	630.10
309	0.326	39.66	309	1.207	39.01	294	3.483	640.10
349	0.585	49.66	350	0.178	49.02	294	1.748	650.10
365	0.250	53.86	365	4.790	53.14			
405	0.515	63.88	406	-2.326	63.16			
421	0.530	68.04	421	4.875	67.20			
459	0.518	78.10	460	-1.583	77.20			
477	0.670	82.99	477	-1.400	81.88			
513	0.893	93.01	514	1.924	91.90			
533	1.020	98.64	534	0.128	97.50			
567	1.209	108.70	568	0.743	107.50			
589	1.596	115.50	587	-0.266	113.70			
622	2.228	125.60	621	0.499	123.80			
644	2.742	132.70	644	1.068	131.00			
675	3.585	142.70	675	2.100	141.00			
699	4.264	150.20	699	2.926	148.80			
730	5.207	160.30	730	4.120	158.90			
755	6.009	168.80	755	5.085	167.10			
785	7.075	178.80	784	6.377	177.20			
810	8.026	187.10	810	7.428	185.60			
839	9.132	197.20	839	8.860	195.60			
866	10.268	206.70	866	10.436	205.20			
895	11.636	216.70	895	11.831	215.30			
922	12.969	225.70	922	13.030	224.10			
950	14.398	235.70	950	14.447	234.10			
978	15.767	245.50	977	15.911	244.00			
1006	16.969	255.60	1005	17.384	254.00			
1034	18.102	265.50	1034	18.584	263.90			
1062	18.818	275.50	1061	19.491	273.90			
1090	19.251	285.40	1089	20.205	283.90			
1116	19.808	295.30	1115	21.098	293.90			
1121	19.812	305.30	1125	21.102	303.90			
1117	19.730	306.70	1117	21.010	307.20			
1091	19.178	316.70	1089	20.378	317.30			
1063	18.366	326.70	1062	19.439	327.30			
1036	17.489	336.70	1034	18.204	337.20			
1007	16.368	346.70	1007	16.949	347.20			
980	15.252	356.70	980	15.532	357.20			
951	13.906	366.70	950	14.070	367.20			
924	12.646	376.70	924	12.752	377.20			
894	11.185	386.70	894	10.889	387.20			
867	9.928	396.00	867	9.291	396.50			
839	8.701	406.00	839	7.983	406.50			
811	7.469	415.50	810	6.476	416.20			
781	6.298	425.60	781	5.021	426.30			
755	5.293	434.30	755	3.198	434.90			
726	4.241	444.30	726	4.251	445.00			
700	3.302	453.10	700	1.011	453.70			
669	2.227	463.20	669	2.897	463.70			
645	1.430	471.00	645	0.362	471.50			
614	0.828	481.10	614	2.684	481.60			
590	0.652	488.60	589	-0.765	489.30			
558	0.211	498.60	556	0.452	499.40			
534	0.250	505.90	534	1.882	506.40			
500	1.112	516.00	500	0.895	516.50			
478	0.924	522.30	478	1.040	522.60			
443	1.056	532.40	444	0.584	532.60			
422	0.902	537.90	422	1.228	537.90			
387	0.855	547.90	386	0.383	548.00			
367	0.843	553.10	367	0.420	553.00			
326	-0.106	563.20	329	0.347	563.10			
310	-0.076	570.10	311	0.031	570.00			
295	3.553		302	-0.307	580.10			
			297	4.412	590.10			

SENSOR RFS-S1

RF Sputtered Sensor on Silicon Carbide

Seven Cycles

First Cycle			Second Cycle			Third Cycle		
TEMP K	EMF MV	TIME MIN	TEMP K	EMF MV	TIME MIN	TEMP K	EMF MV	TIME MIN
295	0.112	0	295	0.115	0	295	0.116	0
295	0.111	0.25	296	0.115	0.22	295	0.115	0.09
308	0.140	3.13	305	0.114	4.18	305	0.150	4.48
363	0.396	5.12	306	0.149	4.23	306	0.155	4.53
419	0.749	7.04	309	0.157	4.34	308	0.159	4.58
476	1.198	8.94	362	0.423	6.43	361	0.444	6.91
524	1.639	10.49	419	0.751	8.19	420	0.807	8.86
586	2.269	12.42	475	1.178	9.97	475	1.232	10.64
650	2.981	14.39	530	1.685	11.70	534	1.770	12.47
689	3.422	15.54	579	2.186	13.18	591	2.411	14.31
755	4.171	17.59	636	2.820	14.89	637	2.925	15.68
802	4.621	19.12	689	3.443	16.49	707	3.806	17.74
871	4.993	21.34	741	4.047	18.08	739	4.049	18.67
909	5.058	22.60	799	4.602	19.89	802	4.666	20.59
880	5.222	27.16	870	4.967	22.16	807	4.704	20.77
825	5.015	29.35	910	5.019	23.52	812	4.726	20.86
765	4.549	31.58	879	5.225	28.04	823	4.796	21.21
710	3.970	33.62	820	4.998	30.16	864	4.968	22.55
656	3.381	35.61	764	4.552	32.17	866	4.971	22.61
588	2.642	38.06	713	4.036	33.93	875	4.990	22.90
547	2.238	39.46	632	3.127	36.83	882	4.999	23.12
488	1.676	41.75	602	2.794	37.95	917	5.014	24.27
425	1.109	45.27	546	2.210	40.06	950	5.040	25.45
372	0.665	50.27	484	1.624	42.56	964	5.118	25.84
372	0.661	50.32	424	1.090	45.89	967	5.010	25.93
341	0.429	55.33	370	0.649	50.86	976	5.020	26.28
323	0.302	60.34	339	0.420	55.87	990	4.963	26.71
315	0.247	63.79	322	0.293	60.88	1009	5.049	27.39
307	0.196	68.79	314	0.240	64.32	1019	5.064	27.72
303	0.164	73.79	307	0.189	69.33	1039	5.104	28.51
300	0.145	78.80	304	0.172	72.06	1051	5.124	28.89
298	0.133	83.81	301	0.148	77.06	1110	4.864	30.98
297	0.125	88.81	299	0.133	82.06	1112	4.803	31.05
			297	0.125	87.07	1120	4.592	31.36
			296	0.120	92.08	1139	3.965	31.99
						1147	3.173	32.53
						1145	2.761	32.84
						1101	2.374	34.59
						1070	2.867	35.71
						1065	2.982	35.93
						1052	3.298	36.45
						1005	4.220	38.17
						996	4.384	38.50
						994	4.437	38.62
						960	4.870	39.75
						941	5.040	40.41
						929	5.123	40.81
						908	5.236	41.58
						883	5.288	42.48
						877	5.290	42.68
						867	5.287	43.03
						809	5.038	45.08
						807	5.022	45.18
						750	4.499	47.18
						740	4.397	47.52
						737	4.346	47.68
						733	4.314	47.79
						722	4.199	48.15
						679	3.705	49.69
						665	3.526	50.25
						629	3.097	51.60
						619	3.000	51.97
						567	2.441	53.93
						480	1.624	57.28

SENSOR RFS-S1

RF Sputtered Sensor on Silicon Carbide
Seven Cycles

Third Cycle (Continued)

Fourth Cycle

Fourth Cycle (Continued)

TEMP K	EMF MV	TIME MIN	TEMP K	EMF MV	TIME MIN	TEMP K	EMF MV	TIME MIN
428	1.117	60.44	295	0.112	0	482	1.608	62.03
371	0.662	65.45	295	0.112	0.25	426	1.082	65.50
340	0.426	70.46	307	0.156	4.63	371	0.646	70.70
323	0.298	75.47	363	0.472	7.31	323	0.297	80.70
315	0.248	78.64	420	0.870	9.53	314	0.241	84.54
308	0.195	83.65	476	1.316	11.47	304	0.173	92.53
303	0.164	88.66	531	1.820	13.33	299	0.138	102.60
300	0.144	93.67	590	2.457	15.28	297	0.122	112.60
299	0.132	98.68	607	2.605	15.72			
297	0.124	103.70	635	2.941	16.67			
297	0.119	108.70	655	3.180	17.32			
295	0.115	113.70	663	3.262	17.55			
295	0.114	118.70	663	3.262	17.6			
295	0.114	118.70	671	3.367	17.86			
			720	3.937	19.41			
			809	4.868	22.39			
			823	4.960	22.88			
			857	5.114	24.07			
			866	5.130	24.39			
			884	5.114	25.03			
			944	4.738	27.22			
			961	4.567	27.88			
			965	4.517	28.07			
			1021	3.928	30.17			
			1051	3.659	31.34			
			1076	3.387	32.3			
			1099	2.740	33.26			
			1103	2.600	33.41			
			1105	2.473	33.5			
			1129	-0.526	35.99			
			1130	-0.503	36.05			
			1100	0.238	37.21			
			1100	0.295	37.27			
			1085	0.810	37.88			
			1082	0.916	38.02			
			1070	1.376	38.49			
			1064	1.573	38.7			
			1059	1.760	38.9			
			1054	1.947	39.12			
			1035	2.622	39.94			
			1031	2.744	40.09			
			993	3.805	41.63			
			977	4.124	42.19			
			966	4.382	42.71			
			954	4.582	43.18			
			940	4.776	43.71			
			902	5.147	45.24			
			900	5.154	45.32			
			889	5.206	45.76			
			880	5.243	46.11			
			871	5.261	46.43			
			862	5.265	46.79			
			827	5.154	48.13			
			809	5.037	48.83			
			793	4.892	49.53			
			787	4.855	49.72			
			767	4.667	50.47			
			761	4.593	50.73			
			745	4.409	51.39			
			733	4.270	51.83			
			719	4.140	52.35			
			638	3.211	55.54			
			624	3.035	56.18			
			554	2.289	59.05			

SENSOR RFS-S1
RF Sputtered Sensor on Silicon Carbide
Seven Cycles

Fifth Cycle

TEMP	EMF	TIME
-------------	------------	-------------

Sixth Cycle

TEMP	EMF	TIME
-------------	------------	-------------

Seventh Cycle

TEMP	EMF	TIME
-------------	------------	-------------

SENSOR RFS-S2
 RF Sputtered Sensor on Silicon Carbide
 One Cycle

First Cycle			Second Cycle		
TEMP K	EMF MV	TIME MIN	TEMP K	EMF MV	TIME MIN
297	0.127	0	573	2.308	0
297	0.126	0.11	535	2.242	1.15
307	0.157	4.86	479	1.637	3.24
308	0.161	4.91	423	1.797	6.36
311	0.170	5.04			
364	0.429	7.46			
419	0.787	9.68			
476	1.208	11.67			
530	1.673	13.45			
587	2.256	15.37			
644	2.854	17.17			
687	3.347	18.58			
742	3.936	20.39			
800	4.545	22.35			
856	5.170	24.23			
907	6.041	26.06			
967	7.864	28.24			
1027	11.840	30.52			
1089	19.100	32.94			
1105	21.285	33.53			
1132	25.200	34.62			
1129	27.007	36.63			
1100	24.142	37.83			
1039	19.242	40.30			
990	15.365	42.28			
934	11.358	44.48			
880	8.391	46.58			
826	6.399	48.65			
770	5.070	50.80			
714	4.127	52.98			
659	3.400	55.14			
603	2.756	57.35			
547	2.171	59.63			
480	1.560	62.48			
424	1.067	65.81			
370	0.636	70.97			

APPENDIX B
SUMMARY OF SAMPLES AND TESTING TIMES

I. $\text{Y}_2\text{O}_3:\text{Eu}$ (e-beamed)

1. Mullite

- a. PWA/MEB1 9:20 @ 1000 – 1400°C (4 cycles)
- b. PWA/MEB2 5:20 @ 1300 – 1500°C (3 cycles)
- c. PWA/MEB3 4:14 @ 1400°C (1 cycle)
- d. PWA/MEB4 10:00 @ 1200°C (no laser)

2. Zirconia

- a. PWE/CGEB1 12:00 @ 1200°C
- b. PWF/CGEB2 _____
- c. PWG/CGEB3 4:30 @ 1200°C, 1400°C
- d. PWH/CGEB4 2:10 @ 1000°C, 1400°C

3. Silicon Carbide

- a. PWI/SCEB1 11:15 @ 1000°C, 1200°C
- b. PWJ/SCEB2 0:20 @ 1400°C
- c. PWK/SCEB3 0:30 @ 1400°C
- d. PWL/SCEB4 10:00 @ 1200°C (no laser)

4. Silicon Nitride

- a. PWM/SNEB1 _____
- b. PWN/SNEB2 10:10 @ 1200°C
- c. PWO/SNEB3 15:50 @ 1000 – 1400°C (7 cycles)
- d. PWP/SNEB4 2:45 @ 1400°C

5. Compglas®

- | | |
|-------------|---------------------------------------|
| a. PWQ/ZEB1 | 4:50 @ 1200 - 1400°C (melt at 1400°C) |
| b. PWR/ZEB2 | _____ |
| c. PWS/ZEB3 | _____ |
| d. PWT/ZEB4 | _____ |

II. Y₂O₃:Eu (RF sputtered)

1. Silicon Nitride

- | | |
|--------------|--------------------------|
| a. PW2/SNSP3 | 3:50 @ 1200 - 1400°C |
| b. PW3/SNSP1 | 5:20 @ 1000°C (2 cycles) |
| c. PW4/SNSP2 | _____ |
| d. PW5/SNSP4 | 12:35 @ 1200°C |

2. Silicon Carbide

- | | |
|--------------|----------------------------------|
| a. PW6/SCSP1 | 10:00 @ 1200°C (no laser) |
| b. PW7/SCSP2 | 11:30 @ 1000 - 1200°C (3 cycles) |
| c. PW8/SCSP3 | _____ |
| d. PW9/SCSP4 | 2:20 @ 1400°C |

3. Compglas®

- | | |
|--------------|-------|
| a. PWV/CGRF1 | _____ |
| b. PWY/CGRF2 | _____ |
| c. PWZ/CGRF3 | _____ |
| d. PWO/CGRF4 | _____ |

4. Zirconia

- a. PWU/ZRF1 0:30 @ 1200°C
- b. PWW/ZRF2 7:15 @ 1000°C, 1400°C
- c. PWX/ZRF3 14:00 @ 1200°C

III. YAG:Tb (e-beamed)

1. Mullite

- a. PU1/MYT1 0:25 @ 1300°C
- b. PU2/MYT2 4:05 @ 1400°C
- c. PU3/MYT3 4:00 @ 1500°C
- d. PU4/MYT4 10:00 @ 1500°C

2. Zirconia

- a. PU5/ZYT1 1:10 @ 1400°C
- b. PU6/ZYT2 2:51 @ 1400°C
- c. PU7/ZYT3 11:00 @ 1300 – 1500°C (3 cycles)
- d. PU8/ZYT4 4:15 @ 1500°C

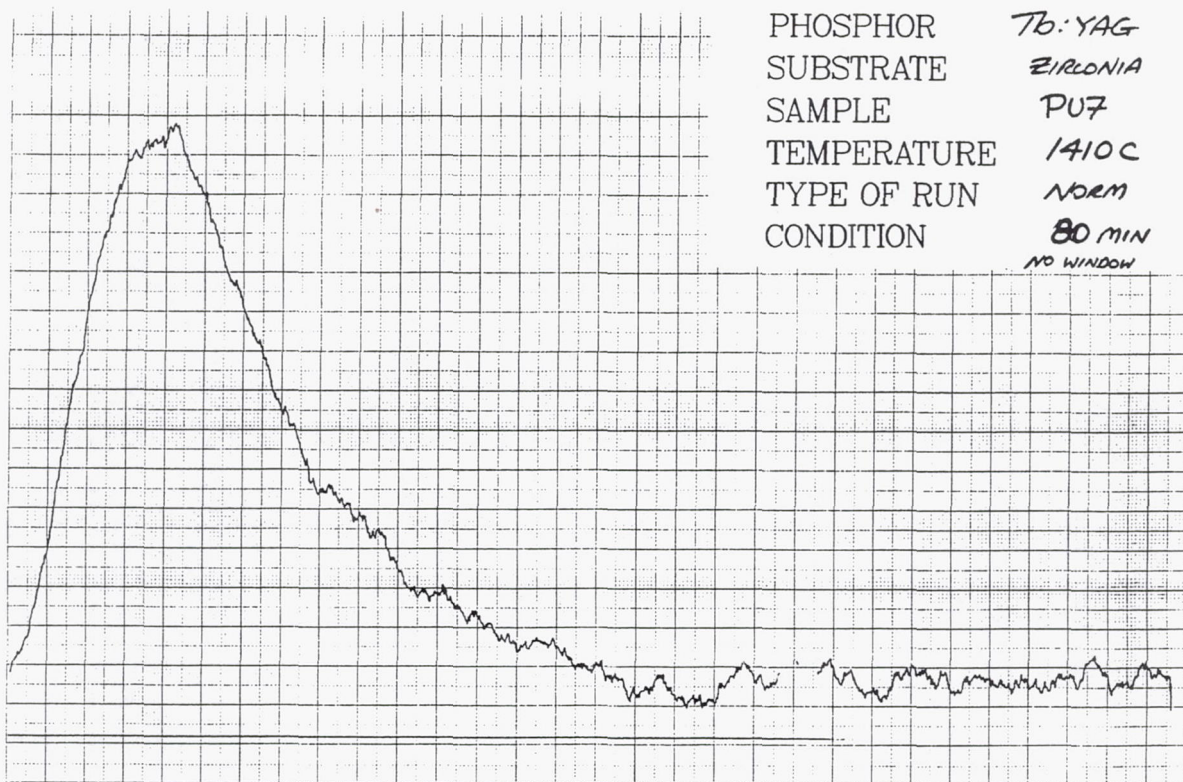
3. Silicon Carbide

- a. PUE/SCYT1 0:25 @ 1400°C
- b. PUF/SCYT2 0:40 @ 1500°C
- c. PUG/SCYT3 12:05 @ 1000°C, 1500°C
- d. PUH/SCYT4 4:05 @ 1500°C

4. Silicon Nitride

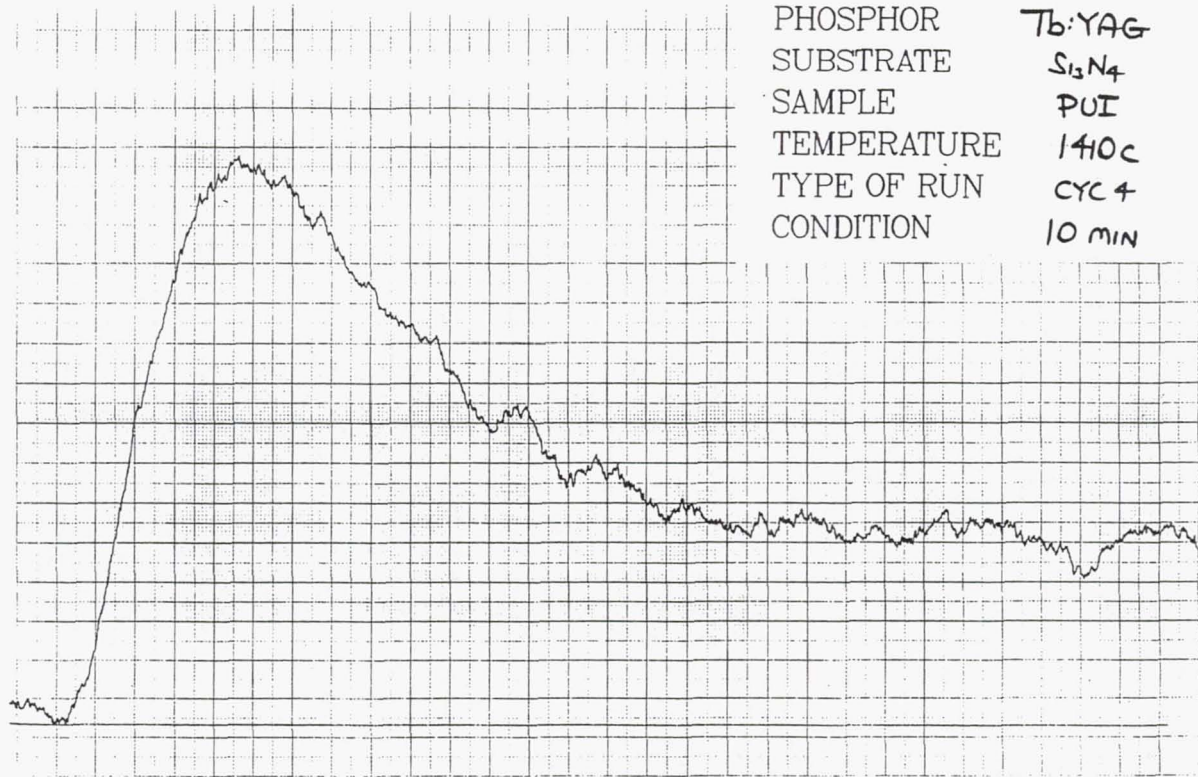
- a. PUI/SNYT1 4:54 @ 1400°C
- b. PUJ/SNYT2 1:50 @ 1400°C
- c. PUK/SNYT3 3:50 @ 1500°C
- d. PUL/SNYT4 10:00 @ 1500°C

APPENDIX C
SAMPLE RAW DATA OF THE PHOSPHOR SYSTEMS



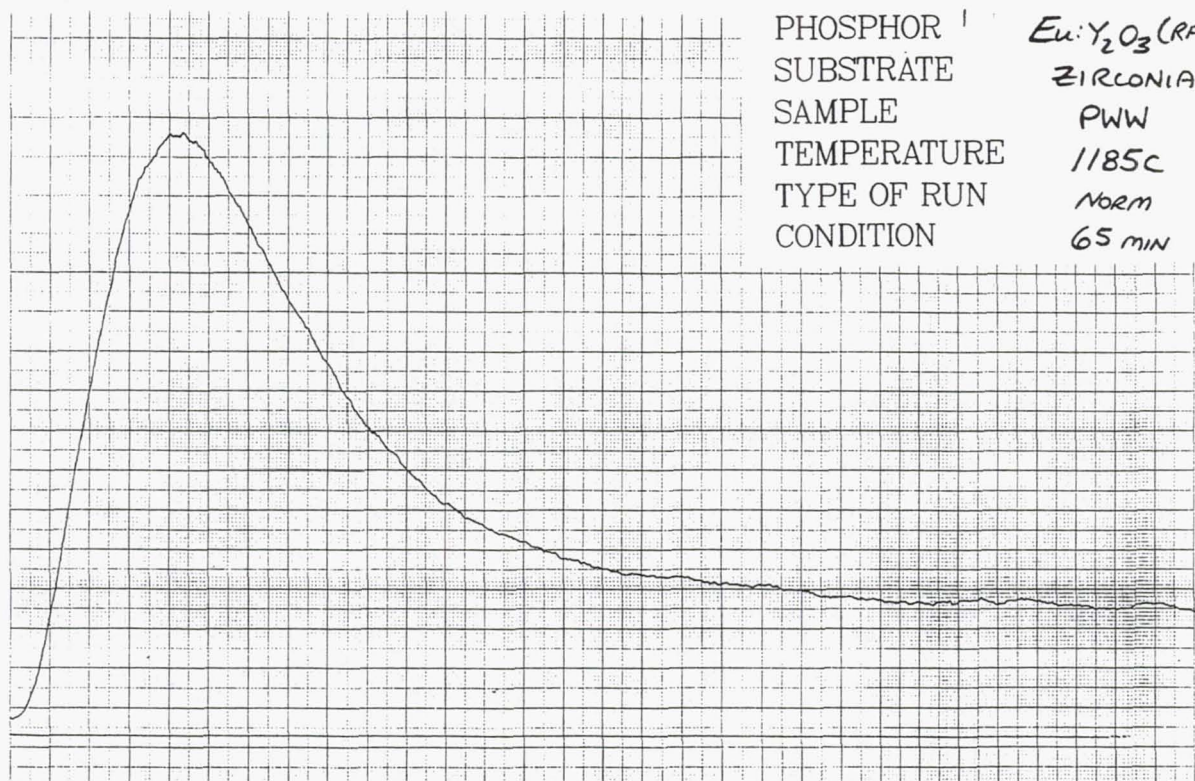
PHOSPHOR
SUBSTRATE
SAMPLE
TEMPERATURE
TYPE OF RUN
CONDITION

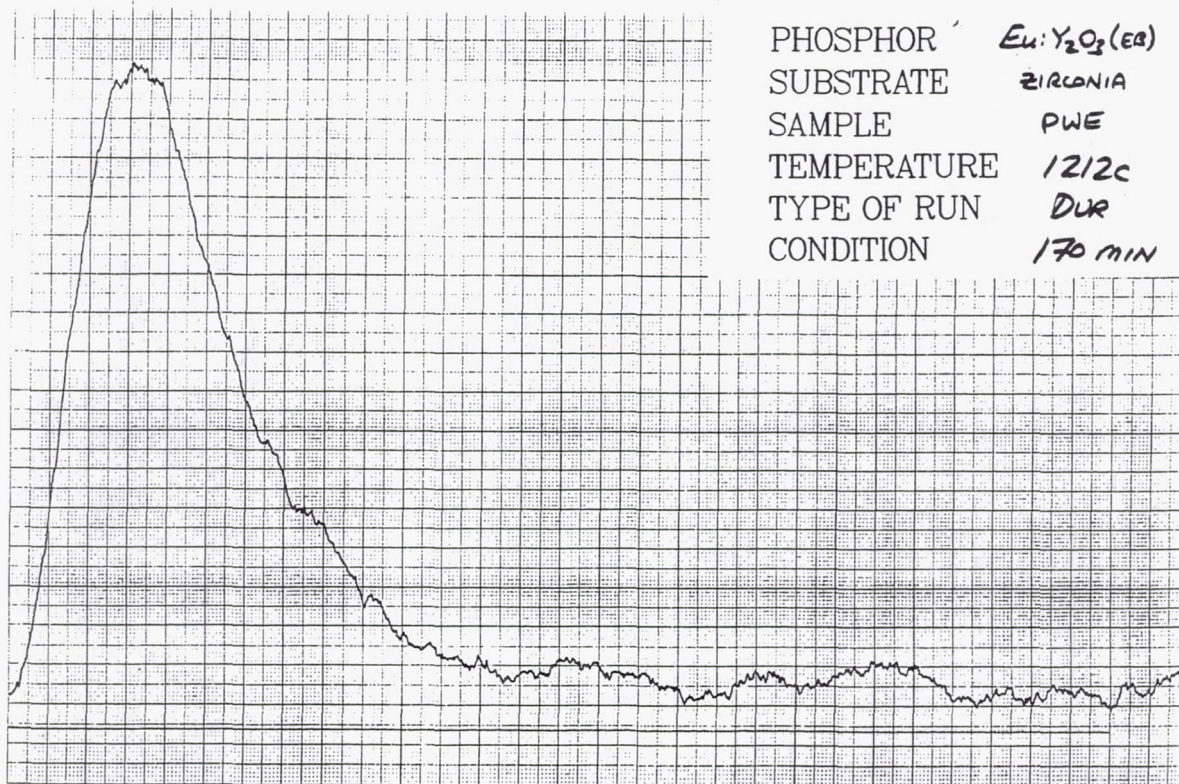
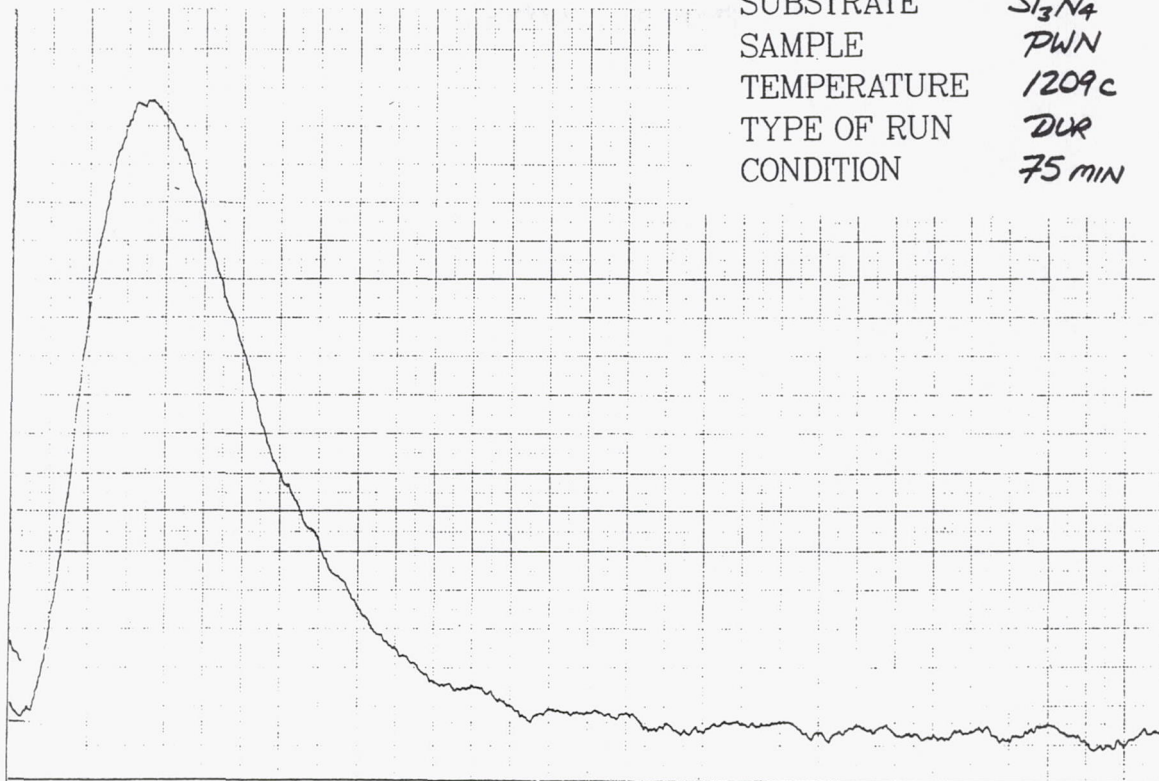
Tb:YAG
 $S_{13}N_4$
PUI
140C
CYC 4
10 MIN



PHOSPHOR
SUBSTRATE
SAMPLE
TEMPERATURE
TYPE OF RUN
CONDITION

$Eu:Y_2O_3$ (RF)
ZIRCONIA
PWW
1185C
Norm
65 min





REFERENCES

1. Atkinson, W. A., M. A. Cyr and R. R. Strange, "Development of Sensors for Ceramic Components in Advanced Propulsion Systems," NASA Contractor Report 182111, June 1988.
2. Dewitt, D. P., R. E. Taylor and P. E. Johnson, "Spectral Emissivity of Ceramics at High Temperatures: Silicon Carbide and Silicon Nitride," ASME Paper 79-Ht-24, August 1979.
3. Thermophysical Properties of High Temperature Solid Materials, Volumes 4 and 5, Perdue Research Foundation, 1967.
4. Wood, W. D., H. W. Deem and C. F. Lucks, "The Emittance of Ceramics and Graphites," Battelle Memorial Institute, December 9, 1986.
5. Liebert, C. H., "Emittance and Absorptance of NASA Ceramic Thermal Barrier Coating System," NASA TP1190, June 1978.
6. Saggese, S. J., J. A. Harrington and G. H. Segel, Jr., "Hollow Sapphire Waveguides for Remote Radiometric Temperature Measurements," *Electronics Letters*, Vol. 27, No. 9, 25 April 1991.
7. Noel, B. W., D. L. Beshears, et al., "Evaluating Thermographic Phosphors in an Operating Turbine Engine," 1990 ASME Turbo Expo - Land, Sea and Air, Brussels, Belgium, June 11-14, 1990 (ASME Paper 90-GT-266).
8. Bugos, A. R., S. W. Allison, D. L. Beshears and M. R. Cates, "Emission Properties of Phosphors for High Temperature Sensor Applications," Proceedings of the IEEE Southeastern Conference, Knoxville, Tennessee, April 10-13, 1988.
9. Tobin, K. W., S. W. Allison, M. R. Cates, G. J. Capps, D. L. Beshears and M. Cyr, "Remote High-Temperature Thermometry of Rotating Test Blades Using YVO₄:Eu and Y₂O₃:Eu Thermographic Phosphors," AIAA/ASME/SAE/ASEE 24th Joint Propulsion Conference, Boston, Massachusetts, AIAA-88-3147, July 11-13, 1988.
10. Noel, B. W., S. W. Allison, D. L. Beshears, et al., "Thermographic-Phosphor Temperature Measurements in Turbine Engines: Program Review 1986," Los Alamos National Laboratory, Los Alamos, New Mexico, March 1987 (LA-UR-87-979).
11. Lewis, W., W. D. Turley, H. M. Borella and B. W. Noel, "Noncontact Thermometry in Excess of 2500°F Using Thermographic Phosphors," ISA Proceedings 1990 (ISA, 1990 - Paper No. 90-103).

MAILING LIST

NASA Lewis Research Center
Attn: Dan Ng (25 copies)
MS 77-1
Cleveland, OH 44135

NASA Lewis Research Center
Attn: Report Control Office
MS 60-1
21000 Brookpark Road
Cleveland, OH 44135

NASA Lewis Research Center
Attn: Library
M. S. 60-3
21000 Brookpark Road
Cleveland, OH 44135

NASA Lewis Research Center
Attn: Wayne Girard
MS 500-305
21000 Brookpark Road
Cleveland, OH 44135

NASA Headquarters
Attn: Pam Richardson
Code R
Washington, DC 20546

NASA Center for Aerospace
Information
Attn: Accession Branch (25 copies)
P. O. Box 8757
Baltimore, MD 21240-0757

NASA Marshall Space Flight Center
Attn: William T. Powers
EB-225
Marshall Space Flight Center, AL
35813

NASA Marshall Space Flight Center
Attn: Joseph Zimmerman
Code EB-22
Marshall Space Flight Center, AL
35812

Air Force Wright Aeronautical
Laboratory
Attn: William Stange
WL/POTC
Wright Patterson AFB, OH 45433-7251

Air Force Wright Aeronautical
Laboratory
Attn: Mr Mervis Schmidt
WL/POTA
Wright Patterson AFB, OH 45433-7251

Arnold Engineering Development
Center
DOT
Attn: C. T. Kidd
Air Force Systems Command
Arnold Air Force Station, TN 37389

Arnold Engineering Development
Center
Attn: Carlos Tirres
AEDC/XXR
Arnold Air Force Station, TN
37389-1214

Arnold Engineering Development
Center
Attn: Gere Matty
AEDC/DOTP
Arnold Air Force Station, TN
37389-1214

Aviation Applied Technology Dir.
Attn: AMSAT-R-TP (Henry Morrow)
Ft. Eustis, VA 23604-5577

Los Alamos National Laboratory
ATTN: B. W. Noel
MS J572
P. O. Box 1663
Los Alamos, NM 87545

National Institute of Standards and
Technology
Attn: George Burns
Gaithersburg, MD 20899

National Institute of Standards and
Technology
Attn: Ken Kreider
221-B312
Gaithersburg, MD 20899

Oak Ridge National Lab
ATTN: M. Cates
P. O. Box 2003
MS 7280
Oak Ridge, TN 37831

Oak Ridge National Lab
ATN: S. Allison
P. O. Box 2003
MS 7280
Oak Ridge, TN 37831

AVCO Lycoming Textron
Lycoming Division
Attn: Steve Curry
Building 6
550 South Main Street
Stratford, CT 06497

Allied Signal Engines
Harvey Niska
P. O. Box 52181
Mail Stop 302-202
Phoenix, AZ 85010

Allied Signal Engines
Attn: Steve Mina
P. O. Box 52181
Mail Stop 302-202
Phoenix, AZ 85010

Allison Engine Co
Attn: Andrew Brewington
MS-W03A
P.O. Box 420
Indianapolis, IN 46206-0420

Allison Engine Co
Attn: Craig Dorste
MS-W03A
P. O. Box 420
Indianapolis, IN 46206-0420

Beamalloy Corp.
Attn: Cliff Lewis
6360 Dublin Industrial Lane
Dublin, OH 43017

Caterpillar Tractor Company
Research Department
Attn: Donald W. Heston
Technical Center, Building L
100 Northeast Adams Street
Peoria, IL 61629

EG&G Energy Measurements, Inc.
ATTN: W. D. Turley
MS 04
130 Robin Hill Road
Goleta, CA 93116

Eaton Corporation
Attn: Les Hayes
Director of Program Development
P. O. Box 766
Southfield, MI 48037

General Electric Company
Aircraft Engine Business Group
Attn: W. H. Bennethum
H78
Evendale, OH 45215

Kaman Sciences Corporation
Attn: Jolene Schneider
1500 Garden of the Gods Rd.
P. O. Box 7463
Colorado Springs, CO 80933-7463

Kulite Semiconductor Products, Inc.
Attn: David Goldstein
One Willow Tree Road
Leonia, NJ 07605

Lewis Engineering Company
Attn: James Dobbs
238 Water Street
Naugatuck, CT 06770

Massachusetts Inst. of Technology
Attn: Alan Epstein
Rm. 31-266
Cambridge, MA 02139

Medtherm Corp
Attn: Larry Jones
27604 Newby Rd
Huntsville, AL 35805

Orbital Technologies Corporation
Attn: Eric E. Rice
402 Gammon Place, Suite 10
Madison, WI 53719

PRC System Service
Attn: M. M. Lemcoe
P. O. Box 273
Facility Support Complex (FSC)
Edwards, CA 93523-5000

Public Service Elect. & Gas Company
Attn: Melvin L. Zwillenberg
Research & Development Dept.
80 Park Plaza
Newark, NJ 07101

RdF Corporation
Attn: Frank Hines
P. O. Box 490
23 Elm Avenue
Hudson, NH 03051

Rockwell International
Rocketdyne Division
Attn: Sarkis Barkhoudarian
6633 Canoga Avenue
Canoga Park, CA 91303

Rosemont, Inc.
Technical Library
Attn: Carolyn Hagford, Mail Stop
FL-21
P.O. Box 959
14300 Judicial Road
Burnsville, MN 55306

Spire Corporation
ATTN: Charles Blatchley
One Patriot Park
Bedford, MA 01730-6000

Spire Corporation
Attn: Roger G. Little
One Patriots Park
Bedford, MA 01730-2396

Stanford University
Attn: R. J. Moffatt
Asst. Prof., Mech. Engr.
Thermosciences Division
Stanford, CA 94305

Stein Engineering Services, Inc.
Attn: Peter K. Stein
5602 East Monte Rosa
Phoenix, AZ 85018-4646

Teledyne CAE
Attn: Marlene Dondell, Librarian
1330 Laskey Road
Toledo, OH 43612-0971

Thermogage, Inc.
Attn: Charles E. Brookley
330 Allegany Street
Frostburg, MD 21534

Titan Spectron
Attn: Pete Kenefick
1582 Parkway Loop
Suite B
Tustin, CA 92680

University of California, Los Angeles
Attn: Prof. R.F. Bunshah
Dept. of Materials Science and Engineering
6532 Boelter Hall
Los Angeles, CA 90024

University of Rhode Island
Attn: Prof. Otto Gregory
Room 110 Crawford Hall
Dept Chemical Engineering
Kingston, RI 02881

Williams International
Attn: Lance Shew
MS 4-10
P.O. Box 200
Walled Lake, MI 48390-2052

REPORT DOCUMENTATION PAGE

*Form Approved
OMB No. 0704-0188*

Public reporting burden for this collection of information is estimated to average 1 hour per response, including the time for reviewing instructions, searching existing data sources, gathering and maintaining the data needed, and completing and reviewing the collection of information. Send comments regarding this burden estimate or any other aspect of this collection of information, including suggestions for reducing this burden, to Washington Headquarters Services, Directorate for Information Operations and Reports, 1215 Jefferson Davis Highway, Suite 1204, Arlington, VA 22202-4302, and to the Office of Management and Budget, Paperwork Reduction Project (0704-0188), Washington, DC 20503.

1. AGENCY USE ONLY (Leave blank)			2. REPORT DATE October 1994		3. REPORT TYPE AND DATES COVERED Final Contractor Report	
4. TITLE AND SUBTITLE Sensors for Ceramic Components in Advanced Propulsion Systems Phase II—Temperature Sensor Systems Evaluation			5. FUNDING NUMBERS WU-505-62-50 C-NAS3-25141			
6. AUTHOR(S) W.H. Atkinson, M.A. Cyr, and R.R. Strange						
7. PERFORMING ORGANIZATION NAME(S) AND ADDRESS(ES) United Technologies Corporation Pratt & Whitney East Hartford, Connecticut 06108			8. PERFORMING ORGANIZATION REPORT NUMBER PWA-6113-55			
9. SPONSORING/MONITORING AGENCY NAME(S) AND ADDRESS(ES) National Aeronautics and Space Administration Lewis Research Center Cleveland, Ohio 44135-3191			10. SPONSORING/MONITORING AGENCY REPORT NUMBER NASA CR-195283 E-8627			
11. SUPPLEMENTARY NOTES Project Manager, Daniel L. P. Ng, Instrumentation and Control Technology Division, NASA Lewis Research Center, organization code 2510, (216) 433-3638.						
12a. DISTRIBUTION/AVAILABILITY STATEMENT Unclassified - Unlimited Subject Category 35				12b. DISTRIBUTION CODE		
13. ABSTRACT (Maximum 200 words) The "Development of Sensors for Ceramic Components in Advanced Propulsion Systems" program is divided into two phases. The objectives of Phase I were to analyze, evaluate and recommend sensor concepts for the measurement of surface temperature, strain and heat flux on ceramic components for advanced propulsion systems. The results of this effort were previously published in NASA CR-182111. As a result of Phase I, three approaches were recommended for further development: pyrometry, thin-film sensors, and thermographic phosphors. The objectives of Phase II were to fabricate and conduct laboratory demonstration tests of these systems. Six materials, mutually agreed upon by NASA and Pratt & Whitney, were investigated under this program. This report summarizes the Phase II effort and provides conclusions and recommendations for each of the categories evaluated.						
14. SUBJECT TERMS Ceramic; Temperature; Strain; Heat flux					15. NUMBER OF PAGES 158	
					16. PRICE CODE A08	
17. SECURITY CLASSIFICATION OF REPORT Unclassified		18. SECURITY CLASSIFICATION OF THIS PAGE Unclassified		19. SECURITY CLASSIFICATION OF ABSTRACT Unclassified		
20. LIMITATION OF ABSTRACT						